Dieter Scholz, Egbert Torenbeek (Editors)

Continuous Open Access Special Issue "Aircraft Design"

Number 3 / 2021
in the Journal "Aerospace"
Basel, Switzerland: MDPI, 2021

Affiliated to the CEAS Technical Committee Aircraft Design (TCAD)

Special Issue "Aircraft Design (SI-3/2021)"

Special Issue Editors

Prof. Dr. Dieter Scholz, MSME
Guest Editor
E-Mail: info@ProfScholz.de
Website: http://english.ProfScholz.de
Aircraft Design and Systems Group (AERO),
Department of Automotive and Aeronautical Engineering,
Hamburg University of Applied Sciences, Berliner Tor 9, 20099 Hamburg, Germany
Interests: aircraft design; flight mechanics; aircraft systems; open access publishing

Prof. em. Egbert Torenbeek
Honorary Guest Editor
Website: https://en.wikipedia.org/wiki/Egbert_Torenbeek
Flight Performance and Propulsion, Delft University of Technology, Kluyverweg 1,
2629 HS Delft, The Netherlands
Interests: aircraft design

Special Issue Information

Dear Colleagues,

Aircraft design is, as we know, the first fascinating step in the life of an aircraft, where visions are converted into reality.

In a practical sense, aircraft design supplies the geometrical description of the aircraft. Traditionally, the output is a three-view drawing and a list of aircraft parameters. Today, the output may also be an electronic 3D model. In the case of civil aircraft, a fuselage cross-section and a cabin layout are provided in addition.

In an abstract sense, aircraft design determines the design parameters to ensure that the requirements and constraints are met and design objectives are optimized. The fundamental requirements for civil aviation are payload and range. Many constraints come from certification rules demanding safety. The objectives are often of a financial nature, like lowest operating costs. Aircraft design always strives for the best compromise among conflicting issues.

The design synthesis of an aircraft goes from the conceptual design to the detailed design. Frequently, expert knowledge is needed more than computing power. Typical work involves statistics, the application of inverse methods, and use of optimization algorithms. Proposed designs are analyzed with respect to aerodynamics (drag), structure (mass), performance, stability and control, and aeroelasticity, to name just a few. A modern aircraft is a complex, computer-controlled combination of its structure, engines, and systems. Passengers demand high comfort at low fares, society demands environmentally friendly aircraft, and investors demand a profitable asset.

Overall aircraft design (OAD) comprises all aircraft types in civil and military use, considers all major aircraft components (wing, fuselage, tail, undercarriage) as well as the integration of engines and systems. The aircraft is seen as part of the air transport system and beyond contributing to multimodal transport. Aircraft design applies the different aerospace sciences and considers the aircraft during its whole life cycle. Authors from all economic sectors (private, public, civic, and general public) can submit to this Special Issue (SI). Education and training in aircraft design is considered as important as research in the field.

The SI can be a home for those active in the European Workshop on Aircraft Design Education (EWADE) or the Symposium on Collaboration in Aircraft Design (SCAD), both independent activities under the CEAS Technical Committee Aircraft Design (TCAD). Please see http://AircraftDesign.org for details.

Following the successful initial Special Issue on "Aircraft Design (SI-1/2017)" and the relaunch with "Aircraft Design (SI-2/2020)", this is already the third SI in sequence named "Aircraft Design (SI-3/2021)". The editorial "Publishing in 'Aircraft Design' with a Continuous Open Access Special Issue" describes the history, the set up, and idea behind this SI. It was published on 14 Jan 2020 as https://doi.org/10.3390/aerospace7010005.

Activities in the past showed that aircraft design may be a field too small to justify its own (subscription-based) journal. A continuous open access special issue may fill the gap. As such, the Special Issue "Aircraft Design" can be a home for all those working in the field who regret the absence of an aircraft design journal.

The Special Issue "Aircraft Design" is open to the full range of article types. It is a place to discuss the "hot topics" (zero-emission airplanes, electric flight, urban air mobility – you name it). The classic topics in aircraft design remain:

- Innovative aircraft concepts
- Methodologies and tools for aircraft design and optimization
- Reference aircraft designs and case studies with data sets

It is up to us as authors to shape the Special Issue "Aircraft Design" according to our interests through the manuscripts we submit.

Prof. Dr. Dieter Scholz and Prof. em. Egbert Torenbeek, Guest Editors

Table of Contents

Article

Oil Fumes, Flight Safety, and the NTSB

Judith Anderson [1,*] and Dieter Scholz [2]

1 Department of Air Safety, Health & Security, Association of Flight Attendants-CWA AFL-CIO, 501 3rd St. N.W., Washington, DC 20001, USA
2 Aircraft Design and Systems Group (AERO), Hamburg University of Applied Sciences, Berliner Tor 9, 20099 Hamburg, Germany; info@ProfScholz.de
* Correspondence: judith@afanet.org

Abstract: During its investigations into a series of ten aircraft crashes from 1979 to 1981, US National Transportation Safety Board (NTSB) officials were presented with a hypothesis that "several" of the crashes could have been caused by pilot impairment from breathing oil fumes inflight. The NTSB and their industry partners ultimately dismissed the hypothesis. The authors reviewed the crash reports, the mechanics of the relevant engine oil seals, and some engine bleed air data to consider whether the dismissal was justified. Four of the nine aircraft crash reports include details which are consistent with pilot impairment caused by breathing oil fumes. None of the tests of ground-based bleed air measurements of a subset of oil-based contaminants generated in the engine type on the crashed aircraft reproduced the inflight conditions that the accident investigators had flagged as potentially unsafe. The NTSB's conclusion that the hypothesis of pilot incapacitation was "completely without validity" was inconsistent with the evidence. Parties with a commercial conflict of interest should not have played a role in the investigation of their products. There is enough evidence that pilots can be impaired by inhaling oil fumes to motivate more stringent design, operation, and reporting regulations to protect safety of flight.

Keywords: aircraft; accident; flight safety; fumes; engine oil; hydraulic fluid

1. Introduction

With the exception of the Boeing 787, commercial and military aircraft are designed to "bleed" (or extract) ventilation air, either off the main aircraft engine compressors or from an auxiliary compressor when the aircraft is on the ground. This hot compressed "bleed air" is then cooled, dehumidified, typically mixed with some fraction of recirculated air, and routed to the cabin and flight deck for ventilation and pressurization [1]. To greater or lesser degrees—engine oil can contaminate the compressed air, whether it migrates across engine seals, spills from an overserviced reservoir, or is vented improperly, for example [2]. The problem with this design is that a fraction of that compressed air is then bled off the engine and routed to the air conditioning system for cabin ventilation and pressurization. The "bleed air" stream is not filtered, so oil fumes from the engine can be delivered directly to the occupied zones of the aircraft.

Concerns about aircrew exposure to either suspected or confirmed bleed-sourced fumes inflight have been raised globally since the 1930s on all types of aircraft [3–13]. One of the early references to pilots breathing "hot oil fumes" inflight acknowledged that "the symptoms in these cases have been similar to those of carbon monoxide poisoning," but noted that various aldehyde breakdown products are "probably the causative agents," which the author describes as present at concentrations that are "obviously sufficient to be dangerous to safety inflight" [14] (pp. 178–180).

Within this history, there are two documents which explicitly refer to fatal accidents associated with pilot impairment caused by oil-contaminated bleed air. One of those documents refers to "several unexplained fatal crashes involving single pack, carrier-based,

turbine-powered aircraft . . . attributed (rightly or wrongly) to contaminated engine bleed air" [15] (p. 1). In response to those crashes, the United States (U.S.) Air Force, Navy, and manufacturers apparently "initiated efforts to resolve the contamination problem" [15] (p. 1). The other document describes an investigation by the U.S. National Transportation Safety Board (NTSB) conducted in response to ten crashes on privately-operated turbo-prop planes, all equipped with the Garrett TPE331 engine [16]. NTSB investigators had hypothesized that "several" of the crashes could have been the result of the pilots being impaired by breathing oil fumes inflight. The suggested source of the oil fumes was a cracked front main shaft compressor carbon seal in the engine. In response, the NTSB initiated ground-based engine testing to assess what the pilots may have inhaled [16]. In conjunction, the U.S. Federal Aviation Administration (FAA) exposed test animals to oil fumes and observed the physiological effects [17]. Ultimately, the NTSB and their industry partners dismissed the hypothesis that inhaling oil fumes could have impaired any of the pilots [16]. The authors reviewed the evidence to determine if the dismissal was supported by the evidence that was available at the time. The authors also reviewed the relevant aviation regulations in the United States to consider whether they are sufficient to prevent inflight exposure to oil fumes.

2. Materials and Methods

Between August 1979 and April 1981, ten private aircraft, each outfitted with Garrett TPE331 engines lubricated with Exxon 2380 oil, crashed. The dates, location, aircraft types, and registration numbers are listed in Table 1, reproduced from the NTSB investigative reports [16].

Table 1. Accidents investigated for pilot incapacitation.

Crash No.	Date (yyyy-mm-dd)	Location	Aircraft Type	Registration No.
1	1979-08-03	Hays, Kansas	Mitsubishi MU-2B	N208MA
2	1979-11-01	Nashville, Tennessee	Mitsubishi MU-2F	N8730
3	1979-12-21	Provo, Utah	Mitsubishi MU-2B-20	N2-OBR
4	1980-01-11	Atlantic Ocean	Cessna 441	N441NC
5	1980-02-14	Near Houston, Texas	Mitsubishi MU_2B-35	N346MA
6	1980-02-23	New Orleans, Louisiana	Mitsubishi MU-2-40	N962MA
7	1980-12-06	Ramsey, Minnesota	Mitsubishi MU-2-40	N969MA
8	1980-12-15	Richmond, Indiana	Mitsubishi MU-2B-30	N93UM
9	1981-01-07	Burns, Oregon	Aero Commander 690B	N81521
10	1981-04-22	Alpena, Michigan	Mitsubishi MU-2B-20	N9JS

The authors searched online NTSB databases for the crash reports, nine of which were fatal accidents and one of which was a serious incident. The crash reports were only available on microfilm and, because of the COVID-19 pandemic, the NTSB library which houses microfilm reports was closed. Instead, the authors were able to purchase nine of the ten crash reports through a private company (General Microfilm, West Virginia). The remaining report was unavailable. Additional details of the 10 crashes are listed in Table 2.

The authors researched the design of the Garrett TPE331 engine and the associated potential for bearing and seal failures which could cause oil fumes to contaminate the bleed air supply.

The authors reviewed the NTSB investigative report which described the results of bleed air quality engine testing for selected oil-based contaminants in the bleed air supplied by a Garrett TPE331 engine with and without oil contamination [16]. The test protocol had been designed to "investigate the hypothesis that toxic or anesthetic gases could be generated from engine oil that leaked into the engine airflow through a broken seal and that these gases might adversely affect the crew's capacity to control the aircraft during critical phases of flight" [16] (p. 8). Key features of the bleed air tests are listed in Table 3.

Table 2. Additional details of ten accidents investigated for pilot incapacitation.

Crash No.	NTSB Report No.	Flight Phase, Time of Day, Weather	Pilot Age (Years), Flight Time (h)	Probable Causes/Factors (per NTSB)	No. Deaths ***
1 **	MKC79FA046	cruise, night, "clear"	34; 2168.	Forward main shaft bearing failed; improper inflight decisions; failed to obtain or maintain flying speed.	7
2	IAD80FA007	descent, night, three-mile visibility, dry, light fog	PIC age redacted; 1498. Copilot age redacted; 2521	Pilot-in-command (PIC) misjudged the distance and altitude on final approach; inadequate supervision of flight; failed to use checklist.	5
3	DEN80FA012	approach, night, "visibility was around one mile"	46; 12,833	Inadequate pre-flight preparation or planning; improper Instrument Flight Rules (IFR) operation; misjudged altitude; Pilot could not find runway; aircraft came to rest in water.	2
4 *	IAD80AA018	descent, night, check	47; 8000	Miscellaneous, undetermined; unable to obtain a response from crew; uncontrolled descent; aircraft came to rest in water.	3
5	FTW80FA042	approach, evening, two-mile visibility, rain showers	45; 12,500	Improper IFR operation; altimeter setting incorrect.	4
6 **	FTW80FA048	approach, morning, 0.25-mile visibility, fog	51; hrs. not reported	Improper IFR operation; crashed into water.	7
7 **	CHI81FA010	approach, afternoon, "good" weather	54; 4949	Failed to obtain/maintain speed; icing conditions, including sleet, frozen rain, etc.	5
8	CHI81FEG03	approach, night, dense fog	59; 10,587	Improper IFR operation; icing conditions, including sleet, frozen rain, etc.	0
9 **	SEA81FA015	approach, afternoon, overcast, 15-mile visibility, wind calm	32; 2177	Miscellaneous/undetermined; uncontrolled collision with ground/water.	2
10	CHI81FA051	approach, night, two-mile visibility, light rain, fog	53; 16,766	Improper IFR operation; crash on final approach, 1.6 miles short of runway; cause unknown.	3

* Microfilm report was unavailable for crash #4. ** Details in the reports for crash #1, 6, 7, and 9 are consistent with engine oil fumes as a contributory factor. Additional details are provided in Table 5. *** In all but crash #8, everyone onboard was killed. In crash #8, the pilot and one of two passengers were injured.

Table 3. Key features of engine bleed testing, per the NTSB investigative report [16].

Test No.	Carbon Seal Intact or Missing?	Oil Added to Bleed Air?	Glass Filter in Bleed Air Line?	Reflects Potential Onboard Conditions?
1	intact	No	yes	no
2	intact	No	yes	no
3a–3f	intact	yes; 2–12 lb/hr	yes	no
3g	intact	No	no	no
4	intact	No	yes	no
5a	missing	No	yes	no
5b	missing	yes; "dirty start"	yes	no

The authors reviewed the relevant aviation regulations for U.S.-registered aircraft operated on routine commercial flights (Table 4). Globally, aviation regulations are harmonized, so most of these regulations are the same in other countries. This is especially true for design and construction-related regulations which are classified under Part 25 of the Federal Aviation Requirements in the United States and as CS-25 (Certification Standards) in Europe, published by the European Union Aviation Safety Agency (EASA).

Table 4. U.S. aviation regulations relevant to air quality on routine commercial flights.

Regulation	Design/Operation	Description
14 CFR § 25.831(b) * "Ventilation"	Design	"The aircraft air supply system must be designed to ensure that crew and passenger compartment air [is] free from harmful or hazardous concentrations of gases or vapors."
14 CFR § 25.831(b)(1) "Ventilation"	Design	The carbon monoxide concentration in the cabin and flight deck supply air must not exceed 50 ppm.
14 CFR § 25.1309(c) "Equipment, systems, and installation"	Design	"Warning information must be provided to alert the crew to unsafe system operating conditions, and to enable them to take appropriate corrective action. Systems, controls, and associated monitoring and warning means must be designed to minimize crew errors which could create additional hazards."
14 CFR § 121.703(a)(5) "Service difficulty reports"	Operation	Airlines "shall report the occurrence or detection of each failure, malfunction, or defect concerning . . . [a] aircraft component that causes accumulation or circulation of smoke, vapor, or toxic or noxious fumes in the crew compartment or passenger cabin during flight."
14 CFR § 121.705 "Mechanical interruption summary report"	Operation	Airlines shall report each "interruption to a scheduled flight," such as a diversion, cancellation, or tail swap, caused by known or suspected mechanical difficulties or malfunctions that are not required to be reported under the 14 CFR § 121.703.
FAA Order 8020.11D (Chapter 6 and FAA Form 8020-23)	Operation	Airlines shall report accidents and occurrences which are associated with the operation of an aircraft and affect (or could affect) the safety of operation, including smoke/fumes.

* Note that "14 CFR" refers to the Code of Federal Regulations Title 14 which are aviation and aerospace regulations published by the FAA for U.S.-registered aircraft. The symbol "§" is shorthand for "Part" when referring to U.S. regulations. The relevant regulations include "Part 25" (Airworthiness Standards: Transport Category Airplanes) and "Part 121" (Operating Requirements: Domestic, Flag, and Supplemental Operations).

Finally, the authors reviewed some proposals to implement engineering and operational control measures intended to prevent exposure to oil fumes on aircraft.

3. Results

3.1. Accident Reports

For nine of the ten aircraft crashes, the authors were able to obtain the NTSB investigation reports (Tables 1 and 2). The microfilm report for crash number 4 was unavailable. Of these nine crashes, eight were fatal accidents (35 people were killed) and one (crash number 8) was a serious incident (the pilot and one of the two passengers were injured). Details in the accident reports for crash numbers 1, 6, 7, and 9 (Tables 1 and 2) suggest that oil fumes were either a contributory or casual factor (Table 5).

Table 5. NTSB accident report details consistent with exposure to oil fumes.

Crash No.	Description of Crash Conditions
1	The NTSB report describes how, when the pilot was en route, at what may have been top of climb, the pilot "reported a loss of oil pressure in the right engine." At the same time, "the pilot reported smoke and fumes in the cabin." A few minutes later, the pilot reported that he had shut down the right engine. He then stopped communicating with air traffic control and crashed into a field without putting the landing gear down (per witness reports). The subsequent teardown of the right engine "revealed that the forward main shaft bearing had failed."
6	The NTSB report describes how, on approach, the pilot stopped responding to air traffic control. The aircraft descended into a lake and "all aboard perished." The report goes on to say that "[d]uring the course of the investigation, it was reported by various persons that the aircraft had a history of smoke, fumes, and carbon monoxide collecting in the cockpit and cabin area...Examination of the interior of the subject aircraft environmental control system revealed an oily residue in the portion which is supplied by the left engine [with a history of a cracked carbon seal] while that supplied by the right engine was clean."
7	The NTSB report describes how, on approach, the pilot did not respond to air traffic control instructions. Witness reports described how the aircraft came out of the clouds spinning with the nose down and crashed into a field. In the engine tear down report, there were references to "black dirt deposits found throughout the entire gas path of the engine . . . [including] the bleed air ports . . . " The NTSB report stated that the pilot had failed to obtain/maintain speed and the cause of the crash was unknown.
9	The NTSB report describes how ground witnesses observed the aircraft flying away from the airport maneuvering erratically. The aircraft crossed a highway, pitched up steeply, fell, and crashed. The engine tear down was "to determine the condition of the carbon seal and bearing located between the compressor section and gearbox section." The report concluded that "one carbon seal, due to the discoloring of the oil slinger, was leaking some oil past the face." The report also noted that "Bonneville Power maintenance personnel felt the amount of leakage was insignificant," but the basis for their claim and their qualification to make it were not provided.

In addition to the four crashes described in Table 5, crash numbers 5 and 10 (Tables 1 and 2) include details which could be related to oil fumes, although the significance of those details is less clear. Specifically, the NTSB report for crash number 5 describes how, without warning, the aircraft crashed into the trees near the runway on final approach. Another pilot who observed the crash stated: "We feel that the pilot of the MU-2 got disoriented and just flew the airplane into the ground." The autopsy report for the pilot reported 5% carboxyhemoglobin in his blood. The NTSB report for crash number 10 describes how the aircraft crashed on final approach, after which the engine manufacturer performed the engine tear down to determine if oil fumes played a role in the crash. The manufacturer concluded that there was "no indication" of anything other than

normal engine operation and they attributed the engine compressor carbon seal damage to impact. The Civil Aeromedical Institute (CAMI) toxicology lab (the research arm of the FAA) tested a component of the air supply system from the aircraft and found a "trace quantity of petroleum base constituent," although the significance of that finding is not clear.

3.2. Description of the TPE331 Engine and Seal Assembly

The Garrett TPE331 is a fixed-shaft constant-speed turboprop engine (Figure 1). Its gas turbine consists of a compressor, combustion chamber, and turbine. Ambient air is directed to the compressor section through the engine inlet. A two-stage centrifugal compressor increases air pressure and directs it to the combustion chamber. In the combustion chamber, fuel is added to the air through the fuel nozzles. On engine start-up, the gas mixture is ignited by igniter plugs. In a normal operation the igniter is not in use because the combustion is self-sustained. The hot and high-velocity combustion gases flow through the turbine rotors, where the energy of the gases is converted to torque exerted on the main shaft (A in Figure 1). The reduction gear is designed as a planetary gear on the propeller shaft (B in Figure 1). It converts the low torque (at high rpm) of the main shaft to high torque (at low rpm) on the propeller shaft and drives the propeller. The combustion gases leave the turbine to the atmosphere via the exhaust.
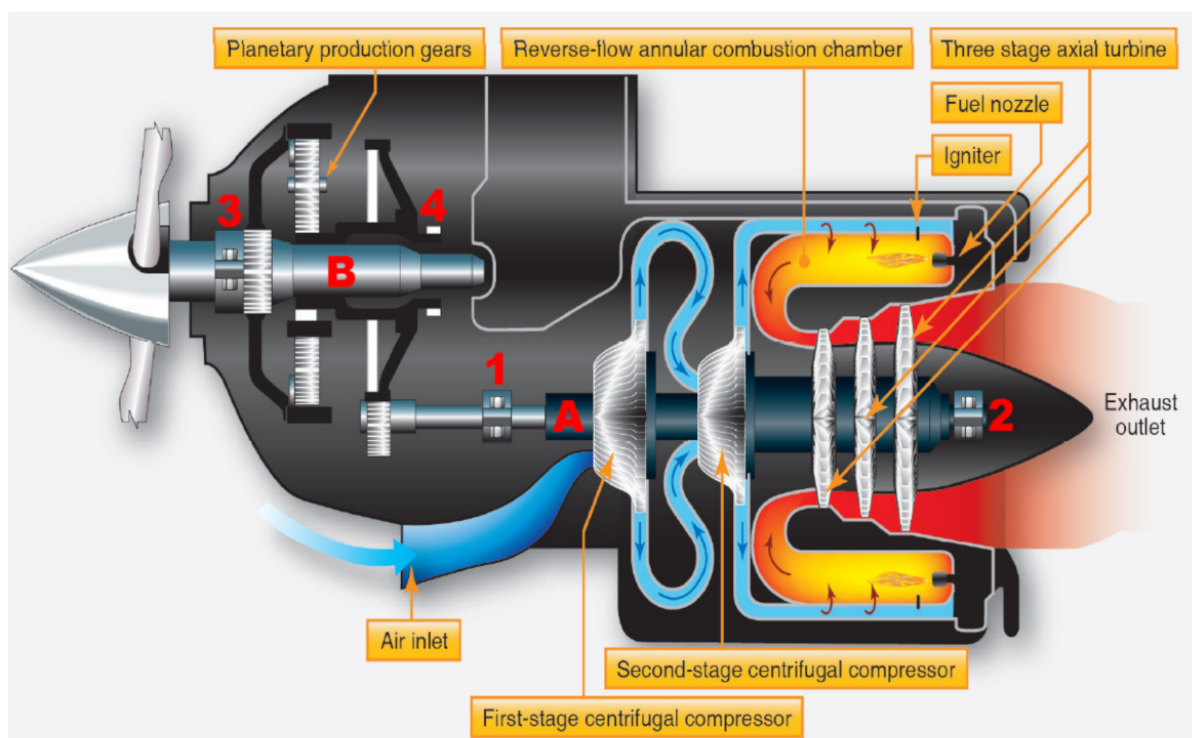
Figure 1. Garrett TPE331 turboprop engine (based on [18], p. 15-3). A. main shaft (engine shaft) with the gas turbine. B. propeller shaft with the reduction gear. 1,2. bearings that support the main shaft. 3,4. bearings that support the propeller shaft. 1. compressor bearing.

The TPE331 is called a fixed-shaft engine because the propeller is firmly connected to the gas turbine. The constant-speed engine maintains its speed by a governor on the propeller. The propeller shaft rotates at a constant speed of 1591 rpm in cruise flight. The main shaft of the engine rotates at a constant speed of 41,730 rpm. Power changes are made by increasing the fuel flow (which increases the torque) rather than the engine speed.

Most of the air (70%) passing through the engine provides internal cooling. Only about 10% of the air that passes through the engine is actually used in the combustion process. Up to approximately 20% of the compressed air may be bled off for the purpose of heating, cooling, cabin pressurization, and pneumatic systems [18], which appears to

be within the average range for other engine types [2]. If the bleed air is contaminated with oil fumes, then the air in the cabin is also contaminated. Normal bleed air pressure is approximately 157 psi (10.82 bar) and the temperature is 360 °C in cruise flight [16].

The engine shafts are supported by rolling bearings. The compressor bearing (1 in Figure 1) is a ball-bearing (Figure 2). The same is true for bearings 2 and 3 in Figure 1.

Figure 2. A typical ball-bearing [19].

The engine cutaway drawing is given in Figure 3 and a detail of that picture enlarged is given in Figure 4.
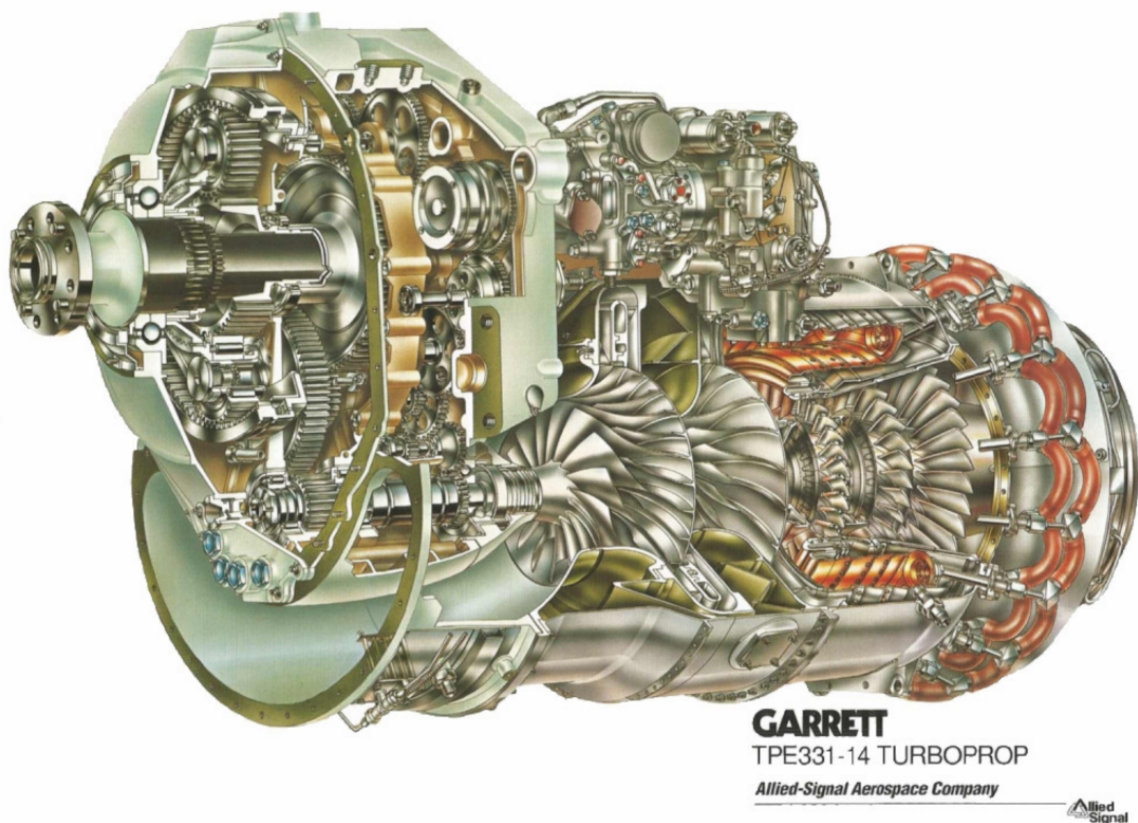
Figure 3. Garrett TPE331 turboprop engine cutaway drawing [20].

In the TPE331 front main shaft compressor seal assembly, two seals are used, acting in series. They prevent the escape of the engine lubricant present in the reduction gearbox via the main shaft and through the compressor bearing into the compressor (Figure 4). The following detailed explanations are reproduced with text elements from [16]:

"First, a mechanical (carbon) seal is provided to prevent leakage if operating oil pressures exceed normal pressures and to prevent potential leakage that might occur during engine

shutdown. The mechanical seal potentially is subject to wear and damage" [16] (p. 2). "When the engine is shutdown, oil drains from the engine walls which increases the oil level above the shaft installation level of the compressor front main shaft; without a mechanical seal, the oil would leak from the reduction gearbox, out the engine inlet and onto the ground. Therefore, a mechanical (carbon-element) seal is necessary to prevent oil leakage when the engine is not operating" [16] (p. 33). This is illustrated in Figure 5.
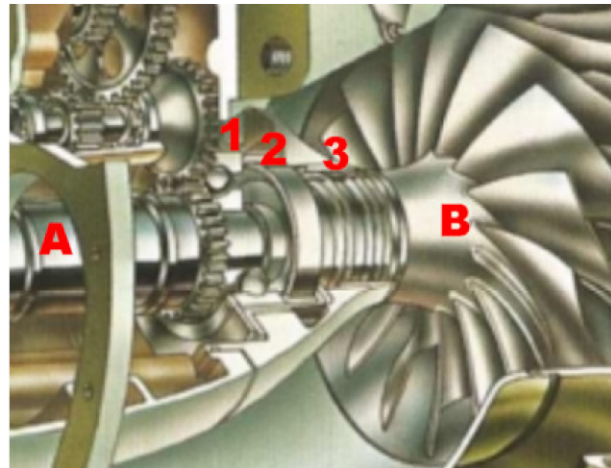
Figure 4. Garrett TPE331 turboprop engine cutaway drawing (detail based on [20]). A. main shaft. B. first-stage centrifugal compressor. 1. compressor bearing (a ball-bearing). 2. carbon seal. 3. labyrinth seal.
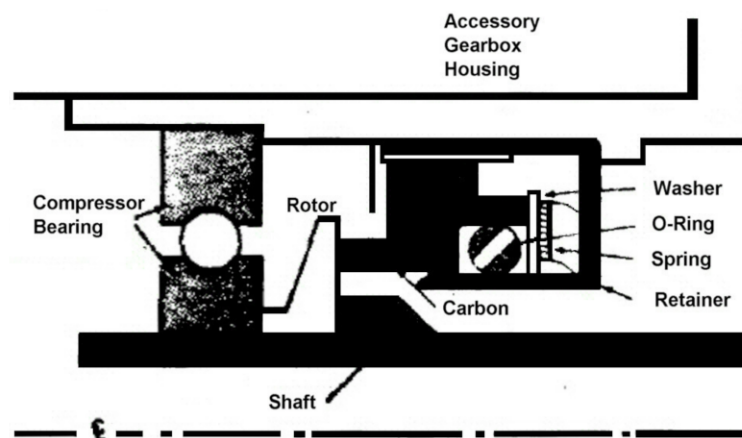
Figure 5. Mechanical (carbon) seal assembly next to the main shaft compressor bearing on the TPE331 engine (based on Figure 3 in [16]).

"Secondly, the TPE331 has a pressurized knife-edge labyrinth air seal that is specifically designed to prevent passage of air/oil mist from the reduction gearbox into the compressor chamber during engine operation" [16] (p. 2). "This pneumatic-type seal is pressurized to approximately 26 psi (1.79 bar) at the inner knife edges. When the engine is operating, the pneumatic seal is independently capable of preventing the air/oil mist from passing out of the reduction gearbox because of a flow of pressurizing air from the seal into the reduction gearbox. However, the labyrinth seal has no sealing capability to prevent engine oil from exiting the reduction gearbox when the engine is not operating and, therefore, requires a mechanical seal to prevent oil leakage when the engine is shut down. The symptom of a failed mechanical seal is oil leaking past the labyrinth seal and running out the engine inlet onto the ground when the engine is not operating" [16] (p. 35). The bleed air passage directs sealing air from the compressor to the labyrinth seal. All of this is illustrated in Figure 6 and additional details are shown in Figure 7.
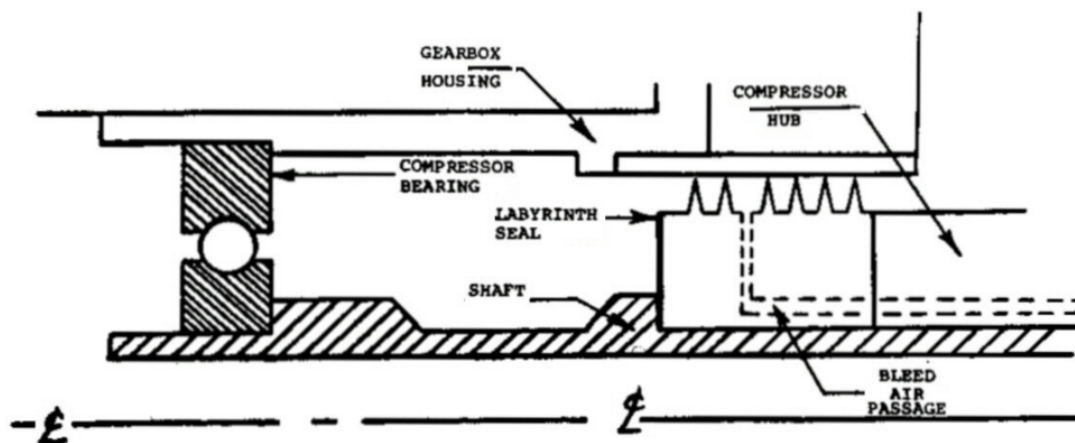
Figure 6. Labyrinth seal close to the main shaft compressor bearing (based on Figure 11 in [16]). Note: The carbon seal is located in between the compressor bearing (**on the left**) and the labyrinth seal (**on the right**) in the empty space but is not shown in this figure.
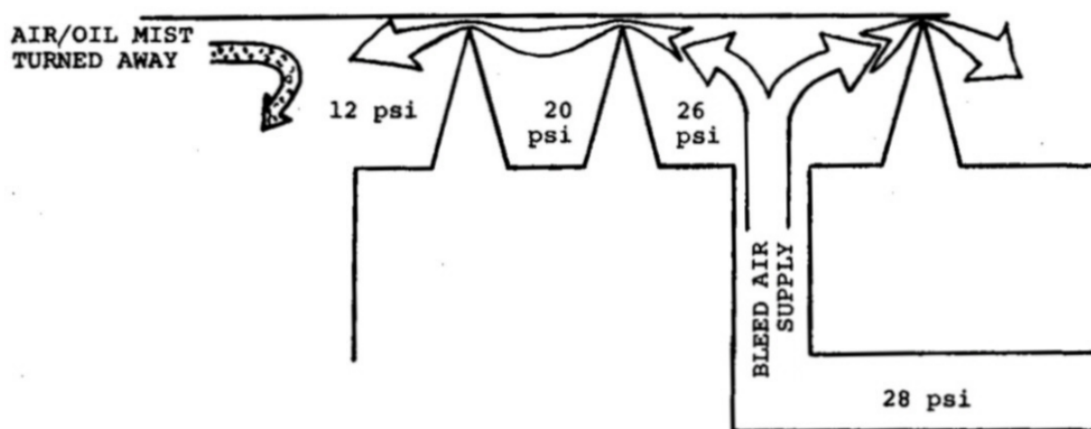
Figure 7. Flow through the labyrinth seal in the TPE331 engine next to the compressor bearing and resulting pressure. The flow to the left pushes back the oil that still comes through the carbon seal (based on Figure 13 in [16]).

"The pressure balances that are maintained may be clearly understood by considering that the chamber containing the air/oil mist operates at approximately 12 psia (−2 psig) while the center of the labyrinth is pressurized to 26 psia (+12 psig). Since air will always flow from a higher pressure area to a lower pressure area, air will flow outward from the center of the labyrinth. Each of the knife-edges operates with only slight clearance from the outer wall, resulting in a high local velocity as the air crosses into the next chamber. With a high local velocity, the air/oil mist cannot flow past the knife edges and enter the compressor air flow" [16] (p. 36). This is illustrated in Figure 7.

"In addition to the labyrinth seal, there are two other pneumatic sealing actions incorporated in the oil containment design of the TPE331 engine ... [First, there is] a negative pressure of approximately 2 psi inside the reduction gearbox with respect to atmospheric conditions. This is accomplished by pumping the oil out of the reduction gearbox at a rate twice that at which it is being pumped in. (Nine gallons per minute in, versus 18 gallons per minute out.) The extra nine gallons pumped per minute is air and this creates a negative pressure (slight vacuum) in the reduction gearbox. If the mechanical seal should fail, the overscavenging will draw air into the reduction gearbox and will prevent the air/oil mist from flowing out ... Secondly the negative pressure effect is supplemented by raising the pressure in the chamber on the air side of the mechanical seal to a positive six psi above ambient" [16] (p. 36). This higher pressure is produced by the centrifugal compressor.

3.3. Bleed Air Testing

In July 1981, the NTSB and a team of government and industry partners formed an "Ad Hoc Investigative Committee" to respond to the hypothesis that oil fumes could contaminate pilots' breathing air through the main shaft compressor carbon seal in the Garrett TPE331 turboprop engine. All the crashed aircraft flew with this engine type. The team proposed to measure selected gaseous contaminants (carbon monoxide, carbon dioxide, nitrous oxides, and total hydrocarbons) in the bleed air produced by that engine type. The goal was to attempt to reproduce the conditions on the crashed aircraft to determine whether the pilots could have been subjected to toxic or anesthetic gases sufficient to impair their ability to operate the aircraft.

Because oil leakage through the carbon seal was the suspected source of oil fumes in the bleed air, selected gaseous contaminants were measured in the bleed air downstream of the compressor, first through an intact seal and second with the seal removed (considered worst-case), during conditions that ranged from no oil to 12 pounds of oil per hour (lb/hr).

The sampling methods were developed by the Exxon Research and Engineering Company and the test conditions, summarized in Table 3, were performed on an engine test stand at the Garrett Turbine Engine Company. During two of the tests, oil mist samples were also collected and analyzed. Largely though, gases were sampled because the investigators "expected that particulate matter would not form" [16] (p. 9).

3.3.1. Primary Bleed Air Testing Conditions

The key features of the 12 primary engine bleed testing conditions, as described in the NTSB report [16] are summarized in Table 3. Additional salient details of the engine bleed testing are summarized in Table 6.

Table 6. Description of TPE331 engine bleed testing, per NTSB report [16].

Trial No.	Description of Sampling Conditions
1–2	These two trials were intended to characterize background levels of contaminants in the bleed air stream. The engine compressor carbon seal was intact, and a glass wool filter was installed in the bleed line. Moreover, oil was not purposefully injected into the bleed air stream.
3a–3f	These six trials were intended to characterize levels of oil-based contaminants in the bleed air stream through an intact engine compressor carbon seal and a glass wool filter. Oil was injected into the bleed air stream for 90 min at a rate of 2–12 pounds per hour while the bleed air was sampled for carbon monoxide, carbon dioxide, nitrous oxides, and hydrocarbons.
3g	This trial was intended to characterize levels of oil-based contaminants in the bleed air stream through an intact engine compressor carbon seal but without a glass wool filter in the bleed stream. The tester injected oil for 15 min, during which time the same gaseous bleed air measurements were made.
4	This trial was intended to simulate the potential for worst-case bleed air contamination by removing the engine compressor carbon seal. Of note, though, a glass wool filter was installed in the sampling line and no oil was injected.
5a	During this trial, the tester did not collect measurements but ran the engine for 10 min and then shut it down to prepare for a "dirty start" in the following test.
5b	During this trial, the engine underwent a simulated "dirty start" which involved internal oil ingestion. The tester measured the concentrations of carbon monoxide, carbon dioxide, nitrous oxides, and hydrocarbons for the first 10 min after the engine was started.

3.3.2. Additional Engine Bleed Air Testing

During two of the oil injection tests (3c and 3f), the tester collected oil mist samples on "membrane filters" which were subsequently analyzed for tricresyl phosphates. The authors of the report noted that no "para or ortho isomers" of tricresyl phosphate were

present above the detection limit [16] (p. 24), although the authors did not define the detection limit or mention the concentrations of meta and mixed meta/para isomers which comprise more than 99% of commercial blends [21].

During tests 1–3, carbon sorbent tubes and impingers were used to collect samples that were subsequently analyzed by GC-MS [16]. The authors stated that these "analyses performed by the Environmental Protection Agency (EPA) [lab] . . . did not lend themselves to meaningful interpretation because of apparent contamination of the samples and lack of parallel quantitation of known compounds . . . " [16] (p. 27). Still, the authors affirmed that "based on the analyses, there was no significant toxicological gaseous content of the TPE331 engine bleed air . . . " [16] (p. 27). The authors also referred to the presence of "a number of compounds in the bleed air under various conditions of the test protocol," but described occupational exposure limits as protective for workers. The report noted that, by comparison, "the concentration of those substances [measured by the EPA] appears to be at such a low level as to cause no acute degradation of pilot performance" [16] (p. 66). Specifically, the authors stated that "it is apparent that toxic effects to aircraft crewmembers would only result from breathing air contamination of sufficient concentrations to cause acute effects" [16] (p. 66).

3.4. Regulations

Aircraft regulations stipulate that the cabin and flight deck ventilation supply systems must be designed to provide air that is "free from harmful or hazardous concentrations of gases and vapors" (14 CFR § 25.831(b)), which includes no more than 50 ppm of carbon monoxide and 5000 ppm of carbon dioxide (Table 4). Moreover, crews must be provided with "warning information" to alert them to unsafe conditions and enable them to take "appropriate corrective action" (14 CFR § 25.1309(c)) (Table 4). To date, though, these regulations have not been applied to monitor contaminants in the cabin air and alert pilots to the presence of oil fumes.

In addition to the design regulations, U.S. airlines are required to comply with three FAA reporting regulations for fume events (Table 4), but all are underutilized [22].

4. Discussion
4.1. Accident Reports

In the investigated crashes (Table 1), eight of the ten aircraft were Mitsubishi MU-2 aircraft. The Mitsubishi MU-2 is a twin-engine turboprop aircraft with a pressurized cabin (Figure 8). The aircraft is known for its difficult handling and high rate of accidents, including fatal accidents [23]. Crash numbers 7 and 8 with this aircraft were in icing conditions which may be relevant, given an Australian Bureau of Air Safety Investigation report on two fatal crashes on MU-2 aircraft, both of which were also in icing conditions [24]. However, even for the 1988 and 1990 fatal crashes in Australia, "icing on the airframe" was only listed as the "probable" cause and, for one of those two crashes, pilot fatigue was also referenced extensively. Thus, the reference to icing conditions in crash 7 in this investigation should be acknowledged but does not rule out cabin air contamination, either as a causal or contributory factor.

Regarding the remaining two crashed aircraft (Table 1), one was a Cessna 441 Conquest II and the other was an Aero Commander 690B. As with the MU-2, each of these is a turboprop aircraft with a pressurized cabin.

In at least four of these ten crashes, there are details which are consistent with impairment caused by oil fumes (Table 5). For each of the crashes, the NTSB identified "probable causes" (including "undetermined"), all of which are reproduced in Table 2. In many cases, though, the "probable cause" is more of a description than an explanation. The real question is, why? Why did the pilot in command "misjudge distance and altitude" or "fail to obtain/maintain speed"? Why was air traffic control "unable to get response from crew"? Was it because these pilots were distracted or fatigued, or were they impaired by fumes?

Figure 8. Mitsubishi MU-2B (Photograph by Alan Lebeda [25], trimmed, GFDL 1.2).

It is tempting to blame crashes on "pilot error," typically attributed to either to inexperience or fatigue. Regarding inexperience, the flight time for the pilots on the crashed planes ranged from 1498 to 16,766 h (average 7999) (Table 2). One analysis estimated that, during the time of these crashes, turboprop pilots logged an average flight time of 528 h per year [26], so if the pilots on the crashed planes reflect this average, they are not novices. Regarding fatigue, the accident reports did not consistently cite either each pilot's total flight time specific to the aircraft type they crashed or the number of hours they flew during the 24 h prior to the accident flights. As a result, the impact of pilot fatigue cannot be assessed.

The authors of this paper are unaware of other challenges to the basis for the claims in the NTSB report [16] that it is not possible for oil fumes to either have contaminated the bleed air on these aircraft or to have played any role in any of these accidents.

Theirs is not the first report, however, to either overlook or downplay the flight safety implications of breathing oil or hydraulic fluid fumes. For example, one published case study investigated the findings of six documented fume event investigations and identified specific oversights and misconceptions about the potential for oil to contaminate the bleed air, as well as a tendency to dismiss the crew-reported symptoms as stress reactions [27]. Another investigation described an event during which pilots reported a blue haze shortly after reaching cruise altitude, prompting a precautionary landing [28]. The initial ground-based engine runs failed to identify any fault. Only additional (and non-standard) high-power engine runs identified the source of fumes—a fractured bearing seal in the compressor. This is important because high-power runs were not part of the fault-finding procedure endorsed by the aircraft manufacturer.

Another investigation described how both pilots reported fumes during approach and felt dizzy and nauseous, with irritated eyes and throat [29]. The pilots donned oxygen and requested priority landing clearance. The auxiliary power unit (APU) was not operating during the approach phase, so it was not investigated as a potential source of oil contamination. However, the aircraft manufacturer has published bulletins alerting airlines that, when the APU is in use, oil fumes can contaminate the downstream environmental control system and ducting, and fumes from that initial contamination can continue to manifest inflight, even when the APU is not in use [30]. Still, the APU was not checked, and the investigation was inconclusive; "no explanation" for either the fumes or the symptoms was found.

In 2020, the French Bureau of Enquiry and Analysis for Civil Aviation Safety (BEA) investigated a serious incident on a commercial flight during which the pilots reported a strong, acrid odor accompanied by irritant symptoms during taxi, shortly after the APU had been turned on [31]. During the climb out, both pilots reported dizziness, among other symptoms. They eventually donned oxygen masks and diverted to the nearest airport.

Although the details are consistent with breathing bleed-sourced oil fumes, maintenance inspections did not identify an obvious mechanical failure. As a result, the accident investigator concluded that the incident—including fumes, persistent symptoms, and a diversion—was most likely caused by the pilots inhaling "an excessive quantity of carbon monoxide." Failing to find a more plausible explanation, the accident investigators hypothesized that the source of the fumes may have been engine exhaust from a small business jet as it taxied about 80 m away from the incident aircraft in the presence of a "calm wind." However, the report added that it "cannot be excluded that the crews were intoxicated by another substance." This incident highlights the value of installing and operating sensors onboard, both to provide real-time information to the pilots and assist maintenance in subsequent troubleshooting.

Other than its investigation into these ten turboprop crashes in 1979–1981, the NTSB has not weighed in on the flight safety implications of pilots inhaling oil-contaminated bleed air inflight. This is contrary to its counterparts in Australia [32,33], Germany [4], Iceland [34], Ireland [35], New Zealand [36], Spain [5], Sweden [37], Switzerland [7], and the UK [3,6], for example. Each of those safety boards has investigated one or more commercial flights involving pilots whose inflight impairment compromised flight safety and has concluded that breathing contaminated bleed air either likely or definitively played a role. The NTSB does require airlines to report onboard fume/smoke events, but only if either the aircraft sustained structural damage or if specific health impacts were reported by one or more occupant (49 CFR § 830.2). However, oil fume events that meet the NTSB reporting criteria have not been investigated.

4.2. Bearing and Seal Failures in the TPE331 Engine

The description in [16] of the two seals in series contains some contradictions. According to the explanation, the carbon seal is necessary because "when the engine is shutdown, oil drains from the engine walls which increases the oil level above the shaft installation level of the compressor" [16] (p. 33). The labyrinth seal is necessary because the carbon seal is potentially "subject to wear and damage" [16] (p. 2). So, if the carbon seal is worn or damaged, then the oil will flow out of the reduction gearbox into the compressor and contaminate the cabin air when the engine is next started up. This situation was investigated in test 5 [16].

It is known that all seals leak in small quantities [38]. Pressure differentials assumed by the manufacturer may not be present in failure cases. Moreover, pressure differentials may not be sufficient during rapid thrust reduction or at idle thrust. In test 4, it was assumed only that one of the two seals in series (the carbon seal) would have failed. The labyrinth seal was left intact. Certainly, a mechanical failure that causes the carbon seal to fail may also cause the labyrinth seal to fail at the same time. For example, a failure of the main shaft compressor bearing could cause the main shaft to vibrate or rotate eccentrically which could severely damage (or even destroy) both seals.

In addition to crash number 1 (Table 5), an TPE331 compressor bearing failure which caused the engine to fail was documented by the Australian Transport Safety Bureau (ATSB) [39], although without either fatalities or reference to oil fumes. That report described the history of compressor bearing failures on the TPE331 engine which peaked in the early to mid-1980s. Garrett attributed the compressor bearing failures to propeller strikes and subsequently revised the engine maintenance manual, which—by the 1990s—reduced the number of failures. In the accident investigated by the ATSB, when the compressor bearing failed, the bearing cage fractured which caused the balls to come loose. Such loose components can collide with and cause damage to numerous internal rotating engine components, including the compressor seals.

4.3. Bleed Air Testing

Regarding the engine bleed air testing reported by the NTSB [16], the conditions in trials 1–4 did not represent the conditions of concern on the crashed aircraft because the

engine compressor carbon seal was intact and, in all but one case, the air was filtered for vapor and particulate. No measurements were collected during trial 5a. Regarding the relevance of conditions tested during trial 5b, on the one hand, the bleed air would have contained oil from the dirty engine start, but it is not clear if this is the same volume and pattern of oil as with a faulty engine compressor carbon seal inflight. Moreover, the bleed air had been passed through a glass wool filter for vapors and particulate, unlike on the crashed aircraft. Finally, it is not clear if the temperatures in the test stand compressor reflected inflight conditions.

It is important to carefully consider the question of the temperature in the engine compressor on these crashed aircraft. In its report, the NTSB referenced some certification data collected by a major engine manufacturer after injecting oil into a large turbofan engine. The tests showed that that carbon monoxide formation was detectable starting around 316 °C [16] (p. 7). The report also notes that TPE331 engine has a standard compressor discharge temperature of 360 °C [16] (p. 6) with a maximum temperature of 386 °C [16] (p. 25). The compressor temperature was high enough for carbon monoxide to be generated in the presence of oil, but the authors claim that the concentration of carbon monoxide would have been too low to cause impairment [16] (p. 2). The authors also rule out the presence of other oil decomposition products (such as acrolein) sufficient to irritate the mucous membranes by noting that "a number of participants sniffed the bleed air lines . . . [and] no one described an acrid or irritating quality"; [rather] "the consensus was that the odor was that of a warm oil, not a decomposed oil" [16] (p. 27).

In a companion study, CAMI researchers exposed test animals to Exxon 2380 oil for seven hours without, what the NTSB called, "any immediate or delayed behavioral change" [16] (p. 28). The CAMI report does describe an experiment with rats and chickens exposed to aerosolized (but unheated oil) in which the animals seemed unaffected [17] (p. 14). However, in the same study the CAMI researchers reported that, when the engine oil was heated, carbon monoxide started to form at 306 °C and when rats in one trial were exposed to oil fumes heated to 350 °C for 30 min, "it was obvious that the animals were approaching incapacitation" [17] (p. 8). Moreover, when the temperature was further increased, the animals "expired." Unlike the rats, the pilots on the crashed planes would have inhaled oil fumes in a reduced pressure environment with a corresponding reduction in the partial pressure of oxygen in the ambient air.

More recent sampling data has highlighted the presence and potential health impact of elevated levels of ultrafine particles in the bleed air supplied to the cabin and flight deck on commercial aircraft [40–44]. As noted above, the authors of the NTSB report assumed that "particulate matter would not form" [16] (p. 9), and so did not assess any associated toxicity.

4.4. Regulations

In the 1960s, a report from an aircraft manufacturer (Douglas Aircraft Corporation) describes the need to "show that the level of contamination required for olfactory warning is well below the generally accepted tolerance limits for the toxic materials produced" [15] (p. 3). In 1960, U.S. aircraft manufacturers would have been required to demonstrate to the U.S. Civil Aeronautics Board (which predated the FAA) that aircraft systems were designed to provide ventilation air "free from harmful or hazardous concentrations of gases or vapors", which included (but was not limited to) the carbon monoxide concentration not exceeding 50 ppm [45]. Presumably, this is what motivated Douglas Aircraft Corporation to propose testing to demonstrate that, "under all possible oil leakage rates," olfactory warnings would give pilots sufficient time to "permit effective crew countermeasures." [15] (p. 3). Essentially, tests needed to show that pilots would smell oil fumes before they would be impaired, proving that the presence of oil-based contaminants in bleed air was safe.

Since then, many studies and reports discuss the presence of airborne contaminants in cabin air and comment on whether the levels are "safe" or "acceptable" [40,46–48]. "Acceptability" has more commonly been framed in the context of comparing aircraft data

to published exposure limits for individual chemical constituents [16,40,49,50], although this approach is not without criticism [51,52].

The quest to define "safe" or "acceptable" concentrations of oil-based compounds is likely borne from the need for industry to comply with the regulation that the aircraft supply system be designed to supply air that is "free from harmful or hazardous concentrations of gases or vapors" (14 CFR § 25.831(b)). If something is acceptable—if it is not harmful—then the design meets the regulation. Interestingly, though, the FAA does not define "harmful or hazardous" beyond its limits for carbon monoxide (14 CFR § 25.831(b)(1)) and carbon dioxide (14 CFR § 25.831(b)(2)) and it had not done so in the early 1980s either. Applying published exposure limits for individual chemicals to complex mixtures [53] (Appendix 10) is problematic [54], especially in a reduced pressure and safety-sensitive environment [52]. This is in part because exposure limits do not exist for every constituent in these mixtures and the various constituents have a variety of toxicity endpoints. Moreover, the diversity of exposure limits published by different authorities for a single chemical illustrates the fallacy that a single number can define the boundary between what is and is not acceptable. In the case of the FAA, their limits for carbon monoxide and carbon monoxide are as high—or higher—than published chemical exposure limits for ground-based application. So, given this gap in the regulatory framework, in 1981, the NTSB and their industry colleagues defined "safety" for themselves—not in the context of certification regulations, but in the context of whether pilots could have been impaired.

The authors of the 1984 NTSB report acknowledged that carbon monoxide would be generated when oil was purposefully introduced into the compressor section of the TPE331 engine, but they noted that it should be "well below permissible limits in the bleed air" [16] (p. 2). However, the permissible exposure limit for carbon monoxide is not a useful benchmark for safety. An applied research study into the effects of exposure to carbon monoxide inflight concluded that "the maximum permissible concentration of carbon monoxide in pressurized passenger airplane cabins should be 0.01 mg/liter," which is equivalent to 8.7 ppm [55]. By comparison, the permissible aircraft design limit for carbon monoxide is 50 ppm (14 CFR § 25.831(b)(1)) which is, inexplicably, as high, or higher than ground-based limits. This, even though it is primarily applied in a reduced pressure environment (14 CFR § 25.841(a)) with a corresponding reduction in the partial pressure of oxygen available to occupants. Safety of flight depends on pilots' alertness and reaction time which can be compromised by exposure to asphyxiants, such as carbon monoxide [56]. Moreover, aircraft occupants have no means of egress once the doors are closed, such that an additional safety factor regarding exposure to carbon monoxide is warranted. Finally, carbon monoxide is only one element of a complex chemical mixture.

4.5. Exposure Control Measures

Just as the flight safety implications of breathing oil and hydraulic fluid fumes have been well documented, the need for control measures has also long been recognized. In 1966, an aircraft manufacturer reported that, in response to the evidence that contaminated bleed air could have caused some fatal crashes, the Navy required that crewmembers breathe 100% oxygen from takeoff to landing [15]. In 1955, an engineer with North American Aviation described the outcome of a two-year investigation into engineering solutions to prevent bleed air contamination, recommending either a separate compressor or a bleed air filter [57]. In response to one oil fume event during the descent phase of a commercial flight, the UK Air Accidents Investigation Board recommended that the FAA and EASA "consider requiring" a system to warn pilots about the presence of "smoke or oil mist in the air delivered from each air conditioning unit" [58]. Engineering and operational measures continue to be called for, including bleed air filtration, sensors to provide early warning of airborne contaminants, improved maintenance procedures, more targeted troubleshooting procedures, relocating the air inlet for the auxiliary power unit, and airline worker training and education [59,60].

5. Conclusions

Between 1979 and 1981, NTSB investigators suggested that inhaling oil fumes inflight may have been a causal factor in "several" fatal crashes of turboprop aircraft. In response, the agency partnered with the very companies that had a commercial interest in the outcome of the investigation. Aside from noting the potential for some people to develop "extreme chemical sensitivity" [16] (p. 28) to chemicals in oil fumes, the NTSB and their industry partners soundly dismissed the hypothesis that oil fumes may have impaired some of the pilots on the crashed planes, affirming that it was "completely without validity" [16] (p. 3). However, their conclusions are not supported by the evidence for three key reasons.

First, it was not—and is not—possible to draw any definitive conclusions regarding the cause of these crashes because real-time bleed air testing and suitable post-mortem blood analyses were not available. However, the accident reports for four of the fatal crashes on these turboprop aircraft include details consistent with (and suggestive of) the pilots being impaired by oil fumes (Table 5). Moreover, this is consistent with similar concerns and reports of pilot impairment documented since the 1930s, such that "pilot error" and "undetermined" are insufficient explanations. Without air supply monitoring equipment to provide real-time warning, and without options for a blood test to investigate inhalation of oil fumes, aircraft crashes that are attributable to bleed air contaminants will not be recognized as such.

Second, none of the tests of ground-based bleed air measurements of a subset of oil-based contaminants generated in the engine type that had been on the crashed aircraft reproduced the types of inflight conditions that the accident investigators had flagged as potentially unsafe (Tables 3 and 5). Specifically, the engine test stand conditions did not assess the impact of oil seeping through a cracked or otherwise damaged compressor seal on the quality of unfiltered bleed air downstream. As a result, the bleed air testing results are not relevant to the question of whether oil fumes could have impaired the pilots inflight. As such, the argument that they somehow discount the potential for impairment is invalid.

Finally, to interpret the bleed air data they collected, the authors of the report used published exposure limits as a benchmark for whether the concentration of gaseous compounds in oil fumes would have been sufficient to cause pilot impairment. However, published exposure limits are not appropriate for assessing the risks associated with inhaling a complex mixture of compounds in an enclosed and reduced pressure environment.

The significant concerns raised by these crashes and the history of pilot impairment associated with breathing oil fumes all support more stringent design, operation, and reporting regulations to protect safety of flight.

6. Recommendations

- For current aircraft that are equipped with bleed air systems, engineering control measures such as sensors and filters should be mandated to prevent inflight exposure to fumes and, thus, improve flight safety. For new aircraft types, non-bleed air supply systems should be standard.
- Given the flight safety implications, all crewmembers should be trained to recognize and respond to the presence of bleed air contaminants [61].
- The NTSB should reopen the 1984 report and update the conclusions based on what was known then about oil fumes and flight safety, and considering the data and reports published since then. The NTSB should also issue recommendations to the FAA on necessary actions to minimize the flight safety impacts of exposure to oil fumes.
- Until suitably protective measures are implemented fleet-wide, the NTSB should consider pilot impairment from bleed-sourced fumes as a potential casual factor in future aircraft accident investigations. This is particularly important when an accident includes either relevant maintenance history or a pilot's failure to communicate, for example.
- If only to avoid the appearance of bias, future investigations should be independent of all commercial interests. Even though it is not unusual for the NTSB to include the FAA and manufacturers in accident investigations, both the poorly conceived design

of the air sampling trials and the sweeping conclusions, suggest that commercial conflicts influenced this project.

Abbreviations

The following abbreviations are used in this manuscript.

CAMI	United States Civil Aeromedical Institute
CFR	United States Code of Federal Regulations
CS	Certification Specification (issued by EASA)
EASA	European Union Aviation Safety Agency
FAA	United States Federal Aviation Administration (issued by the FAA)
FAR	United States Federal Aviation Regulation
lb/hr	pounds per hour
NTSB	United States National Transportation Safety Board
psia	pound-force per square inch absolute (relative to zero or absolute vacuum)
psig	pound-force per square inch gauge (relative to atmospheric pressure; at sea level 14.7psi)
rpm	revolution per minute
TPE	turboprop engine

References

1. Scholz, D. Aircraft cabin air and engine oil—An engineering view. In Proceedings of the 2017 International Aircraft Cabin Air Conference, London, UK, 19–20 September 2017. [CrossRef]
2. Michaelis, S. Aircraft clean air requirements using bleed air systems. *Engineering* **2018**, *10*, 142–172. [CrossRef]
3. UK Air Accidents Investigation Branch (AAIB). *Bulletin No. AAIB-26125, Airbus A320-232, G-EUYB*; UK Department for Transport: Aldershot, UK, 2020, Available online: https://perma.cc/GWD2-RWVW (accessed on 30 September 2021).
4. Bundesstelle für Flugunfalluntersuchung (BFU). *Study of Reported Occurrences in Conjunction with Cabin Air Quality in Commercial Transport Aircraft. Report No. BFU 803.1-14*; German Federal Bureau of Aviation Accident Investigation: Braunschweig, Germany, 2014, Available online: https://perma.cc/XPR9-GE6E (accessed on 30 September 2021).
5. Civil Aviation Accident and Incident Investigation Commission (CIAIAC). *Interim Statement A-008/2013: Accident Occurred to Aircraft Boeing B-757-300, Registration D-ABOC, Operated by Condor Flugdienst GmbH, at Gran Canaria Airport on 22 March 2013*; Civil Aviation Accident and Incident Investigation Commission (CIAIAC): Madrid, Spain, 2014, Available online: https://perma.cc/89DJ-Y42Q (accessed on 1 October 2021).
6. UK Air Accidents Investigation Branch (AAIB). *Bulletin No. 3/2013, Boeing 757-28A, G-FCLA, EW/G2012/10/09*; UK Department for Transport: Aldershot, UK, 2013, Available online: https://perma.cc/QE5D-SLDX (accessed on 30 September 2021).
7. Swiss Aircraft Accident Investigation Bureau (SAAIB). *Investigation Report Concerning the Serious Incident to Aircraft AVRO 146-RJ 100, HB-IXN Operated by Swiss International Air Lines Ltd. Under Flight Number LX1103 on 19 April 2005 on Approach to Zurich-Kloten Airport*; Swiss Aircraft Accident Investigation Bureau (SAAIB): Berne, Switzerland, 2006, Available online: https://perma.cc/3GK4-KPPE (accessed on 1 October 2021).
8. Federal Aviation Administration (FAA). *Airworthiness Directive 2004-12-05: BAE Systems (Operations) Limited Model BAe 146 Series Airplanes. Docket No. 2003-NR-94-AD*; Federal Aviation Administration (FAA): Washington, DC, USA, 2004.
9. Bobb, A.J.; Still, K.R. *Known Harmful Effects of Constituents of Jet Oil Smoke*; Naval Health Research Center, Toxicology Detachment, Wright-Patterson Air Force Base: Dayton, OH, USA, 2003. [CrossRef]
10. Kelso, A.G.; Charlesworth, J.M.; McVea, G.G. *Contamination of Environmental Control Systems in Hercules Aircraft: MRL-R-1116, AR-005-230*; Australian Government Department of Defence: Melbourne, Australia, 1988, Available online: https://perma.cc/WS8C-B83F (accessed on 22 October 2021).
11. Rayman, R.B.; McNaughton, G.B. Smoke/fumes in the cockpit. *Aviat. Space Environ. Med.* **1983**, *54*, 738–740. [PubMed]

12. Montgomery, M.R.; Wier, G.T.; Zieve, F.J.; Anders, M.W. Human intoxication following inhalation exposure to synthetic jet lubricating oil. *Clin. Toxicol.* **1977**, *11*, 423–426. [CrossRef]

13. White, J.J. *Carbon Monoxide and Its Relation to Aircraft. United States Naval Medical Bulletin*; United States Government Printing Office: Washington, DC, USA, 1932, Available online: https://perma.cc/B4NW-DULT (accessed on 1 October 2021).

14. Armstrong, H.G. Noxious fluids and gases in aviation: Hot oil fumes. In *Principles and Practice of Aviation Medicine*; Williams and Wilkins Company: Baltimore, MD, USA, 1939; pp. 178–180.

15. Douglas Aircraft Corporation (DAC). *Suitability of Engine High Pressure Bleed Air for Environmental Control Usage—Assurance Tests*; Douglas Aircraft Corporation (DAC): Santa Monica, CA, USA, 1966, Available online: https://perma.cc/6EPA-DM8X (accessed on 1 October 2021).

16. US National Transportation Safety Board (NTSB). *Special Investigation Report: An Evaluation of the Garrett TPE 331 Engine's Potential for Turbine Oil By-Product Contamination of an Aircraft Cabin Environmental System. Report No. NTSB/SIR-84/01*; US National Transportation Safety Board (NTSB): Washington, DC, USA, 1984, Available online: https://perma.cc/T46K-FRUS (accessed on 1 October 2021).

17. Crane, C.R.; Sanders, D.C.; Endecott, B.R.; Abbott, J.K. *Inhalation Toxicology: III. Evaluation of Thermal Degradation Products from Aircraft and Automobile Engine Oils, Aircraft Hydraulic Fluid, and Mineral Oil*; Report No. FAA-AM-83-12; US Federal Aviation Administration (FAA) Office of Aviation Medicine: Washington, DC, USA, 1983, Available online: https://perma.cc/V6CN-GCDU (accessed on 1 October 2021).

18. US Federal Aviation Administration (FAA). *Airplanes Flying Handbook, FAA-H-8083-3C*; US Federal Aviation Administration Flight Standards Service: Washington, DC, USA, 2021, Available online: https://n2t.net/ark:/13960/t3720ss1s (accessed on 28 October 2021).

19. Kugellager Express GmbH. Ball-Bearing 6204, Open. Picture. 2021. Available online: https://perma.cc/E6C6-93GJ (accessed on 4 November 2021).

20. The Archive. British Aerospace Memorabilia, Garrett TPE331 Turboprop. 2020. Available online: https://perma.cc/3CXE-NQQ9 (accessed on 3 November 2021).

21. Hecker, S. IV.B.1. Engine oil and hydraulic fluid sample analysis. In *Cabin Air Quality Incidents Project Report*; Occupational Health Research Consortium in Aviation (OHRCA): Eugene, OR, USA, 2014, Available online: https://perma.cc/WD9K-499J (accessed on 22 October 2021).

22. Anderson, J. Sources of onboard fumes and smoke reported by U.S. airlines. *Aerospace* **2021**, *8*, 122. [CrossRef]

23. Horne, T.A. *Turbine Pilot Used Turbine Review: Mitsubishi MU-2s*; Aircraft Owners and Pilots Association (AOPA): Frederick, MD, USA, 1994, Available online: https://perma.cc/P5FK-RQHF (accessed on 22 October 2021).

24. Bureau of Air Safety Investigation (BASI). *MU-2 Accident Investigation and Research Report*; Bureau of Air Safety Investigation (BASI): Canberra, Australia, 1992, Available online: https://perma.cc/3FLS-LL82 (accessed on 22 October 2021).

25. Lebeda, A. Mitsubishi MU-2B. Photograph. 2005. Available online: https://commons.wikimedia.org/wiki/File:Mitsubishi_MU-2B_AN1706942.jpg (accessed on 21 October 2021).

26. McDougall, G.; Cho, D.W. Estimating practical maximum flight hours for general aviation turboprop and jet aircraft. *Transp. Res. Rec.* **1989**, *1214*, 52–55. Available online: https://perma.cc/SHX7-5YQ4 (accessed on 22 October 2021).

27. Michaelis, S. Air Accident Bureau incident reports—Case study review. In Proceedings of the 2021 International Aircraft Cabin Air Conference, Online, 15–18 March 2021. [CrossRef]

28. UK Air Accidents Investigation Branch (AAIB). *Bulletin No. 6/2009, Boeing 757-204, G-BYAO, EW/C2006/10/08*; UK Air Accidents Investigation Branch (AAIB): Aldershot, UK, 2009, Available online: https://perma.cc/TQX5-TASE (accessed on 29 October 2021).

29. UK Air Accidents Investigation Branch (AAIB). *Bulletin No. 5/2013, Airbus A321-131, D-AIRX, EW/G2012/10/12*; UK Air Accidents Investigation Branch (AAIB): Aldershot, UK, 2009, Available online: https://perma.cc/JRK4-CKSZ (accessed on 29 October 2021).

30. Blumenfeld, L. A clean APU means clean cabin air. *Flight Airworth. Support Technol. (FAST)* **2013**, *52*, 4–9, Airbus SAS. Available online: https://perma.cc/ZK7P-JZ8V (accessed on 29 October 2021).

31. French Bureau of Enquiry and Analysis for Civil Aviation Safety (BEA). Serious Incident to the Airbus A320-214 Registered EC-HQJ on 17 November 2017 en Route between Geneva and Barcelona. Report No. BEA2017-0658; French Bureau of Enquiry and Analysis for Civil Aviation Safety (BEA): Paris, France, 2020, Available online: https://perma.cc/2FMQ-VGVW (accessed on 2 November 2021).

32. Australian Transport Safety Bureau (ATSB). *An Analysis of Fumes and Smoke Events in Australian Aviation, 2008–2012*; Aviation Research Report AR-2013-213; Australian Transport Safety Bureau (ATSB): Canberra, Australia, 2014, Available online: https://perma.cc/7P3W-WDDU (accessed on 5 October 2021).

33. Parliament of the Commonwealth of Australia (PCA). *Air Safety and Cabin Air Quality in the BAE 146 Aircraft*; Senate Rural and Regional Affairs and Transport References Committee of the Parliament of the Commonwealth of Australia: Canberra, Australia, 2000, Available online: https://perma.cc/QPB3-RUL3 (accessed on 6 October 2021); ISBN 0-642-71093-7.

34. Rannsóknarnefnd Flugslysa (RNF). *Final Report: Aircraft Serious Incident—Smoke in Flight Deck and Cabin, Engine Shut Down and an Emergency Landing*; Report No. M-01409/AIG-09; Rannsóknarnefnd Flugslysa (RNF): Reykjavik, Iceland, 2009, Available online: https://perma.cc/6DDS-R9TA (accessed on 6 October 2021).

35.   Air Accident Investigation Unit (AAIU). *Serious Incident: Boeing 737-8AS, EI-EFB near Stansted, United Kingdom*; Report No. 2016-013; Ireland Department of Transport, Tourism, and Sport Air Accident Investigation Unit: Dublin, Ireland, 2016, Available online: https://perma.cc/DKR2-AZNX (accessed on 25 October 2021).

36.   New Zealand Transport Accident Investigation Commission (TAIC). *Dornier 228-202 ZK-VIR. Partial Incapacitation of Flight Crew en Route Westport to Christchurch, 30 March 2007*; Report No. 07-002; New Zealand Transport Accident Investigation Commission (TAIC): Auckland, New Zealand, 2008, Available online: https://perma.cc/9A4F-RMTA (accessed on 8 October 2021).

37.   Statens Haverikommission (SHK). *Accident Investigation into Incident Onboard Aircraft SE-DRE during Flight between Stockholm and Malmo M County, Sweden*; Report No. RJ 2001:41e; Statens Haverikommission (SHK): Stockholm, Sweden, 2001, Available online: https://perma.cc/K2RT-FXKZ (accessed on 1 October 2021).

38.   Scholz, D. Aircraft cabin air and engine oil—An engineering view. *J. Health Pollut.* **2019**, *9*, 93–98. [CrossRef]

39.   Australian Transport Safety Bureau (ATSB). *In-Flight Engine Failure 23 km N of Ardrossan, SA 25 July 2007 VH-OAA Cessna Aircraft Company "Conquest II" 441. Aviation Occurrence Investigation—AO-2007-030*; Australian Transport Safety Bureau (ATSB): Canberra, Australia, 2009, Available online: https://perma.cc/A3WS-3R7Q (accessed on 2 November 2021).

40.   Crump, D.; Harrison, P.; Walton, C. *Aircraft Cabin Air Sampling Study: Part 1 of the Final Report*; Institute of Environment and Health: Cranfield, UK, 2011, Available online: https://perma.cc/G3FA-Q8LL (accessed on 22 October 2021).

41.   Michaelis, S.; Loraine, T.; Howard, C.V. Ultrafine particle levels measured on board short-haul commercial passenger jet aircraft. *Environ. Health* **2021**, *20*, 1–14. [CrossRef] [PubMed]

42.   Williams, P.I.; Trembath, J. Simultaneous inboard and outboard, inflight measurements of ultrafine particle concentrations. *Aerosol Sci. Technol.* **2021**, *55*, 614–622. [CrossRef]

43.   Howard, C.V.; Johnson, D.W.; Morton, J.; Michaelis, S.; Supplee, D.; Burdon, J. Is a cumulative exposure to a background aerosol of nanoparticles part of the causal mechanism of aerotoxic syndrome? *J. Nanomed. Nanosci. Res.* **2018**, *139*, Available online: https://perma.cc/2CU6-L7HN (accessed on 15 October 2021).

44.   Jones, B.W.; Amiri, S.N.; Roth, J.W.; Hosni, M.H. The nature of particulates in aircraft bleed air resulting from oil contamination. Paper no. LV-17-C046. In Proceedings of the 2017 ASHRAE Winter Conference, Las Vegas, NV, USA, 28 January–1 February 2017; American Society of Heating Refrigerating and Air Conditioning Engineers: Atlanta, GA, USA. Available online: https://perma.cc/UAS8-BTLH (accessed on 22 October 2021).

45.   Civil Aeronautics Board (CAB). *Section 4b.371(b): Ventilation, Heating, and Pressurization. Civil Air Regulations Part 4b: Airplane Airworthiness Transport Categories*; Civil Aeronautics Board (CAB): Washington, DC, USA, 1953, Available online: https://perma.cc/JS2Y-TMPH (accessed on 22 October 2021).

46.   Federal Aviation Administration Office (FAA). *Aircraft Cabin Bleed Air Contaminants: A Review. Report No. DOT/FAA/AM-15/20*; Federal Aviation Administration Office of Aerospace Medicine: Washington, DC, USA, 2015, Available online: https://perma.cc/ZF7Z-P45P (accessed on 5 October 2021).

47.   Spengler, J.D.; Vallarino, J.; McNeely, E.; Estephan, H. *In-Flight/Onboard Monitoring: ACER's Component for ASHRAE 1262, Part 2*; Report No. RITE-ACER-CoE-2012-6; National Air Transportation Center of Excellence for Research in the Intermodal Transport Environment (RITE), Airliner Cabin Environment Research (ACER) Program: Boston, MA, USA, 2012, Available online: https://perma.cc/D68W-XW56 (accessed on 6 October 2021).

48.   UK Civil Aviation Authority (CAA). *Cabin Air Quality: Report 2004/04*; UK Civil Aviation Authority (CAA): West Sussex, UK, 2004, Available online: https://perma.cc/MP4H-3AUG (accessed on 22 October 2021).

49.   Chen, R.; Fang, L.; Liu, J.; Herbig, B.; Norrefeldt, V.; Mayer, F.; Fox, R.; Wargocki, P. Cabin air quality on non-smoking commercial flights: A review of published data on airborne pollutants. *Indoor Air* **2021**, *31*, 926–957. [CrossRef] [PubMed]

50.   Waters, M.A.; Bloom, T.F.; Grajewski, B.; Deddens, J. Measurements of indoor air quality on commercial transport aircraft. In Proceedings of the 9th International Conference on Indoor Air Quality and Climate, Santa Cruz, CA, USA, 30 June–5 July 2002; pp. 782–787. Available online: https://perma.cc/M86Y-QMP2 (accessed on 8 October 2021).

51.   Howard, C.V. Inappropriate use of risk assessment in addressing health hazards posed by civil aircraft cabin air. *Open Access J. Toxicol.* **2020**, *4*, 049–056. [CrossRef]

52.   Watterson, A.; Michaelis, S. Use of exposure standards in aviation. *2017 Int. Aircr. Cabin Air Conf.* **2019**, *9*, S132–S137. [CrossRef]

53.   Michaelis, S. *Aviation Contaminated Air Reference Manual*; Printed and bound by CPI Antony Rowe: Eastbourne, UK, 2007; ISBN 978-0-9555672-0-9.

54.   American Conference of Governmental Industrial Hygienists (ACGIH). Appendix E: Threshold limit values for mixtures. In *TLVs and BEIs Based on the Documentation of Threshold Limit Values for Chemical Substances and Physical Agents and Biological Exposure Indices*; American Conference of Governmental Industrial Hygienists: Cincinnati, OH, USA, 2021.

55.   Gilinskiy, V.A.; Chapek, A.V.; Kozlova, A.G.; Kulikova, N.M.; Loshak, A.Y. The effects of low concentrations of carbon monoxide on man in pressurized cabins of passenger planes. In *Aviation and Space Medicine, NASA Technical Translation F-228*; Parin, V.V., Ed.; US National Aeronautics and Space Administration: Washington, DC, USA, 1964, Available online: https://perma.cc/XAB2-KETY (accessed on 1 October 2021).

56.   United States Air Force (USAF). *Environmental Control Airborne. Appendix B: Air Force Guide Specification MIL-E-87145A*; United States Air Force Wright Patterson Air Force Base: Dayton, OH, USA, 1992, Available online: https://perma.cc/N8UV-CTAV (accessed on 1 October 2021).

57. Reddall, H.A. Elimination of engine bleed air contamination. In Proceedings of the SAE Golden Anniversary Aeronautic Meeting, Los Angeles, CA, USA, 11–15 October 1955, Available online: https://perma.cc/9WMT-CESM (accessed on 1 October 2021).

58. UK Air Accidents Investigation Branch (AAIB). *Bulletin 4/2007, Bombardier DHC-8-400, G-JECE, EQ/C2005/08/10*; UK Air Accidents Investigation Branch (AAIB): Aldershot, UK, 2007, Available online: https://perma.cc/L2GG-ZSLX (accessed on 6 October 2021).

59. American Society of Heating, Refrigerating, and Air Conditioning Engineers (ASHRAE). *Guideline 28-2021: Air Quality within Commercial Aircraft.* American Society of Heating, Refrigerating, and Air Conditioning Engineers (ASHRAE): Atlanta, GA, USA, 2021. Available online: https://www.techstreet.com/ashrae/searches/33473309 (accessed on 28 October 2021).

60. American Society of Heating, Refrigerating, and Air Conditioning Engineers (ASHRAE). *ANSI/ASHRAE Standard 161-2018: Air Quality within Commercial Aircraft.* American Society of Heating, Refrigerating, and Air Conditioning Engineers (ASHRAE): Atlanta, GA, USA, 2018. Available online: https://www.techstreet.com/ashrae/searches/33473313 (accessed on 28 October 2021).

61. International Civil Aviation Organization (ICAO). *Guidelines on Education, Training, and Reporting Practices Related to Fume Events. Circular 344-AN/202*; International Civil Aviation Organization (ICAO): Montreal, QC, Canada, 2015, Available online: https://www.icao.int (accessed on 1 November 2021).

Aircraft Configuration Parameter Boundaries Based on Closed-Loop Flying Qualities Requirements

Lixin Wang [1], **Kun Yang** [1] ⓘ, **Peng Zhao** [2] **and Ting Yue** [1],*

[1] School of Aeronautic Science and Engineering, Beihang University, Beijing 100191, China; wlx_buaa@163.com (L.W.); guerremondiale@buaa.edu.cn (K.Y.)
[2] Chinese Flight Test Establishment, Xi'an 710089, China; qq645980019@163.com
* Correspondence: yueting_buaa@163.com; Tel.: +86-138-1017-1251

Abstract: For aircraft employing the fly-by-wire technique, the closed-loop dynamic characteristics are determined by both the configuration design and the flight control system. As the capacity of the control system has certain limitations, the configuration parameters are also constrained by the requirements of the closed-loop flying qualities. This paper presents an aircraft configuration parameter boundaries determination method based on closed-loop flying qualities requirements independent of the actual flight control law design, mainly aiming at the parameters that affect the stability and control characteristics. First, a nonlinear dynamic inversion-based flight control law is adopted to decouple the control law gains from the configuration parameters and to study the relationship between the configuration parameters and closed-loop flying qualities. Second, a flying qualities evaluation scheme is established by selecting the most severe flight conditions and the evaluation criteria that are most sensitive to changes in the parameters. Finally, the parameter boundaries according to the requirements of Level 1 flying qualities are determined by searching for the critical values that lead to degradation of the flying qualities. The proposed method is verified by an application example of the design ranges of a sample aircraft's wing position, horizontal tail area, center of gravity, vertical tail area and vertical tail position.

Keywords: configuration design; flying qualities; flight control law

1. Introduction

Aircraft configuration design depends on the design requirements of different types of parameters [1,2]. For example, the determination of wing area, fuselage geometry and cross section mainly considers the payload requirement; the airfoil, aspect ratio and sweep angle of the wing are designed according to the aerodynamic characteristics requirements; wing position, horizontal tail area, center of gravity (CG), vertical tail area and position have considerable influences on the dynamic characteristics of aircraft, and the design of these parameters is conducted mainly in consideration of stability and control requirements [3].

The flying qualities evaluation can comprehensively assess the stability and control characteristics, the performance of the flight control system, and the adaptability to the flight missions [4–8]. Thus, the configuration design should take into account the flying qualities requirements. As the developments of digital flight control systems and the fly-by-wire technique allow more advanced flight control laws (FCL) to be implemented on aircraft [9–15], the configuration design has become more diversified. However, the capacity of FCL has certain limitations, and flying qualities cannot be guaranteed only relying on the control system. Considering that the flying qualities of the closed-loop aircraft are determined by both the configuration design and the flight control system, the configuration parameters are also constrained by the closed-loop flying qualities requirements [16]. Therefore, it is necessary to establish the relationship between the configuration parameters and the closed-loop flying qualities requirements in the conceptual aircraft design.

Recently, there has been renewed interest in the closed-loop flying qualities prediction and assessment in conceptual aircraft design [17–22]. The Institute of Aeronautics and Astronautics of RWTH Aachen University developed a methodology for the prediction and assessment of flying qualities and implemented it into a preliminary aircraft design tool [20]. Arthur Rizzi et al. achieved the multidisciplinary optimization of a canard configured TransCruiser with flight control by using CEASIOM, a multidisciplinary software environment for aircraft design [21]. Stefano Cacciola et al. realized the optimization of the longitudinal control law, as well as the three-surface configuration for better flying qualities [22]; however, the FCLs involved in these studies were mainly stability augmentation systems (SAS) or stability and control augmentation systems (SCAS), which are based on linear control theory and well-established gain-scheduling methods [16]. As a result, the controller gains are coupled with the configuration parameters of the aircraft, and thus, it is impossible to identify the influence of the configuration parameters separately from the influence of the controller gains on the closed-loop flying qualities. Due to this lack of flexibility, the traditional FCLs are not suitable to study the relationship between the configuration parameters and the closed-loop flying qualities requirements.

Inverse model-based control techniques, e.g., nonlinear dynamic inversion (NDI) as well as incremental nonlinear dynamic inversion (INDI), offer a great advantage to continuously changing plants [23,24]. The studies of DLR (German Aerospace Center) and others [25,26] show that the flight control law based on the NDI method can effectively adapt to changing aircraft configurations. Therefore, this paper proposes an aircraft configuration parameter boundaries design method based on closed-loop flying qualities requirements. This method realizes the configuration parameter boundaries design independent of actual flight control law design by using the NDI method, and the closed-loop flying qualities requirements are transformed into the design ranges of target configuration parameters. The parameter boundaries simplify the stability and control design, so that the configuration design can be more focused on aerodynamic, structural and other requirements.

The remainder of this paper is structured as follows. Section 2 introduces the determination method of configuration parameter boundaries based on flying qualities requirements. Section 3 defines the wing position, horizontal tail area, CG position, vertical tail area and vertical tail position as the target configuration parameters. Section 4 describes the modelling of the closed-loop aircraft and proposes the selection of flight conditions and evaluation criteria. An application example comprising the target parameter design of a medium-range transport aircraft is then shown in Section 5. Finally, a concluding summary is given in Section 6.

2. Configuration Parameter Boundaries Based on Flying Qualities Requirements

Conceptual design is the first phase of the aircraft design process. It involves sketching a variety of possible configurations that meet the design requirements, such as aerodynamics, propulsion, flight performance, structural and control systems.

The steps of conceptual design are described as [1,2,27]:

- Preliminary Sizing: definition of requirements, selection of an aircraft configuration, selection of a propulsion system, etc.
- Layout sizing: fuselage sizing, wing sizing, empennage sizing, design for high lift, etc.
- Specific design: stability and control design, flight control system design, landing gear design, structures design, etc.
- Aircraft performance analysis: aerodynamic analysis, polar estimation, mass estimation, flying qualities evaluation, mission analysis, etc.

The whole design process has an iterative nature to realize optimization design [27].

Stability and control design and flying qualities evaluation are often in later stages of the design phase. Configuration parameters adjustment due to stability and control requirements or flying qualities requirements may lead to much iterative work. This paper proposes a method to determine the configuration parameter boundaries based on closed-

loop flying qualities requirements to simplify the stability and control design. The proposed parameter boundaries aim to transform the closed-loop flying qualities requirements into the design ranges of target configuration parameters. In this way, the flying qualities requirements can be considered at the layout sizing stage during optimization design.

The determination process of the parameter boundaries is as follows. The first step is to construct a high-order closed-loop aircraft model according to the basic configuration design; the model can be divided into an aircraft motion model and the FCL based on the model reference NDI method. The second step is to establish the flying qualities evaluation scheme by selecting the most stringent flight conditions and the evaluation criteria that are most sensitive to the parameter changes. The third step is to establish a reasonable variation series of the target parameters and to search for the critical values that lead to degradation of the flying qualities. Finally, the parameter boundaries according to the requirements of the Level 1 flying qualities (Level 1 FQ) are determined. The method for determining parameter boundaries is shown in Figure 1.
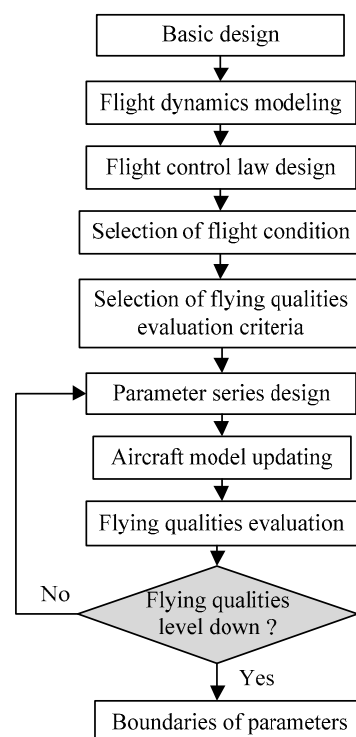
Figure 1. Configuration parameter boundaries based on closed-loop flying qualities requirements.

It should be emphasized that the parameter boundaries proposed in this paper correspond to specific flying qualities criteria, so they only reflect a part of stability and control requirements. Meanwhile, these configuration parameters should also meet other requirements. For example, the CG position design should meet the trim requirements, the vertical tail design should meet the controllability requirements in the single-engine out condition at take-off, and so forth. Designers should seek to reach the design configuration that satisfactorily meets all requirements in the optimization design process.

3. Configuration Parameter Analysis

3.1. Wing Position and Horizontal Tail Area

The longitudinal stability and control characteristics of aircraft are determined mainly by the stability and damping derivatives of the pitch moment, and these derivatives are affected by the wing position, CG position, horizontal tail position, horizontal tail area, and other parameters. The horizontal tail is usually installed at the rear end of the fuselage to ensure the control power of the elevator, and the variation range of the tail position is small.

Thus, the longitudinal characteristics are governed predominantly by the wing position and horizontal tail area [1]. These two parameters are usually designed in collaboration according to the requirements of the longitudinal flying qualities.

The stability derivative of the pitch moment $C_{m\alpha}$ can be expressed as [28]:

$$C_{m\alpha} = C_{L\alpha.WB}\left(x_{c.g.} - x_{ac.WB}\right) - C_{L\alpha.T}V_T + C_{m\alpha.p} \quad (1)$$

where $x_{ac.WB}$ is the mean aerodynamic center of the wing-body configuration and is affected mainly by the wing position; $C_{L\alpha.WB}$ is the lift coefficient derivative of the wing-body configuration; $x_{c.g.}$ is the CG position of the aircraft; $C_{L\alpha.T}$ is the lift coefficient derivative of the horizontal tail; V_T is the horizontal tail volume ratio, affected mainly by the horizontal tail position and its area; and $C_{m\alpha.p}$ is the pitch moment derivative of the propulsion system. V_T is defined as:

$$V_T = \frac{l_T S_T}{cS} \quad (2)$$

where l_T is the distance between the aircraft CG and the aerodynamic center of the horizontal tail, S_T is the horizontal tail area, c is the mean aerodynamic chord of the aircraft wing, and S is the wing area. Consequently, forward movement of the wing position and a decrease in the horizontal tail area lead to a decrease in $|C_{m\alpha}|$ and a reduction in the static longitudinal stability. Similarly, rearward movement of the wing position and an increase in the horizontal tail area lead to an increase in $|C_{m\alpha}|$ and an increase in the demand on the pitch control moment.

The damping derivatives of the pitch moment, namely, C_{mq} and $C_{m\dot{\alpha}}$, are generated mainly by the horizontal tail, whereas the influence of the wing-body configuration accounts for only about 10% of the overall influence [28]. The contributions of the tail to C_{mq} and $C_{m\dot{\alpha}}$ are [28]:

$$\left.\begin{array}{l} C_{mq.T} = -2C_{L\alpha.T}V_T\frac{l_T}{c} \\[2mm] C_{m\dot{\alpha}.T} = -2C_{L\alpha.T}V_T\frac{l_T}{c}\frac{\partial\varepsilon}{\partial\alpha} \end{array}\right\} \quad (3)$$

where $\partial\varepsilon/\partial\alpha$ is the derivative of the downwash angle of the horizontal tail with respect to the angle of attack. A decrease in horizontal tail area leads to a decrease in both $|C_{mq}|$ and $|C_{m\dot{\alpha}}|$.

The stability and damping derivatives of the pitch moment mainly affect the longitudinal short-period mode characteristics of aircraft. The natural frequency $\omega_{n.sp}$ and damping ratio ξ_{sp} of the short-period mode can be expressed as:

$$\left.\begin{array}{l} \omega_{n.sp} = \sqrt{-\left(M_\alpha + M_q Z_\alpha\right)} \\[3mm] \xi_{sp} = -\dfrac{M_q + M_{\dot{\alpha}} - Z_\alpha}{2\omega_{n.sp}} \end{array}\right\} \quad (4)$$

where M_α, M_q, $M_{\dot{\alpha}}$, and Z_α are the dimensional dynamic derivatives related to $C_{m\alpha}$, C_{mq}, $C_{m\dot{\alpha}}$ and $C_{L\alpha}$, respectively. The detailed derivation process from (3) to (4) is described in the references [29,30].

Combining Equations (3) and (4) demonstrates that a decrease in the horizontal tail area leads to a decrease in ξ_{sp}, slows down the short-period convergence, and decreases the dynamic stability of the aircraft; in contrast, an increase in the tail area leads to an increase in the damping ratio and restrains the pitch response to the pilot control input.

In a general conceptual design process, the horizontal tail is first of all sized from static conditions as done with the "V-diagram" [27,31,32], which corresponds to the basis of the longitudinal stability and control requirements. Then, the horizontal tail design should consider the dynamic stability and control requirements, which are the primary focus of this paper.

According to the above analysis, the longitudinal dynamic stability requirements of the aircraft should be considered to determine the forward range of the wing position and the maximum limit of the horizontal tail area. Furthermore, the rearward range of the wing position and the minimum limit of the horizontal tail area should be determined by the longitudinal maneuverability requirements.

3.2. Center of Gravity Position

The CG is not a fixed point but moves with the initial loading condition and fuel consumption of the aircraft. For an aircraft with determined aerodynamic shape, a change in the CG position x_{cg} causes $C_{m\alpha}$ to vary and thus affects the longitudinal characteristics. Therefore, the range of the CG location needs to be strictly designed according to the requirements of the longitudinal flying qualities.

A forward CG represents a large $|C_{m\alpha}|$ and requires a larger pitch control moment, while a rearward CG position represents a small $|C_{m\alpha}|$ and poor longitudinal stability. Therefore, in this paper, the forward CG limit mainly considers the longitudinal maneuverability requirements, and the rearward CG limit is determined by the longitudinal stability requirements.

Additionally, the forward CG limit should allow the aircraft to be trimmed at maximum lift coefficient in ground effect. The final forward CG limit will be determined by both the longitudinal maneuverability and trim requirements, which leads to future investigations.

3.3. Vertical Tail Area and Position

Directional stability, also known as weathercock stability, is provided primarily by the vertical tail. Meanwhile, a large vertical tail is accessible spiral stability. However, a large vertical tail surface may produce an excessive aerodynamic drag force during high-speed flight at high altitudes in cruise, and such a large surface would require a higher structural strength and mass of the airframe. Therefore, it is necessary to restrict the vertical tail area to optimize both the aerodynamic characteristics in cruise and the airframe structure. To ensure the directional stability after the vertical tail area is reduced, it is necessary to increase the vertical tail arm by adjusting the position of the vertical tail. Similar to the horizontal tail, the vertical tail is also installed at the end of the fuselage to ensure the control power of the rudder. Thus, the vertical tail position should be adjusted by changing the chord length, sweep angle and other parameters without moving the root position. It should be noted that a large sweep angle may lead to the decrease of the vertical tail lift coefficient. Thus, the vertical tail design should avoid a large sweep angle [29,30].

The contributions of the vertical tail to the stability and damping derivatives of the directional moment $C_{n\beta.V}$ and $C_{nr.V}$ can be expressed as [28]:

$$\left.\begin{aligned}
C_{n\beta.V} &= -C_{Y\beta.V}V_V \\
C_{nr.V} &= -2C_{Y\beta.V}V_V \frac{l_V}{b} \\
V_V &= \frac{l_V S_V}{bS}
\end{aligned}\right\} \tag{5}$$

where $C_{Y\beta.V}$ is the lift coefficient derivative of the vertical tail; V_V is the vertical tail volume ratio; S_V is the vertical tail area; l_V is the force arm of the vertical tail; and b is the wingspan of the aircraft.

The stability and damping derivatives of the directional moment affect mainly the Dutch roll mode characteristics of the aircraft. The natural frequency $\omega_{n.dr}$ and damping ratio ζ_{dr} of the Dutch roll mode can be expressed as:

$$\left.\begin{aligned}
\omega_{n.dr} &= \sqrt{N_\beta - N_\beta Y_r + N_r Y_\beta} \\
\zeta_{dr} &= -\frac{N_r + Y_\beta}{2\omega_{n.dr}}
\end{aligned}\right\} \tag{6}$$

where N_β, N_r, Y_β, and Y_r are the dimensional dynamic derivatives related to $C_{n\beta}$, C_{nr}, $C_{Y\beta}$ and C_{Yr}, respectively. The detailed derivation process from (5) to (6) is also described in the references [29,30]. Combining Equations (5) and (6) reveals that a reduced vertical tail arm and a decrease in the tail area cause a reduction in both $\left|C_{n\beta}\right|$ and ξ_{dr} and decreases the directional static and dynamic stability.

In a general conceptual design process, vertical tail sizing for static stability has to compensate for the destabilizing effect of the fuselage; vertical tail sizing for static control has to compensate the yaw moment from a one-engine out flight case [29,30]; vertical tail sizing for roll response control requires the proper balance of the rolling time constant and the roll sensitivity; there are also spiral stability and directional dynamic stability requirements. Directional dynamic stability mainly refers to the Dutch roll mode stability, which is the primary focus of this paper. The eventual vertical tail area will be the minimum area that meets all these requirements.

4. Aircraft Modeling, Selection of Flight Conditions and Evaluation Criteria

4.1. Aircraft Modelling

The aircraft motion model is based on the six-degree-of-freedom equations of motion. To determine the configuration parameter boundaries based on closed-loop flying qualities requirements, the motion model should be constantly updated according to the changes in the configuration parameters.

To easily adapt the control laws to continuously change the aircraft configuration during the design process, NDI controllers offer considerable advantages. For instance, the model reference NDI control law [33,34] uses transfer function-based reference models to describe the desired aircraft dynamics. The reference models can be expressed as [33]:

$$\left.\begin{array}{l} \dfrac{q_r}{q_c} = \dfrac{K_{q.r}\omega_{sp.r}^2(s + 1/T_{\theta2.r})}{s^2 + 2\xi_{sp.r}\omega_{sp.r}s + \omega_{sp.r}^2} \\[3mm] \dfrac{p_r}{p_c} = \dfrac{K_{p.r}}{s + \omega_{p.r}} \\[3mm] \dfrac{r_r}{r_c} = \dfrac{\omega_{r.r}}{s + \omega_{r.r}} \end{array}\right\} \tag{7}$$

where p_c, q_c, and r_c are the rate commands of the pilot; p_r, q_r, and r_r are the corresponding reference rate commands generated by the reference models; $K_{q.r}$ and $K_{p.r}$ are the control gains; $\xi_{sp.r}$, $\omega_{sp.r}$, and $T_{\theta2.r}$ are the desired damping ratio, natural frequency and time constant of the short-period mode, respectively; and $\omega_{p.r}$ and $\omega_{r.r}$ are the desired roll and directional frequencies. The reference commands are achieved by the actual dynamic inversion at the core of the control law, which computes the necessary surface positions. A proportional-integral (PI) compensator is added to drive down the error between the desired dynamics and the actual dynamics. Filters are also needed to attenuate undesirable noise from the feedback sensors. The structure of the high-order closed-loop aircraft model with the model reference NDI control law is shown in Figure 2.

The parameters of the model reference NDI control law are designed according to the desired dynamic characteristics and do not need to be adjusted according to changes in the configuration parameters [25]. As a result, the FCL achieves the desired closed-loop flying qualities of the varying aircraft configuration and eliminates the disturbance attributable to variation in the control system. Therefore, the model reference NDI method is employed to design the control law in this paper, which is convenient for studying the relationship between the configuration parameters and the closed-loop flying qualities.
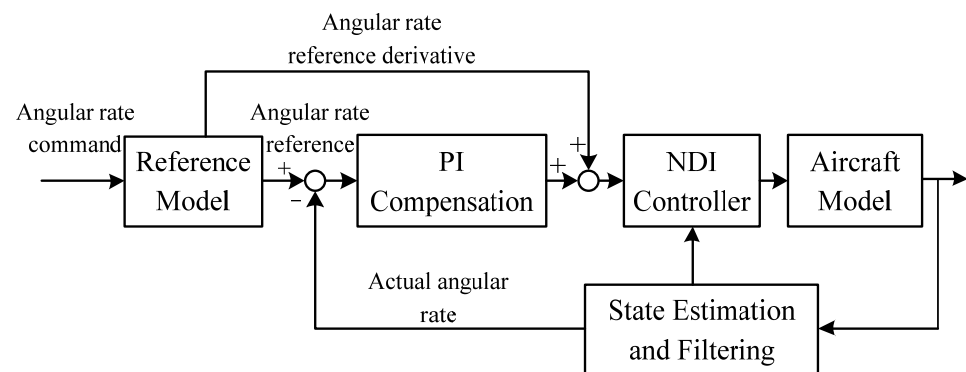
Figure 2. Structure of the high-order closed-loop aircraft model.

It should be emphasized that the design ranges of the configuration parameters derived from the NDI control law represent the capability of control laws that makes the closed-loop aircraft meet the flight quality requirements. For aircraft adopting other control laws, such as SCAS, the conclusions are still valid.

4.2. Selection of Flight Conditions for Evaluation

Any variation in the flight conditions will lead to a change in the flying qualities evaluation results, so the requirements for the configuration parameters differ under different flight conditions. Consequently, to determine configuration parameter boundaries based on closed-loop flying qualities requirements, it is necessary to determine the flight conditions with the most severe requirements for the configuration parameters [1,3].

The previous discussion shows that the forward range of the wing position, the minimum limit of the horizontal tail area, and the rearward CG limit are the main factors influencing the longitudinal dynamic stability requirements of the aircraft. In contrast, the longitudinal maneuverability requirements are governed primarily by the rearward range of the wing position, the maximum limit of the horizontal tail area and the forward CG limit. For aircraft whose load and fuel are arranged mainly in the front region of the airframe, the forward CG limit appears during the take-off phase [1]. In this case, the stability margin of the aircraft is large during the take-off phase, and the longitudinal maneuverability is poor. Considering the low flight speed during the take-off phase, the aerodynamic efficiency of the control surface is low, which worsens the maneuverability. Therefore, the rearward range of the wing position, the maximum limit of the horizontal tail area and the forward CG limit should be determined in the take-off phase. The flight speed, flight altitude, weight distribution, flaps, landing gear and other settings should be consistent with the most forward CG position. With loading and fuel consumption, the CG position reaches the rearward limit in landing phase, during which the stability margin of the aircraft decreases and the most stringent requirements for the longitudinal stability are generated. Therefore, the forward range of the wing position, the minimum limit of the horizontal tail area and the rearward CG limit should be determined in landing phase, and the exact flight condition should be set to the state with the most rearward CG position. The selected flight conditions for evaluating an aircraft whose load and fuel are arranged mainly at the rear of the airframe are the opposite. For an aircraft whose load and fuel cannot be judged clearly whether they are arranged in the front or rear position (for example, the fuel is in the wings and the wingbox), the flight conditions for longitudinal flying qualities evaluation can be selected directly according to the change of the CG position during flight.

The vertical tail design for the directional dynamic stability should be determined under the flight condition with the most stringent requirements. Due to the decrease in damping coefficients during high-speed and high-altitude flight, the Dutch roll mode of the aircraft will deteriorate, thereby increasing the dynamic stability requirements. Therefore, the cruise phase at high speed and high altitude is selected to determine the

design ranges of the vertical tail area and position based on the directional dynamic stability requirements. The exact flight condition should be set to the state with the most decreased damping coefficients.

4.3. Selection of the Flying Qualities Evaluation Criteria

Current flying qualities standards provide multiple evaluation criteria [35–38]. Each evaluation criterion has its own inspection focus, and thus, the same configuration design may yield different evaluation results according to different criteria. To determine configuration parameter boundaries based on closed-loop flying qualities requirements, it is necessary to determine the evaluation criteria that are most sensitive to changes in the configuration parameters to obtain the strictest parameter design ranges.

4.3.1. CAP Criterion

The control anticipation parameter (CAP) is defined as the ratio of the initial pitch acceleration to the steady-state normal acceleration [38]. The CAP value can reflect the short-period mode flying qualities of an aircraft, including the longitudinal stability and maneuverability. To apply the CAP criterion to a high-order closed-loop aircraft, the low-order equivalent system (LOES) theorem is adopted to match the characteristics of the high-order system. The longitudinal LOES of the aircraft can be expressed as:

$$
\left.
\begin{aligned}
\frac{\alpha}{F_e} &= \frac{K_\alpha}{s^2 + 2\zeta_{\text{sp}}\omega_{\text{n.sp}}s + \omega_{\text{n.sp}}^2} e^{-\tau_\alpha s} \\
\frac{q}{F_e} &= \frac{K_q(s + 1/T_{\theta_2})}{s^2 + 2\zeta_{\text{sp}}\omega_{\text{n.sp}}s + \omega_{\text{n.sp}}^2} e^{-\tau_q s}
\end{aligned}
\right\}
\tag{8}
$$

where α is the aircraft angle of attack; q is the pitch rate; F_e is the pitch control input; $1/T_{\theta_2}$ is the zero of the pitch attitude transfer function; K_α and K_q are the equivalent system gains of the transfer functions; and τ_α and τ_q are the equivalent time delays.

The CAP of the LOES is defined as:

$$
\text{CAP} = \omega_{\text{n.sp}}^2 \Big/ \left(\frac{V}{g} \cdot \frac{1}{T_{\theta 2}} \right)
\tag{9}
$$

where V is the flight speed and g is the acceleration due to gravity. The Level 1 FQ of the CAP criterion are defined by the short-period damping ratio ζ_{sp} of the equivalent system and the CAP value.

The upper boundary of the CAP value and the lower boundary of ζ_{sp} reflect the stability requirements of an aircraft. A large CAP value and small ζ_{sp} indicate a lack of longitudinal stability, and thus, a pilot's small control input may lead to a violent pitch response. Therefore, the upper boundary of the CAP value and the lower boundary of ζ_{sp} can be used to determine the forward range of the wing position, the minimum limit of the horizontal tail area and the rearward CG limit.

In contrast, the lower boundary of the CAP value and the upper boundary of ζ_{sp} reflect the maneuverability requirements. A small CAP value and large ζ_{sp} represent a large longitudinal stability margin, which may increase the pilot's workload to achieve pitch motion. Thus, the rearward range of the wing position, the maximum limit of the horizontal tail area and the forward CG limit should be designed according to the lower boundary of the CAP value and the upper boundary of ζ_{sp}.

4.3.2. Chalk Criterion

The Chalk criterion is a time-domain criterion that focuses on the characteristics of the pitch rate response and defines three parameters for evaluation: the effective time delay t_1, the transient peak ratio $\Delta q_{\max}/\Delta q_{\min}$ and the effective rise time Δt, as shown in Figure 3 [38].
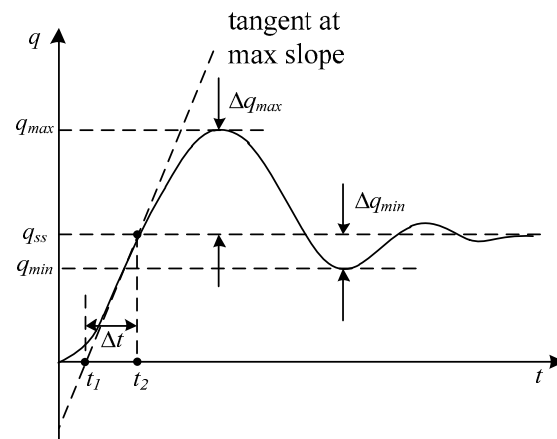
Figure 3. Definitions of the Chalk criterion parameters.

In Figure 3, q_{ss} is the steady-state pitch rate; $q_{\max}$ is the maximum pitch rate; $q_{\min}$ is the first minimum pitch rate; the instant t_1 is defined by the intersection between the tangent at the maximum slope and the time axis; the instant t_2 is defined by the intersection between the tangent at the maximum slope and the horizontal line of the steady-state pitch rate; and Δt is the difference between t_1 and t_2. t_1 reflects the time delay between the real pitch rate response and an ideal pitch rate response with the maximum pitch acceleration, $\Delta q_{\max}/\Delta q_{\min}$ reflects the short-period damping ratio of the pitch response, and Δt reflects the rise time to accelerate to the steady-state pitch rate of the pitch rate ideal response.

The Chalk criterion is based on the time-domain pitch response of the aircraft without identifying the frequency-domain characteristics. Thus, the Chalk criterion can be used to avoid the situation in which a frequency-domain criterion is not applicable to aircraft with an unconventional response. The design ranges of the configuration parameters should be determined according to the more stringent requirements of the CAP and Chalk criteria to enhance the universality of the design method based on closed-loop flying qualities requirements.

4.3.3. Dutch Roll Criterion

The flying qualities with respect to the yaw axis can be evaluated by the characteristics of the lateral-directional oscillatory (Dutch roll) response to the yaw controller. The Dutch roll frequency and damping ratio can be defined by matching the higher-order sideslip response to the yaw control input to the following lower-order form [38]:

$$\frac{\beta}{F_r} = \frac{K_\beta}{(s^2 + 2\xi_{dr}\omega_{n.dr}s + \omega_{n.dr}^2)} e^{-\tau_{e\beta}s} \tag{10}$$

where β is the sideslip angle; F_r is the yaw control input; K_β is the equivalent system gain of the transfer function; and $\tau_{e\beta}$ is the equivalent time delay of the transfer function.

The flying qualities requirements of the Dutch roll criterion are specified in terms of the minimum values of $\omega_{n.dr}$, ξ_{dr} and $\xi_{dr}\omega_{n.dr}$, and the evaluation results can reflect the lateral-directional stability of the aircraft. This criterion can be used to determine the vertical tail area and position boundaries.

5. Application of the Proposed Parameter Boundaries Design Method

This section takes a medium-range transport aircraft as an application example of the configuration parameter boundaries design method. The definitions of the target configuration parameters of the sample aircraft are illustrated in Figure 4. The wing position x_W and the vertical tail position x_V are defined as the distance from the nose to the quarter chord point on the mean aerodynamic chord (MAC) of the wing and the vertical

tail. The CG position $\bar{x}_{cg}$ is defined as the percentage of the distance from the CG to the leading edge of the wing MAC [1].
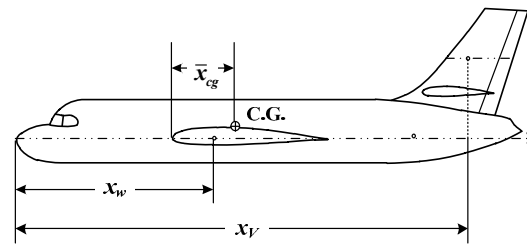

Figure 4. Target configuration parameters of the sample aircraft.

The configuration parameters of the basic aircraft design are depicted in Table 1. The aircraft motion model and the inner loop of the NDI control law are based on the basic aircraft design, and the reference model parameters of the NDI control law are designed according to the flying qualities requirements, as shown in Table 2. By combining the motion model with the FCL, the high-order closed-loop aircraft model is established.

Table 1. Configuration parameters of the basic aircraft design.

Parameters	Values
Length overall (m)	32
Wing position (m)	12.6
Wing area (m^2)	115.3
Wing mean aerodynamic chord (MAC) (m)	6.2
Center of gravity	33.4% (TO) 38.2% (LD)
Horizontal tail position (m)	28.6
Horizontal tail area (m^2)	27.5
Horizontal tail MAC (m)	2.9
Vertical tail position (m)	29.8
Vertical tail area (m^2)	15.9
Vertical tail MAC (m)	3.2

Table 2. Reference model parameters design.

$K_{q.r}$	$\zeta_{sp.r}$	$\omega_{sp.r}$ (rad/s)	$T_{\theta2.r}$ (s)	$K_{p.r}$	$\omega_{p.r}$ (rad/s)	$\omega_{r.r}$ (rad/s)
7.5	0.9	3.5	0.5	4.2	2.5	3.5

5.1. Boundaries of the Wing Position and Horizontal Tail Area

For the sample aircraft, the forward CG limit appears in the take-off phase (sea-level, low-speed, forward CG position, maximum take-off weight, maximum thrust, flaps and landing gear retracted), while the rearward CG limit appears in the landing phase (sea-level, low-speed, rearward CG position, minimum landing weight, landing engine setting, flaps and landing gear down). According to the previous discussion, the forward range of x_W and the minimum limit of S_T should be designed by evaluating the flying qualities in landing phase according to the most stringent requirement among the upper boundary of the CAP value, the lower boundary of ζ_{sp}, and the Chalk criterion. Likewise, the rearward range of x_W and the maximum limit of S_T should be designed in take-off phase according to the most stringent requirement among the lower boundary of the CAP value, the upper boundary of ζ_{sp} and the Chalk criterion.

Preliminary sizing requires that the CG position is on the MAC of the wing; thus, the first estimate of x_W ranges from 10 m to 16 m. Then, according to the requirements of the longitudinal Level 1 FQ of closed-loop aircraft, the design range of S_T corresponding to different x_W is determined. Since the rearward range of x_W and the maximum limit of S_T both reflect the maneuverability requirements, the upper boundary of S_T corresponding to

different x_W can also be regarded as the rearward boundary x_W corresponding to different S_T. Similarly, the lower boundary of S_T corresponding to different x_W can also be regarded as the forward boundary of x_W corresponding to different S_T. The design range of x_W is determined by the design range of S_T.

- Maximum limit of the horizontal tail area

The variation series of x_W is established as follows: within the preliminary range from 10 m to 16 m, one point is selected every 1 m, yielding seven points in total. For each X_W, a series of S_T with an interval of 2 m^2 is selected. Then, the CAP criterion is applied to evaluate the flying qualities of aircraft with different x_W–S_T combinations in the take-off phase. Partial evaluation results with x_W values of 10 m, 12 m, 14 m, and 16 m are shown in Figure 5. The CAP criterion characteristics with x_W values of 12 m and 14 m are shown in Table 3.
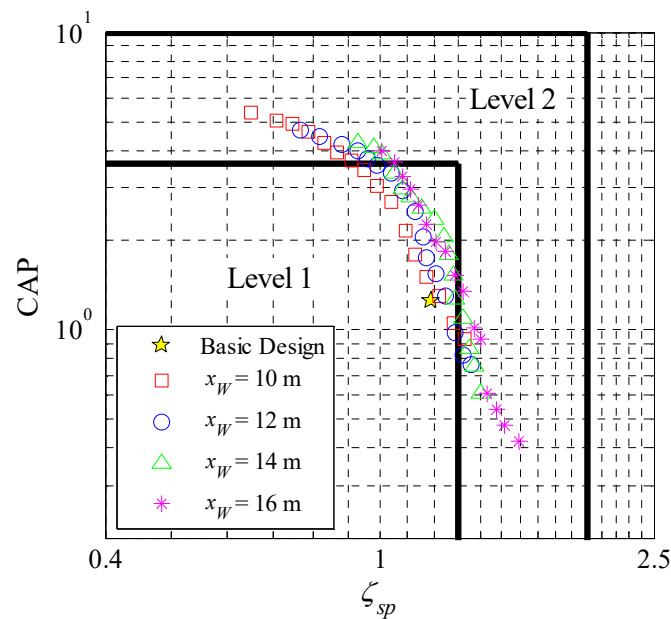

Figure 5. CAP criterion evaluation results in take-off phase.

Table 3. CAP criterion evaluation results with x_W = 12 m and 14 m in the take-off phase.

x_W (m)	S_T (m^2)	ζ_{sp}	CAP	Level	x_W (m)	S_T (m^2)	ζ_{sp}	CAP	Level
12	18	0.96	3.76	2	14	14	1.01	3.87	2
12	20	0.99	3.56	1	14	16	1.05	3.35	1
12	22	1.04	3.35	1	14	18	1.08	2.96	1
12	24	1.08	2.92	1	14	20	1.11	2.79	1
12	26	1.13	2.49	1	14	22	1.15	2.57	1
12	28	1.16	2.06	1	14	24	1.20	2.36	1
12	30	1.17	1.75	1	14	26	1.24	2.05	1
12	32	1.21	1.55	1	14	28	1.26	1.79	1
12	34	1.25	1.29	1	14	30	1.28	1.52	1
12	36	1.29	0.98	1	14	32	1.29	1.27	1
12	38	1.32	0.82	2	14	34	1.32	1.09	2

For a certain x_W, the CAP value decreases gradually with increasing S_T, and the damping ratio ζ_{sp} increases. The maximum limit of S_T defined by the CAP criterion is the critical value that leads to the degradation of the flying qualities to Level 2. When x_W is set to 12 m and 14 m, the corresponding maximum limit of S_T is 36 m^2 and 32 m^2, respectively. Hence, as the wing position moves rearward, the maximum limit of S_T gradually decreases.

According to all the above evaluation results, the level boundaries of the x_W–S_T combination defined by the CAP criterion in take-off phase are presented in Figure 6.

According to this figure, to ensure the Level 1 FQ of the CAP criterion, when x_W is set as 10 m, the corresponding design range of S_T is from 24 m^2 to 38 m^2; when x_W is set as 16 m, the S_T design range is from 14 m^2 to 26 m^2. The right boundary of Level 1 in Figure 6 determines the maximum limit of S_T corresponding to different x_W, and the rearward range of x_W corresponding to different S_T.
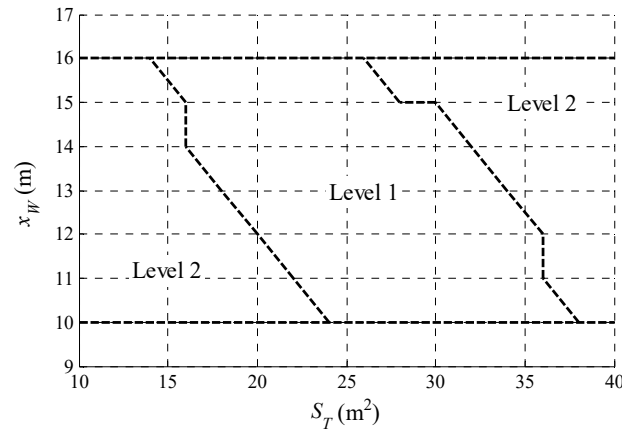

Figure 6. Parameter level boundaries defined by the CAP criterion in the take-off phase.

The Chalk criterion is also applied to evaluate the flying qualities in the take-off phase. Figure 7 shows the influence of changing S_T on the pitch rate response with x_W = 12 m. The variations in the tail area exert the main influences on the response peak and response speed of the pitch rate. As S_T increases, the response peak decreases, and the response time delay increases. The influence of the rearward displacement of the wing is similar to that of changing S_T, which means that decreasing x_W will reduce both the response peak and the response speed.
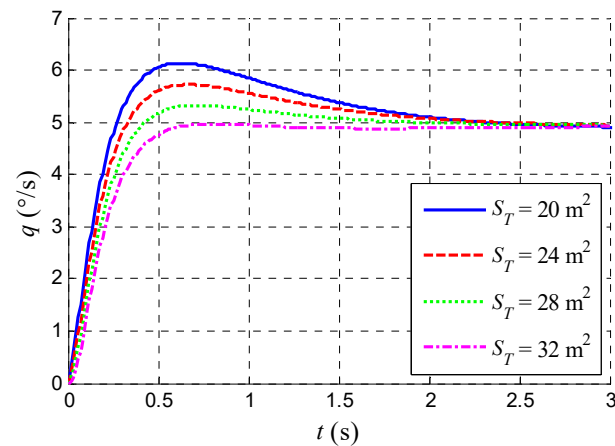

Figure 7. Pitch rate responses with different S_T.

Among all Chalk criterion parameters, the effective time delay t_1 is the most affected by the variations in and S_T. The evaluation results of t_1 are shown in Table 4. The transient peak ratio $\Delta q_{max}/\Delta q_{min}$ and the effective rise time Δt are also affected, but the FQ Level is not degraded. With the rearward movement of the wing and an increase in the tail area, the t_1 of the pitch response increases, which indicates poor maneuverability. The FQ Level is degraded to Level 2 (0.12 s < t_1 < 0.17 s) or even Level 3 (t_1 > 0.17 s). In the chosen ranges of x_W and S_T, an increase in x_W and a decrease in S_T will not degrade the flying qualities of the Chalk criterion.

Table 4. Chalk criterion evaluation results in the take-off phase (t_1, seconds).

x_W (m) \ S_T (m²)	18	20	22	24	26	28	30	32	34	36	38	40
10	0.049	0.055	0.065	0.071	0.076	0.083	0.091	0.098	0.107	0.112	0.118	0.129
11	0.055	0.063	0.072	0.082	0.082	0.095	0.103	0.105	0.109	0.115	0.125	0.137
12	0.063	0.071	0.081	0.091	0.089	0.102	0.109	0.109	0.112	0.118	0.132	0.152
13	0.075	0.079	0.089	0.098	0.095	0.107	0.112	0.113	0.117	0.142	0.156	0.169
14	0.081	0.087	0.095	0.103	0.106	0.113	0.116	0.118	0.135	0.158	0.171	0.182
15	0.092	0.096	0.101	0.109	0.112	0.118	0.128	0.145	0.152	0.167	0.185	0.196
16	0.098	0.102	0.107	0.115	0.119	0.129	0.142	0.155	0.163	0.172	0.192	0.212
Background	Level 1					Level 2				Level 3		

The level boundaries of the x_W–S_T combination defined by the Chalk criterion in the take-off phase are shown in Figure 8. According to this figure, to ensure the Level 1 FQ of the Chalk criterion, the maximum limit of S_T is 38 m² when x_W = 10 m, and the maximum limit is 26 m² when x_W = 16 m. Compared with the parameter boundaries defined by the CAP criterion shown in Figure 6, the Chalk criterion defines a more relaxed Level 1 boundary of the rearward range of x_W and the maximum limit of S_T. In contrast, the Level 2 boundary defined by the Chalk criterion is stricter and can be used as a supplement to the CAP criterion boundaries.
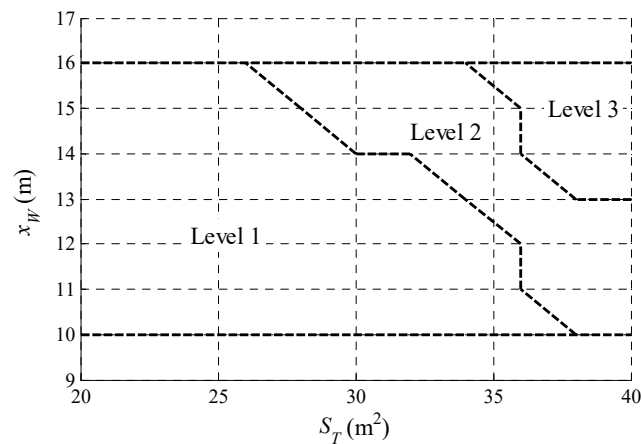

Figure 8. Parameter level boundaries defined by the Chalk criterion in the take-off phase.

- Minimum limit of the horizontal tail area

The selection of the x_W and S_T series is the same as the design of the maximum S_T range. The CAP criterion is applied to evaluate the flying qualities in the landing phase. Partial evaluation results with x_W values of 10 m, 12 m, 14 m, and 16 m are shown in Figure 9, where the corresponding minimum limits of S_T are 26 m², 22 m², 20 m², and 16 m², respectively. As the wing position moves forward, the minimum limit of S_T gradually increases.

The level boundaries of the x_W–S_T combination defined by the CAP criterion in landing phase are shown in Figure 10. According to this figure, to ensure the Level 1 FQ of the CAP criterion, the design range of S_T is from 26 m² to 40 m² when x_W = 10 m and from 16 m² to 32 m² when x_W = 16 m. The left boundary of Level 1 in Figure 10 can determine the minimum limit of S_T corresponding to different x_W, and the forward range of x_W corresponding to different S_T.
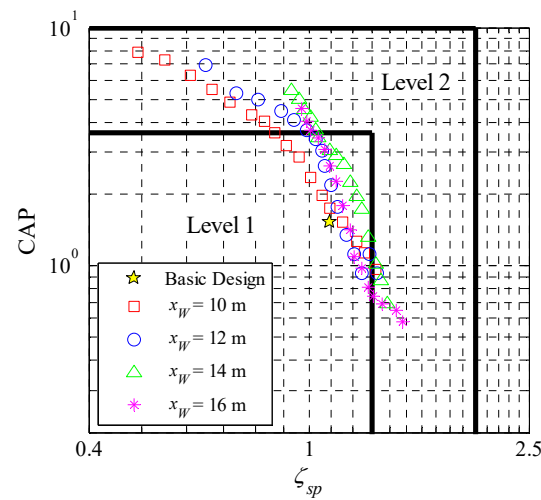
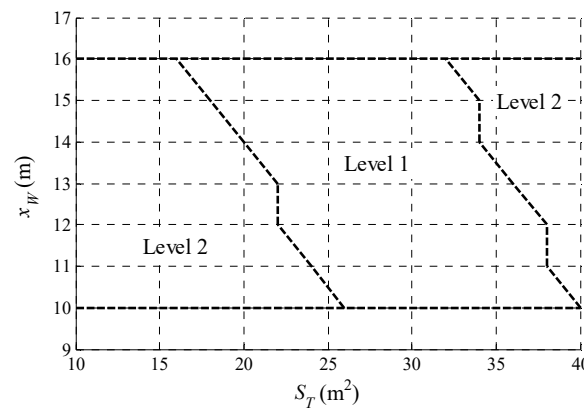**Figure 9.** CAP criterion evaluation results in the landing phase.

Figure 10. Parameter level boundaries defined by the CAP criterion in the landing phase.

According to the evaluation results of the Chalk criterion in the landing phase, the effective rise time and the response time delay decrease as the wing moves forward and the tail area decreases, which represents a better response speed of the pitch rate. Meanwhile, the pitch damping characteristics become worse as the transient peak ratio $\Delta q_{max}/\Delta q_{min}$ increases, but the FQ Level is not degraded. Therefore, the forward boundary of x_W and the minimum limit of S_T should be determined only by the CAP criterion.

- Level boundaries of the wing position and horizontal tail area

To determine the design ranges of x_W and S_T according to the Level 1 FQ requirements in the entire flight envelope, the most stringent boundaries in Figures 6, 8 and 10 are combined to form the final parameter level boundary diagram, as shown in Figure 11.

According to Figure 11, the Level 1 boundary of the rearward x_W and the maximum S_T (right side in Figure 11) is determined by the evaluation results in the take-off phase; the upper half is defined by the Chalk criterion and the lower half is defined by the CAP criterion. The Level 2 boundary (top right in Figure 11) is determined in take-off phase by the Chalk criterion. The Level 1 boundary of the forward x_W and the minimum S_T (left side in Figure 11) is defined in the landing phase by the CAP criterion. The design range of S_T determined by the Level 1 FQ requirements is from 26 m^2 to 38 m^2 when x_W = 10 m and from 16 m^2 to 26 m^2 when x_W = 16 m. In the configuration design process, the design range of S_T can be defined as the horizontal interval within the Level 1 zone (shaded part in Figure 11) corresponding to the designed x_W. Similarly, the design range of x_W is defined as the vertical interval within the Level 1 zone according to the designed S_T.
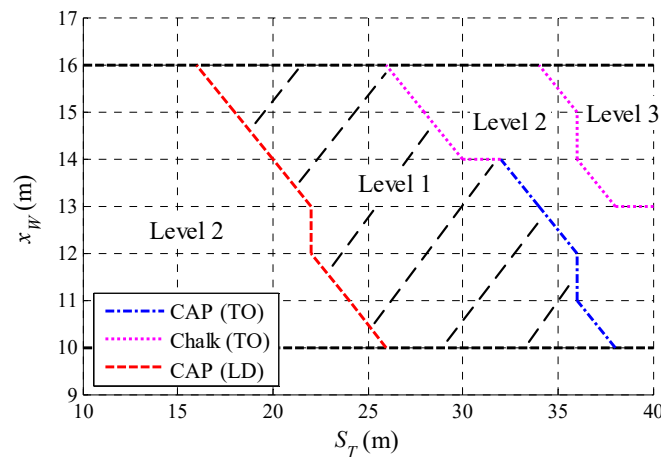
Figure 11. Complete level boundaries of x_W and S_T.

5.2. Boundaries of the Center of Gravity Position

The forward limit of $\overline{x}_{cg}$ should be designed in the take-off phase according to the most stringent requirement among the lower boundary of the CAP value, the upper boundary of ζ_{sp}, and the Chalk criterion. Likewise, the rearward limit of $\overline{x}_{cg}$ should be designed by evaluating the flying qualities in the landing phase according to the most stringent requirement among the upper boundary of the CAP value, the lower boundary of ζ_{sp}, and the Chalk criterion.

The series for the forward $\overline{x}_{cg}$ limit design is set as follows: from 6% to 36%, a point is selected every 3% of the wing MAC, yielding ten points in total. Likewise, the series for the rearward $\overline{x}_{cg}$ limit design is set as follows: from 38% to 65%, a point is selected every 3% of the wing MAC, also yielding ten points in total. Then, the CAP criterion is applied to evaluate the flying qualities of the aircraft with the forward $\overline{x}_{cg}$ in the take-off phase, while the rearward $\overline{x}_{cg}$ designs are evaluated in the landing phase. The evaluation results are presented in Figure 12. Compared with the basic design of the sample aircraft in the take-off phase, as the CG position moves forward (TO phase, $\overline{x}_{cg}$–), the CAP value decreases gradually, the damping ratio ζ_{sp} increases, and the FQ Level is degraded from Level 1 to Level 2. In the landing phase, as the CG position moves rearward (LD phase, $\overline{x}_{cg}$+), the CAP value increases, and the damping ratio ζ_{sp} decreases.

The forward $\overline{x}_{cg}$ designs are also evaluated by the Chalk criterion in the take-off phase. The effective time delay t_1 is the parameter most affected by the variation in $\overline{x}_{cg}$; the evaluation results of t_1 are shown in Table 5. As CG moves forward, the t_1 value of the pitch response increases, which indicates poor maneuverability. The FQ Level is degraded to Level 2 or even Level 3.

Table 5. Chalk criterion evaluation results of the forward $\overline{x}_{cg}$ (t_1, seconds).

$\overline{x}_{cg}$ (% MAC)	t_1 (s)	Level	$\overline{x}_{cg}$ (% MAC)	t_1 (s)	Level
33	0.05	1	18	0.121	2
30	0.061	1	15	0.137	2
27	0.074	1	12	0.155	2
24	0.088	1	9	0.172	3
21	0.103	1	6	0.189	3

According to the evaluation results of the Chalk criterion in the landing phase, the pitch damping characteristics of the aircraft become worse as the CG moves rearward, but the FQ Level is not degraded. Therefore, the Chalk criterion is only applied to design the forward $\overline{x}_{cg}$ limit.

The level boundaries of $\overline{x}_{cg}$ are defined as in Figure 13. According to this figure, the Level 1 boundary of the forward CG limit is 21% of the wing MAC, determined by the

upper boundary of ξ_{sp} in the CAP criterion in the take-off phase. The Level 2 boundary of the forward CG limit is 12% of the wing MAC, determined by the Chalk criterion. Finally, the Level 1 boundary of the rearward CG limit is 59% of the wing MAC, determined by the upper boundary of the CAP value in the landing phase. The $\overline{x}_{cg}$ range should be kept within the Level 1 zone (shaded part in Figure 13).
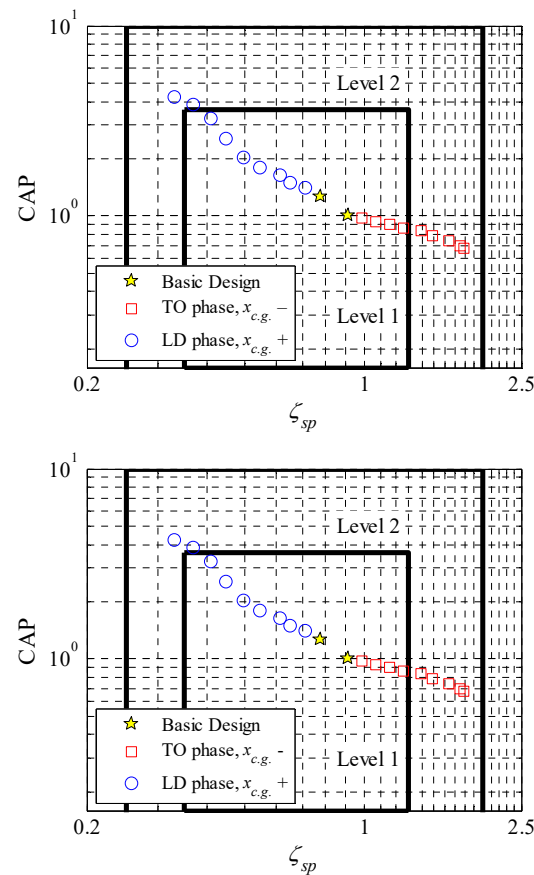

Figure 12. CAP criterion evaluation results of $\overline{x}_{cg}$.
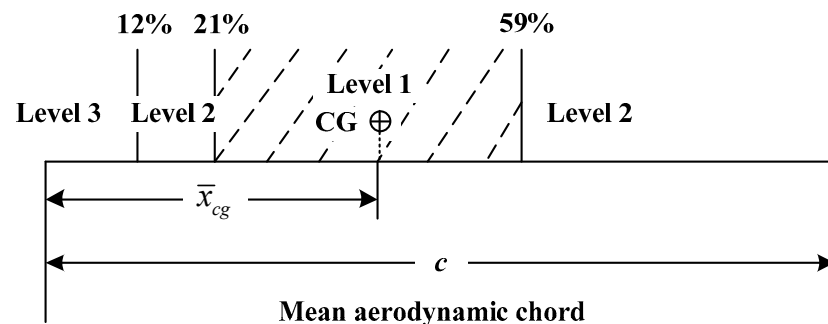
Figure 13. Level boundaries of $\overline{x}_{cg}$.

5.3. Boundaries of the Vertical Tail Area and Position

The vertical tail area S_V and position x_V should be designed in the cruise phase (high speed, high altitude, cruise engine setting and configuration) according to the requirements of the Dutch roll criterion. The variation series of S_V is set as follows: below the basic value of S_V, a point is selected every 1 m^2, and for each S_V, a series of x_V with an interval of 1 m is selected. As x_V is adjusted by changing the quarter chord point of the vertical tail without moving the root position, the design range of x_V is limited from 26 m to 31 m.

Then, the Dutch roll criterion is applied to evaluate the flying qualities of different S_V–x_V combinations. Partial evaluation results with S_V values of 10 m², 12 m², 14 m², and 16 m² are shown in Figure 14, and the Dutch roll characteristics with S_V values of 12 m² and 14 m² are shown in Table 6.
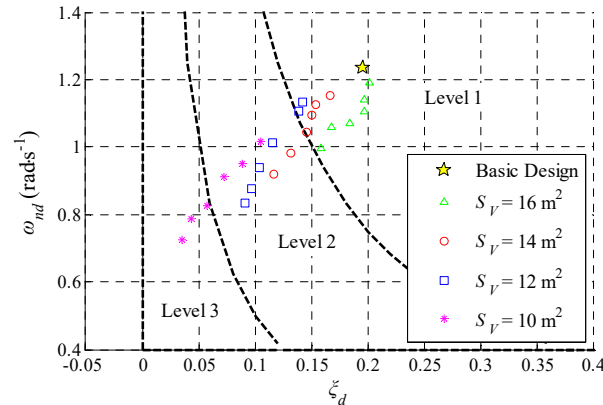

Figure 14. Dutch roll criterion evaluation results in the cruise phase.

Table 6. Dutch roll criterion evaluation results with x_W = 12 m, 14 m in the cruise phase.

S_V (m²).	x_V (m)	ζ_{dr}	$\omega_{n.dr}$ (rad/s)	Level	S_V (m²)	x_V (m)	ζ_{dr}	$\omega_{n.dr}$ (rad/s)	Level
12	31	0.142	1.132	1	14	31	0.166	1.153	1
12	30	0.138	1.107	1	14	30	0.154	1.127	1
12	29	0.115	1.012	2	14	29	0.150	1.093	1
12	28	0.104	0.937	2	14	28	0.145	1.044	1
12	27	0.097	0.878	2	14	27	0.132	0.981	2
12	26	0.091	0.835	2	14	26	0.117	0.920	2

For a certain S_V, both $\omega_{n.dr}$ and ζ_{dr} of the Dutch roll mode decrease gradually with the forward movement of the tail. The forward range of x_V is defined as the critical value that leads to the degradation of directional flying qualities. When S_V is set as 12 m² and 14 m², the corresponding forward range of x_V is 30 m and 28 m, respectively. With decreasing S_V, the design range of x_V gradually decreases. The minimum limit of S_V is defined as the critical value without the corresponding x_V that meets the requirements of the Level 1 FQ.

According to all evaluation results, the level boundaries of the S_V–x_V combination are defined as in Figure 15.

Considering that the drag force due to the vertical tail is largely related to the vertical tail area, it is necessary to restrict the tail area while satisfying the flying qualities requirements. According to Figure 15, x_V within the design range can ensure Level 1 FQ of the closed-loop aircraft when S_V is not less than 15 m². The minimum limit of S_V is 11 m² and the corresponding x_V is 31 m. In the configuration design process, the design range of S_V can be defined as the horizontal interval within the shaded Level 1 zone in Figure 15, corresponding to the designed x_V. Similarly, the design range of x_V is defined as the vertical interval within the Level 1 zone according to the designed S_V.
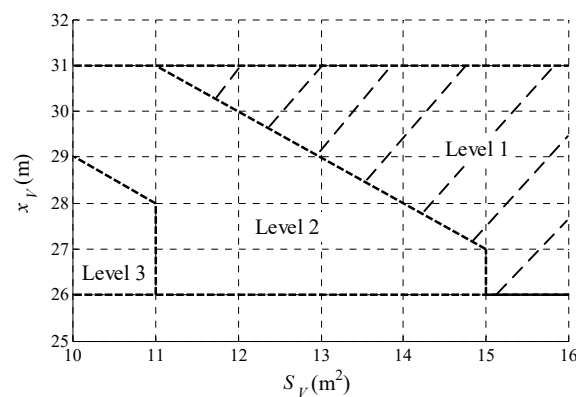
Figure 15. Complete level boundaries of S_V and x_V.

6. Conclusions

In this study, the influences of typical configuration parameters on flying qualities are analyzed, and a configuration parameter boundaries design method based on closed-loop flying qualities requirements is proposed and verified by an application example.

(1) Five typical configuration parameters that should be designed based on flying qualities requirements are determined: wing position, horizontal tail area, center of gravity position, vertical tail area and position.

(2) The proposed configuration parameter boundaries design method based on closed-loop flying qualities requirements is achieved as follows. First, the flight control law is designed based on the model reference nonlinear dynamic inversion method, and a high-order closed-loop aircraft model is established. Second, the most stringent flight conditions and the evaluation criteria that are most sensitive to the target parameters are determined. Third, by searching for the critical values that lead to the degradation of flying qualities, the closed-loop flying qualities requirements are transformed into the design ranges of target configuration parameters.

(3) An application example involving the typical parameter boundaries design of a sample aircraft is provided. The wing position of the sample aircraft ranges from 10 m to 16 m, the design range of the horizontal tail area corresponding to the forward limit of wing position is from 26 m^2 to 38 m^2, and the horizontal tail area range corresponding to the rear limit of wing position is from 16 m^2 to 26 m^2. The design ranges of the wing position and horizontal tail area are defined by the level boundary diagram. The forward limit of the center of gravity is 21% of the average aerodynamic chord, while the rearward limit is 59%. The minimum limit of the vertical tail area is 11 m^2, and the design ranges of the vertical tail area and position are defined by the level boundary diagram.

Author Contributions: Conceptualization, L.W. and K.Y.; methodology, L.W.; software, K.Y.; validation, L.W., K.Y. and T.Y.; formal analysis, K.Y.; investigation, K.Y.; resources, P.Z.; data, P.Z.; writing—original draft preparation, K.Y. and T.Y.; writing—review and editing, T.Y.; project administration, L.W. All authors have read and agreed to the published version of the manuscript.

Institutional Review Board Statement: Not applicable.

Informed Consent Statement: Not applicable.

Data Availability Statement: The high-order closed-loop aircraft model (Figure 2) and data presented in this study can be obtained from the corresponding author on request.

Conflicts of Interest: The authors declare no conflict of interest.

Abbreviations:

CG	Center of Gravity
FCL	Flight Control Laws
SAS	Stability Augmentation System
SCAS	Stability and Control Augmentation System
NDI	Nonlinear Dynamic Inversion
INDI	Incremental Nonlinear Dynamic Inversion
FQ	Flying Qualities
PI	Proportional-Integral
CAP	Control Anticipation Parameter
LOES	Low-Order Equivalent System
MAC	Mean Aerodynamic Chord
TO	Take-Off
LD	Landing

References

1. Raymer, D.P. *Airplane Design: A Conceptual Approach*, 2nd ed.; American Institute of Aeronautics and Astronautics, Inc.: Washington, DC, USA, 1989; ISBN 0-930403-51-7.
2. Anton, E.; Lammering, T.; Henke, R. Fast estimation of top-level aircraft requirement impact on conceptual aircraft designs. In Proceedings of the 10th AIAA Aviation Technology, Integration, and Operations (ATIO) Conference, Fort Worth, TX, USA, 13–15 September 2010. [CrossRef]
3. Cook, M.V. *Flight Dynamics Principles: A Linear Systems Approach to Aircraft Stability and Control*, 2nd ed.; Butter-worth-Heinemann: Burlington, NJ, USA, 1997; ISBN 978-0-7506-6927-6.
4. Wang, L.; Yin, H.; Guo, Y.; Yue, T.; Jia, X. Closed-loop motion characteristic requirements of receiver aircraft for probe and drogue aerial refueling. *Aerosp. Sci. Technol.* **2019**, *93*, 105293. [CrossRef]
5. Campos, L.M.B.C.; Marques, J.M.G. On the Handling Qualities of Two Flying Wing Aircraft Configurations. *Aerospace* **2021**, *8*, 77. [CrossRef]
6. Nicolosi, F.; De Marco, A.; Vecchia, P.D. Stability, flying qualities and longitudinal parameter estimation of a twin-engine CS-23 certified light aircraft. *Aerosp. Sci. Technol.* **2013**, *24*, 226–240. [CrossRef]
7. Wang, L.; Guo, Y.; Zhang, Q.; Yue, T. Suggestion for aircraft flying qualities requirements of a short-range air combat mission. *Chin. J. Aeronaut.* **2017**, *30*, 881–897. [CrossRef]
8. Wang, L.; Xu, Z.; Yue, T. Dynamic characteristics analysis and flight control design for oblique wing aircraft. *Chin. J. Aeronaut.* **2016**, *29*, 1664–1672. [CrossRef]
9. Schulze, M.; Neumann, J.; Klimmek, T. Parametric Modeling of a Long-Range Aircraft under Consideration of Engine-Wing Integration. *Aerospace* **2020**, *8*, 2. [CrossRef]
10. Zhu, J. A survey of advanced flight control theory and application. In Proceedings of the Multiconference on Computational Engineering in Systems Applications, Beijing, China, 4–6 October 2006. [CrossRef]
11. Bauer, C.; Lagadec, K.; Bès, C.; Mongeau, M. Flight Control System Architecture Optimization for Fly-By-Wire Airliners. *J. Guid. Control. Dyn.* **2007**, *30*, 1023–1029. [CrossRef]
12. Zhao, X.; Guerrero, J.M.; Wu, X. Review of aircraft electric power systems and architectures. In Proceedings of the International Energy Conference, Dubrovnik, Croatia, 13–16 May 2014; Available online: https://core.ac.uk/reader/60556259 (accessed on 15 November 2021).
13. Zhu, Z.; Guo, H.; Ma, J. Aerodynamic layout optimization design of a barrel-launched UAV wing considering control capability of multiple control surfaces. *Aerosp. Sci. Technol.* **2019**, *93*, 105297. [CrossRef]
14. Sanchez-Carmona, A.; Cuerno-Rejado, C. Design Process and Environmental Impact of Unconventional Tail Airliners. *Aerospace* **2021**, *8*, 175. [CrossRef]
15. Attar, M.; Wahnon, E.; Chaimovitz, D. Advanced Flight Control Technologies for UAVs. In Proceedings of the 2nd AIAA Unmanned Unlimited Conf. and Workshop & Exhibit, San Diego, CA, USA, 15–18 September 2003. [CrossRef]
16. Brockhaus, R. *Flugregelung*; Springer: Berlin/Heidelberg, Germany, 2001; ISBN 978-3-662-07265-3.
17. Kim, J.P.; Kunz, D.L. Handling Qualities Assessment of an Unmanned Aircraft Using Performance and Workload Metrics. *J. Guid. Control. Dyn.* **2017**, *40*, 1–9. [CrossRef]
18. Humphreys-Jennings, C.; Lappas, I.; Sovar, D.M. Conceptual Design, Flying, and Handling Qualities Assessment of a Blended Wing Body (BWB) Aircraft by Using an Engineering Flight Simulator. *Aerospace* **2020**, *7*, 51. [CrossRef]
19. Liu, F.; Wang, L.; Tan, X. Digital virtual flight testing and evaluation method for flight characteristics airworthiness compliance of civil aircraft based on HQRM. *Chin. J. Aeronaut.* **2014**, *28*, 112–120. [CrossRef]
20. Risse, K.; Anton, E.; Henke, R. Methodology for Flying Qualities Prediction and Assessment in Preliminary Aircraft Design. In Proceedings of the 10th AIAA Aviation Technology, Integration, and Operations (ATIO) Conference, Fort Worth, TX, USA, 13–15 September 2010. [CrossRef]

21. Rizzi, A.; Eliasson, P.; Goetzendorf-Grabowski, T.; Vos, J.B.; Zhang, M.; Richardson, T.S. Design of a canard configured TransCruiser using CEASIOM. *Prog. Aerosp. Sci.* **2011**, *47*, 695–705. [CrossRef]
22. Cacciola, S.; Riboldi, C.E.D.; Arnoldi, M. Three-Surface Model with Redundant Longitudinal Control: Modeling, Trim Optimization and Control in a Preliminary Design Perspective. *Aerospace* **2021**, *8*, 139. [CrossRef]
23. Sonneveldt, L.; Van Oort, E.R.; Chu, Q.; Mulder, J.A. Nonlinear adaptive flight control law design and handling qualities evaluation. In Proceedings of the Joint 48h IEEE Conference on Decision and Control and 28th Chinese Control Conference, Shanghai, China, 15–18 December 2009. [CrossRef]
24. Samadikhoshkho, Z.; Ghorbani, S.; Janabi-Sharifi, F.; Zareinia, K. Nonlinear control of aerial manipulation systems. *Aerosp. Sci. Technol.* **2020**, *104*, 105945. [CrossRef]
25. Hasan, Y.J.; Flink, J.; Freund, S.; Klimmek, T.; Kuchar, R.; Liersch, C.M.; Looye, G.; Moerland, E.; Pfeiffer, T.; Schrader, M.; et al. Stability and Control Investigations in Early Stages of Aircraft Design. In Proceedings of the 2018 Applied Aerodynamics Conference, Atlanta, GA, USA, 25–29 June 2018. [CrossRef]
26. Ji, C.-H.; Kim, C.-S.; Kim, B.-S. A Hybrid Incremental Nonlinear Dynamic Inversion Control for Improving Flying Qualities of Asymmetric Store Configuration Aircraft. *Aerospace* **2021**, *8*, 126. [CrossRef]
27. Scholz, D. *Aircraft Design, Lecture Notes*; Hamburg University of Applied Sciences: Hamburg, Germany, 2015; Available online: http://hoou.ProfScholz.de (accessed on 15 November 2021).
28. Etkin, B.; Teichmann, T. *Dynamics of Flight: Stability and Control*; John Wiley & Sons, Inc.: New York, NY, USA, 1996; ISBN 0-471-03418-5.
29. Scholz, D. *Flight Dynamics, Stability and Control, Lecture Notes*; Hamburg University of Applied Sciences: Hamburg, Germany, 2003; Available online: https://perma.cc/4GHQ-SP33 (accessed on 15 November 2021).
30. McRuer, D.; Ashkenas, I.; Graham, D. *Aircraft Dynamics and Automatic Control*; Princeton University Press: Princeton, NJ, USA, 1973; Available online: https://perma.cc/G9GQ-GJAD (accessed on 15 November 2021).
31. Scholz, D. Empennage sizing with the tail volume complemented with a method for dorsal fin layout. *INCAS Bull.* **2021**, *13*, 149–164. [CrossRef]
32. Barua, P.; Sousa, T.; Scholz, D. *Empennage Statistics and Sizing Methods for Dorsal Fins*; Hamburg University of Applied Sciences: Hamburg, Germany, 2013; Available online: http://purl.org/AERO/TN2013-04-15 (accessed on 15 November 2021).
33. Miller, C.J. Nonlinear Dynamic Inversion Baseline Control Law: Architecture and Performance Predictions. In Proceedings of the AIAA Guidance, Navigation, and Control Conference, Portland, OR, USA, 8–11 August 2011; Available online: https://core.ac.uk/reader/10562991 (accessed on 15 November 2021).
34. Miller, C.J. Nonlinear Dynamic Inversion Baseline Control Law: Flight-Test Results for the Full-scale Advanced Systems Testbed F/A-18 Airplane. In Proceedings of the AIAA Guidance, Navigation, and Control Conference, Portland, OR, USA, 8–11 August 2011; Available online: https://core.ac.uk/reader/10562995 (accessed on 15 November 2021).
35. Harper, R.P.; Cooper, G.E. Handling qualities and pilot evaluation. *J. Guid. Control. Dyn.* **1986**, *9*, 515–529. [CrossRef]
36. United States Department of Defense. *MIL-F-8785, Military Specification, Flying Qualities of Piloted Airplanes*; United States Department of Defense: Arlington, TX, USA, 1980; Available online: https://perma.cc/FN56-6YAG (accessed on 15 November 2021).
37. United States Department of Defense. *MIL-STD-1797A, Military Standard, Flying Qualities of Piloted Aircraft*; United States Department of Defense: Arlington, TX, USA, 1990; Available online: https://perma.cc/EVM7-RW6Z (accessed on 15 November 2021).
38. United States Department of Defense. *MIL-HDBK-1797, Military Standard, Flying Qualities of Piloted Aircraft*; United States Department of Defense: Arlington, TX, USA, 2004; Available online: https://perma.cc/978D-RJFG (accessed on 15 November 2021).

Article

A Physics-Based Multidisciplinary Approach for the Preliminary Design and Performance Analysis of a Medium Range Aircraft with Box-Wing Architecture

Karim Abu Salem [1,*] **, Vittorio Cipolla** [1] **, Giuseppe Palaia** [1] **, Vincenzo Binante** [2] **and Davide Zanetti** [2]

[1] Department of Civil and Industrial Engineering, University of Pisa, Via G. Caruso 8, 56122 Pisa, Italy; vittorio.cipolla@unipi.it (V.C.); giuseppe.palaia@phd.unipi.it (G.P.)
[2] SkyBox Engineering, Via G. Caruso 8, 56122 Pisa, Italy; v.binante@skyboxeng.com (V.B.); d.zanetti@skyboxeng.com (D.Z.)
[*] Correspondence: karim.abusalem@gmail.com

Abstract: The introduction of disruptive innovations in the transport aviation sector is becoming increasingly necessary. This is because there are many very demanding challenges that the transport aviation system will have to face in the years ahead. In particular, the reduction in pollutant emissions from air transport, and its impact on climate change, clearly must be addressed; moreover, sustainable solutions must be found to meet the constantly increasing demand for air traffic, and to reduce the problem of airport saturation at the same time. These three objectives seem to be in strong contrast with each other; in this paper, the introduction of a disruptive airframe configuration, called PrandtlPlane and based on a box-wing lifting system, is proposed as a solution to face these three challenges. This configuration is a more aerodynamically efficient alternative candidate to conventional aircraft, introducing benefits in terms of fuel consumption and providing the possibility to increase the payload without enlarging the overall aircraft wingspan. The development and analysis of this configuration, applied to a short-to-medium range transport aircraft, is carried out through a multi-fidelity physics-based approach. In particular, following an extensive design activity, the aerodynamic performance in different operating conditions is investigated in detail, the structural behaviour of the lifting system is assessed, and the operating missions of the aircraft are simulated. The same analysis methodologies are used to evaluate the performance of a benchmark aircraft with conventional architecture, with the aim of making direct comparisons with the box-wing aircraft and quantifying the performance differences between the two configurations. Namely, the CeRAS CSR-01, an open-access virtual representation of an A320-like aircraft, is selected as the conventional benchmark. Following such a comparative approach, the paper provides an assessment of the potential benefits of box-wing aircraft in terms of fuel consumption reduction and increase in payload capability. In particular, an increase in payload capability of 66% and a reduction in block fuel per pax km up to 22% is achieved for the PrandtlPlane with respect to the conventional benchmark, while maintaining the same maximum wingspan.

Keywords: box-wing; PrandtlPlane; disruptive aircraft; innovation; future aviation

1. Introduction

In the near future, the aviation industry will have to face several challenging tasks; the most relevant issue is related to the environmental impact of transport aviation, which has to drastically reduce its pollutant footprint and its impact on climate change [1–6]. At the same time, the demand for commercial air transport is growing quickly [7–10], whereas airports are gradually addressing saturation problems using aprons [11]. Meeting the growing demand for flights and reducing the environmental impact of air transportation seem to be contrasting objectives of aviation research and industry; a possible way to face this problem is to explore and study disruptive technologies, both in the field of propulsion

and aircraft design. Regarding propulsion, several studies are dedicated to the analysis and design of new types of engines, alternative to the conventional internal combustion one, such as hybrid and electrical powertrains [12–17]; also, alternative energy sources to fossil fuels, such as hydrogen [18–21] or biofuels [22–24], are currently under study. Regarding aircraft development, studies have been conducted on the optimisation of the tube-and-wing aircraft to reach the maximum potential of the conventional configuration [25–28], but great effort is currently dedicated to the study and development of new unconventional architectures [29–34], such as the blended wing–body configuration [35–37] or the joined wings architecture [38,39], which may represent a real breakthrough in aircraft evolution.

In this paper, the focus is on an unconventional configuration called PrandtlPlane [40–43], a concept based on the box-wing lifting architecture, which is represented in Figure 1; for the PrandtlPlane (PrP) configuration, the box-wing is designed according to Prandtl's "best wing system" theory [44], which allows one to minimise the induced drag of the lifting system [45,46]. This configuration has been extensively studied in the PARSIFAL project [47,48], a research project funded by the European Commission in the framework of the Horizon2020 program.

Figure 1. Artistic views of PrandtlPlane aircraft of different categories: ultra-light amphibious (**left**) [43], executive class (**centre**) [49], hybrid electric regional airliner (**right**) [15].

Some of the main challenges that will be faced by aeronautical research in the near future are summarised in Table 1, together with some general possible solutions.

Table 1. Challenges ahead for the transport aviation and related general solutions.

Challenge	Possible Solution
To meet the large air traffic demand increase expected in the coming years, in particularly for short/medium routes [7] *.	To design an aircraft with an increased cabin capacity compared to the present aircraft operating on short/medium routes.
To avoid airport saturation problems, already relevant today [11].	To limit the size and overall dimensions of the aircraft.
To reduce the environmental impact of the aircraft [2], thus minimising fuel consumption per passenger.	To increase the aerodynamic efficiency as much as possible and/or to adopt new types of propulsion (i.e., electric or hydrogen).

* The forecasts used as reference were provided before the COVID-19 outbreak; the pandemic will have a direct impact on the air traffic demand and on the related forecast. The main consequence is related to a shift-forward of the peak increase in the demand with respect the previous market outlooks. However, the overall scenario is supposed to be the same, in a delayed time scale.

To effectively address the issues ahead, aircraft configuration must comply with the three indicated solutions at the same time. Concerning the issue of the saturation of airport areas, it should be pointed out that using larger existing aircraft to reduce the number of flights does not represent a solution to the problem; for example, using an Airbus A350 in place of two Airbus A321s on medium-haul flights (leaving aside the fact that A350 aircraft are not designed to accomplish these missions) would reduce the number of slots occupied, but the size of the Airbus A350 would require the occupation of a much larger apron (ICAO Aerodrome Code C: max wingspan 36 metres vs. ICAO Aerodrome Code E: max wingspan 65 m) and taxiway. It is clear that this operation does not bring any advantages. On the contrary, it would imply further disadvantages, considering the fact that the majority of

worldwide airport slots are represented by ICAO C aprons, while there are significantly fewer ICAO E aprons [50].Wingspan definitely plays a key role in ground operations, as it is constrained by the standardised dimensions of the apron and taxiways.

The general solutions proposed to the three challenges presented above indicate that a technological step forward is necessary for commercial aviation aircraft: it is difficult to try to solve these problems through the adoption of aircraft with conventional architecture and/or conventional propulsion system [51].

In this work, a suitable solution to the presented challenges is proposed through the introduction of the non-conventional PrandtlPlane architecture, while aspects related to innovative propulsion systems are not considered; in particular, a detailed analysis is conducted to answer the question: "can the introduction of the PrandtlPlane configuration be a possible solution to face the challenges of commercial aviation in the near future?"

The PrandtlPlane configuration is a candidate to satisfy the three challenges previously presented; in particular, considering the short/medium-haul market sector, it allows:

1. The transport of a larger number of passengers compared to the present aircraft operating on medium routes, by exploiting the increased lifting capacity of the box-wing system, and using a new fuselage design, in order to increase the number of travellers without increasing the number of flights;

2. The exploitation of the increased lifting capacity of the box-wing to design an aircraft with the same overall dimensions, in particular of wingspan, of present aircraft operating on short/medium routes, while improving the passenger capability, in order to avoid the increase in required apron space; namely, this requires the design of a box-wing with wingspan limited to the standard related to short-to-medium-route aircraft, i.e., maximum 36 m (ICAO Aerodrome Code C), to be compliant with the airport infrastructure (aprons, taxiways), but at the same time, to transport a larger payload;

3. The exploitation of the box-wing architecture designed according to the "Best Wing System" theory to maximise the aerodynamic efficiency; indeed, a properly designed box-wing aircraft allows one to theoretically minimise the induced drag, by exhibiting Oswald factor efficiencies larger than 1 [45], as well as to increase the lifting capability (i.e., to trim a larger weight), and thus to reduce the fuel consumption per passenger–kilometre compared to conventional aircraft.

In this paper, first of all, the multidisciplinary design methodology adopted to develop a short/medium-haul PrandtlPlane aircraft is presented by describing the multi-fidelity design and analysis strategy implemented in detail. The main focus is given to the aerodynamic and structural design of the innovative box-wing lifting system, together with a detailed assessment of the mission performance. Then, the PARSIFAL project case study is presented and described in detail, starting from the definition of the design requirements to the aerodynamic and mission performance evaluation. The box-wing aircraft performance are then compared with those of a reference conventional tube-and-wing benchmark aircraft; the performance assessment methods used are the same in both cases, to provide direct and fair comparisons between two totally different aircraft architectures.

2. Design Methodology Description

The design strategy adopted for the development of the box-wing aircraft is schematically summarised in Figure 2; three main different stages were performed: a conceptual design initialisation, a reference aerodynamic layout definition through aerodynamic optimisation and a subsequent model refinement and performance evaluation. These three main blocks of the design process are detailed in the following.
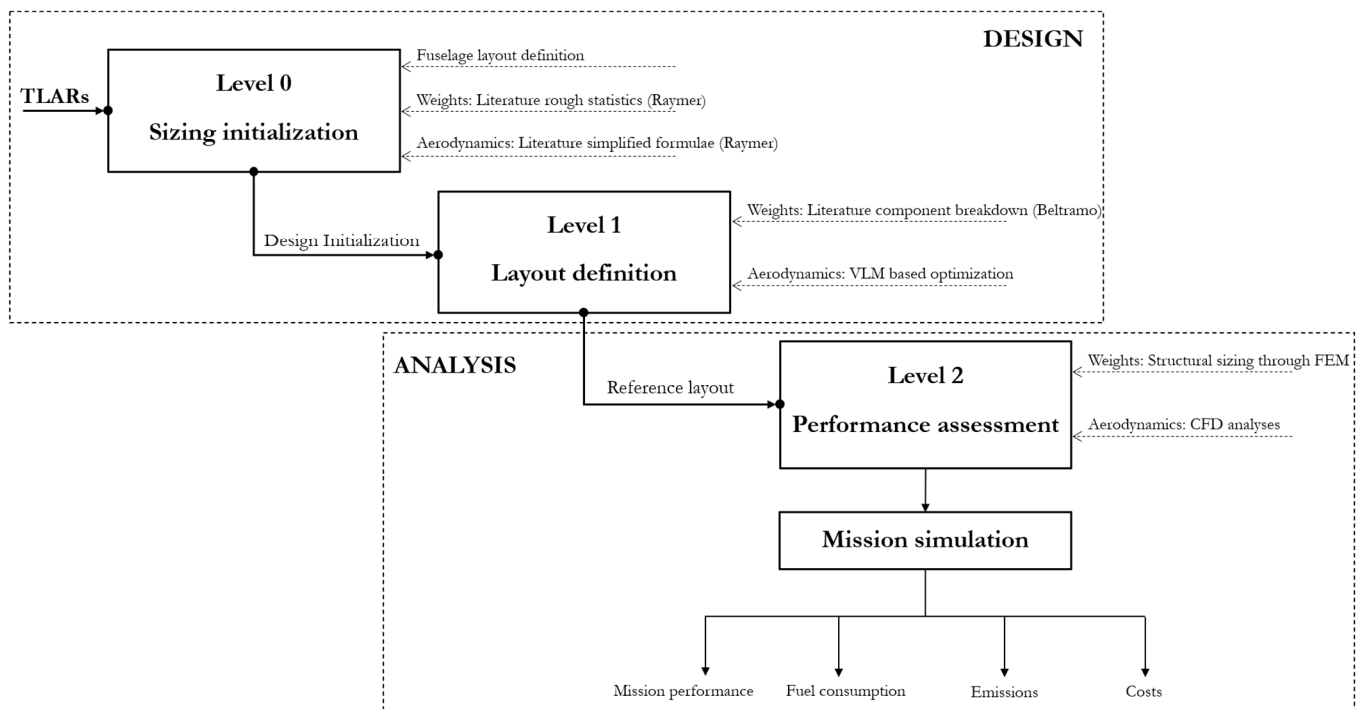
Figure 2. Multi-level aircraft design and analysis diagram (abbreviations used: VLM = Vortex Lattice Method, FEM = Finite Element Model, CFD = Computational Fluid Dynamics).

2.1. Conceptual Design Initialisation

The first step of the initial conceptual sizing is represented by the definition of the fuselage layout, its overall size, and the characterisation of the cabin section layout and the internal arrangement; this is fundamental, because one of the main requirements to be satisfied is represented by the maximum number of passengers: to accomplish this specification, a proper fuselage design is needed to start the following aircraft design process. Then, the conceptual design initialisation mainly consists of a rough evaluation of the aircraft aerodynamic performance and the related estimation of the initial guess of the maximum take-off weight. The inputs of the procedure are the Top Level Aircraft Requirements (TLARs), namely the design payload and range, the operating conditions and the size constraints. As far as the aerodynamic performance is considered, a simplified model to estimate the aircraft drag was used by separately calculating the induced drag coefficient, C_{Di}, the parasite drag coefficient, C_{D0}, and the wave drag coefficient, C_{Dwave}, of the aircraft (Equation (1)).

$$C_{D\ tot} =\ C_{Di} +\ C_{D0} +\ C_{D\ wave} \tag{1}$$

The induced drag coefficient, C_{Di} , is estimated by considering only the lifting components (Equation (2)); namely, the contribution of the front and rear wings are considered, as the contributions to the induced drag of the vertical wings and the fuselage are neglected at this stage.

$$C_{Di} = C_{Di}{}^{Front} + C_{Di}{}^{Rear} + C_{Di}{}^{Vertical} + C_{Di}{}^{Fus} \tag{2}$$

The induced drag coefficient, $C_{Di}{}^{wing}$, of each lifting component is evaluated by using the relations of Equations (3)–(4), where C_L represents the wing lift coefficient, AR is the related aspect ratio, and e is the Oswald factor. As the considered configuration is a box-wing designed according to the Prandtl's theory on the best wing system [44], the Oswald factor, e, used in this phase is fixed equal to 1.46 [52]. Since the aircraft geometry does not exist at this initialisation stage, some reference parameters must be set reasonably, as indicated in the reference literature. This is the case for the Oswald factor, as, although it

depends on the wings' height to span ratio, h/b [44], it is set as equal to the theoretical maximum value for a box lifting system [52]. This does not represent a misalignment, since in the following design phases (Section 2.2) the Oswald factor is calculated for each configuration considered (taking into account its geometrical and lift distribution characteristics) by means of the VLM aerodynamic solver.

$$C_{Di}{}^{wing} = kC_L{}^2 \tag{3}$$

$$k = 1/(\pi\, AR\, e) \tag{4}$$

The parasite drag coefficient, C_{D0}, is evaluated by the *equivalent skin friction model* described in [53]; namely, the $C_{D0\ tot}$ of the aircraft is the sum of each aircraft component, $C_{D0}{}^{comp}$, evaluated by means of the formula of Equation (5).

$$C_{D0}{}^{comp} = C_{fe}\left(S_{wet}{}^{comp}/S_{ref}\right) \tag{5}$$

$$C_{D0\ tot} = \Sigma C_{D0}{}^{comp} \tag{6}$$

where C_{fe} is the equivalent skin friction coefficient, equal to 0.0030 for civil transport aircraft from the approximation reported in [53]; the same reference presents a simplified way to estimate the components' wetted surface, $S_{wet}{}^{comp}$, both in the case of a wing component (i.e., lifting surfaces, vertical tip-wing, tail, fin, Equation (7)) and cylindrical components (i.e., fuselage, nacelle, Equation (8)):

$$S_{wet}{}^{Wing} = S_{exposed}\left[1.997 + 0.52\,(t/c)\right] \tag{7}$$

$$S_{wet}{}^{cyl} = \pi\, d^{cyl} l^{cyl} \tag{8}$$

where $S_{exposed}$ is the planform area of the wing exposed to the flow, (t/c) is the wing thickness-to-chord ratio, and d^{cyl} and l^{cyl} are the diameter and the length, respectively, of the considered cylinder. For aircraft cruising in transonic flight, the wave drag coefficient, C_{Dwave}, is fixed as constant and equal to 0.002, according to the Boeing definition of transonic drag rise reported in [53].

Several simplified models are presented in the literature to evaluate the aircraft gross weight in the very initial stage of the aircraft design. In this phase, to initialise the design process, the aircraft maximum take-off weight, *MTOW*, is estimated by individually evaluating the contribution of the payload weight, W_{pay}, the fuel weight, W_{fuel}, and the operating empty weight, W_{oe} (Equation (9)):

$$MTOW = W_{pay} + W_{fuel} + W_{oe} \tag{9}$$

where, concerning the payload, 95 kg per passenger is assumed ([54]), the fuel weight, W_{fuel}, is evaluated by using the well-known Breguet formula [55], and the operating empty weight, W_{oe}, is estimated by the statistic interpolation of historical trends proposed in [53].

2.2. Optimisation Driven Preliminary Design

The main information obtained from the conceptual design initialisation is the first estimation of the aircraft maximum take-off weight, which is useful to start the second level of the aircraft design process (Figure 2). In particular, in this stage, the aerodynamic design is driven by an optimisation procedure implemented in an in-house tool called AEROSTATE [56–58]; the schematic representation of the AEROSTATE code is reported in Figure 3.
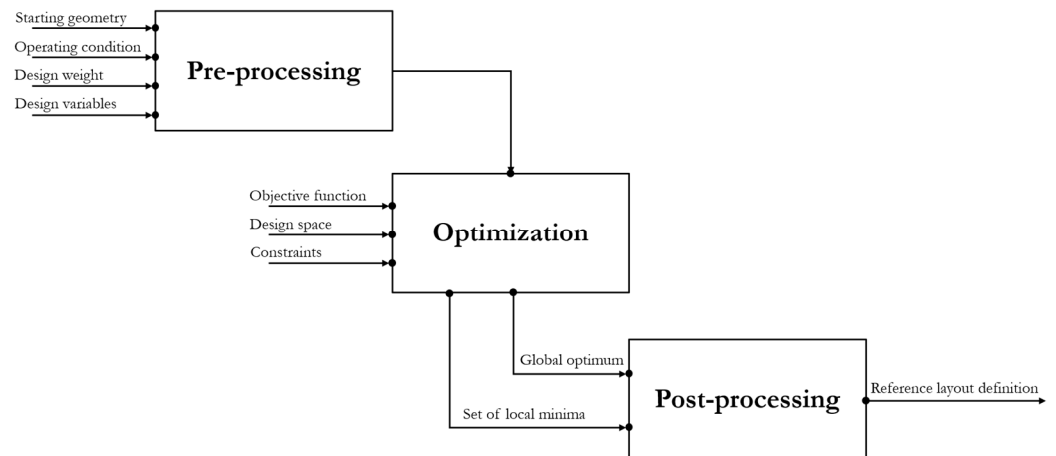
Figure 3. AEROSTATE workflow.

The general constrained aerodynamic optimisation problem addressed in this tool is summarised in the following Equations (10)–(12):

- Objective function

$$\min(-L(\boldsymbol{x})/D(\boldsymbol{x})) \tag{10}$$

- Set of inequality constraints

$$g(\boldsymbol{x}) \geq 0 \tag{11}$$

- Design space

$$\boldsymbol{lb} < \boldsymbol{x} < \boldsymbol{ub} \tag{12}$$

where the objective function to be minimised is the *-L/D* ratio, which is equivalent to the maximisation of the aerodynamic efficiency (lift-to-drag ratio) evaluated in a reference point of the cruise (e.g., the 25% of the stage length); the optimisation is constrained by a set of inequality constraints *g(x)*; the design variables *x*, limited by lower and upper boundaries (*lb* and *ub*, respectively), are reported in Figure 4.
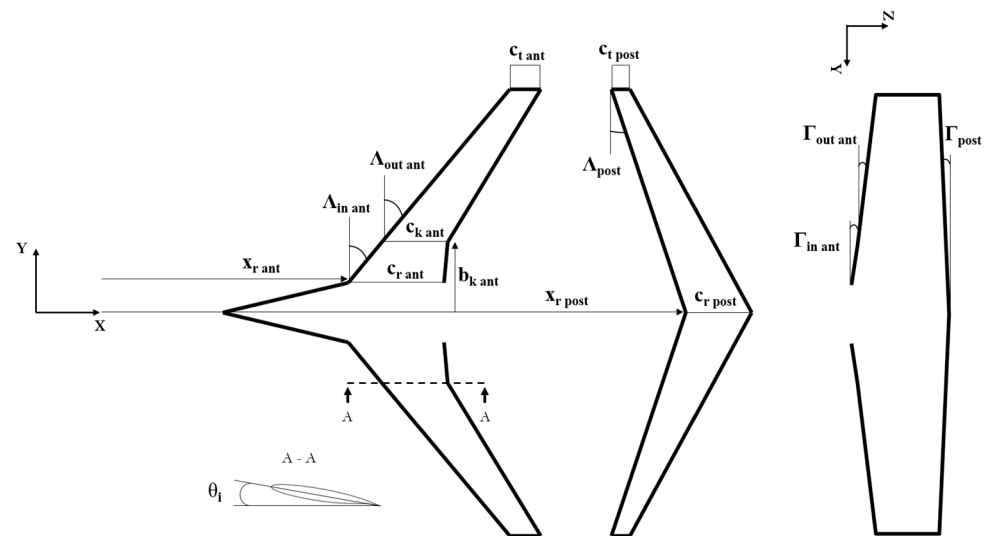

Figure 4. Design variables of the aerodynamic optimisation.

The optimisation tool allows one to introduce constraints to search feasible configurations, from aerodynamic and aeromechanic standpoints; the set of inequality constraints are summarised in Equations (13)–(19):

- Vertical trim

$$W_{des} - \varepsilon_L \;\leq\; L(\boldsymbol{x}) \;\leq\; W_{des} + \varepsilon_L \tag{13}$$

- Longitudinal static stability

$$SSM_{\min} \;\leq\; SSM(\boldsymbol{x}) \;\leq\; SSM_{\max} \tag{14}$$

- Pitch trim

$$-\varepsilon_M \;\leq\; C_M(\boldsymbol{x}) \;\leq\; \varepsilon_M \tag{15}$$

- Max local lift coefficient

$$\max(c_l(y,\,\boldsymbol{x})) \;\leq\; \hat{c}_{lTH} \tag{16}$$

- Wing loading constraints

$$(L/S)_{\min} \;\leq\; (L(\boldsymbol{x})_{wing}/S(\boldsymbol{x})_{wing}) \;\leq\; (L/S)_{\max} \tag{17}$$

- Taper ratio

$$\lambda_j(\boldsymbol{x}) < 1 \tag{18}$$

- Relative wings position

$$x_{LE\ tip}^{front\ wing} + c_{tip}^{front\ wing} \;<\; x_{LE\ tip}^{rear\ wing} + \Delta x \tag{19}$$

where W_{des} is the input design weight; SSM is the longitudinal static stability margin; C_M is the pitching moment coefficient; $c_l(y)$ is the spanwise distribution of local lift coefficient and $\hat{c}_{lTH}$ is the related threshold value; (L_{wing}/S_{wing}) is the *i-th* lifting surface wing loading; λ_j is the *j-th* wing bay taper ratio; $x_{LE\ tip}$ is the longitudinal position of the wing tip leading edge; c_{tip} is the wing tip chord; ε is a tolerance. Several details about the optimisation procedure and algorithms implemented in the AEROSTATE tool are described in [58–60]. This tool evaluates the lift-to-drag ratio at the reference design point by estimating the overall drag, as reported in Equation (1); nevertheless, in this case, the geometry of the lifting system is known, as it is computed at each iteration of the optimisation process, so the parasite drag coefficient of the wing components, C_{D0}^{Wing} (i.e., front/rear wing, vertical tip-wing, fin), is computed by integrating spanwise the airfoil drag contribution, as expressed in Equation (20):

$$C_{D0}^{Wing} = \frac{1}{S_{ref}} \int_{-b}^{b} C_{D\ foil}(y)\ c(y)\ dy \tag{20}$$

where the function $C_{Dfoil} = f(Re, M, C_{Lfoil})$ is calculated by Xfoil [61] and is provided as input to the procedure, S_{ref} is the wing reference surface, and $c(y)$ is the spanwise chord distribution. The C_{D0}^{Fus} is computed by means of the *component build-up method* described in [53]; in particular:

$$C_{D0}^{Fus} = Q\ C_f\ FF\ \frac{S_{fus}}{S_{ref}} \tag{21}$$

where the friction coefficient, C_f, the form factor, FF, and the interference factor, Q, are reported in [53]. Concerning the lift induced drag, once the design weight is defined as

an input, the optimiser uses a Vortex Lattice Solver to evaluate the vertical trim condition (Equation (13)), and so extracting the aircraft $C_{L\ trim}$ and C_{Di} values. The solver used is the Vortex-Lattice-based AVL [62], and a typical representation of a box-wing configuration within this solver is reported in Figure 5.
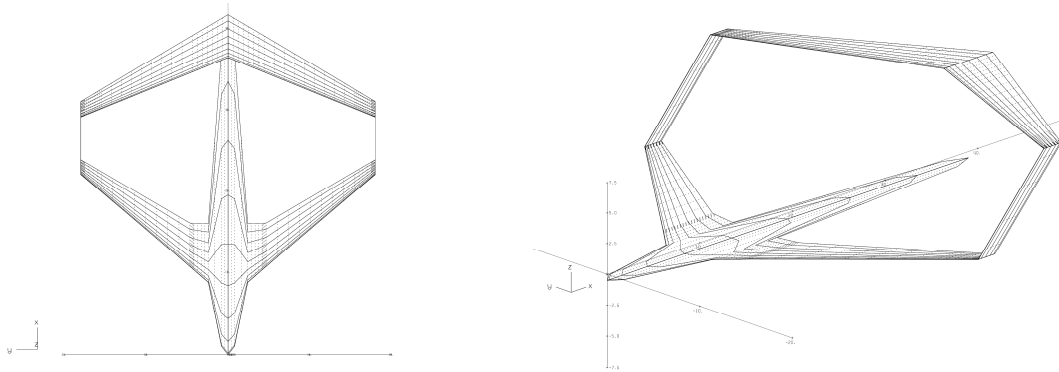

Figure 5. AVL model for a box-wing configuration.

As it is chosen to represent the fuselage as a flat plate in AVL, the vertical trim is evaluated in AVL with the fuselage always aligned to the flow; namely, the trim is solved with the angle of attack $\alpha = 0°$, and by acting on the wings' twist distributions, so as to not introduce the lift-induced drag coming from the simplified fuselage modelling.

Additionally, in this second block of the design process, the maximum take-off weight of the aircraft is evaluated by means of the breakdown described by Equation (9); again, the payload and the fuel weight are calculated as described in Section 2.1, while the operating empty weight is subdivided as follows:

$$W_{oe} = W^{Wings} + W^{Fus} + W^{Eng} + W^{Sys} + W^{Oper} \tag{22}$$

where W^{Wings} represents the weight of the lifting system, W^{Fus} is the fuselage weight, W^{Eng} is the engine weight, W^{Sys} represents the weight of the on-board systems, and W^{Oper} represents the weight of the aircraft operating items. As the geometry of each configuration designed in this phase is known, single contributions can be estimated by means of slightly more accurate methods than those used in the initialisation phase; in particular, the wing weight and the systems and operating weights are estimated by means of the method proposed in [63], and the fuselage weight and the engine weight are evaluated by means of the methodology used in [64]. During the optimisation, these estimations are also useful to evaluate the centre of gravity position, and so to evaluate the constraints concerning the pitch trim and the longitudinal stability.

At the end of the process, it is possible to select an aerodynamic layout provided in output from the optimisation process, and to re-estimate the maximum take-off weight by means of Equations (9) and (22); if this value differs from the input provided by the starting initialisation within a prescribed tolerance, the procedure is iterated until the convergence is reached (Figure 6).

Transonic Aerodynamic Assessment: Level 1 and 1/2

If the design process involves transonic aircraft, such as commercial medium/long range airliners, it is necessary to provide some information about the transonic behaviour of the lifting system from the conceptual stage of the design. This aspect is relevant as, after a specific condition in transonic flight called *drag rise*, the aircraft performance deteriorates severely; in particular, for certain combinations of cruise Mach number, trim lift coefficient and wings geometry, a massive drag increase occurs; this is caused by the rise in shock waves (wave drag contribution), and by the interaction of these waves with the boundary layer, that thickens until local separation is reached, causing increases in pressure drag.

The *drag rise* condition needs to be avoided in the whole standard operating envelope of an aircraft. However, the transonic phenomena are very difficult to be detected and properly described by the low-fidelity methods that are typically used in the conceptual stages of the design process to provide fast and adequately reliable assessments. This because the transonic phenomena strictly depend on the local geometry of the wings, on the airfoil shape, on the joints and on the fillets' design; moreover, transonic fluid physics is strongly three-dimensional and exhibits strong coupling and interaction between the boundary layer and the sonic phenomena such as shock waves. It is evident that potential methods, such as the VLM, cannot predict any of these physic phenomena, as they are not designed to take the fluid compressibility (and so the shock waves) and the fluid friction actions (and so the boundary layer) into account. In the literature, some simplified methods are provided that take transonic effect into account in the early stages of the design process: in [65], a quasi-3D model is presented, which couples a VLM solver with a strip model considering 2D airfoil transonic performance computed by means of a CFD solver; in [66], the wave drag coefficient is estimated by means of semi-empiric formulae provided by the Korn–Locke method. Although these methods are useful to identify relevant correlations between the aerodynamic performance and some macro-parameters (such as the airfoil shape, the wings' sweep angles, the thickness distribution and the local lift coefficient), they may fail to provide reliable absolute performance prediction to be used with enough confidence in the conceptual design phase. In other words, with these models, we cannot ensure that a specific design coming from the *Level 1* stage of the design process (Figure 2) is far from the *drag rise* conditions; this may compromise the development of the design, as it is possible to specifically evaluate the transonic performance only at *Level 2* stage of the design process (Figure 2), where higher fidelity methods as CFD RANS solver are used. To avoid that, the design of configurations at *Level 1* may present possible transonic issues at *Level 2*, and so to prevent restarting the design process from the beginning, a preliminary transonic assessment was performed for the specific design problem described in Section 3. In particular, a CFD campaign was carried out to improve the knowledge on the transonic behaviour of the box-wing lifting system, and to obtain information and data to calibrate the *Level* 1 aerodynamic optimisation set-up (design variables boundaries, aerodynamic constraints), with the aim of designing configurations that are confidently far from the *drag rise* condition; as this high-fidelity assessment was useful in properly tuning the *Level 1* design stage, this procedure can be used as a *Level 1 and* 1/2 block, parallel to the *Level 1* design block.
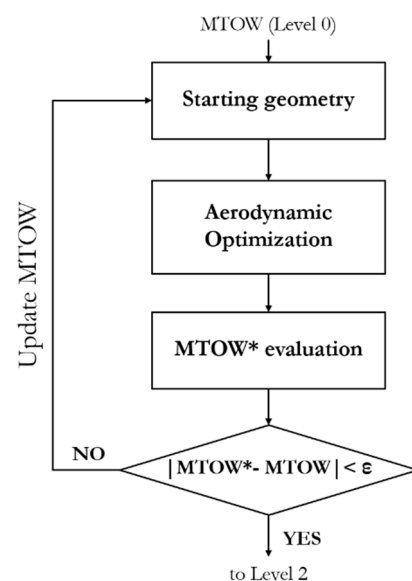

Figure 6. *Level 1* sizing procedure scheme.

Steady compressible RANS simulations were used to investigate the box-wing in transonic flight, and the performance correlation with some relevant parameters; in particular, a focus on some macro parameters together with an analysis on some local effects have been provided, as described in [67]. The airfoil that was selected to be used for the box-wing is a supercritical profile and it is not considered as a design variable. Concerning the macro parameters, major effort was given to the role of the wing loading (Figure 7) and to the wings' sweep angles; the effect of cruise Mach was investigated as well.
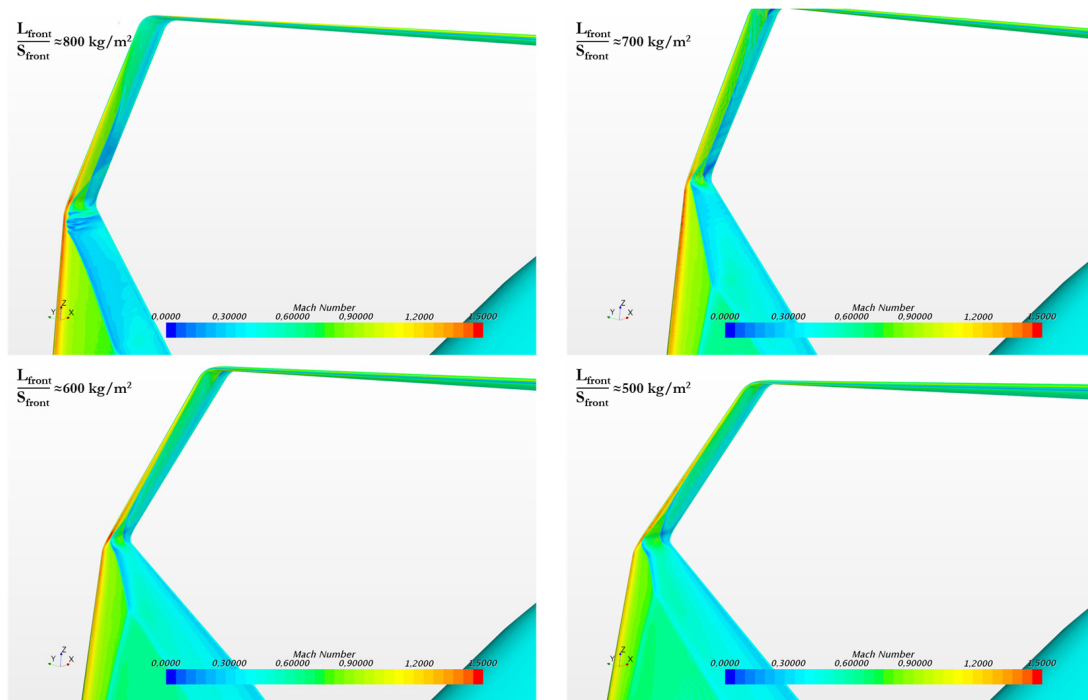

Figure 7. Wing loading variation effect on flow over the front wing (Mach contours @M_∞ = 0.79).

Some local geometrical parameters were identified as more influential with respect to the transonic drag increase; in particular, the twist distribution in the tip zone of the front wing proved to be crucial to be properly set in order to avoid detrimental shock-induced drag increase (Figure 8 (left)). The load of the front wing tip region is enhanced by the aerodynamic behaviour of a positive swept wing; moreover, differently from a conventional wing in which the tip is free, for the box-wing, there are flow accelerations on the fillet with the vertical wing, which ease the flow to reach sonic conditions. The opposite happens for the rear wing, as the aerodynamic behaviour of the forward swept wing leads to a spanwise enhancement of the lift coefficient in the root zone; moreover, in the root zone, there is a significant straightening of the isobars, as the rear wing is not directly constrained to the fuselage: this effect reduces the aerodynamic sweep of this portion of wing. These two features of the forward swept wing can lead to transonic issues in the root zone (Figure 8 (left)).

This qualitative information was then used to properly tune the *Level 1* optimisation framework for the preliminary aerodynamic design. A conservative design approach was chosen for this stage; in particular, a set of constraints and boundaries for the design variables was identified to allow the optimiser to design configurations that are confidently far from the detrimental transonic drag increase effects. For the design case described in Section 3, concerning a medium range transport box-wing aircraft, the boundaries/constraints selected are summarised in Table 2.
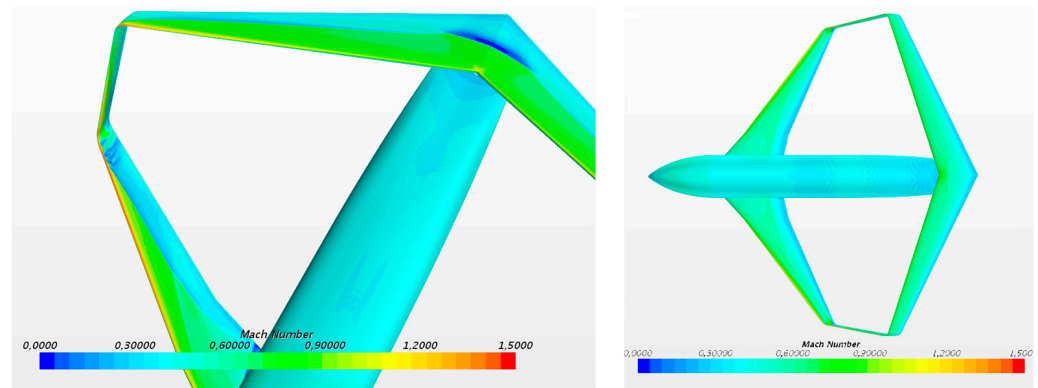
Figure 8. Local transonic critical issues (**left**); box-wing without transonic issues (**right**). Mach contours referring to freestream $M_\infty = 0.79$.

Table 2. *Level 1 and $^1/_2$ calibration of the preliminary aerodynamic optimisation.*

Front wing loading, L_{front}/S_{front}	<600 kg/m^2
Rear wing loading, L_{rear}/S_{rear}	<600 kg/m^2
Front wing sweep angle, Λ_{front}	$>35°$
Rear wing sweep angle, Λ_{rear}	*free*
Cruise Mach	<0.79
Front wing tip twist angle, $\theta_{front}{}^{tip}$	$<-1°$
Rear wing root twist angle, $\theta_{rear}{}^{root}$	$<+1°$
Spanwise local lift coefficient, $c_l(y)$	<0.7

2.3. High-Fidelity Performance Assessment

2.3.1. Aerodynamic Performance

In the third phase (*Level 2*, Figure 2), the aerodynamic layout provided by the optimisation process was subject to refined analysis, concerning aerodynamics, structural sizing, weight estimation and performance assessment. First of all, the information gained through the design process allowed one to generate the 3D CAD model of the box-wing aircraft (Figure 9).

Figure 9. CAD model of the reference PrandtlPlane.

The designed configuration was available to be processed for detailed aerodynamic analysis. The high-fidelity aerodynamic assessment was performed by means of CFD simulations; drag polar curves were obtained by simulating the steady aerodynamics for different flight conditions, representative of the relevant operating conditions during the mission. The solver adopted was a steady compressible RANS with the k-ε turbulence

model; the volume mesh was composed of a prism layer of 20 layers with a growth rate of 1.1, and tetrahedral cells outside; the volume mesh size typically adopted was about 20 million cells for the half model, as a symmetry condition with respect to the longitudinal plane was applied. The software used to perform the computations was ANSYS Fluent [68]. In Figure 10, an example of the surface mesh is represented, and in Figure 11, an example of postprocessing of results is proposed.
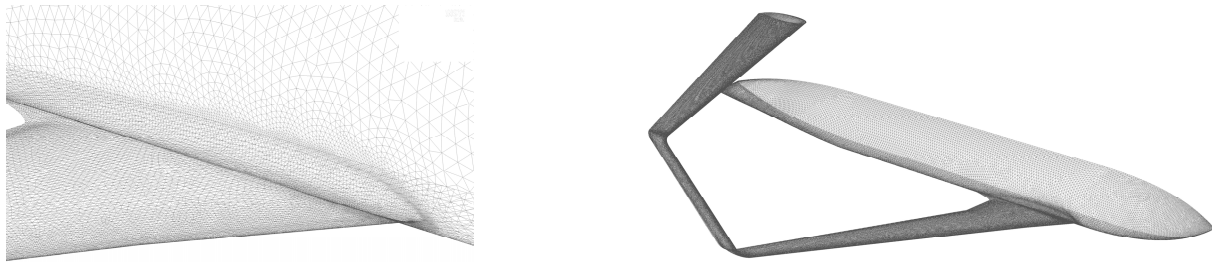

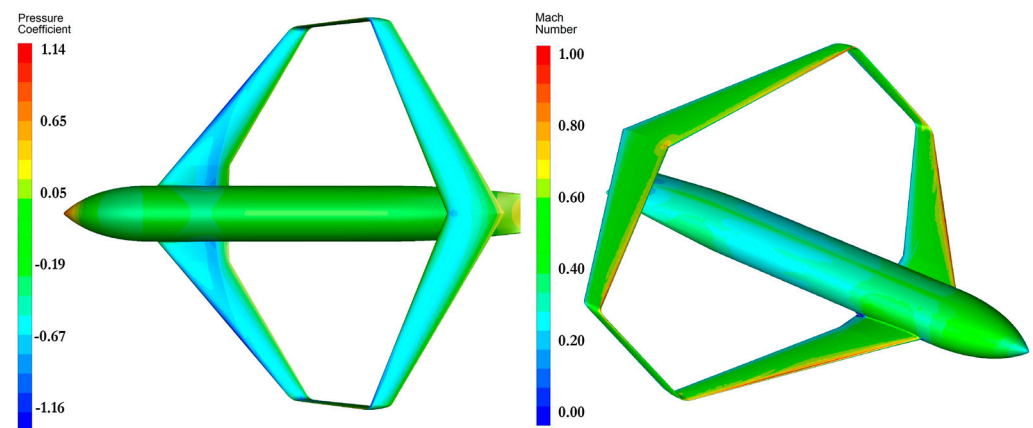**Figure 10.** Surface mesh details (aircraft half-model).

Figure 11. Example of postprocessing.

To reduce the computational cost, the component modelled was the wing–body assembly, while the drag of the vertical tails and engine nacelles were evaluated with the simplified models described in [53]. The solution chosen for the vertical tail assembly was a V-tail configuration; this has been shown to be necessary to alleviate potential flutter issues [69], as reported in [70–72]. This solution proved to be effective in meeting the flutter requirements in the case of the aircraft described in this article, as reported in [73]. The sizing of the V-tail was carried out with the aim of satisfying the directional stability requirements, as described in [74]; the flutter assessments were carried out subsequent to this sizing.

2.3.2. Structural Design and Mass Estimation

The mass breakdown was updated in this phase; in particular, the refinements regard the structural mass evaluation. As the simplified methods used to estimate the operating empty weight (and so also the structural weight) in the first two design stages are mainly referred to as statistical extrapolations concerning the structural data of classical aircraft architecture (tube-wing-tail), it was necessary to introduce specific physics-based models to evaluate the box-wing aircraft structural mass. The structural behaviour of a box-wing is very different from that of a conventional aircraft, concerning both the lifting system and fuselage structures. The main difference is related to the fact that the box-wing lifting system is over-constrained to the fuselage, as the main wing of a conventional aircraft is a statically determinate cantilevered lifting surface. The fuselage is a doubly supported beam in the case of a box-wing, borne in correspondence of the front and rear wing connections,

differently from the case of the conventional monoplane. To properly size and design the aircraft structural components, an in house-tool called WAGNER [75] was developed; the main goal of the WAGNER tool is to provide the preliminary structural design of the aircraft concerning the wings, the fuselage and the tailplanes' structural components. The sizing procedure relies on an FEM-based solver, namely the ABAQUS commercial software [76]; the WAGNER tool provides the automatic generation of the 3D geometry of the aircraft structures and the mesh of the structural components, such as stringers, frames, ribs, pressurisation bulkheads, floor beams and struts (Figure 12); the load cases' setting and computation through an ABAQUS solver (Figure 15); and the postprocessing of the results (Figure 16).
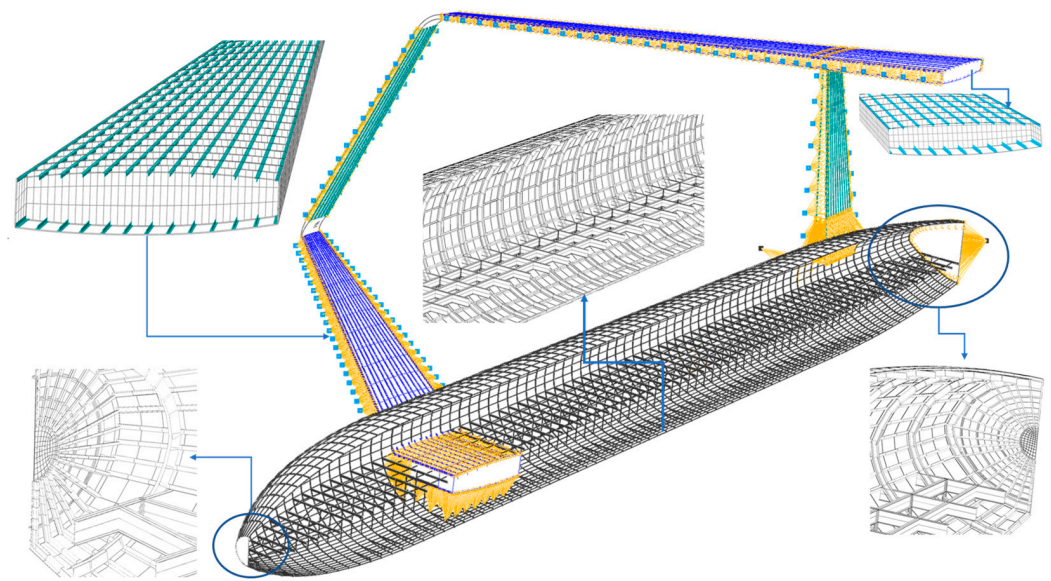
Figure 12. Typical Finite Element mesh of a PrP configuration (aircraft half-model) with some structural details.

The WAGNER code follows the sizing scheme reported in Figure 13; the main input is represented by the geometry from the *Level 1* block of the design process.
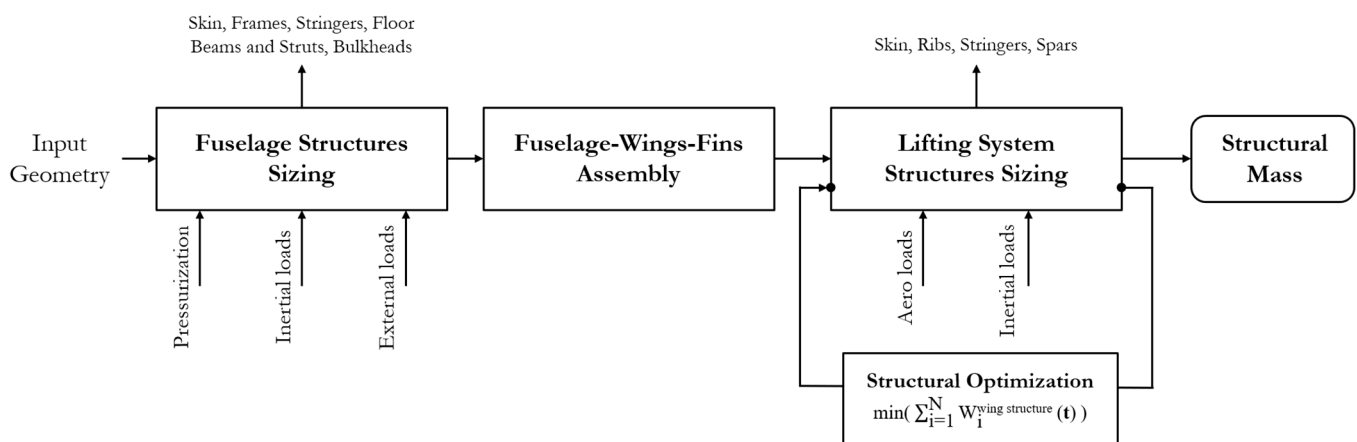
Figure 13. WAGNER structural sizing workflow.

The first step of the structural design workflow of Figure 13 provides the fuselage's structural sizing: the structure is modelled with shell elements for the skin, whereas stringers and frames are modelled with beam elements. The FE model of the fuselage is delimited by the end bulkheads, modelled as flat panels stiffened by beams in both radial (stringers) and circumferential (frame or ring) directions. Secondary structural parts of

the fuselage are considered as concentrated masses linked to the bulkhead structure (e.g., tail-cone) by means of multipoint constraints. Concentrated masses are also used to model landing gears and fuselage-mounted engines, connected to fuselage main frames. Finally, non-structural masses are spread over the mesh elements to account for the weight of payload, systems and operatings [63], as well as for doors, windows and special reinforcement structures [77,78].

Concerning the loading conditions for fuselage structural sizing, combined pressurisation and inertial loads are considered; limit and/or ultimate pressure are superimposed to gravity load related to load factor, n_z, ranging from -1 to $+2.5$. The sizing criterion is that the equivalent stress should be less than the allowable stress, with the latter being given by the yielding stress of the material divided by an appropriate safety factor, which usual standards require to be at least equal to 1.5. Figure 14 shows the global FE mesh of a half fuselage together with some example contour plots of stress and deformation induced by pressurisation and gravity loads.
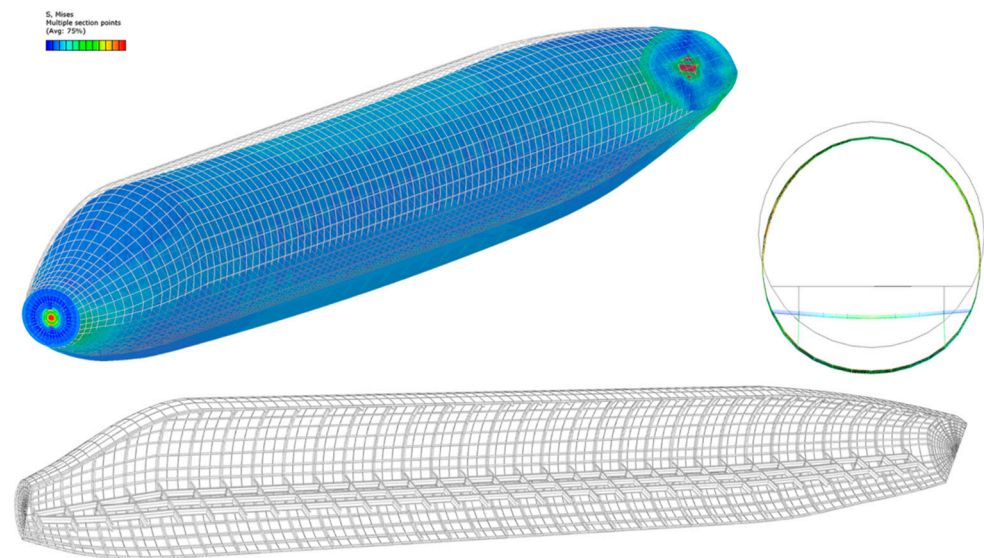

Figure 14. FE mesh of half a fuselage and example of contour plots of stress and deformation induced by ultimate pressurisation and gravity load with $n_z = +2.5$ (deformed scale factor: 20).

The second step concerns the assembly of the fuselage with the lifting system; the WAGNER software models the wings' geometry and meshes the structural components; the arrangement of structural components, such as frames and stringers pitch, is provided in input by reference cases available in literature for transport box-wing [79,80]; referring to Figure 12, the front wing is fixed to the fuselage by means of surface-based constraints; in particular, the spar webs (front and rear) are fixed to the main frames of the fuselage, while the ribs of the front wing are fixed to the floor beams. The same type of connection is used to attach the fin structure to the fuselage. Then, the lifting system structural sizing is performed; in particular, the wings' structural design is carried out by only considering static loads, according to a loading condition corresponding to a pull-up manoeuvre in cruise ($M = 0.79$, h = 11,000m, $n_z = 2.5$, $W = MTOW$); qualitatively, two constraints are imposed into the sizing procedure: (1) the wing-tip deflection, intended as the maximum deflection occurring in one of the main wings, should be such that large displacements are avoided; (2) the structure must support the limit load (given as a combination of aerodynamic and gravity loads) within the elastic field, so the equivalent Von Mises stress in both wings is constrained to be lower than the yielding stress of the material (divided by a safety factor) [81]. The aerodynamic loads, such as the spanwise lift distribution on the lifting surfaces, are provided as inputs from the AVL code. The wing structural sizing process is integrated into an optimisation procedure; the objective function is the structural mass of the lifting systems, $W^{wing\ structure}$ (Equation (23)); the constraints are those related

to structural stiffness, expressed as a maximum limitation on wings' tip displacement, δ_i^{tip} (Equation (24)), and structural strength, expressed as maximum limitation on the equivalent stress, σ_i^{eq} (Equation (25)), for the *i*-th wing; the design variable is the vector t of the thicknesses of the *k*-th structural component of the *i*-th wing t_{ik} (Equation (26)).

- Objective function

$$\min\left(\sum_{i=1}^{N} W_i^{wing\ structure}(t)\right) \tag{23}$$

- Stiffness constraint

$$\delta_i^{tip}(t) \leq \delta_{MAX}^{tip} = k_{tip}\frac{b}{2} \tag{24}$$

- Strength constraint

$$\sigma_i^{eq}(t) \leq \sigma_{MAX}/k_{SF} \tag{25}$$

- Design variables

$$t = t_{ik} \tag{26}$$

- Design space

$$t_{\min} < t_{ik} < t_{MAX} \tag{27}$$

In Equation (24), the maximum wing tip displacement, δ_{MAX}^{tip}, is defined as a fraction, k_{tip}, of the half-wingspan, *b/2*; k_{tip} is considered equal to 0.1 for all the analyses carried out. In Equation (25), σ_{MAX} is fixed as equal to the yielding stress of the material, and k_{SF} is the safety factor; k_{SF} is set to 1.5. The wings are divided in a primary structure, i.e., the structure in which all the loads are concentrated, namely the wing-box consisting of upper/lower stiffened panels, spars, ribs, and in a secondary structure, mainly composed of components related to fixed leading/trailing structure and movables installation. The FEM-based sizing only involves the primary wing structure, as the secondary structures are evaluated by the method presented in [82] and are modelled in the FEM as distributed mass properly placed spanwise (Figures 15 and 16).
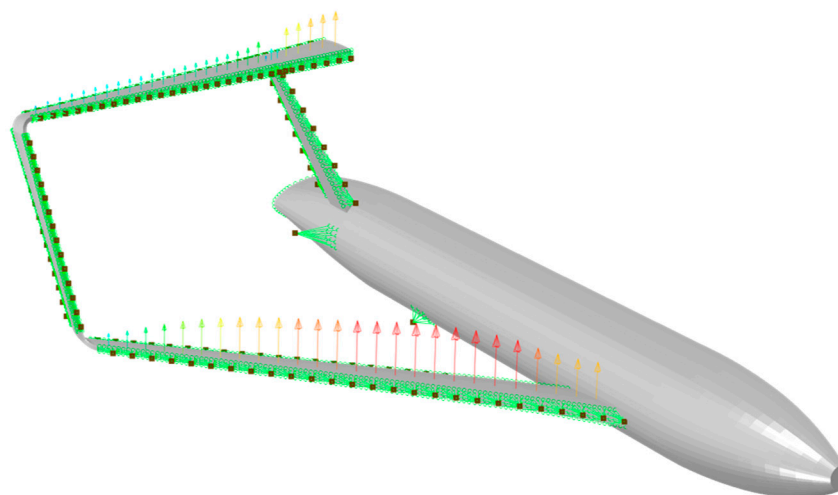
Figure 15. Secondary structures of the box-wing lifting system and aerodynamic forces (aircraft half-model).
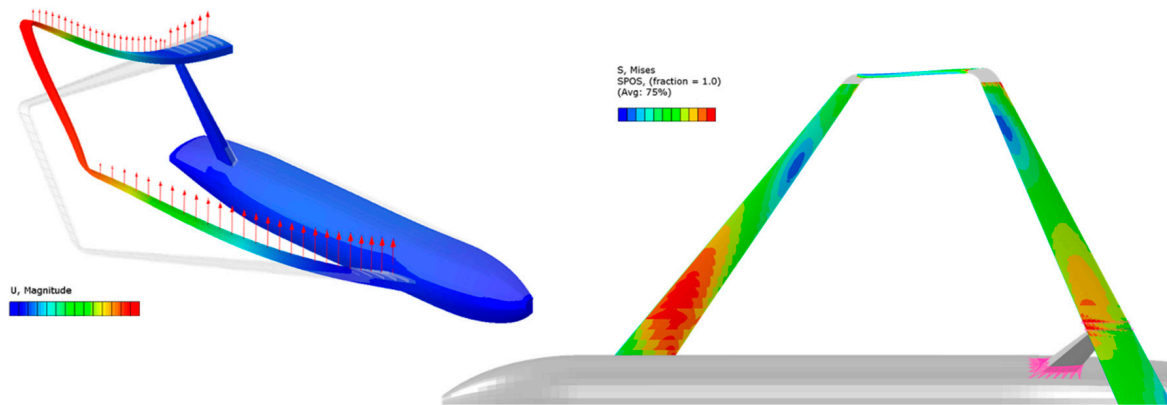
Figure 16. Example of deformed shape of the PrP configuration and Von Mises stress on both wings (aircraft half-model).

The output of the procedure is a complete structural mass breakdown of the main structures of the aircraft; the evaluation of non-structural components, i.e., cabin furnishings, on-board systems, etc., is performed in WAGNER by using the model described in [63]. The final output of the WAGNER tool is represented by the total mass of the configuration and the related components' breakdown, the coordinates of centre of gravity and the components of the inertia tensor.

2.3.3. Mission Simulation

The information collected in the *Level 2* stage, concerning the refinement of the weight estimation and the aerodynamic performance assessment, are useful to integrate in an in-house-developed mission simulation tool; this simulator allows one to estimate relevant output regarding the aircraft mission performance; in particular, the main outputs achievable from the simulation are the range and the related fuel burnt, for every mission inside the payload-range envelope of the aircraft. The mission performance is computed by integrating the equation of motion of the aircraft [55,83]; the reference mission is divided into taxing, take-off, climb, cruise, descent and diversion (Figure 17).

Figure 17. Mission simulation scheme.

Each mission segment is subdivided in timesteps Δt; the equations of motion are integrated by using the Euler algorithm, as reported in Equation (28) for a generic parameter k:

$$k(t + \Delta t) = k(t) + \dot{k}(t)\Delta t \qquad (28)$$

The inputs for the simulation process are, for each time step: the aircraft's aerodynamic performance, expressed as response surfaces of the drag as a function o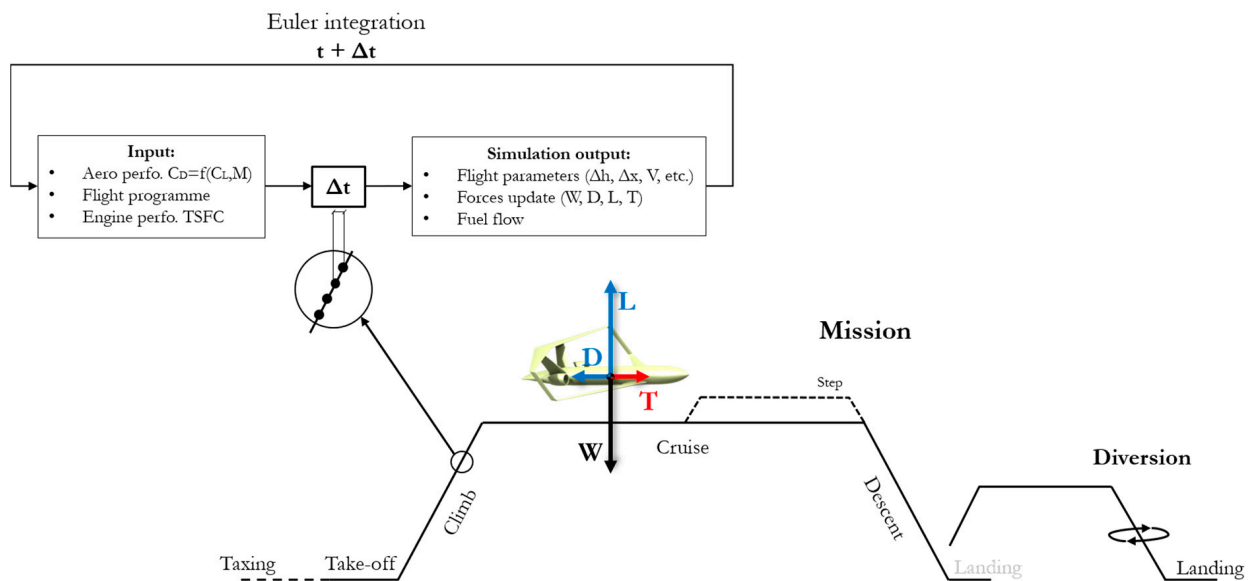f lift and flight condition ($C_D = f(C_L, M)$, derived by the CFD simulations results); the initial mass breakdown, depending on the payload and on the initial fuel mass; the flight programme for each mission segment; the main performance of the propulsion system, namely the thrust specific fuel consumption, *TSFC*. The simulation models used for each mission stage are briefly described in the following:

- The taxing fuel consumption is extrapolated by the data reported in [84]. The take-off phase was simulated by integrating the equation of motion of the aircraft in the longitudinal plane, also considering its pitch dynamics; the take-off simulation and analysis procedure used in this work is widely described in [85];
- The climb phase was simulated by integrating the equation of motion of the aircraft considered as a point mass in the longitudinal plane:

$$\tan \gamma = \frac{T - D}{L} \qquad (29)$$

$$\dot{x} = V \cos \gamma \qquad (30)$$

$$\dot{z} = V \sin \gamma \qquad (31)$$

$$\dot{W} = -TSFC\ T \qquad (32)$$

The climb programme was set as suggested in [86], namely by dividing the climb into segments flown at constant IAS or Mach number; the reference climb programme selected is "250 kt/300 kt/M_{cruise}". According to this programme: (1) the aircraft flies at IAS equal to 250 kt until it reaches an altitude of 10,000 ft; (2) the aircraft accelerates in an almost level flight until the IAS is 300 kt, and then flies at this speed until the crossover altitude (the crossover is defined as the altitude where the current Mach reaches the target cruise Mach); (3) the aircraft flies at a constant Mach number until it reaches the cruise altitude. During the climb, the aircraft changes its altitude, so its TAS increases as depicted in Figure 18 (left); an example of the aircraft climb trajectory is depicted in Figure 18 (right).
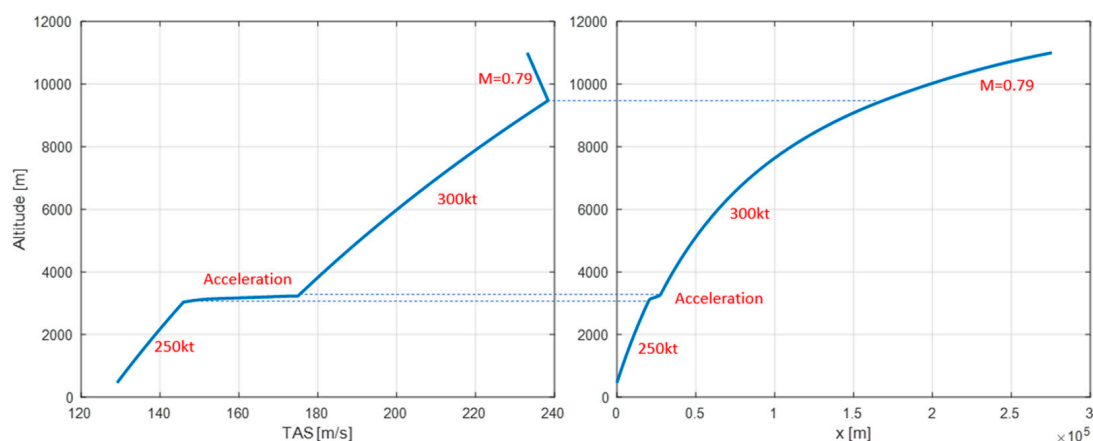

Figure 18. Reference climb programme.

- The cruise phase was simulated by integrating the equations of steady and level flights for the aircraft point mass model (Equations (33)–(35)); a constant altitude ($\dot{z}$) = 0 and constant speed ($\dot{x} = V$ = constant) flight programme was considered; the simulation, taking aircraft aerodynamic performance and cruise length into account, provided stepped cruise programmes if it resulted in performance gains.

$$L = Wg \tag{33}$$

$$T = D \tag{34}$$

$$\dot{W} = -TSFC\,T \tag{35}$$

- The descent starts at the cruise altitude and ends at an altitude of 1500 ft; the equations of motion are obtained for the climb, and in the same manner, the flight programme for the descent is made by segments at constant IAS or Mach number [85]; the reference selected programme is "M_{cruise}/300 kt/250 kt", namely: (1) the aircraft flies at a constant Mach number from the cruise altitude to the crossover altitude; (2) the aircraft flies at IAS = 300 kt from the crossover altitude to an altitude of 10,000 ft; (3) the aircraft decelerates in an almost level flight until the IAS is 250 kt, and then flies at this IAS until an altitude of 1500 ft is reached.
- Concerning diversion and loiter, analogous considerations about climb, cruise and descent were implemented.

3. Results of the Design Process

3.1. Input Data

The design methodology described in Section 2 was applied to the design case of a box-wing transport aircraft; in particular, the specific case of the PARSIFAL project [74,87–89] is presented.

To initialise the whole design process, it is necessary to define the Top Level Aircraft Requirements (TLARs). For the case study, the main TLARs are summarised in Table 3.

Table 3. PrandtlPlane main TLARs.

Max n° of passengers	310
Design range	5000 km
Cruise Mach	0.79
Initial Cruise Altitude	11,000 m
Max Wingspan	36 m

The selection of TLARs for the PARSIFAL case is widely described in [90]; in particular, the aim of introducing the PrandtlPlane as an alternative to conventional tube-and-wing aircraft follows two main design drivers, provided by the forecasts for the commercial air traffic scenario of the future:

- A huge increase in air traffic, especially on short/medium routes (up to 5000 km) [8] is expected;
- At the same time, relevant problems of airport saturation are forecasted [11].

To address these contrasting objectives, the expected higher lifting capability of a box-wing architecture is exploited; in particular, the aim of this design study is to develop an aircraft with an increased payload (up to 310 passengers), but the with same overall dimensions (compatibly with airport apron constraints) of the conventional competitor currently operating in the sector of the medium routes (e.g., Airbus A320 family or Boeing 737 family). The maximum wingspan is limited to 36 metres, compatibly with the apron

constraint provided by the ICAO Aerodrome Reference Code "C" [91]. Moreover, as the main objective for the commercial aviation of the future is to drastically cut the noxious emissions, the result of this design will be satisfactory only if a significant pollutant emission reduction is provided; this is theoretically possible by exploiting the expected better aerodynamic performance of the box-wing system. To properly assess the performance comparison with a conventional aircraft, it is necessary to identify a proper benchmark; the conventional benchmark selected is the CeRAS CSR-01 [92], a short/medium-range aircraft developed in the framework of the project CeRAS (*"Central Reference Aircraft data System"*, [93]); the CeRAS project provides an open-access platform in which designs, geometries, data and procedures relevant to the CSR-01 configuration (*CeRAS Short Range version 01*, Figure 19) are collected. The CeRAS CSR-01 is a virtual simulacrum of an aircraft similar to the Airbus A320 [94] in terms of key features (Table 4), dimensions, payload and utilisation.

Figure 19. CeRAS CSR-01 configuration.

Table 4. Main features of the CeRAS CSR-01.

Ref. wing area	122.4 (+32.2 *) m^2
Design range	5000 km
Max n° pax	186
Wingspan	34.1 m
Fuselage length	37.5 m
Cruise altitude	11,000 m
Cruise Mach	0.79

* Horizontal tail.

3.2. Conceptual Design and Reference Layout Selection

As the TLARs for the box-wing design have been defined, the first level of the design process is performed, providing the fuselage design and the general information to initialise the aerodynamic optimisation in the *Level 1* block of the design process (Figure 2). Concerning the fuselage design, the focus is mainly on the external shape, the cabin section layout and the internal arrangement, as the main design driver is represented by the target number of passengers. For the PARSIFAL case study, the fuselage of the box-wing aircraft was selected with the following main features: a double-aisle cabin section was selected, with a 2-4-2 seats layout (Figure 20(left)); the fuselage length is set equal to 44.2 m, similar to the longest fuselage of a competitor operating in the medium range sector (Airbus A321); the cabin section external shape is near-elliptical, following the studies provided in [95]. This fuselage, arranged in a high-density layout, is able to transport a number of passengers equal to 308 (Figure 20 (right)).

Previous designs of wide body fuselage for box-wing aircraft were proposed in [40,96,97]; however, in the case of PARSIFAL, some actions to prevent penalisations in terms of turnaround time with respect to conventional competitors were provided, such as the introduction of enlarged aisles and of an extra boarding/de-boarding path; both

these aspects are highlighted in Figure 21, and their effects on turnaround time are widely discussed in [98,99]. In particular, the data provided by the simulations described in [98,99] show that the introduction of the PrP in the same sector as the A320-type aircraft implies a slight increase in turnaround time (+11% outstation, +25% full service) against a relevant increase in payload capacity (+66% passengers, +71% containers); these results were obtained by considering the same apron space (ICAO Code "C") for the two aircraft. The abovementioned simulations take all the main aspects of airport operations into account, from passenger arrival at the terminal to aircraft take-off.
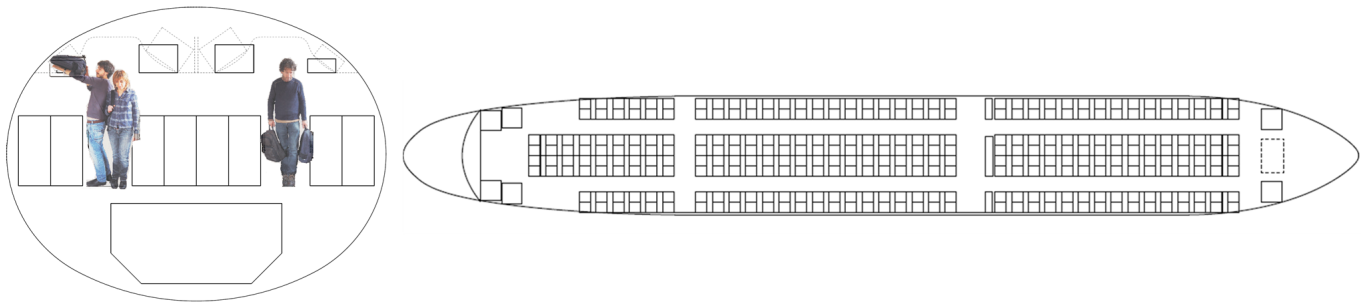

Figure 20. Cabin section layout (**left**); cabin arrangement (**right**).
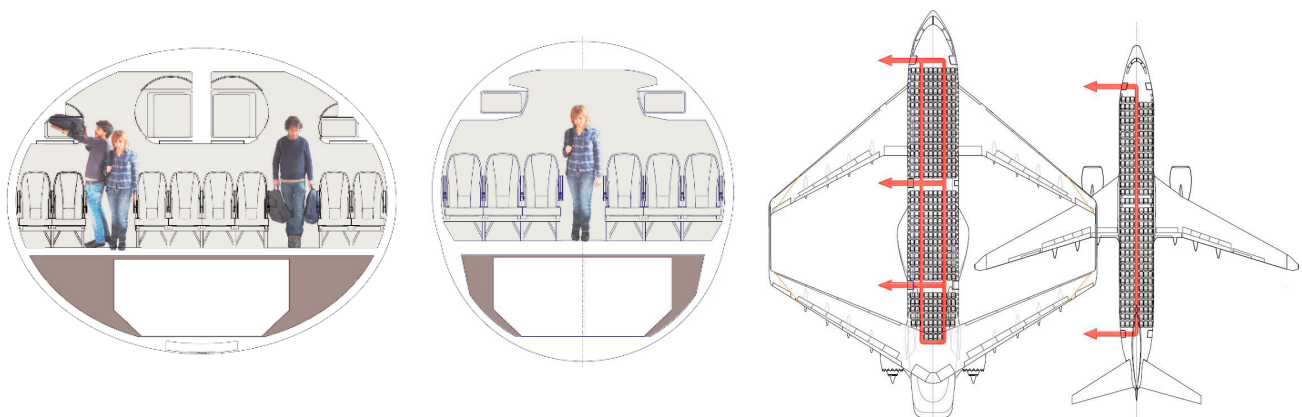
Figure 21. Cabin layout comparison between the PARSIFAL solution and a conventional single-aisle aircraft.

Once the fuselage is defined, the next step required to initialise the design process (*Level 0*) is to identify the main characteristics of the lifting system to apply simplified models for the estimation of the aerodynamic performance; to define an initial study case, a wing loading similarity was set between the box-wing and the CeRAS: in particular, to define the initial lifting system surface, the same wing-loading of the CeRAS was selected for the box-wing. By using this assumption in the relations of Equations (1), (4) and (6) for the initial aerodynamic evaluations and Equation (9) for the rough weight estimation, as described in Section 2.1, the data were obtained as input to initialise the second stage of the design process (*Level 1*). In this phase, several layouts of the box-wing aircraft were evaluated by means of the aerodynamic optimisation described in Section 2.2; at the end of the process, the output selected for the final performance analysis is represented by the configuration reported in Figure 22, whose main features are described in Table 5.

As detailed aspects related to the aeromechanical analysis of the box-wing aircraft may be out of the context of this paper, it is worth noting that such aspects have always been taken into account during the development of the aircraft. Specifically, general aspects of aeromechanical behaviour in the longitudinal plane of box-wing aircraft are extensively reported in [87]; a detailed summary of the design of the lifting system, with a focus on stability and controllability requirements, is given in [56]. The methods used to assess the aeromechanical characteristics of box-wing aircraft are extensively reported

in [87]; the approach used in the study involves a multi-fidelity approach, starting from the use of literature models [100], passing through extensive analysis campaigns with VLM solvers [58,74], up to the verification of requirements with CFD [74,88].
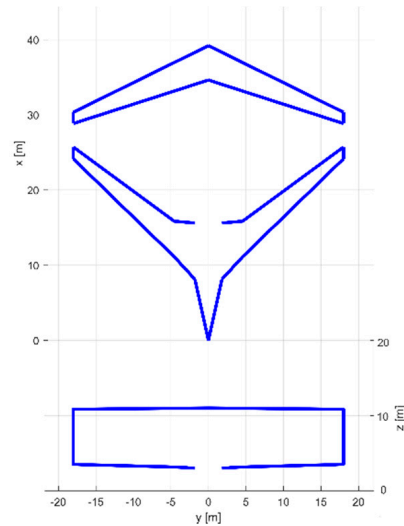
Figure 22. Reference box-wing layout.

Table 5. Main features of the reference box-wing.

@ Design Point	
M	0.79
h_{in}	11,000 m
L/D	21.62
C_L	0.4473
C_D	0.02068
$(L/S)_{front}$	604 kg/m^2
$(L/S)_{rear}$	477 kg/m^2
$(L/S)_{rear}/(L/S)_{front}$	0.789
SSM	0.10

It is worth pointing out the result concerning the wing loadings ratio $(L/S)_{rear}/(L/S)_{front}$ reported in Table 5: this value is in agreement with what is reported in [58]: the parameter $(L/S)_{rear}/(L/S)_{front}$ is the key lever to provide the maximum aerodynamic efficiency for box-wing aircraft compatibly with the constraints of static longitudinal stability and pitch trim; the result is also in agreement with what is described in [101], i.e., it provides the maximum performance in terms of C_{Lmax} in clean conditions (unflapped) for box-wing lifting systems.

3.3. Mission Performance Analysis

The selected configuration was analysed through the *Level 2* block of the workflow of Figure 2, by evaluating the aerodynamic behaviour and the structural mass in a more refined way to properly analyse the mission performance.

The CFD simulation model presented in Section 2.3.1 was used to evaluate the box-wing aircraft aerodynamics in different flight conditions; in Figure 23, the wing–body aerodynamic efficiency curves (namely *E* = lift-to-drag ratio, *L/D*) versus the lift force generated are reported for four different flight conditions.
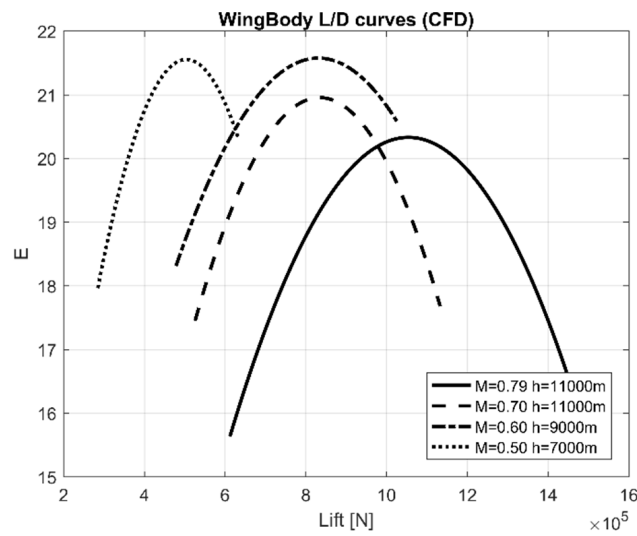
Figure 23. PrandtlPlane aerodynamic efficiency for different flight conditions.

Details of the aerodynamic performance in the cruise condition (M = 0.79 and h = 11,000 m) is reported in Figure 24; in particular, Figure 24 (left) reports the cruise aerodynamic efficiency for the wing–body assembly (CFD results) and for the whole configuration, including the estimation of the parasite drag of vertical tail planes and nacelles ([53] model); in this graph, some reference points are reported corresponding to the required lift to trim the aircraft in some reference conditions, to highlight the aerodynamic efficiency envelope of this configuration varying weight through the mission (MTOW = maximum take-off weight; ZFW = zero fuel weight, WOE = operating empty weight, LF = cabin load factor). In Figure 24 (centre) the C_D-C_L polar curve is reported, together with the breakdown of the C_D contribution of each aircraft component; Figure 24 (right) reports the viscous pressure breakdown of the polar curve.
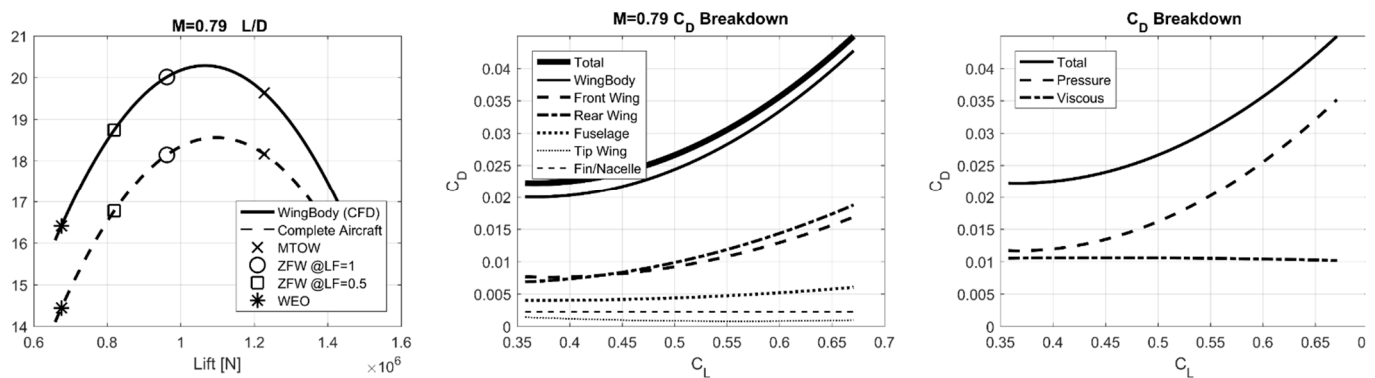
Figure 24. Details of the aerodynamic performance for PrandtlPlane in cruise condition; lift-to-drag curves (left), C_D breakdown -aircraft components- (centre), C_D breakdown -viscous/pressure- (right).

The second main input to the mission simulation platform is the mass breakdown of the aircraft; in the *Level 2* stage, the structural sizing has been performed through the FEM-based design and optimisation tool (Section 2.3.2); Table 6 reports the structural mass breakdown for the reference box-wing configuration.

Table 6. PrandtlPlane structural mass breakdown.

Component	Mass (kg)
Front Wing	7166
Rear Wing	6614
Vertical Tip-Wing	460
Fuselage	11,230
Vertical Tail Plane	1026

By calculating the other mass components as described in Section 2.3.2, the total mass evaluation of the reference box-wing conduces to a MTOW = 12,5126 kg, and a percentage repartition in components mass as reported in Figure 25; following the [63] model, the *Systems* category includes hydraulic, electric, pneumatic, fuel, engine, air conditioning, anti-ice, flight control, load systems, APU, avionics and instruments; *Operatings* includes cabin furnishings, cabin crew, crew seats, passengers seats, catering, emergency equipment, toilet fluid, oil and documentation.
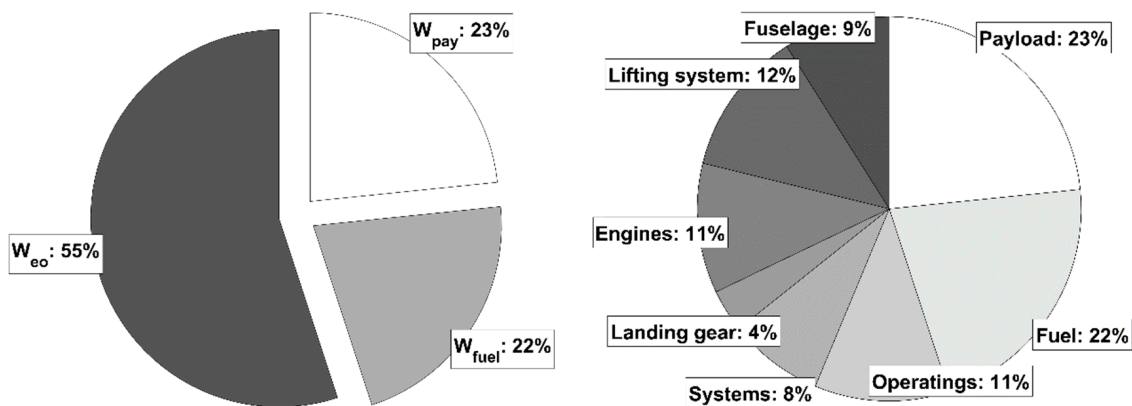
Figure 25. PrandtlPlane mass breakdown: general (**left**), components detail (**right**).

The information on the aerodynamic performance and weight of the aircraft are necessary to perform the mission simulations by means of the model described in Section 2.3.3. The simulations allow one to compute the mission performance of the reference box-wing; in particular, fuel burnt, range, flight time and other mission parameters such as time evolution of instant fuel consumption, speed, height, weight, etc., can be extracted from the simulation. Considering the box-wing harmonic mission, namely the mission with the maximum range at the maximum payload, the main results obtained are summarised in Table 7, and the main mission parameters are reported in Figure 26.

Table 7. Box-wing harmonic mission performance.

Number of passengers	308
Mission range	5722 km
Mission time	415 min
Mission fuel	21,844 kg
Total fuel	26,937 kg
Mission fuel per pax/km	0.01239 kg/km pax
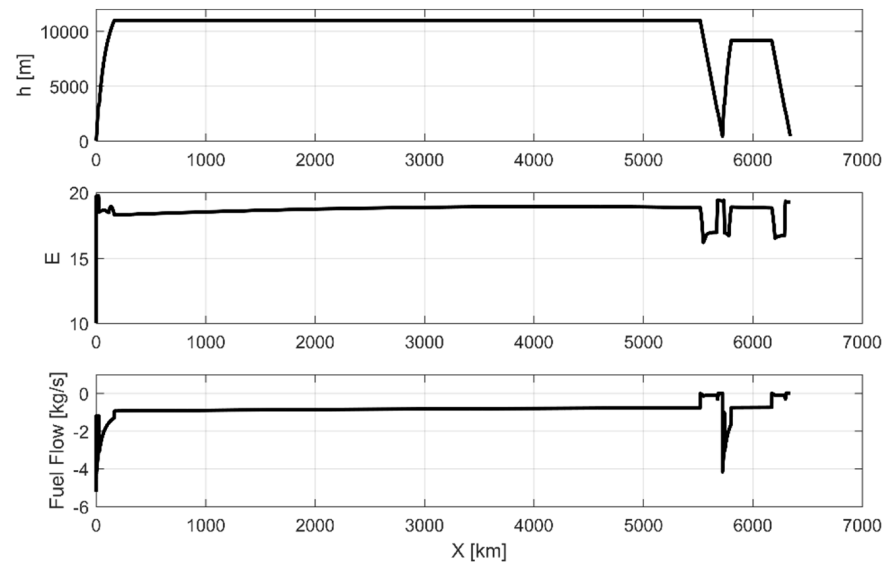
Figure 26. Box-wing harmonic mission height, aerodynamic efficiency and fuel flow evolution.

3.4. Box-Wing Performance Comparison with Respect to the Conventional Benchmark

The most relevant outcome of this work is the performance comparison between the unconventional PrandtlPlane aircraft and a conventional tube-and-wing benchmark. As reported in Section 3.1, the benchmark monoplane selected is the CeRAS CSR-01, a virtual mock-up of an Airbus A320-like aircraft, thus operating in the same routes of the reference box-wing; a top/front view comparison of the two aircraft is reported in Figure 27.
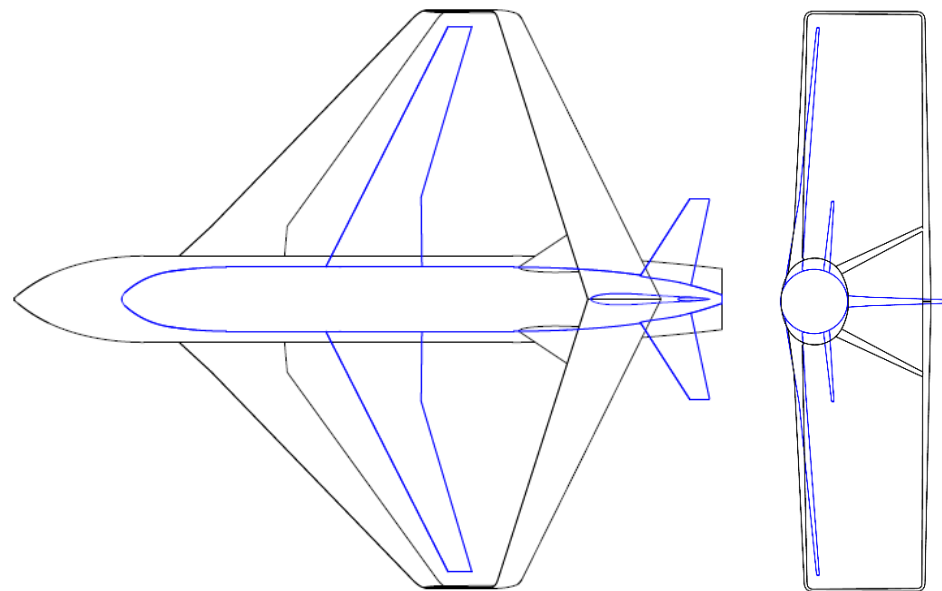
Figure 27. Views comparison between the PARSIFAL PrandtlPlane and the CeRAS conventional aircraft.

As far as the multilevel aircraft design and analysis diagram of Figure 2 is concerned, the activity on the CeRAS CSR-01 was limited to the *ANALYSIS* block, as the design and the geometrical characteristics of the aircraft are provided by the CeRAS database. Indeed, to make fair comparison between the box-wing aircraft and the benchmark monoplane, it is necessary to perform the aerodynamic, structural and flight analysis assessments with the same methods, tools and degree of fidelity. So, the same CFD analyses, the FEM based-structural sizing, the mass breakdown estimation and the mission simulation carried out for the box-wing aircraft were also performed for the CeRAS CSR-01. Figure 28 reports

the comparison of the aerodynamic performance of the two configurations: the wing–body aerodynamic efficiency (lift-to-drag ratio) curve trend with respect to the generated lift is reported in four flight conditions. Focusing on the cruise condition, namely at $M = 0.79$ and $h = 11,000$ m, it emerges that the box-wing aircraft is able to generate a larger amount of lift to trim larger weights, with a relevant increment in aerodynamic efficiency. Considering the point of maximum aerodynamic efficiency, the box-wing aircraft exhibits an increase in trim lift of +66% and a related increase in aerodynamic efficiency equal to +24%, while satisfying the same constraint on the maximum wingspan of the monoplane competitor.
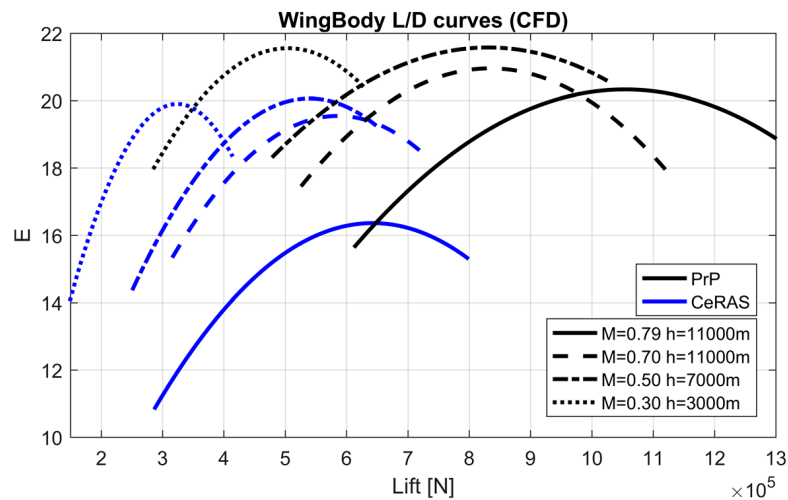
Figure 28. Comparison of aerodynamic efficiency curves: PrandtlPlane vs. CeRAS.

Figure 29 shows the detail of the operating points (from MTOW to W_{oe}) reported on the aerodynamic efficiency curves for both the configurations; the dashed curves represent the result corrected with the additional drag of fins and nacelles calculated by the approximate method [53].
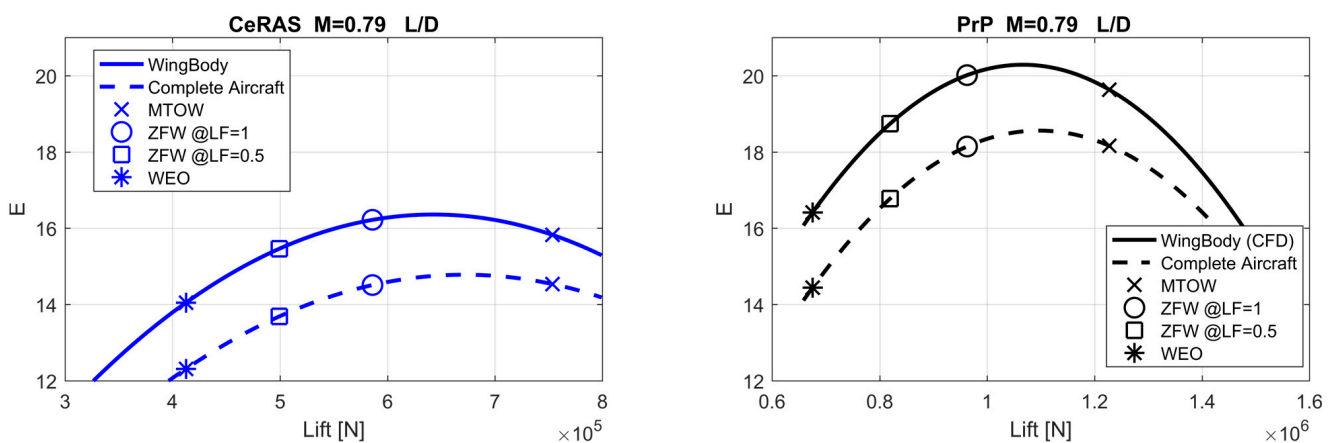
Figure 29. Detail of cruise aerodynamic efficiency for the PrandtlPlane and the CeRAS.

Figure 30 and Table 8 report the relevant data of the mass breakdown for the two aircraft; it is worth underlining that the fraction of the fuselage and lifting systems mass, together with the overall operating empty mass fractions, are very similar for the two configurations; the box-wing architecture does not introduce any significant penalisation in terms of structural mass with respect the conventional tube-and-wing solution.

CeRAS CSR-01 MTOW = 76824 kg

PrandtlPlane MTOW = 125126 kg
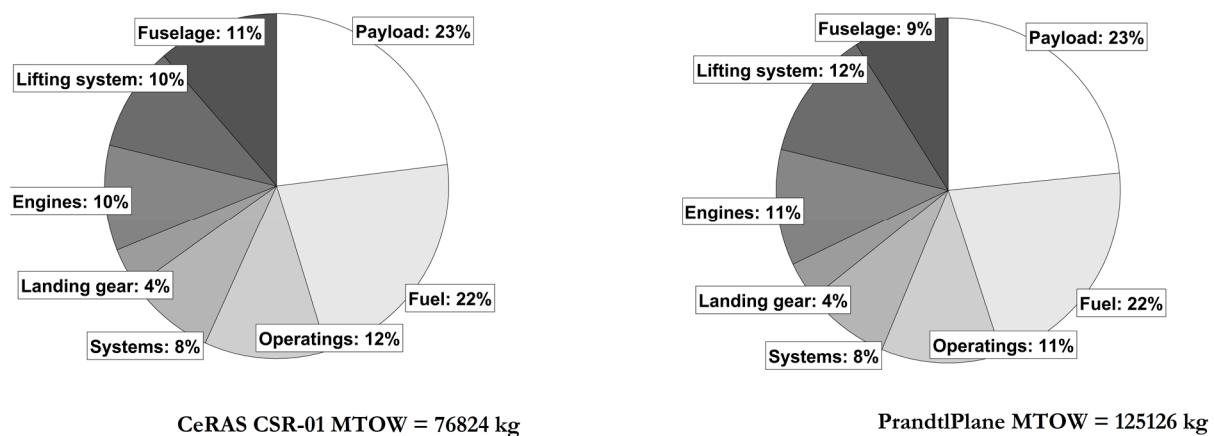
Figure 30. Components mass breakdown comparison.

Table 8. Mass breakdown comparison.

	CeRAS CSR-01	**PrandtlPlane**
W_{oe} (kg)	42,054	68,866
W_{oe}/MTOW	54.7%	55.0%
W_{fuel} (kg)	17,100	27,000
W_{fuel}/MTOW	22.3%	21.6%
W_{pay} (kg)	17,670	29,260
W_{pay}/MTOW	23.0%	23.4%
MTOW (kg)	76,824	12,5126

The information on aerodynamic performance and weights were used as input for the simulation of the harmonic mission of the CeRAS CSR-01 configuration; Table 9 reports the main data relevant to the CeRAS harmonic mission together with the mission data for the same range for the PrandtlPlane.

Table 9. Main mission data comparison.

	CeRAS CSR-01	**PrandtlPlane**
Number of passengers	186	308
Mission range	4790 km	4790 km
Mission fuel	13,670 kg	18,108 kg
Mission fuel per pax/km	0.01537 kg/km pax	0.01227 kg/km pax

The main outcome of this comparison is that the PrandtlPlane solution allows one to reduce the fuel consumption per passenger of a quantity equal to 20% with respect to CeRAS, if the CeRAS harmonic range is considered. It is worth stressing the fact that a conventional aircraft needs a larger wingspan to satisfy increases in MTOW as that exhibited by the PrP. On the other hand, the PrP, while having a higher payload capability and consequently a larger MTOW, has an advantage in fuel consumption per passenger–kilometre, although it does not demand more apron space than the conventional plane (CeRAS CSR-01).

Some relevant outputs of this mission simulation comparison, such as the flight trajectory, the mission aerodynamic efficiency and the instant fuel flow, are reported in Figure 31.
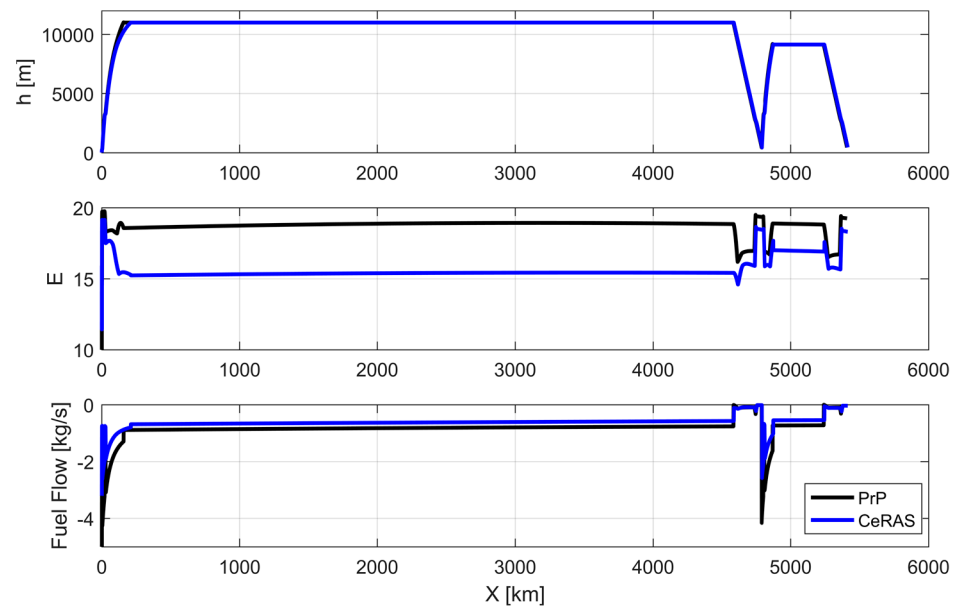
Figure 31. Comparison of flight trajectory, aerodynamic efficiency and fuel flow.

The same comparisons were performed by considering different missions, by varying the initial condition in terms of payload and target mission range. In particular, several missions were simulated by considering a variation of the mission range in the interval of [500 km–4790 km] (the upper bound is fixed equal to the CeRAS harmonic range) and by varying the cabin load factor (namely the number of boarded passengers divided by the maximum number of passengers) in the interval [0.5–1]. Figure 32 shows the comparison, in terms of percentage variation in the averaged mission aerodynamic efficiency (namely, lift-to-drag ratio); the gains for the PrandtlPlane with respect to the CeRAS are relevant in the whole considered envelope, as the increase in mean aerodynamic efficiency ranges from 15% up to 22%.
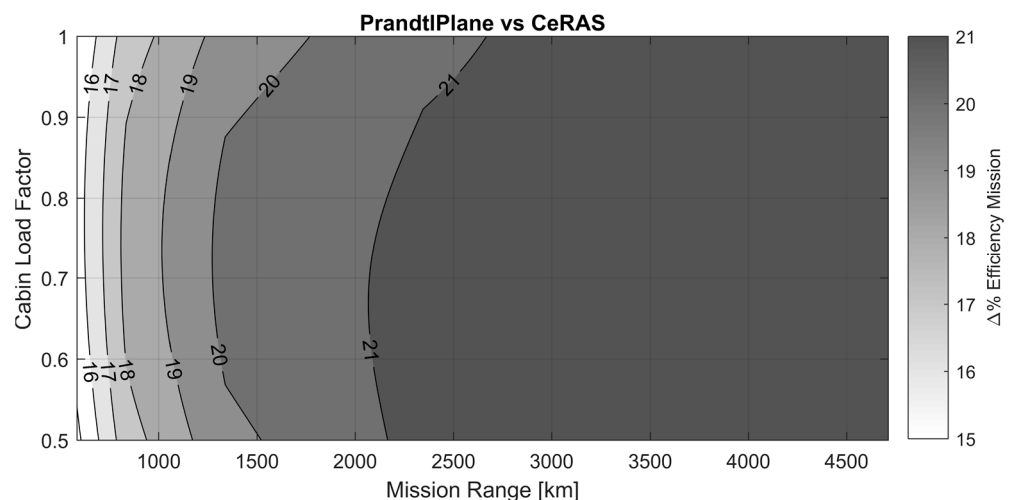
Figure 32. Comparison in terms of mean mission aerodynamic efficiency.

3.5. Box-Wing Operating Performance

In this section, a comparison between the PARSIFAL PrandtlPlane and the CeRAS CSR-01 conventional aircraft is presented in terms of a payload-range diagram. The payload-range diagram and the mission performance inside this envelope were calculated with the mission simulation tool described in Section 2.3.3. In Figure 33, the payload-range diagrams of the two aircraft are superimposed: it emerges that the PARSIFAL box-wing

aircraft covers a wider market space, in terms of the maximum number of passengers (+66%) and maximum achievable ranges, despite having the same wingspan constraints of the CeRAS CSR-01 aircraft (compatibility with ICAO Reference Aerodrome Code "C"), and so operating from the same airports and aprons.
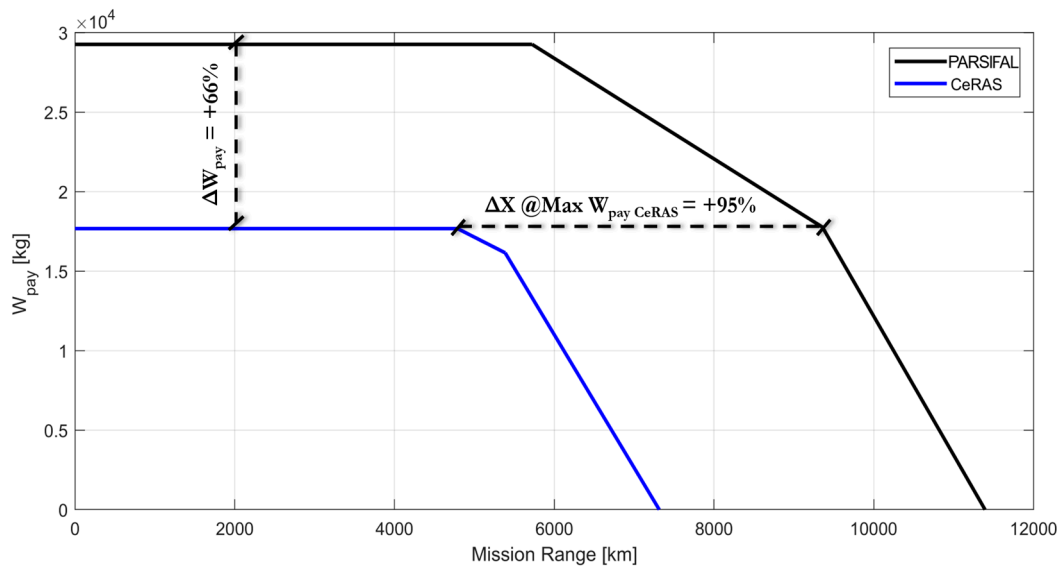
Figure 33. Comparison between the payload-range diagrams (PARSIFAL PrandtlPlane vs. CeRAS CSR-01).

In the PARSIFAL payload-range diagram reported in Figure 34, different and flexible utilisations of the box-wing aircraft are qualitatively described by highlighting the different covered market sectors; in particular, the introduction of the PrandtlPlane allows one to open a new market sector related to the short/medium-haul with an increased payload (the 'PARSIFAL area'); up today, this market sector is not covered by any conventional aircraft compliant with the ICAO Reference Code "C" wingspan constraint, and the upper limit to the maximum payload for this interval of mission lengths is represented by the Airbus A321. Moreover, the same box-wing aircraft satisfies the requirements of the so-called *Middle of the Market* sector [102] by transporting about 200 (250) passengers for 8900 (7400) kilometres. In addition, it is possible to transport a similar number of passengers of the CeRAS CSR-01 (configured in a high-density layout) for long range routes, up to 9350 km.
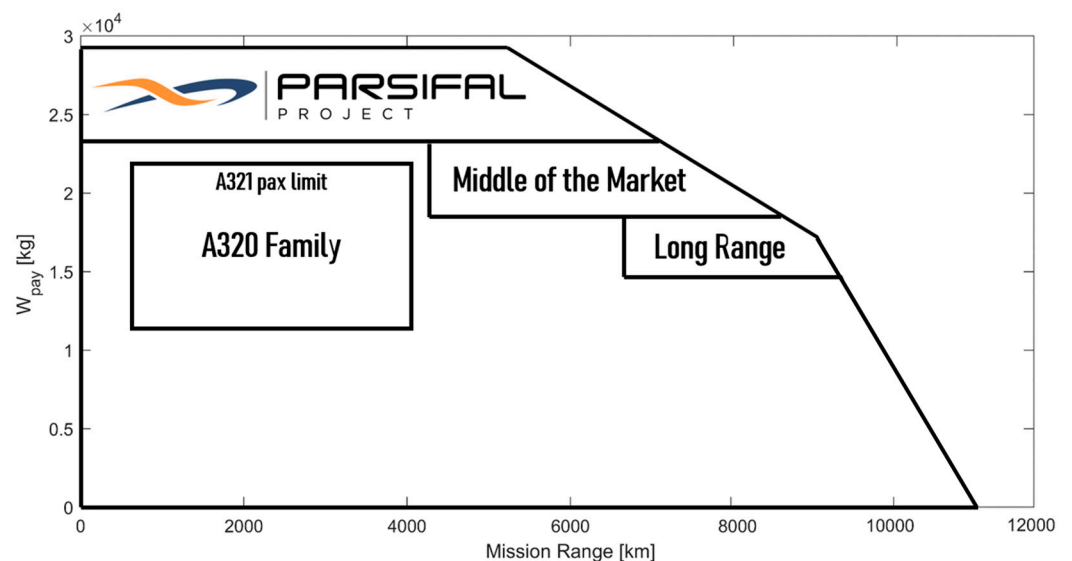
Figure 34. PARSIFAL PrandtlPlane payload-range diagram.

3.6. Discussion of the Performance Comparison between the Box-Wing and the Conventional Competitor

The information presented in Sections 3.4 and 3.5 can be combined in order to compare the two reference aircraft in terms of utilisation and mission performance. In particular, the superimposition of the contour map of the percentage variation of the mission fuel burnt per pax km with the payload-range diagram is shown in Figure 35. Keeping in mind the difference in terms of payload capacity between the two configurations (as described in Figure 33), in the following discussion, the presentation of the performance comparisons refers to the cabin load factor range graphs, to simplify the representation of the data presented, as reported in Figure 35.

The combined analysis of Figures 33 and 35 provides a complete overview of the performance comparison; it shows that:

- The PARSIFAL PrandtlPlane has a larger pax-range envelope with respect to the CeRAS CSR-01 monoplane; in particular, at the harmonic point, the PrandtlPlane presents +66% more passengers and +19% longer range. Both the aircraft are compliant with the ICAO Aerodrome Reference Code "C" constraint (max wingspan equal to 36 m);
- The PARSIFAL PrandtlPlane can transport the same maximum number of passengers of the CeRAS CSR-01 (186 pax in high density) for about 9350 km, 95% more than the reference aircraft.
- The PARSIFAL PrandtlPlane exhibits a gain in terms of mission fuel per pax km in the relevant area of the pax-range diagram, up to the harmonic range of the CeRAS CSR-01; considering the harmonic ranges, the PrandtlPlane needs 19% less fuel per passenger–kilometre; the reduction in fuel per passenger is relevant, from −13% up to −22%, in the whole operating space considered; this also reflects the aircraft environmental performance: the introduction of the PrandtlPlane configuration allows a reduction in pollutant and greenhouse gas emissions per passenger, as widely discussed in [99,103];
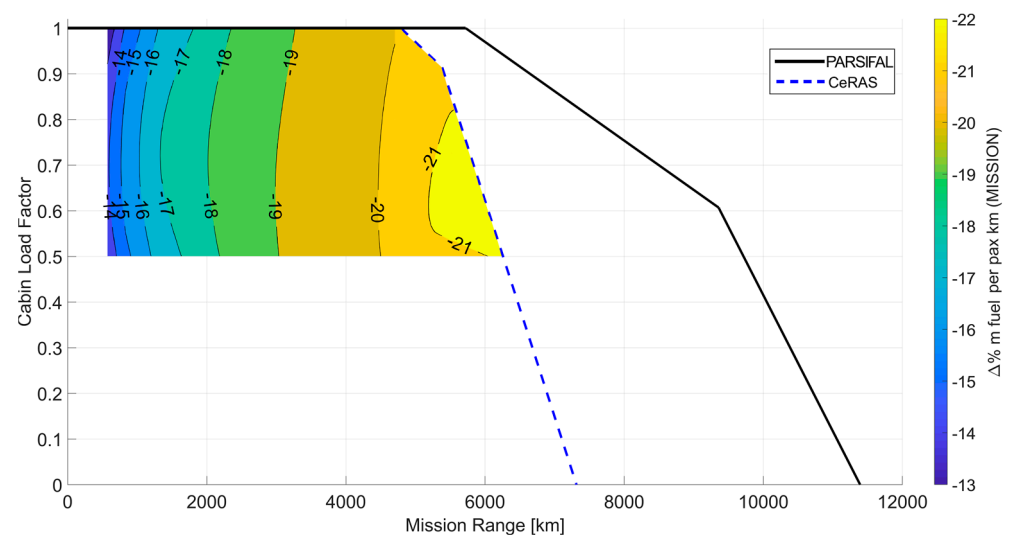
Figure 35. Comparison between the cabin load factor range diagrams (PARSIFAL PrandtlPlane vs. CeRAS CSR-01) and fuel consumption per pax km.

- The diagram in Figure 36 shows the contour maps of the percentage difference of the fuel consumption per passenger–kilometre for the two aircraft, both for the zone inside the CeRAS CSR-01 envelope and outside this limit, up to the CeRAS CSR-01 ferry range. It is clear that direct comparisons (i.e., with the same cabin load factor and range) can only be made within the limits of the CeRAS envelope; beyond this limit, the PARSIFAL PrandtlPlane can fly longer distances with the same cabin load factor, or have higher cabin load factors for the same range, with respect to the CeRAS competitor. In this area, the comparison in terms of fuel burnt per passenger–kilometre

cannot be made considering the same range and cabin load factor for the two aircraft; thus, the values obtained for PARSIFAL are compared with those relevant to the best performance of CeRAS, i.e., the missions at the border of the envelope (maximum cabin load factor for each considered range). As a result, the comparisons are carried out considering a same range for the two aircraft, but with different cabin load factors. In this zone of the diagram, the higher fuel efficiency of the PARSIFAL PrandtlPlane is combined with the capability to fly with higher cabin load factors for the considered ranges, and therefore the reduction in fuel consumption per passenger–kilometre increases very sensitively as the range increases, as shown in Figure 36.
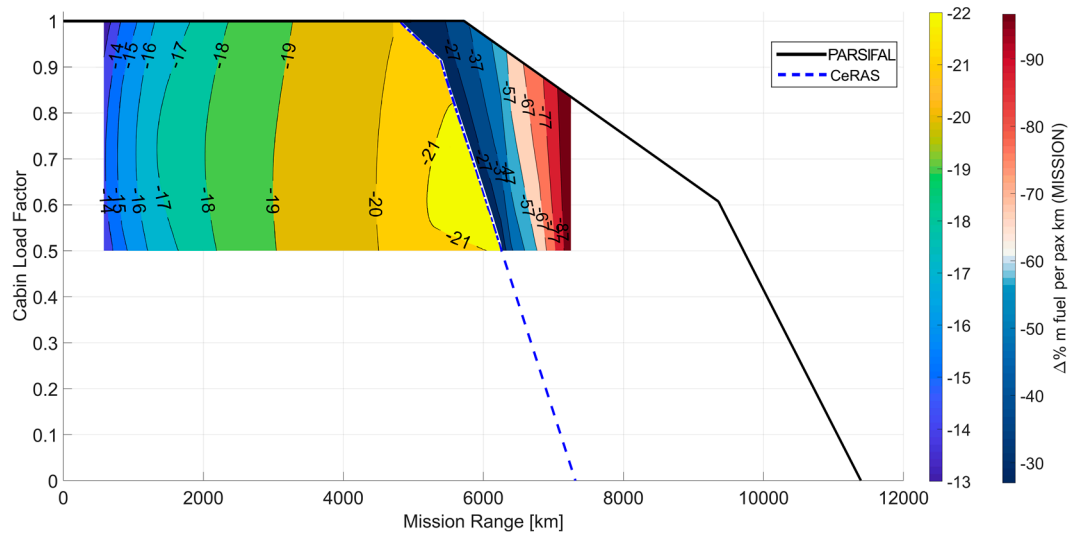
Figure 36. Overview of the comparison (PARSIFAL PrandtlPlane vs. CeRAS CSR-01) of the fuel per passenger–kilometre and cabin load factor range diagrams, up to the CeRAS ferry range.

- In the area of the cabin load factor range diagram beyond the ferry range of the CeRAS CSR-01 configuration, it is not possible to make comparisons in terms of fuel consumption. This region is highlighted in amaranth in the diagram of Figure 37. The PARSIFAL PrandtlPlane, with the same constraints on maximum wingspan of the reference monoplane competitor, is able to fly longer routes with a number of passengers comparable to the CeRAS CSR-01, thus offering an additional advantage in terms of operational flexibility.
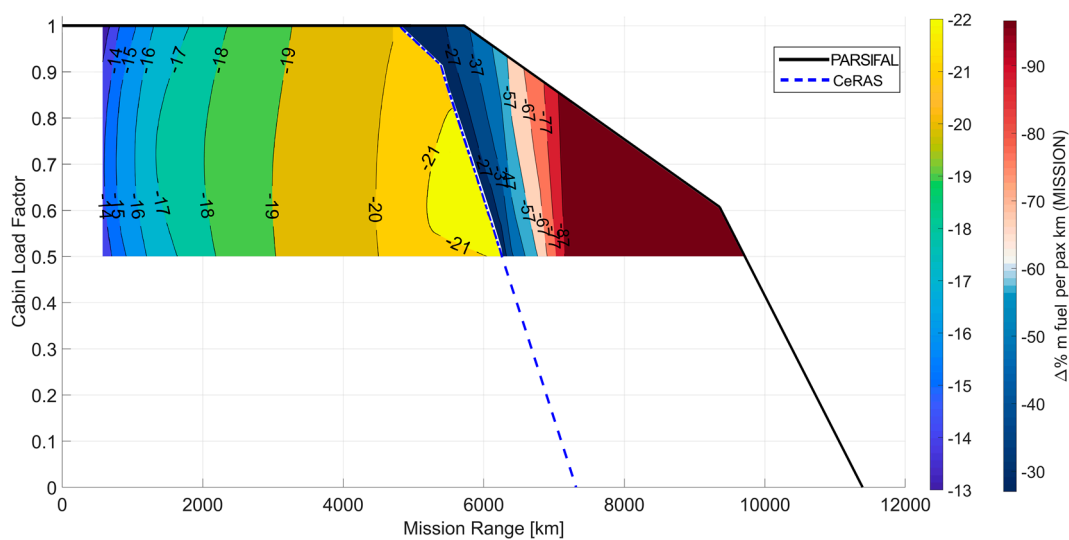
Figure 37. Overview of the comparison (PARSIFAL PrandtlPlane vs. CeRAS CSR-01) of the fuel per passenger–kilometre and cabin load factor range diagrams, beyond the CeRAS ferry range.

4. Conclusions

This paper described the potential effects of the introduction of PrandtlPlane aircraft in the short/medium-haul air traffic sector. The characteristics of this unconventional configuration, which is based on a box-wing lifting system, allow an increase in payload capability, without the need to increase the overall size of the aircraft compared to competitors in the same sector. Furthermore, the features of the lifting system enable the enhancement of the aerodynamic performance, in particular in terms of the lift-to-drag ratio, and therefore to achieve benefits in terms of reduction in fuel consumption per passenger. The introduction of this disruptive configuration is thus a possible solution to the main challenges of aviation in the near future, namely: the need to reduce pollutant and climate-changing emissions; the need to satisfy an expected growth in air traffic demand, especially on short/medium routes; and the need to alleviate problems of congestion and saturation of airport areas.

Since the aerodynamic benefits may be reduced when a new configuration is assessed from the point of view of other disciplines, a multidisciplinary design and analysis methodology was developed and used to develop a reference box-wing aircraft, and to analyse its operational potential and its performance. This methodology was structured with an increasing fidelity strategy, by using progressively more reliable design and analysis tools, with the aim of obtaining the best preliminary performance assessment. A conventional benchmark aircraft was identified to carry out the performance comparison; the selected aircraft was the CeRAS CSR-01, a virtual aircraft mock-up with characteristics similar to an Airbus A320.

The analysis and performance comparison was carried out with the same procedures and tools for the two considered configurations. The results obtained proved that the PrandtlPlane aircraft is able to carry 66% more passengers than the conventional benchmark, while maintaining the same dimensional constraints, hence keeping the possibility of operating from the same airport aprons. In addition, the PrandtlPlane is able to carry the same maximum payload as the CeRAS CSR-01 for up to 95% longer routes and, more importantly, it is able to reduce the fuel consumption per passenger over the whole envelope of the operational missions of interest. In particular, the maximum reduction in fuel consumed per passenger transported was quantified as 22%, when considering the typical operational missions of the CeRAS CSR-01. Finally, this paper shows how the box-wing architecture confers, to aircraft with the typical dimensions of short-to-medium range, the capability to cover additional sectors of the air transport market, such as *Middle of the Market* and long range.

The multidisciplinary design and analysis methodology presented in this paper can be applied to box-wing aircraft of various categories; further investigations will concern the development and the performance analysis of box-wing aircraft for the regional and commuter classes. In addition, the modularity and the flexibility of the design workflow allows the efficient integration of additional design elements, such as the introduction of hybrid-electric powertrains, or the inclusion of analysis and design methodologies of increasing fidelity, such as CFD-driven shape optimisation. Studies concerning the manufacturability and assembly of the box-wing aircraft are also worthy of further investigation: a step forward has been made concerning the actual benefits deriving from the operability of the box-wing, but there is still uncertainty regarding the possibility of setting up effective assembly lines. Investigating this topic may represent a further step towards the actual introduction of box-wing aircraft in the transport aviation sector.

Conflicts of Interest: The authors declare no conflict of interest.

Abbreviations

The following abbreviations have been used in the paper:

APU	Auxiliar Power Unit
AR	Aspect Ratio
AVL	Athena Vortex Lattice
CAD	Computer Aided Design
CeRAS	Central Reference Aircraft Data System
CFD	Computational Fluid Dynamics
CSR	CeRAS Short Range
FEM	Finite Element Method
IAS	Indicated Air Speed
ICAO	International Civil Aviation Organization
LF	Load Factor (passenger cabin)
MTOW	Maximum Take-Off Weight
PrP	PrandtlPlane
RANS	Reynolds Averaged Navier–Stokes equations
SSM	Static Stability Margin
TLARs	Top Level Aircraft Requirements
TSFC	Thrust Specific Fuel Consumption
VLM	Vortex Lattice Method

Symbols

The following symbols have been used in the paper:

b	Wingspan	m
c	Chord	m
C_D	Drag coefficient	
C_{D0}	Parasite drag coefficient	
C_{Di}	Induced drag coefficient	
C_{Dwave}	Wave drag coefficient	
$C_{D\,foil}$	Airfoil drag coefficient	
$C_{D\,tot}$	Total drag coefficient	
C_f	Friction coefficient	
C_{fe}	Equivalent skin friction coefficient	
C_L	Lift coefficient	
C_l	Section lift coefficient	
C_M	Pitch moment coefficient	
d	Diameter	m
D	Drag	N
e	Oswald factor	
E	Aerodynamic efficiency (Lift to Drag ratio)	
FF	Form factor	
$\boldsymbol{g}$	Inequality constraint	
g	Gravity acceleration	m/s^2
h	Altitude	m
h/b	Wings height to span ratio	
k	Polar drag coefficient	
k_{tip}	Stiffness constraint factor	

k_{SF}	Strength constraint safety factor	
l	Length	m
L	Lift	N
lb	Lower boundary	
L/S	Lifting surface wing loading	kg/m^2
M	Mach number	
n_z	Vertical load factor	
Q	Interference factor	
$S_{exposed}$	Planform area of the wing exposed to the flow	m^2
S_{ref}	Reference surface	m^2
S_{wet}	Wetted surface	m^2
$\boldsymbol{t}$	Vector of thicknesses of structural wingbox components	mm
t/c	Thickness to chord ratio	
T	Thrust	N
ub	Upper boundary	
V	Speed	m/s
W	Weight	kg
W_{des}	Design weight	kg
W_{oe}	Operating empty weight	kg
$\boldsymbol{x}$	Design variables vector	
x	Aircraft longitudinal position	m
x_{LE}	Longitudinal leading edge coordinate	m
y	Spanwise coordinate	m
z	Aircraft vertical position	m
α	Angle of attack	deg
γ	Trajectory slope	deg
δ_{tip}	Wing tip displacement	mm
ε	Tolerance	
θ	Section twist	deg
λ	Taper ratio	
Λ	Sweep angle	deg
σ_{eq}	Equivalent stress	MPa

Other subscripts:

comp	Component
cruise	Cruise
cyl	Cylinder
eng	Engine
front	Front wing
fus	Fuselage
fuel	Fuel
max	Maximum
min	Minimum
oper	Operating items
pay	Payload
rear	Rear wing
root	Root section
sys	On board systems
TH	Threshold
tip	Tip section
trim	Trim condition
vertical	Vertical tail
wing	Wing

References

1. Lee, D.S.; Fahey, D.W.; Forster, P.M.; Newton, P.J.; Wit, R.C.; Lim, L.; Owen, B.; Sausen, R. Aviation and global climate change in the 21st century. *Atmos. Environ.* **2009**, *43*, 3520–3537. [CrossRef]
2. Lee, D.S.; Pitari, G.; Frewe, V.; Gierens, K.; Penner, J.E.; Petzold, A.; Prather, M.J.; Schumann, U.; Bais, A.; Berntsen, T.; et al. Transport impacts on atmosphere and climate: Aviation. *Atmos. Environ.* **2010**, *44*, 4678–4734. [CrossRef] [PubMed]
3. Dessens, O.; Köhler, M.O.; Rogers, H.L.; Jones, R.L.; Pyle, J.A. Aviation and climate change. *Transp. Policy* **2014**, *34*, 14–20. [CrossRef]
4. Wuebbles, D. Evaluating the impacts of aviation on climate change. *Eos Trans. Am. Geophy. Union* **2007**, *88*, 157–160. [CrossRef]
5. Brasseur, G.P.; Gupta, M. Impact of aviation on climate. *Am. Meteorol. Soc.* **2016**, *97*, 561–583. [CrossRef]
6. Eurocontrol. European Aviation in 2040, Challenges of Growth, Annex 2, Adapting Aviation to a Changing Climate. 2018. Available online: https://perma.cc/842G-4A3R (accessed on 18 July 2021).
7. Eurocontrol. European Aviation in 2040, Challenges of Growth, Annex 1, Flight Forecast to 2040. 2018. Available online: https://perma.cc/YW6Y-JU7J (accessed on 18 July 2021).
8. PARSIFAL Project Consortium. Report on Socio Economic Scenarios and Expectations. PARSIFAL Project Deliverables, D 1.1. 2017. Available online: https://perma.cc/JYL5-K9ST (accessed on 18 July 2021).
9. Airbus. Cities, Airports & Aircraft—2019–2038. Global Market Outlook. 2019. Available online: https://perma.cc/WSW3-7JK5 (accessed on 18 July 2021).
10. Boeing. Commercial Market Outlook—2019–2038. 2019. Available online: https://perma.cc/WQ53-7WEB (accessed on 18 July 2021).
11. Eurocontrol. European Aviation in 2040, Challenges of Growth. 2018. Available online: https://perma.cc/2A2J-B7PW (accessed on 18 July 2021).
12. Schäfer, A.W.; Barrett, S.R.; Doyme, K.; Dray, L.M.; Gnadt, A.R.; Self, R.; O'Sullivan, A.; Synodinos, A.P.; Torija, A.J. Technological, economic and environmental prospects of all-electric aircraft. *Nat. Energy* **2019**, *4*, 160–166. [CrossRef]
13. Hoelzen, J.; Yaolong, L.; Bensmann, B.; Winnefiled, C.; Elham, A.; Fiedrichs, J.; Hanke-Rauschenbach, R. Conceptual design of operation strategies for hybrid electric aircraft. *Energies* **2018**, *11*, 217. [CrossRef]
14. Pornet, C.; Isikveren, A.T. Conceptual design of hybrid-electric transport aircraft. *Prog. Aerosp. Sci.* **2015**, *79*, 114–135. [CrossRef]
15. Palaia, G.; Zanetti, D.; Abu Salem, K.; Cipolla, V.; Binante, V. THEA-CODE: A design tool for the conceptual design of hybrid-electric aircraft with conventional or unconventional airframe configurations. *Mech. Ind.* **2021**, *22*, 19. [CrossRef]
16. Friedrich, C.; Robertson, P.A. Hybrid-electric propulsion for aircraft. *J. Aircr.* **2015**, *52*, 176–189. [CrossRef]
17. Brelje, B.J.; Martins, J.R. Electric, hybrid, and turboelectric fixed-wing aircraft: A review of concepts, models, and design approaches. *Prog. Aerosp. Sci.* **2019**, *104*, 1–9. [CrossRef]
18. Khandelwal, B.; Karakurt, A.; Sekaran, P.R.; Sethi, V.; Singh, R. Hydrogen powered aircraft: The future of air transport. *Prog. Aerosp. Sci.* **2013**, *60*, 45–59. [CrossRef]
19. Baroutaji, A.; Wilberforce, T.; Ramadan, M.; Olabi, A.G. Comprehensive investigation on hydrogen and fuel cell technology in the aviation and aerospace sectors. *Renew. Sustain. Energy Rev.* **2019**, *106*, 31–40. [CrossRef]
20. Nojoumi, H.; Dincer, I.; Naterer, G.F. Greenhouse gas emissions assessment of hydrogen and kerosene-fueled aircraft propulsion. *Int. J. Hydrogen Energy* **2019**, *34*, 1363–1369. [CrossRef]
21. Ng, W.; Datta, A. Hydrogen fuel cells and batteries for electric-vertical takeoff and landing aircraft. *J. Aircr.* **2019**, *56*, 1765–1782. [CrossRef]
22. Azami, M.H.; Savill, M. Comparative study of alternative biofuels on aircraft engine performance. *Inst. Mech. Eng. Part G J. Aerosp. Eng.* **2017**, *231*, 1509–1521. [CrossRef]
23. Moore, R.H.; Thornhill, L.; Weinzierl, B.; Sauer, D.; D'Ascoli, E.; Kim, J.; Lichtenstern, M.; Scheibe, M.; Beaton, B.; Beyersdorf, A.; et al. Biofuel blending reduces particle emissions from aircraft engines at cruise conditions. *Nature* **2017**, *543*, 411–415. [CrossRef] [PubMed]
24. Mazlan, N.M.; Savill, M.; Kipouros, T. Effects of biofuels properties on aircraft engine performance. *Aircr. Eng. Aerosp. Technol.* **2015**, *87*, 437–442. [CrossRef]
25. Liem, R.P.; Martins, J.R.; Kenway, G.K. Expected drag minimization for aerodynamic design optimization based on aircraft operational data. *Aerosp. Sci. Technol.* **2017**, *63*, 344–362. [CrossRef]
26. Zhu, J.H.; Zhang, W.H.; Xia, L. Topology optimization in aircraft and aerospace structures design. *Arch. Comput. Methods Eng.* **2015**, *23*, 595–622. [CrossRef]
27. Lei, R.; Bai, J.; Xu, D. Aerodynamic optimization of civil aircraft with wing-mounted engine jet based on adjoint method. *Aerosp. Sci. Technol.* **2019**, *93*, 105285. [CrossRef]
28. Gu, X.; Ciampa, P.D.; Jepsen, J.; Nagel, B. High fidelity aerodynamic optimization in distributed overall aircraft design. In Proceedings of the AIAA Aviation Forum, 17th AIAA/ISSMO Multidisciplinary Analysis and Optimization Conference, Washington, DC, USA, 13–17 June 2016. [CrossRef]
29. Lange, R.H. Review of unconventional aircraft design concepts. *J. Aircr.* **1988**, *25*, 385–392. [CrossRef]
30. Schmitt, D. Challenges for unconventional transport aircraft configurations. *Air Space Eur.* **2001**, *3*, 67–72. [CrossRef]

31. Iwanizki, M.; Wöhler, S.; Fröhler, B.; Zill, T.; Méheut, M.; Defoort, S.; Carini, M.; Gauvrit-Ledogar, J.; Liaboeuf, R.; Tremolet, A.; et al. Conceptual Design Studies of Unconventional Configurations. 3AF Aerospace Europe Conference 2020, Bordeaux. 2020. Available online: https://hal.archives-ouvertes.fr/hal-02907205 (accessed on 18 July 2021).

32. Bijewitz, J.; Seitz, A.; Isikveren, A.T.; Hornung, M. Multi-disciplinary design investigation of propulsive fuselage aircraft concepts. *Aircr. Eng. Aerosp. Technol.* **2016**, *88*, 257–267. [CrossRef]

33. Defoort, S.; Méheut, M.; Paluch, B.; Liaboeuf, R.; Murray, R.; Mincu, D.C.; David, J.M. Conceptual design of disruptive aircraft configurations based on High-Fidelity OAD process. In Proceedings of the AIAA Aviation Forum, 2018 Aviation Technology, Integration, and Operations Conference, Atlanta, GA, USA, 25–29 June 2018. [CrossRef]

34. Werner-Westphal, C.; Heinze, W.; Horst, P. Multidisciplinary integrated preliminary design applied to unconventional aircraft configurations. *J. Aircr.* **2008**, *45*, 581–590. [CrossRef]

35. Liebeck, R.H. Design of the blended wing body subsonic transport. *J. Aircr.* **2004**, *41*, 10–25. [CrossRef]

36. Qin, N.; Vavalle, A.; Le Moigne, A.; Laban, M.; Hackett, K.; Weinerfelt, P. Aerodynamic considerations of blended wing body aircraft. *Prog. Aerosp. Sci.* **2004**, *40*, 21–343. [CrossRef]

37. Okonkwo, P.; Smith, H. Review of evolving trends in blended wing body aircraft design. *Prog. Aerosp. Sci.* **2016**, *82*, 1–23. [CrossRef]

38. Cavallaro, R.; Demasi, L. Challenges, ideas, and innovations of joined-wing configurations: A concept from the past, an opportunity for the future. *Prog. Aerosp. Sci.* **2016**, *87*, 1–93. [CrossRef]

39. Wolkovitch, J. The joined wing: An overview. *J. Aircr.* **1986**, *23*, 161–178. [CrossRef]

40. Frediani, A.; Cipolla, V.; Rizzo, E. The Prandtl plane configuration: Overview on possible applications to civil aviation. In *Variational Analysis and Aerospace Engineering: Mathematical Challenges for Aerospace Design*; Springer Optimization and Its Applications; Springer: Boston, MA, USA, 2012; Volume 66. [CrossRef]

41. Frediani, A.; Rizzo, E.; Bottoni, C.; Scanu, J.; Iezzi, G. A 250 Passenger Prandtl plane transport aircraft preliminary design. *Aerotecnica Missili Spazio* **2005**, *84*. Available online: http://hdl.handle.net/11568/99885 (accessed on 18 July 2021).

42. Frediani, A. The Prandtl Wing. VKI, Lecture Series: Innovative Configurations and Advanced Concepts for Future Civil Transport Aircraft. 2005. Available online: https://perma.cc/XU6F-8YLG (accessed on 18 July 2021).

43. Frediani, A.; Cipolla, V.; Oliviero, F. Design of a prototype of light amphibious Prandtl Plane. In Proceedings of the AIAA SciTech Forum, 56th AIAA/ASCE/AHS/ASC Structures, Structural Dynamics, and Materials Conference, Kissimmee, FL, USA, 5−9 January 2015. [CrossRef]

44. Prandtl, L.; Induced Drag of Multiplanes. NACA TN-182. 1924. Available online: https://ntrs.nasa.gov/citations/19930080964 (accessed on 18 July 2021).

45. Frediani, A.; Montanari, G. Best wing system: An exact solution of the Prandtl's problem. In *Variational Analysis and Aerospace Engineering*; Springer Optimization and Its Applications; Springer: New York, NY, USA, 2009; Volume 33. [CrossRef]

46. Demasi, L.; Dipace, A.; Monegato, G.; Cavallaro, R. Invariant formulation for the minimum induced drag conditions of nonplanar wing systems. *AIAA J.* **2014**, *52*. [CrossRef]

47. PARSIFAL Project. Available online: https://perma.cc/5ULW-HCP4 (accessed on 18 July 2021).

48. Abu Salem, K.; Binante, V.; Cipolla, V.; Maganzi, M. PARSIFAL project: A breakthrough innovation in air transport. *Aerotecnica Missili Spazio* **2018**, *97*. [CrossRef]

49. Abu Salem, K. Studio Sulla Configurazione Aerodinamica di Velivoli Civili di Tipo PrandtlPlane di Piccole e Medie Dimensioni. M.Sc. Thesis, University of Pisa, Italy, 2016. Available online: https://etd.adm.unipi.it/theses/available/etd-06222016-110207/ (accessed on 18 July 2021).

50. Bishop, K. Assessment of the Ability of Existing Airport Gate Infrastructure to Accommodate Transport Category Aircraft with Increased Wingspan for Improved Fuel Efficiency. M.Sc. Thesis, Dept. of Aeronautics and Astronautics, Massachusetts Institute of Technology, Boston, MA, USA, 2012. Available online: http://hdl.handle.net/1721.1/76095 (accessed on 18 July 2021).

51. European Commission. Mobility for Growth—Breakthrough Innovation. Funding Action for Research and Innovation. 2015. Available online: https://ec.europa.eu/inea/en/news-events/newsroom/new-transport-projects-selected-horizon-2020-funding (accessed on 18 July 2021).

52. McMasters, J.; Paisley, D.; Hubert, R.; Kroo, I.; Bofah, K.; Sullivan, J.; Drela, M. Advanced configurations for very large subsonic Transport Airplanes. NASA CR 198351. 1996. Available online: https://ntrs.nasa.gov/citations/19970003675 (accessed on 18 July 2021).

53. Raymer, D.P. *Aircraft Design: A Conceptual Approach*; AIAA Education Series: Washington, DC, USA, 1992; ISBN 0-930403-51-7.

54. Association of European Airlines. *Short-Medium Range Aircraft AEA Requirements. Report G(T)*; AEA: Bonn, Germany, 1989.

55. Casarosa, C. *Meccanica del Volo*; Pisa University Press: Pisa, Italy, 2013; ISBN 978-8867410163.

56. Rizzo, E. Optimization Methods Applied to the Preliminary Design of Innovative Non Conventional Aircraft Configurations. Ph.D. Thesis, University of Pisa, Pisa, Italy, 2009. Available online: https://etd.adm.unipi.it/t/etd-05122010-103814/ (accessed on 18 July 2021).

57. Cappelli, L.; Costa, G.; Cipolla, V.; Frediani, A.; Oliviero, F.; Rizzo, E. Aerodynamic optimization of a large PrandtlPlane configuration. *Aerotecnica Missili Spazio* **2016**, *95*, 163–175. [CrossRef]

58. Abu Salem, K.; Palaia, G.; Cipolla, V.; Binante, V.; Zanetti, D.; Chiarelli, M. Tools and methodologies for box-wing aircraft conceptual aerodynamic design and aeromechanic analysis. *Mech. Ind.* **2021**, *22*, 1–19. [CrossRef]

36 of 37

59. Rizzo, E.; Frediani, A. Application of optimisation algorithms to aircraft aerodynamics. In *Variational Analysis and Aerospace Engineering*; Springer Optimization and Its Applications: New York, NY, USA, 2009. [CrossRef]

60. Addis, B.; Locatelli, M.; Schoen, F. Local optima smoothing for global optimization. *Optim. Methods Softw.* **2005**, *20*, 417–437. [CrossRef]

61. Drela, M.; Youngren, H. XFOIL 6.9 User Primer. Online Software Manual. 2001. Available online: https://perma.cc/7AGE-C3XU (accessed on 18 July 2021).

62. Drela, M.; Youngren, H. AVL 3.36 User Primer. Online Software Manual. 2017. Available online: https://perma.cc/R35R-W29F (accessed on 18 July 2021).

63. Beltramo, M.; Trapp, D.; Kimoto, B.; Marsh, D. Parametric Study of Transport Aircraft Systems Cost and Weight. Report NASA CR151970. 1977. Available online: https://ntrs.nasa.gov/citations/19770019162 (accessed on 18 July 2021).

64. Wells, D.; Horvath, B.; McCullers, L. The Flight Optimization System Weights Estimation Method. NASA/TM–2017–219627, Volume I; 2017. Available online: https://ntrs.nasa.gov/citations/20170005851 (accessed on 18 July 2021).

65. Frediani, A.; Cipolla, V.; Abu Salem, K.; Binante, V.; Picchi Scardaoni, M. Conceptual design of PrandtlPlane civil transport aircraft. *Inst. Mech. Eng. Part G J. Aerosp. Eng.* **2019**, *234*, 1675–1687. [CrossRef]

66. Mason, W.H. Analytic models for technology integration in aircraft design. *AIAA Aircr. Des. Syst. Op. Conf. Dayton* **1990**, *90*, 3262-CP. [CrossRef]

67. Cipolla, V.; Frediani, A.; Abu Salem, K.; Binante, V.; Rizzo, E.; Maganzi, M. Preliminary transonic CFD analyses of a PrandtlPlane transport aircraft. *Transp. Res. Procedia* **2018**, *29*, 82–91. [CrossRef]

68. ANSYS, Ansys Fluent—Fluid Simulation Software. Available online: https://perma.cc/L56W-V8FZ (accessed on 18 July 2021).

69. Fazalzadeh, S.; Scholz, D.; Mazidi, A.; Friswell, M. Flutter characteristics of typical wing sections of a box wing aircraft configuration. In Proceedings of the 3AF AEGATS Proceedings 2018, Toulouse, France, 23−25 October 2018. [CrossRef]

70. Divoux, N.; Frediani, A. The lifting system of a PrandtlPlane, Part 2: Preliminary study on flutter characteristics. In *Variational Analysis and Aerospace Engineering*; Springer Optimization and Its Applications: Boston, MA, USA, 2012. [CrossRef]

71. Cavallaro, R.; Bombardieri, R.; Silvani, S.; Demasi, L.; Bernardini, G. Aeroelasticity of the PrandtlPlane: Body freedom flutter, freeplay, and limit cycle oscillation. In *Variational Analysis and Aerospace Engineering: Mathematical Challenges for the Aerospace of the Future*; Springer Optimization and Its Applications: New York, NY, USA, 2016. [CrossRef]

72. Bombardieri, R.; Cavallaro, R.; Demasi, L. A historical perspective on the aeroelasticity of box Wings and PrandtlPlane with new findings. In Proceedings of the AIAA SciTech Forum, 57th AIAA/ASCE/AHS/ASC Structures, Structural Dynamics, and Materials Conference, San Diego, CA, USA, 4−8 January 2016. [CrossRef]

73. PARSIFAL Project Consortium. Aeroelastic Analysis of the Baseline PrandtlPlane. PARSIFAL Project Deliverables, D5.2. 2020. Available online: https://perma.cc/JYL5-K9ST (accessed on 18 July 2021).

74. Abu Salem, K. Development of Design Tools and Methods for Box-Wing Airplanes and Application of the PrandtlPlane Concept to a Short-Medium Range Aircraft. Ph.D. Thesis, University of Pisa, Pisa, Italy, 2021. Available online: https://etd.adm.unipi.it/ (accessed on 18 July 2021).

75. Picchi Scardaoni, M.; Binante, V.; Cipolla, V. WAGNER: A new code for parametrical structural study of fuselages of civil transport aircraft. *Aerotecnica Missili Spazio* **2017**, *96*, 136–147. [CrossRef]

76. 3DS Dassault Systems Simulia, ABAQUS Unified FEA. Available online: https://perma.cc/X8L3-JGSV (accessed on 18 July 2021).

77. Fuchte, J. Enhancement of Aircraft Cabin Design Guidelines with Special Consideration of Aircraft Turnaround and Short Range Operations. Ph.D. Dissertation, DLR-Forschungsbericht, Hamburg, Germany, 2014. Available online: https://perma.cc/YT3N-99 VV (accessed on 18 July 2021).

78. Fuchte, J.; Nagel, B.; Gollnick, V. Weight and fuel saving potential through changed cabin and fuselage design. In Proceedings of the AIAA Aviation Forum, Aviation Technology, Integration, and Operations Conference, Los Angeles, California, USA, 12−14 August 2013. [CrossRef]

79. PARSIFAL Project Consortium. Structural Analysis of the Baseline PrandtlPlane. PARSIFAL Project Deliverables, D5.1. 2020. Available online: https://perma.cc/JYL5-K9ST (accessed on 18 July 2021).

80. Picchi Scardaoni, M.; Montemurro, M.; Panettieri, E. PrandtlPlane wing-box least-weight design: A multi-scale optimisation approach. *Aerosp. Sci. Technol.* **2020**, *106*, 106156. [CrossRef]

81. Cipolla, V.; Abu Salem, K.; Palaia, G.; Binante, V.; Zanetti, D. A DoE-based approach for the implementation of structural surrogate models in the early stage design of box-wing aircraft. *Aerosp. Sci. Technol.* **2021**, *117*, 106968. [CrossRef]

82. Torenbeek, E. Development and Application of a Comprehensive, Design-Sensitive Weight Prediction Method for Wing Structures of Transport Category Aircraft. Delft University of Technology, Faculty of Aerospace Engineering, Report LR-693. 1992. Available online: http://resolver.tudelft.nl/uuid:b45a61fe-317a-4201-82f0-dfae51ceb687 (accessed on 18 July 2021).

83. Filippone, A. *Advanced Aircraft Flight Performance*; Cambridge University Press: Cambridge, United Kingdom, 2012. [CrossRef]

84. Khadilkar, H.; Balakrishnan, H. Estimation of aircraft taxi fuel burn using flight data recorder archives. *Transp. Res. Part D* **2012**, *17*, 532–537. [CrossRef]

85. Abu Salem, K.; Palaia, G.; Bianchi, M.; Zanetti, D.; Cipolla, V.; Binante, V. Preliminary take-off analysis and simulation of PrandtlPlane commercial aircraft. *Aerotecnica Missili Spazio* **2020**, *99*, 203–216. [CrossRef]

86. Airbus. *Getting to Grips with Aircraft Performance*; Airbus SAS: Leiden, The Netherlands, 2002. Available online: https://perma.cc/FQ9P-FET4 (accessed on 18 July 2021).

87. Cipolla, V.; Frediani, A.; Abu Salem, K.; Picchi Scardaoni, M.; Nuti, A.; Binante, V. Conceptual design of a box-wing aircraft for the air transport of the future. In Proceedings of the AIAA Aviation Forum, 2018 Aviation Technology, Integration, and Operations Conference, Atlanta, GA, USA, 25−29 June 2018. [CrossRef]
88. Cipolla, V.; Abu Salem, K.; Picchi Scardaoni, M.; Binante, V. Preliminary design and performance analysis of a box-wing transport aircraft. In Proceedings of the AIAA SciTech 2020 Forum, Orlando, FL, USA, 6−10 January 2020. [CrossRef]
89. Carini, M.; Méheut, M.; Kanellopoulos, S.; Cipolla, V.; Abu Salem, K. Aerodynamic analysis and optimization of a boxwing architecture for commercial airplanes. In Proceedings of the AIAA SciTech 2020 Forum, Orlando, FL, USA, 6−10 January 2020. [CrossRef]
90. PARSIFAL Project Consortium. Requirements for the Adoption of the PrandtlPlane as a Mean of Transport. PARSIFAL Project Deliverables, D 2.1. 2017. Available online: https://perma.cc/BD3L-895C (accessed on 18 July 2021). (public).
91. International Civil Aviation Organization. *Aerodromes: Volume I—Aerodrome Design and Operations. International Standards and Recommended Practices*; ICAO Annex 14: Montréal, QC, Canada, 2009.
92. CeRAS—Central Reference Aircraft System. Available online: https://ceras.ilr.rwth-aachen.de/ (accessed on 18 July 2021).
93. Risse, K.; Schäfer, K.; Schültke, F.; Stumpf, E. Central reference aircraft data system (CeRAS) for research community. *CEAS Aeronaut. J.* **2016**, *7*, 121–133. [CrossRef]
94. Airbus, Aircraft characteristics—Airport and Maintenance Planning, Airbus SAS. 2014. Available online: https://perma.cc/XM64-GZMT (accessed on 18 July 2021).
95. Picchi Scardaoni, M.; Frediani, A. General closed-form solution of piecewise circular frames of aircraft. *AIAA J.* **2019**, *57*, 1338–1342. [CrossRef]
96. Bottoni, C.; Scanu, J. Preliminary Design of a 250 Passenger PrandtlPlane Aircraft. M.Sc. Thesis, University of Pisa, Pisa, Italy, 2004. Available online: https://etd.adm.unipi.it/theses/available/etd-09072004-140314/ (accessed on 18 July 2021).
97. Schiktanz, D.; Scholz, D. Box wing fundamentals—An aircraft design perspective. In Proceedings of the DGLR: Deutscher Luft und Raumfahrtkongress 2011, Bremen, Germany, 27–29 September 2011; pp. 601–615, ISBN 978-3-932182-74-X. Document ID: 241353. Available online: https://perma.cc/2Q7R-WFAF (accessed on 18 July 2021).
98. Picchi Scardaoni, M.; Magnacca, F.; Massai, A.; Cipolla, V. Aircraft turnaround time estimation in early design phases: Simulation tools development and application to the case of box-wing architecture. *J. Air Transp. Manag.* **2021**, *96*, 102122. [CrossRef]
99. PARSIFAL Project Consortium. Report on Operational and Economic Assessment. PARSIFAL Project Deliverables, D 1.2. 2020. Available online: https://perma.cc/U3QF-JQL7 (accessed on 18 July 2021). (public).
100. Cipolla, V.; Abu Salem, K.; Bachi, F. Preliminary stability analysis methods for PrandtlPlane aircraft in subsonic conditions. *Aircr. Eng. Aerosp. Technol.* **2018**, *91*, 525–537. [CrossRef]
101. Cipolla, V.; Abu Salem, K.; Palaia, G.; Binante, V.; Zanetti, D. A semi-empirical VLM-based method for the prediction of maximum lift coefficient of box-wing aircraft. *J. Aerosp. Eng.* **2021**, under review.
102. Arkell, D. Moving toward the Middle, Frontiers Magazine: Boeing. 2003. Available online: https://perma.cc/EK8C-B7RP (accessed on 18 July 2021).
103. Tasca, A.L.; Cipolla, V.; Abu Salem, K.; Puccini, M. Innovative box-wing aircraft: Emissions and climate change. *Sustainability* **2021**, *13*, 3282. [CrossRef]

MDPI

Article

Influence of Novel Airframe Technologies on the Feasibility of Fully-Electric Regional Aviation

Stanislav Karpuk * and Ali Elham *

Institute of Aircraft Design and Lightweight Structures, Technical University Braunschweig,
38106 Braunschweig, Germany
* Correspondence: s.karpuk@tu-braunschweig.de (S.K.); a.elham@tu-braunschweig.de (A.E.)

Abstract: The feasibility of regional electric aviation to reduce environmental impact highly depends on technological advancements of energy storage techniques, available battery energy density, and high-power electric motor technologies. However, novel airframe technologies also strongly affect the feasibility of a regional electric aircraft. In this paper, the influence of novel technologies on the feasibility of regional electric aviation was investigated. Three game-changing technologies were applied to a novel all-electric regional aircraft: active flow control, active load alleviation, and novel materials and structure concepts. Initial conceptual design and mission analysis of the aircraft was performed using the aircraft design framework SUAVE, and the sensitivity of the most important technologies on the aircraft characteristics and performance were studied. Obtained results were compared against a reference ATR-72 aircraft. Results showed that an all-electric aircraft with airframe technologies might be designed with the maximum take-off weight increase of 50% starting from the battery pack energy density of 700 Wh/kg. The overall emission level of an all-electric aircraft with novel technologies is reduced by 81% compared to the ATR-72. On the other hand, novel technologies do not contribute to the reduction in Direct Operating Costs (DOC) starting from 700 Wh/kg if compared to an all-electric aircraft without technologies. An increase in DOC ranges from 43% to 30% depending on the battery energy density which creates a significant market obstacle for such type of airplanes. In addition, the aircraft shows high levels of energy consumption which concerns its energy efficiency. Finally, the sensitivity of DOC to novel technologies and sensitivities of aircraft characteristics to each technology were assessed.

Keywords: aircraft design; airframe technologies; aircraft sizing; all-electric aircraft; multi-disciplinary design optimization

1. Introduction

Significant climate changes and potential environmental impact due to increased transportation in the near future have motivated many industries to focus on reducing CO_2 and NO_x emissions. As a major transportation method, the aviation industry also follows the trend to reduce the emission of new generations of aircraft. Improvements in airframe and engine technologies increase aircraft efficiency and reduce their emission. However, a potential increase in air transportation may still lead to an increase in overall CO_2 and NO_x emissions. Under Flightpath 2050 [1], The European Commission has set a future challenge for the new generation of aircraft to reduce their total emission. Figure 1 shows three schematic trends: if no advancements in aircraft technologies are present, if currently feasible technology advancements are achieved, and if novel technologies are introduced. This challenge leads to developing alternative environmentally-friendly energy sources as one of the main solutions for environmental impact reduction. Aircraft electrification has become one of the most popular approaches to reduce aircraft emissions. Today, many companies work in various directions to make electric flights available: improve battery energy capacity, modify and develop new propulsion systems, and introduce new aircraft configurations more applicable for future electrification.
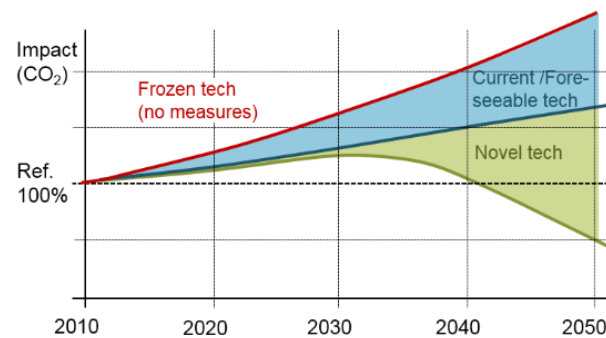
Figure 1. Forecast of CO_2 emission impact due to increased transportation and emission reduction goals [1].

At the moment, research is highly focused on hybrid- and all-electric propulsion systems and aircraft configurations to reduce the environmental impact produced by aircraft. Friedrich introduced a simulation technique for a single-seat hybrid-electric demonstrator, designed the aircraft, and performed a scaling analysis to determine a large fuel savings impact for the small- and mid-scale sector of aircraft [2]. Hamilton investigated the effect of hybrid-electric aircraft from the operational perspective to reach an optimal aircraft operation with battery energy density constraints [3]. A lot of work is also dedicated to the introduction of distributed electric propulsion (DEP) energy networks and aircraft concepts featuring DEP. Kim summarized major contributions towards the development of DEP aircraft and relative technologies [4]. Finger focused on sizing methodologies, and aircraft design of future general aviation aircraft that could be not only hybrid-electric but also fully electric [5–7]. De Vries also developed initial sizing methodologies for hybrid-electric aircraft for conceptual aircraft design but introduced effects of DEP at early conceptual design stages [8,9]. Pornet also introduced a sizing methodology for hybrid-electric aircraft and compared performance between the conventional reference aircraft and its hybrid version [10]. Sguglia introduced an MDO framework for hybrid-electric aircraft with coupled derivatives and performed various optimization analyses to demonstrate the capabilities of the framework [11]. The work of Hepperle [12] addressed the potentials and limitations of all-electric aircraft specifically and introduced aircraft modifications that could potentially improve the aircraft performance at given battery energy densities. The ultimate goal of aircraft electrification is to achieve a fully-electric flight at adequate aircraft weight characteristics to maximize the emission reduction at the aircraft level. However, the availability of all-electric aircraft is limited to the General Aviation sector due to low battery energy density compared to the Jet-A fuel and relatively low maximum power capabilities of modern electric motors. Multiple all-electric concepts have already been introduced or are being developed at the moment. From existing airplanes, Pipistrel has already certified a twin-seat all-electric aircraft that has a maximum speed of 185 km/h and a maximum range of 139 km [13]. Bye Aerospace is currently performing flight tests on a one-seat general aviation aircraft that will be certified under the FAR Part 23 category. The eFlyer has a maximum cruise speed of 250 km/h and endurance of three hours [14]. In 2016, Siemens tested an all-electric energy network by retrofitting the Extra 300 aerobatic aircraft and set two world records [15]. The Equation Aircraft has also demonstrated an all-electric twin-seat amphibious aircraft with the empennage-mounted engine that can fly up to 240 km/h and up to 200 km [16] Airbus has also developed several versions of an experimental all-electric E-fan aircraft to test the capabilities of an all-electric aircraft [17]. The E-Fan concept had multiple versions, from a technology demonstrator to a production variant. MagniX has introduced an all-electric propulsion system and first retrofitted De Havilland Beaver and then 208B Cessna Grand Caravan. The electrified Caravan became the largest all-electric airplane until today [18]. It must be noted that the list of existing all-electric aircraft companies is incomplete and more companies exist and are at different design stages.

To achieve all-electric regional aviation faster, not only the energy source and propulsion system technologies must be improved, but also advanced airframe technologies need to be considered. Such novel technologies may significantly increase the aircraft performance characteristics and overall efficiency that will enable earlier integration of all-electric commercial aircraft into the market before. Liu introduced initial estimations of the impact of novel technologies for a range of aircraft from the short-range to the long-range [19]. Results showed that novel airframe technologies may significantly improve aircraft energy efficiency.

Under the Excellence Cluster Se^{2}A (Sustainable and Energy Efficient Aviation), three energy-efficient aircraft are to be designed to cover the majority of commercial aircraft operations. Figure 2 shows three sample new energy-efficient airplanes: a short-range propeller aircraft that shall be applicable to the ATR-72, the medium-range aircraft having similar mission requirements to the Airbus A320, and the long-range aircraft to cover ranges similar to the Boeing B777.

Figure 2. A family of energy-efficient aircraft under the Se^{2}A cluster.

The initial cluster requirement for the short-range aircraft was to investigate the feasibility and availability of an all-electric short-range aircraft if novel airframe and propulsion technologies are introduced. A few novel technologies have been considered for the design of future regional aircraft. Hybrid laminar flow control (HLFC), load alleviation, and advanced materials and structure concepts. In addition, high-temperature superconducting motors and high-energy capacity batteries have been considered for the present research. An aircraft with similar top-level requirements as ATR-72 is designed considering the mentioned technologies and a battery-based full electric propulsion system.

The present work is divided into multiple sections. Section 2 describes novel technologies implemented in the new short-range aircraft. Section 3 describes methodologies, models, assumptions, and software used to perform novel technology assessments to design the aircraft. Section 4 describes the aircraft's top-level requirements (TLRs). Section 5 describes the aircraft concept selection and its initial sizing. Section 6 presents multidisciplinary design optimization studies of the SE^{2}A aircraft to refine the design and make important design decisions. Finally, Section 7 assesses the influence of novel technologies on aircraft availability and the strength of each technology impact.

2. Novel Airframe and Propulsion Technologies

2.1. Hybrid Laminar Flow Control

The generation and extension of laminar flow over the aircraft surface significantly affect the overall aircraft drag, reducing aircraft weights, fuel burn, and operating costs. Preliminary estimations of an aircraft that features extended laminar flow along the wing, empennage, and fuselage demonstrated significant reduction (up to 50%) in overall drag and proved the importance of laminar flow control (LFC) [20]. Figure 3 shows the effects of the new wing design featuring the LFC and compares overall drag to the reference aircraft.

However, natural laminar flow (NLF) is limited along the shape, so to extend it even more, hybrid laminar flow control (HLFC) is required: the laminar boundary layer is not only extended using NLF design but also using the active suction technology. In this technology, the air is sucked from the aircraft's outer surface to delay the transition of the boundary layer and enable substantially higher percent laminarization compared to conventional surfaces. The skin of each aircraft component is split into two segments:

a porous sheet and an inner sheet that supports the outer sheet. The inner sheet has orifices that suck the air from the boundary layer and delay transition. In each chamber, an individual pressure is adjusted by the throttle orifices, so that the pressure difference between the outside and the chamber delivers the locally desired amount of mass flow through the surface. Figure 4 shows a schematic image of the skin layout and the HLFC system for a wing section. The applied technology in this project is based on [20,21], which describes numerical approaches with active laminar flow control and also describes current progress in this technology.
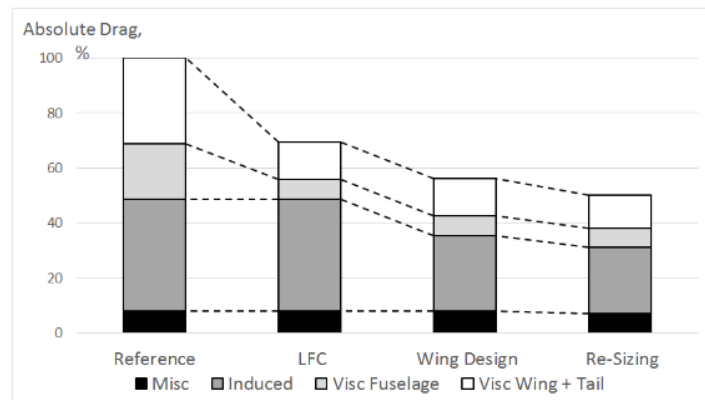
Figure 3. Effect of laminar flow control on overall aircraft drag [20].
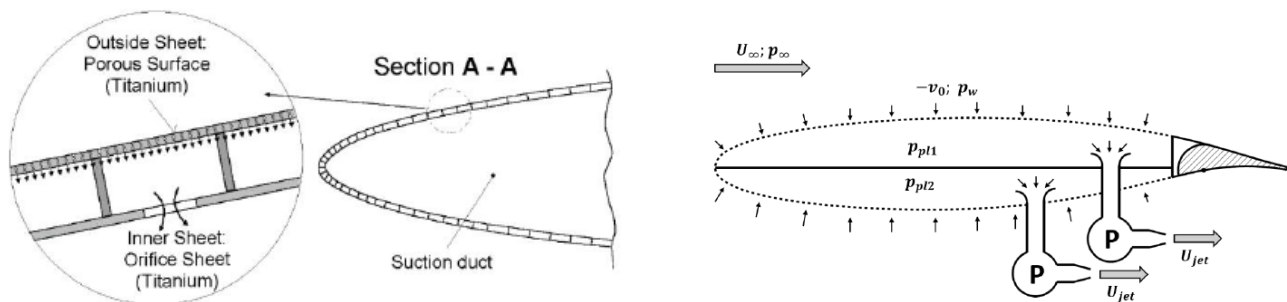
Figure 4. Schematic views of the active suction system [20].

2.2. Load Alleviation

Load alleviation introduces various techniques to reduce the bending moment experienced by the aircraft and that have a passive or active nature. Reduction of maximum bending moment enables the design of lighter wings for lower limit load factors, which will improve aircraft fuel efficiency.

Passive load alleviation solutions consider nonlinear stiffness material design [22], viscoelastic damping design [23], new structural concepts [24,25], and local morphing structures [22]. Nonlinear stiffness materials may improve the load distribution on the wing under low load cases (0.5 g to 1.5 g) and improve performance efficiency at those load cases. Finally, both aeroelastic tailoring and local morphing structures aim to extend the aeroelastic design space. Morphing is considered into two scenarios: deliberate structural non-linearity that affects the wing deformation and reduces effective angle-of-attack of the wing section under the load and change in airfoil shape to achieve load reduction [22].

The wing active load alleviation uses different types of flow control over the wing to achieve a more favorable wing load distribution and reduce the wing bending moment. Previously, researchers have approached the design of active load alleviation systems in different ways. Rossow et al. [26] investigated the feasibility of an aircraft featuring load alleviation technologies; Sun et al. [27] looked at active load alleviation from the

control system perspective; and Zing et al. [28] demonstrated the experimental results of the high aspect-ratio wing wind-tunnel test with active load alleviation while using piezoelectric control. The work of Fezans et al. focused on novel sensors and control systems technologies to enable rapid and robust active load alleviation [29–32]. Finally, active load alleviation could also be reached by fluidic or micro-mechanical flow actuators that change the load distribution along the wing and reduce the bending moment [33].

2.3. New Materials and Structure Concepts

Novel structural concepts and materials are being developed to improve the aircraft structure in terms of stiffness and weight. Bishara et al. [34] describe advanced structural design with the integration of active flow control, which is directly applicable to the presented research. Under the excellence cluster, the reduction in the airframe weight is assumed to be reached by application of CFRP thin ply laminates. In addition, new structural concepts must be applied to satisfy HLFC requirements [22].

2.4. High-Power Superconducting Motors

One of the major problems in hybrid- and all-electric commercial aircraft deals with limitations of maximum available electric motor power. The motor resistance increases rapidly with the increase of its power, which rapidly diminishes the engine efficiency. One solution to preserve the motor efficiency and even increase it is to use superconducting motors. Such motors can be synchronous, trapped flux, and fully superconducting. They may also operate at low and high temperatures. To maintain required temperatures inside the motor, a cryogenic cooling system is required. High-temperature superconducting (HTS) motors can achieve high power-to-weight ratios with high power densities without major weight losses compared to low-temperature superconducting motors. Ref. [35] provides a descriptive survey of HTS motors and their future trends. For the present research, a high-temperature, fully superconducting motor was considered.

2.5. High Energy Capacity Batteries

Currently, the gravimetric energy density of modern batteries generally does not exceed 300 Wh/kg [36]. Such energy densities may be suitable for ultra-light or limited general aviation all-electric aircraft. However, they are insufficient to enable not only all-electric aircraft of the size of ATR-42 and larger, but even the hybrid-electric version of such aircraft is infeasible at the moment since the energy capacities are around 50 times less compared to kerosene-based fuels. On the other hand, the research of high-capacity batteries makes progress. The latest laboratory research demonstrated battery energy capacities of 800 Wh/kg on the cell level and 500 Wh/kg on the pack level for military applications [36]. In addition, the National Academy of Sciences predicts battery pack energy density to achieve 400–600 Wh/kg at Technology Readiness Level (TRL) 6 in the next 20 years (roughly, by 2035) and be commercially available in 30 years [37]. If the prediction becomes real and the linear trend remains, then batteries may reach TRL 6 with energy densities of 550–850 Wh/kg and be commercially available by 2060. To investigate potential scenarios for the far future and examine battery energy impact on the aircraft feasibility, it is assumed that the pack energy densities may range between 500 and 1100 Wh/kg.

3. Implementation of Novel Technologies in Aircraft Analysis and Design

3.1. Initial Aircraft Sizing

The conceptual design was performed using various tools. OpenVSP [38] and CATIA were used for the aircraft geometric modeling, and SUAVE [39] was used for more defined aircraft sizing, performance, and mission analysis. To have more capabilities from the aircraft performance analysis standpoint, SUAVE was extended to have classical performance analysis methods used in [40–43].

The aircraft sizing within SUAVE is performed iteratively. First, initial geometric specifications based on TRLs and any available information are input into the SUAVE.

The information includes the initial wing planform, its section properties, flaps characteristics, empennage and fuselage geometries, the definition of the propulsion system, and all required components such as batteries, gearboxes, power management systems (PMAD), cables, etc. Finally, initial guesses of aircraft weight are input. Then, the first iteration of constraint analysis using equations provided by Gudmundsson [41] is performed. The constraint diagram block includes rapid estimation methods for gas-turbine, piston, and electric aircraft power lapse with altitude and has options to either estimate required aerodynamic properties for the constraint diagram or have them as fixed inputs based on historical trends. Based on the design point selection, the wing loading and power-to-weight ratio are used to run the SUAVE mission analyses to estimate the aircraft performance and its required weight. Then, obtained maximum take-off mass (MTOM) is compared to the initial guess and updated if the tolerance is not reached. In addition, parameters such as the minimum drag coefficient (C_{Dmin}), Oswald efficiency (e), and maximum lift coefficient (C_{Lmax}) for clean and flapped configurations are input into the constraint diagram again to update all constraint curves and run the loop again. When the tolerance is reached, the program moves to the aircraft performance block to obtain performance plots for the given aircraft. Particular care was taken to size the wing flaps to meet take-off and landing field length requirements. Methods of Torenbeek [42] and Roskam [43] were implemented within SUAVE to analyze various types of leading- and trailing-edge devices. The empennage sizing within SUAVE is based on the fixed tail volume ratio and then updated and corrected separately based on the desired CG envelope. Performance analyses within SUAVE included take-off, all engines operative (AEO), and one engine inoperative (OEI) climb, cruise, descent, and landing. Figure 5 shows the sizing process within SUAVE.
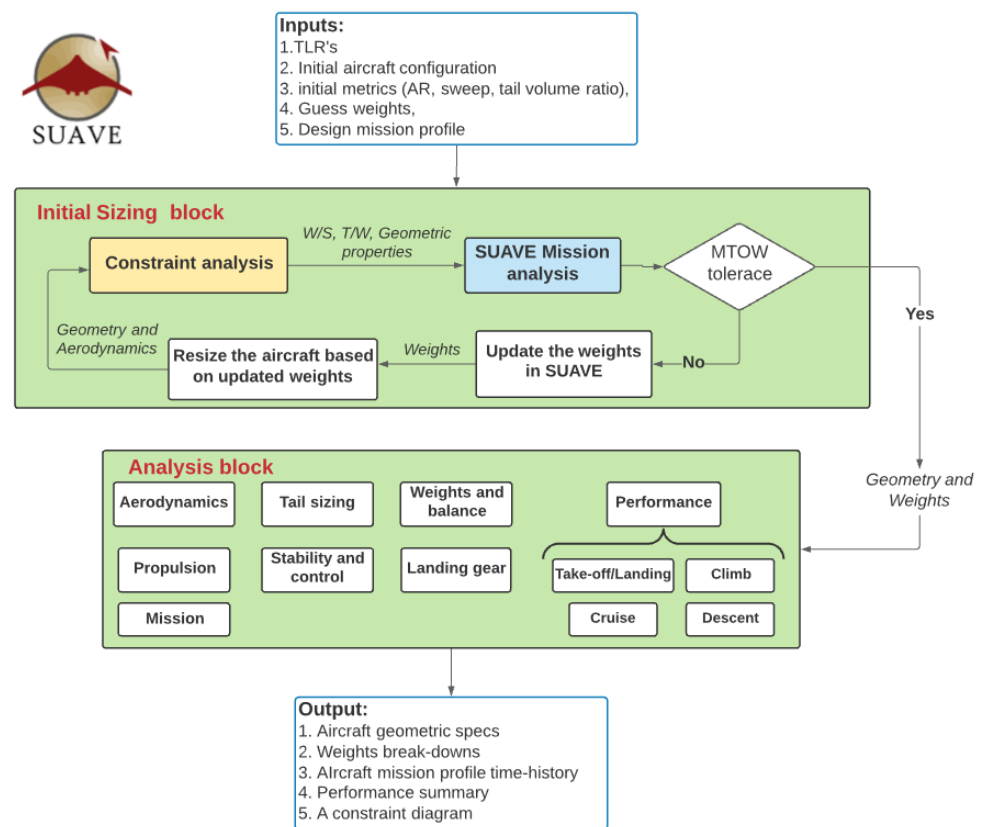
Figure 5. Initial aircraft sizing framework using SUAVE.

3.2. Energy Network

In the SUAVE analysis framework, a propeller electric energy network with HTS motors was implemented. Figure 6 shows the all-electric energy network layout.
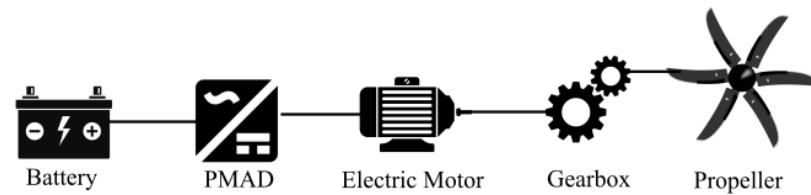
Figure 6. Battery-electric energy network layout.

Propeller modeling was performed using the cubic spline method described by Gudmundsson [41]. Propeller thrust can be described with a cubic spline based on design operating conditions. The thrust is defined by:

$$T = AV^3 + BV^2 + CV + D \tag{1}$$

where A, B, C, D are the coefficients required to fit the curve accurately. To obtain those coefficients, a system of four equations is established. The first equation is the equation for the static thrust. The second equation is derived for the cruise speed and the desired propeller efficiency. The third equation is the derivative of the curve at the cruise speed, which is equal to zero. Finally, the last equation is derived for the desired maximum cruise speed. The final system of equations for the thrust as a function of cruise speed becomes:

$$\begin{bmatrix} 0 & 0 & 0 & 1 \\ V_C^3 & V_C^2 & V_C & 1 \\ 3V_C^2 & 2V_C & 1 & 0 \\ V_{HC}^3 & V_H^2 & V_H & 1 \end{bmatrix} \begin{Bmatrix} A \\ B \\ C \\ D \end{Bmatrix} \begin{Bmatrix} T_{static} \\ T_C \\ -\eta_{prop} P_{sh} / V_C^2 \\ T_H \end{Bmatrix} \tag{2}$$

Solving Equation (2), a general thrust expression is found, which then is used to find the propulsive efficiency of the propeller. Then, knowing efficiencies of components of the energy network shown in Figure 6, the total power at the battery is found to be used during the SUAVE mission analysis.

The propeller was sized using a combination of propeller diameter trends provided by [44] and the sizing method described by Torenbeek [42] where the required propeller RPM depends on the tip Mach number was used to estimate the maximum propeller RPM.

The assumption of the battery gravimetric energy density remains one of the most influential assumptions for aircraft design. Since the availability of a full-electric regional aircraft is challenging to achieve, an optimistic scenario of the energy density at TRL 6 was assumed. This way, if the aircraft is feasible, the task will be to investigate more realistic bounds of minimum energy densities. Otherwise, the availability of the all-electric airplane is highly unlikely. Consequently, the average optimistic pack energy density (ω_B) of 700 Wh/kg was assumed. To ensure safe battery operation, the state-of-charge of 20% was assumed.

High-temperature, fully superconducting motors were used for the airplane since the required power frequently reaches the order of Megawatts. All superconducting components also have cooling systems to enable desired operating temperatures. The cooling system power loss was estimated using the survey provided in [45] and assuming the Carnot efficiency (ϵ) of 30%. Table 1 summarizes all assumptions considered for the gas turbine engine and an electric propulsion network.

Table 1. SE²A SR energy network assumptions.

Component	Parameter	Value	Reference
High-power electric motor	Efficiency	$\eta_M = 99.5\%$	[35]
Motor cryo-cooling system	Power loss	$P_{loss} = 10$ kW	[45]
	Carnot efficiency	$\epsilon = 0.3$	[45]
PMAD	Efficiency	$\eta_{PMAD} = 99\%$	[46]
Battery	Energy density	$\omega_B = 700 \, \dfrac{\text{Wh}}{\text{kg}}$	[35]
Electric cables	Density	$\rho_{cable} = 3.9 \, \dfrac{\text{kg}}{\text{m}}$	[46]
	Efficiency	$\eta_{cable} = 99.5\%$	[46]

3.3. Weights Estimation

Weights estimation analysis was performed using the FLOPS [47] method programmed within SUAVE. To improve the accuracy of high aspect ratio wing weight estimation, FLOPS was coupled with the physics-based wing weight estimation tool EMWET [48]. The EMWET analysis was performed for a metal wing structure and was corrected by a factor based on the composite wing technology level. Loads used for the EMWET weight estimation were obtained within SUAVE using coupling with AVL [49] Vortex-Lattice method software. In the case where the aircraft wing span reaches Class-C airport regulation limits, an additional weight penalty function due to the wing folding was introduced, so the aircraft can maneuver at the airport and maximize its flight efficiency. The estimation method is based on [50] and accounts for the weight of the insert, the folding mechanism, and the pin to fix the wing. The wing weight corrected by the weight of the folding mechanism is defined by

$$m_w^{fold} = m_w^{nonfold}(1 + \bar{m}_{fold}^{ins} + \bar{m}_{fold}^{mech} + \bar{m}_{fold}^{pin}) \tag{3}$$

where $\bar{m}_w^{fold}$ is the mass of the wing with the folding mechanism, $\bar{m}_w^{nonfold}$ is the mass ratio without the folding mechanism, $\bar{m}^{ins}$ is the mass ratio of the folding insert, $\bar{m}_{fold}^{mech}$ is the mass ratio of the folding mechanism inside the insert, and $\bar{m}_{fold}^{pin}$ is the mass ratio of the folding pin. The insert mass ratio was defined based on the curve-fitting of three separate formulations available from [50]: folding at 32%, 48%, and 64% of the span

$$\bar{m}_{fold}^{ins} = \begin{cases} 0.24(\bar{m}_{PWS} - 0.924)^2 - 0.007, & 32\% \text{ span} \\ 0.45(\bar{m}_{PWS} - 0.916)^2 - 0.02, & 48\% \text{ span} \\ 0.84(\bar{m}_{PWS} - 0.98)^2 - 0.107, & 64\% \text{ span} \end{cases} \tag{4}$$

where $\bar{m}_{PWS}$ is the mass ratio of the section outboard of the folding pivot point defined by

$$\bar{m}_{PWS}(y) = \frac{(C_y + C_t)(0.5b - y)(t_y C_y + t_t C_t)}{(C_r + C_t)(t_r C_r + t_t C_t)b} \tag{5}$$

where C is the chord length, b is the wing span, t is the wing thickness-to-chord ratio, and y is the spanwise location of the folding insert. Subscripts r, t, and y correspond to the wing root, tip, and the folding insert.

Finally, folding mechanism and pin masses are defined by

$$\bar{m}_{fold}^{mech} = -3.76(\bar{m}_{PWS} - 0.2)^2 + 0.08 \tag{6}$$

$$\bar{m}_{pin}^{mech} = -0.6(\bar{m}_{PWS} - 0.2)^2 + 0.02 \tag{7}$$

Figure 7 shows the wing weight penalty as a function of the wing joint location along the semi-span.
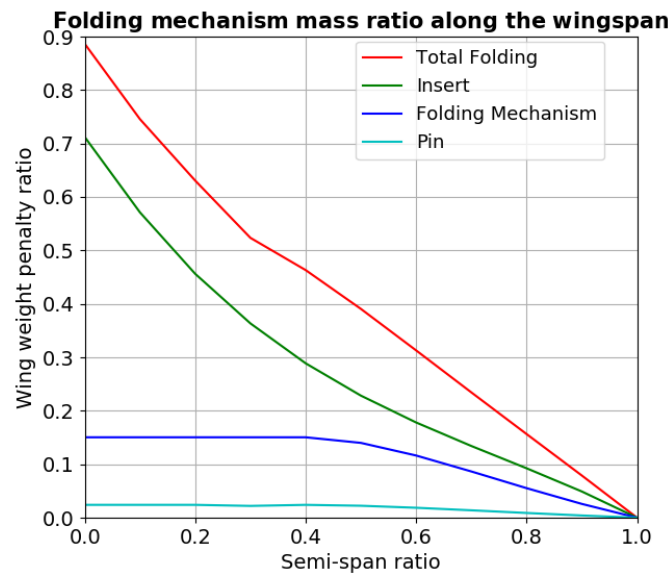
Figure 7. Wing folding penalty as a function of the wing semi-span [50].

HTS motor weight estimation was based on relations defined by Stuckl [35] and account for both the motor and the cooling system weight. The motor power-to-weight ratio is defined by

$$\frac{P}{W} = 2.63(P_{Mot})^{0.277} \qquad (8)$$

where P_{Mot} is the motor power in kW and the power-to-weight ratio P/W is defined in kW/kg.

The cryogenic cooling system weight is defined by

$$m_{cooling} = 27.5 P_{loss} \cdot e^{-1.225(\log_{10}(P_{loss}))} \qquad (9)$$

where P_{loss} is the cooling system input power loss in kW and $m_{cooling}$ is the cooling system weight in kg.

Propeller weight was estimated using a relation described in [51] where the propeller weight depends on the number of blades, the activity factor, the motor power, propeller maximum RPM, and its material. A composite propeller with six blades was considered for the present design.

The gearbox weight was estimated using relations provided by [52] and is defined by

$$m_{gearbox} = K \frac{P_{gearbox}^{0.76} \cdot RPM_{motor}^{0.13}}{RPM_{propeller}^{0.89}} \qquad (10)$$

where P is the power at the gearbox, K is the gearbox technology factor equal to 26 for future gearboxes, RPM_{motor} is the motor power assumed at 4800 RPM, the RPM_{motor}, and the $m_{gearbox}$ is the gearbox mass in kg.

3.4. Novel Airframe Technologies Assumptions

At the conceptual design stage, novel technologies have been integrated into the design process in terms of coefficients and correction factors. Laminar flow control is estimated by modifying the flow transition location along the wing profile. The desired goal within the SE^{2}A for the flow transition is set to 70% for the wing if no disturbances such as the propeller wake or the location of other components is present. Otherwise, specific transition assumptions are prescribed. Wing folding also affects the application of the HLFC. The folding location has four general locations. If the wingspan is less than 36 m (Class C airport limitation), then no folding is applied, and the wing features the

HLFC along the complete span. If the wingspan is longer than 36 m but not longer than 110% of the Part C requirement, then the tip folding is applied, the wing has HLFC until the wing folding location, and the folding tips feature natural laminar flow (NLF). If the folding location occurs at any position which splits the aileron, then the folding position is automatically moved to the position where the flap ends and the aileron start, so the aileron design is significantly simplified. The portion of the wing after the folding joint does not feature HLFC and only has NLF. Finally, if the wingspan is such that the aileron can be located at the folding portion of the wing, the folding joint is fixed to 18 m, and the flap is limited to the outboard position of 18 m. HLFC is also applied before the folding joint. The transition location of the NLF portion of the wing is assumed at 45% [53]. The fuselage laminar flow shall be preserved until the wing-body fairing, which is specified based on the wing position, which is determined by the center-of-gravity (CG) envelope and the empennage characteristics. The active load alleviation effect is estimated by reducing the aircraft limit load factor from the required 2.5 [54] to 2.0. For the load alleviation, it is also assumed that regulations of CS-25 may allow lower limit loads if sufficient maturity of the technology is reached. Advanced structure configurations and material effects are assumed to reduce the empty weight by 19% compared to the metal structure.

4. Top-Level Requirements of the SE^{2}A SR Aircraft

Top-level requirements have been set to match the reference ATR-72 aircraft. Table 2 shows the summary of the SE^{2}A SR TLRs.

Table 2. SE^{2}A SR top-level requirements.

Requirement	Value	Units
Design range for maximum payload	926	km
Maximum payload	7500	kg
Cruise Mach number	0.42	
Service ceiling	7620	m
Take-off field length	1400	m
Landing distance	1100	m
Certification	CS-25 [54]	

Figure 8 shows a mission profile considered for the design. The mission includes the main flight segment, where the airplane cruises at 7300 m, and the required reserve segment which consists of the divert segment and the 30 min hold. In addition, 5% battery energy contingency was assumed after the reserve mission.
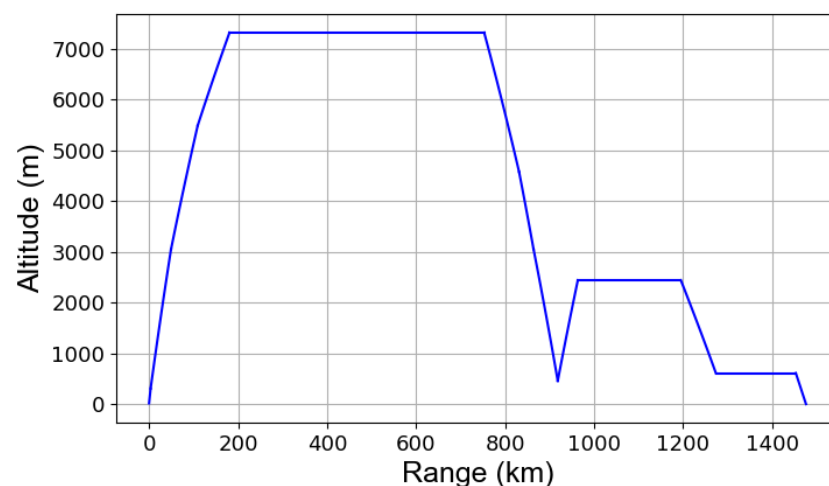

Figure 8. SE^{2}A SR mission profile.

5. Initial Aircraft Design

Concept Selection

In this work, two concepts were considered for the initial aircraft design. The first concept was the top-wing conventional configuration with wing-mounted engines. The battery was split between the fuselage belly and the engine pylons: one segment was located before the landing gear, and the other one was located after the gear. The battery distribution was based on the CG envelope to satisfy all possible passenger loading cases. Battery modules feature a 'quick-swap mechanism, so a mechanic can switch batteries between the flights using a mechanism similar to a high loader. The second configuration is the low-wing configuration with aft-mounted engines. Such configuration, unlike the first configuration, has a fully clear wing which enables laminar flow control along the entire wingspan. Engines are mounted at the aft of the fuselage. The vertical location of the engines approached their maximum to minimize the adverse effect from the wing at high angles of attack. Batteries also feature the 'quick-swap mechanism. Figure 9 shows the described configurations schematically modeled in OpenVSP.
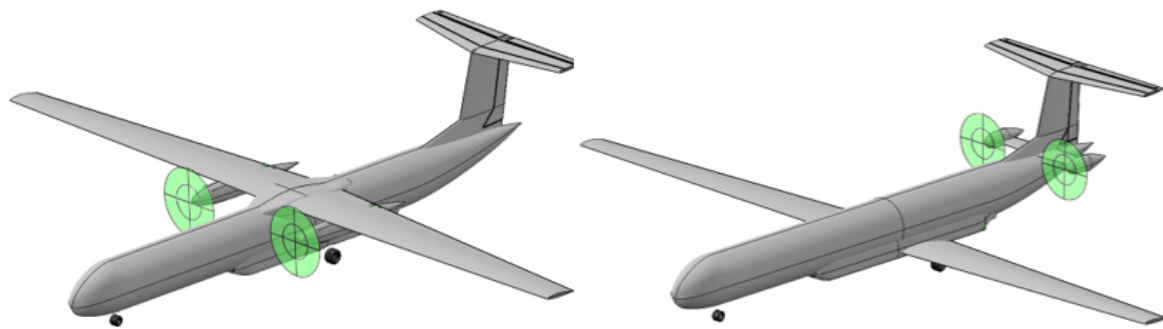
Figure 9. OpenVSP models of two configurations for the selection.

Each configuration has its assumptions, features, and limitations. Assumptions are based on research goals of the SE^{2}A research groups that focus on the research and development of each technology separately. The first concept has a limited range of laminar flow along the wingspan. The region which is subjected to the propeller wash is assumed to have a fully turbulent flow. The remaining wing portion has 70% laminar flow due to the application of the HLFC. To have a favorable CG envelope, the location of the wing was set to 43% of the fuselage length. The second concept has limited laminar flow control before the landing gear at the wing pressure side. The remaining pressure side and the suction side are 70% laminar. It was also possible to shift the wing further aft to 53% of the fuselage length so that extra 10% could be laminarized compared to the conventional configuration.

Comparison among the concepts was performed using the sizing methodology as was described in Section 2. Due to the presence of various novel technologies and, as a consequence, increased aircraft development, and operating costs, the concept selection was based on the magnitude of Direct Operating Costs (DOC). DOC was calculated using the method presented in [55] where the DOC is divided into energy, maintenance, capital, crew costs, and fees. 2121 flight cycles per year were assumed for both aircraft. For the battery pack, 2000 cycles were assumed. The electricity price was taken from [56] for the year 2050 and is equal to 0.118 EUR/kWh that year. The airframe price was assumed similar to the ATR-72 [55] and is equal to 1595 EUR/kg. The remaining parameters for all required cost components were taken from [55]. A major concern is related to the modification of DOC due to novel technologies. It is unknown how much the DOC will increase due to an early stage of all technologies presented in this work. However, the complexity related to the introduction of the porous skin, the suction system and its structure, which is subject to maintenance complexities, NLF front portion, integration of various load alleviation technologies, and the structure to support the wing laminarization and load alleviation

will increase maintenance costs by an order of magnitude. As an optimistic assumption, a scaling factor of 2 was used for the maintenance DOC gain. After the introduction of the maintenance DOC gain, the total DOC formulation becomes

$$DOC_{Total} = DOC_{Energy} + DOC_{Crew} + k_g DOC_{Ma} + DOC_{Cap} + DOC_{Fees} \qquad (11)$$

where DOC_{Energy} are costs of energy, DOC_{Crew} are crew costs, DOC_{Ma} are maintenance costs, DOC_{Cap} are capital costs, DOC_{Fees} are costs of fees, and k_g is the maintenance cost gain factor. Finally, all costs were calculated in 2020 EUR.

　　　Due to the presence of an all-electric propulsion system, a conventional assumption of the best design point at the lowest power-to-weight ratio may not hold, as was previously shown by Finger [5] where the best design points were sensitive to the energy type of networks and could show points of minimum take-off or fuel weight at wing loadings larger than the one with minimum power-to-weight ratio. To ensure that a good initial guess for each concept is selected, an aspect ratio and wing loading trade study were performed using the initial sizing procedure described in Section 3. The procedure has multiple steps. First, the initial aircraft sizing is performed to find the design point corresponding to the maximum possible wing loading. Assuming that the selection of an arbitrary design point will not change the constraint diagram significantly, a set of sample wing loadings ranging from 60% of the maximum wing loading to the maximum possible wing loading were selected. Figure 10 shows the sweep of possible design points along the constraint diagram boundary. The aircraft is then sized for each selected wing loading using SUAVE, and the DOC is estimated. This approach is repeated for a selected set of aspect ratios to determine the combination of the wing loading and aspect ratio that may give the lowest desired aircraft characteristics important for the decision making. A sample set of weights and DOC for a low-wing configuration as a function of the wing loading and the AR is shown in Figure 11. Multiple trends can be observed from the Figure 11. First of all, the battery weight generally reduces with the AR, while the operating empty weight (OEW) and maximum take-off mass (MTOM) trends do not follow such trends. Moreover, DOC and weights show discontinuities for some aspect ratios and particular wing loadings. Points of the curve discontinuity correspond to the folding penalty, which is introduced starting from a specific wing loading.
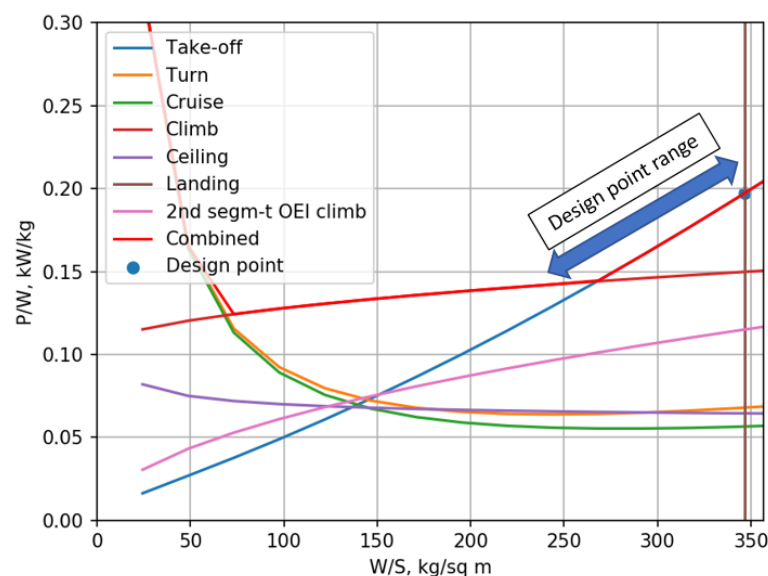
Figure 10. A sample constraint diagram and the range of possible design point or the initial sizing.

Table 3 shows the summary of the high-wing and the low-wing configurations that have the lowest DOC. Based on the given results, the high-wing configuration has larger weights due to more battery required to complete the mission with less laminar flow.

Consequently, the airframe with less possible drag is more favorable. Consequently, the low-wing configuration is more efficient from the performance standpoint.

Table 3. Comparison between the high-wing and low-wing concepts.

Parameter	High wing	Low wing	Units
MTOM (W_0)	38,238	35,369	kg
OEW (W_e)	30,738	27,869	kg
Battery weight (W_b)	14,629	12,783	kg
AR	11.0	11.0	-
Wing span (b)	40.2	38.7	m
taper ratio (λ)	0.5	0.5	-
Wing area (S_w)	147.0	136.0	m^2
Power-to-weight ratio (P/W)	0.144	0.146	kW/kg
DOC	10,074	9603	EUR/flight
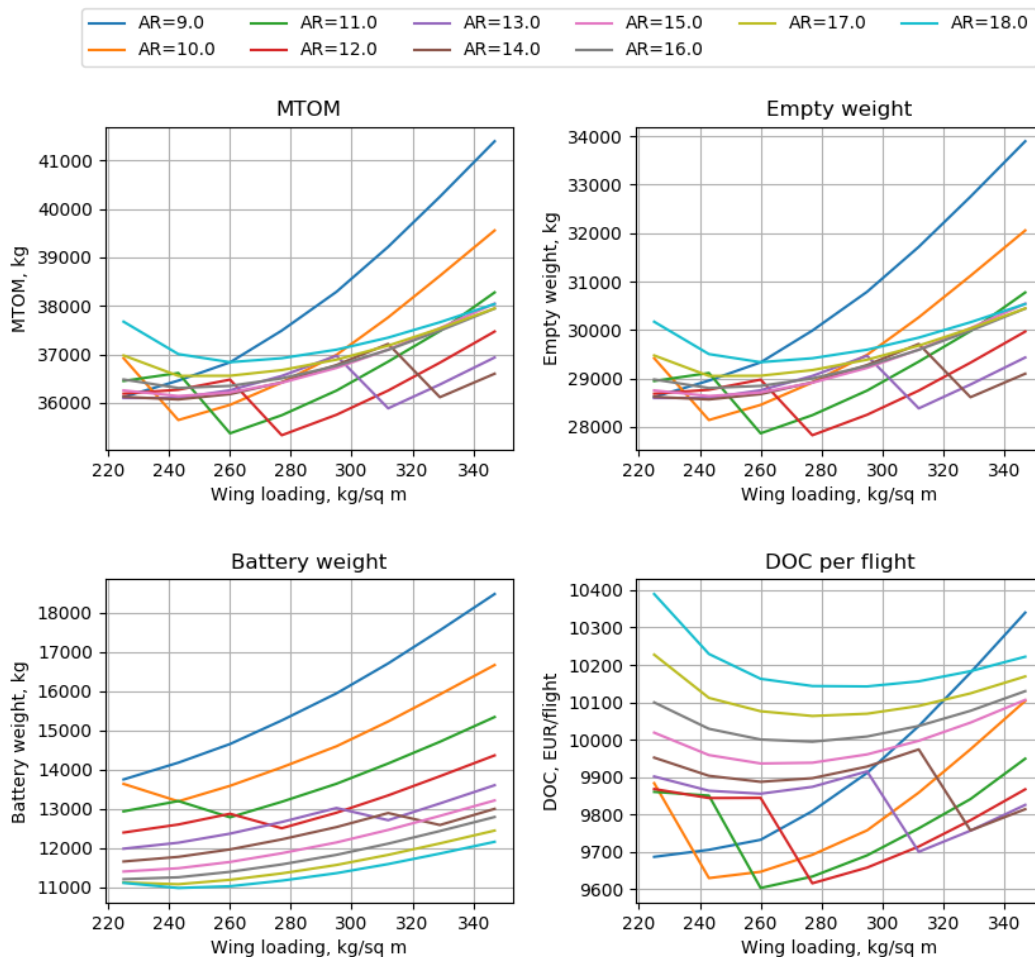
Figure 11. Sensitivity of weights and DOC to the aircraft AR and wing loading for the low-wing configuration (pack energy density of 700 Wh/kg).

Due to an unconventional configuration of the low-wing configuration, a concern related to the aircraft stability and control may occur. Coe [57] has investigated the stability and control characteristics of an aircraft with aft-mounted propeller engines. Results demonstrated a reduction of longitudinal stability for this configuration due to the propeller–pylon interaction. However, minor destabilization can be compensated by a

minor increase of the horizontal tail. Lateral stability is not significantly affected by aft-mounted propellers and may improve directional control due to the boundary layer control introduced by the propeller slipstream. Riley [58] also provided a detailed description of business/commuter turboprop aircraft configuration with aft engines. Although the configuration is a twin-pusher, general information about handling qualities during the approach can be extracted. Generally, the aircraft can have acceptable handling qualities and can be certified, but more care to achieve proper dynamic stability and desired handling characteristics may be required.

6. SE^{2}A SR Design Refinement Using MDO

To refine the initial design, a set of multi-disciplinary design optimizations (MDO) were performed. The main goal of the refinement is to reduce the aircraft DOC further. Multiple cases were considered. The first MDO featured all prescribed assumptions. The second MDO assumed that no folding penalty is present to estimate the influence of the folding penalty of the aircraft. This case is used only as a comparative study to investigate the folding mechanism effect on the optimal design. Finally, a special case of battery weight minimization was calculated to investigate the reduction of the battery weight and increase of DOC with respect to the aircraft optimized for the DOC. This case also directly influences the aircraft CO_2 emission.

Production of electricity also involves emission CO_2 and other greenhouse gases, since modern electricity generation is not a product of renewable energy sources. A major portion of electricity today comes from fossil fuels, consequently, an all-electric aircraft cannot be considered as a zero-emission one. Since the goal of the study was to design and assess the aircraft from the environmental perspective as well as performance and costs, proper metrics of preliminary emission rates must be introduced. Scholz describes a rapid and useful procedure of comparing kerosene-based and battery-electric emission [59,60] to calculate the CO_2 emission including additional factors for each energy source. For aircraft operating with kerosine-based fuels, additional chemicals other than CO_2 contribute to the emission level. In addition, the altitude at which the emission happens plays an important role. To account for secondary effects, the equivalent CO_2 emission level per flight can be described by

$$m_{CO2,eq} = (EI_{CO2}f_{km} + EI_{NOx}f_{km}CF_{midpoint,NOx} + CF_{midpoint,AIC})R_{km} \qquad (12)$$

where f_{km} is the fuel flow per km, EI is the emission index for each species, CF is the characterization factor, and R_{km} is the range in km. The EI_{CO2} is equal to 3.16 kg CO_2 per kg fuel [60]. The EI_{NOx} is found using the Boeing Method 2 [61] where the index is computed based on existing data from the ICAO Engine Emissions Databank [62] and is corrected with respect to the flight altitude. Characterization factors are calculated by

$$CF_{midpoint,NOx} = \frac{SGTP_{O3s,100}}{SGTP_{CO2,100}}s_{O3s} + \frac{SGTP_{O3L,100}}{SGTP_{CO2,100}}s_{O3L} + \frac{SGTP_{CH4,100}}{SGTP_{CO2,100}}s_{CH4} \qquad (13)$$

$$CF_{midpoint,AIC} = \frac{SGTP_{contrails,100}}{SGTP_{CO2,100}}s_{contrails} + \frac{SGTP_{cirrus,100}}{SGTP_{CO2,100}}s_{cirrus} \qquad (14)$$

where $SGTP$ is the sustained global temperature potential, summarized in Table 4 and s is the forcing factor which depends on the altitude and is shown in Figure 12 for each species.

The formulation given in Equation (12) was used for each flight segment of the reference ATR-72 and then added to obtain the total mission equivalent emission level. Segments with variable altitude such as climb and descent used average values of forcing factors s and emission index EI_{NOx}. If the value of the forcing factor was for the altitude lower than the available data, the minimum value represented in the Figure 12 was used.

Table 4. SGTP values [60].

Species	$SGTP_{i,100}$	Units
CO_2	3.58×10^{-14}	K/kg_{CO_2}
O_{3s}	7.79×10^{-12}	K/kg_{NO_x}
O_{3L}	-9.14×10^{-13}	K/kg_{NO_x}
CH_4	-3.90×10^{-12}	K/kg_{NO_x}
Contrails	1.37×10^{-13}	K/km
Cirrus	4.12×10^{-13}	K/km
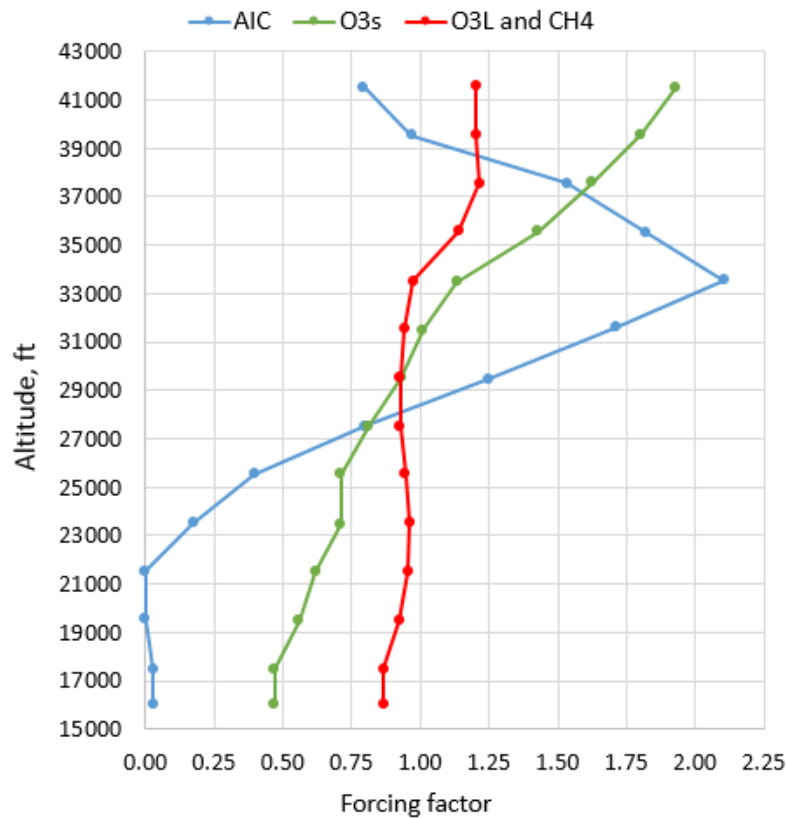
Figure 12. Forcing factor as a function of altitude [60].

Battery emission, on the other hand, depends on the amount of energy used to charge them. The emission then depends on the share of fossil fuel to non-fossil fuel sources participating in the electricity production and the primary efficiency factor—the factor which describes the ratio between the energy required to produce electricity and the final output energy amount. Including all factors described above, the equivalent emission per flight becomes

$$m_{CO2,eq} = EI_{CO2} x_{ff} \frac{k_{PEF} m_{bat} C_{bat}}{\eta_{charge} C_{Jet-A}} \tag{15}$$

where x_{ff} is the fossil fuel share ratio equal to 0.39 according to the forecast of 2050 [63], k_{PEF} is the primary efficiency factor assumed equal to 2 [59], η_{charge} is the battery charging efficiency equal to 0.9 [59], and C_{bat} and C_{Jet-A} are battery and Jet-A fuel energy densities, respectively. From Equation (15), the CO_2 emission is directly proportional to the battery mass, so the optimization for the minimum battery weight corresponds to the minimum emission case.

All problems have similar design variables and constraints, as shown in Table 5. Due to the application of new airframe technologies, requirements for the sea-level climb, take-off, and landing are more significant compared to cruise and OEI requirements, as

shown in Figure 10. Such behavior occurs due to a substantial reduction of the cruise drag, which strongly diminishes the required cruise power. Consequently, optimization problem constraints can be limited to these three main performance metrics. Additional geometric constraints of 51.8 m wingspan (similar to the wingspan of the NASA N+3 strut-braced wing concept [64]) and the wingtip of no larger than 1.4 m were introduced to limit further increase in the wing slenderness. Table 5 describes the formulation of the optimization problem. There, C_r and C_t are the wing root and tip chords, respectively, t/c is the wing thickness, and η_{max} is the maximum throttle during the flight. To perform the MDO, SUAVE was coupled with MATLAB, and the Genetic algorithm was used to find optimal solutions.

Table 5. SE^{2}A SR aircraft optimization problem definition.

		Lower	**Upper**	**Units**
minimize	1. *DOC*			
	2. W_b			
wrt	AR	8.00	16.00	
	λ	0.25	0.75	
	C_r	3.00	7.00	m
	$t/c\vert_{root}$	12.00	18.00	%
	$t/c\vert_{tip}$	12.00	18.00	%
	P/W	0.05	0.30	
subject to	Take-off field length (TOFL)		1400.0	m
	$P/W - P/W\vert_{climb}$	0.0		
	Landing field length (LFL)		1100.0	m
	η_{max}		1.0	
	b		50.0	m
	C_t		1.4	m

To account for the constraints, the penalty function similar to the one defined in [65] was used. The penalty function is defined by

$$f_p = \mu(y - y_c)\left(\frac{y}{y_c}\right)^{\gamma} \tag{16}$$

where y is the design variable, y_c is the design variable constraint, μ is the unit step function equal to zero for $y \leq y_c$, and $\gamma = 3$. With the introduction of the penalty function, the objective function becomes

$$f = f + \sum_{i=1}^{N} f_p \tag{17}$$

where N is the total number of design variables. Sixty species per generation were set to have sufficient population size without major accuracy losses. Take-off and landing constraints were calculated using physics-based time-dependent performance formulations presented in [41]. The climb power-to-weight ratio constraint was calculated using a similar formulation used for the constraint analysis.

Figure 13 shows the aircraft planforms for each optimization problem and Table 6 summarizes important properties of each optimized configuration. Limiting constraints for each optimization were similar to the constraint diagram: the solution was trying to minimize the power-to-weight ratio which reached the constraint limit of either the climb or the take-off. In addition, the top-of-climb throttle constraint was an additional constraint which dominated the others.
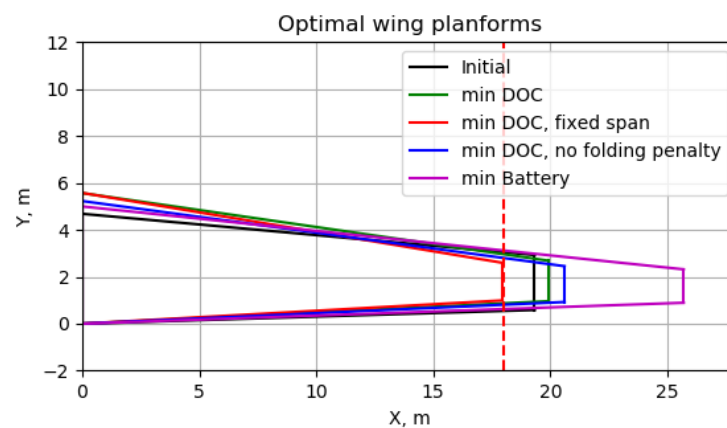
Figure 13. Wing planforms for selected optimization problems.

Table 6. Comparison between optimized concepts.

Parameter	Initial Design	DOC-Optimal Design	DOC-Optimal Design (No Folding)	Battery-Optimal Design	ATR-72	Units
W_0	35,369	34,441	33,649	34,783	23,000	kg
W_e	27,869	26,941	26,149	27,283	13,311	kg
W_b	12,783	12,262	11,527	10,379	-	kg
$W_{fuel,mission}$	-	-	-	-	1913	kg
AR	11.0	10.86	12.23	16.0	12.0	-
b	38.7	39.6	41.3	51.7	27.05	m
λ	0.5	0.31	0.3	0.285	0.55	-
C_r	4.68	5.83	5.23	5.00	2.74	m
S_{wing}	136.0	145.4	139.6	165.5	61.0	m²
$t/c|_{root}$	0.18	0.18	0.18	0.17	0.18	-
$t/c|_{tip}$	0.13	0.13	0.13	0.12	0.13	-
P/W	0.143	0.125	0.13	0.11	0.16	kW/kg
DOC	9603	9479	9397	9838	6740	EUR/flight
m_{CO_2}	2045	1961	1844	1660	11,838	kg
TOFL	1338	1381	1368	1360	1367	m
LFL	1025	972	985	934	1207	m

As shown in Table 6, the optimized aircraft with all imposed assumptions reduced all weights, slightly reduced the aspect ratio, increased the wingspan, reduced the taper ratio, and reduced the aircraft power-to-weight ratio. Minor differences in the field performance occurred. The DOC for the optimized aircraft reduced by 124 EUR/flight. In addition, the difference in emission between the initial and DOC-optimized designs is equal to 84 kg per flight which is not substantial. If the folding penalty is removed, then the wing has more freedom to increase its span and aspect ratio due to the absence of the folding weight penalty. The optimized aspect ratio increased by 1.23, the wingspan increased by 2.6 m compared to the initial design. However, the power-to-weight ratio increased due to a reduced wing planform area. All weights were further reduced compared to the aircraft configuration with the folding mechanism. The DOC was reduced by 206 EUR/flight compared to the initial configuration, which indicates a relatively strong effect of the folding mechanism on the aircraft. The emission level reduced by 201 kg compared to the initial design which is more substantial. Comparing the DOC optimal solutions with and without the folding mechanism, it becomes evident that wing folding affects the final design and cannot be neglected. If the battery minimization strategy is considered, then the wing planform approaches design limits. Due to a stronger reduction of the battery

weight compared to the increase in the wing weight, minor reductions of the MTOM and empty weights are observed. Finally, DOC increased by 235 EUR/flight compared to the initial design or by 359 EUR/flight compared to the optimized configuration. The battery weight reduced by 2404 kg and 1883 kg compared to the initial and DOC-optimized aircraft, respectively. The emission level, however, reduced by 385 kg compared to the initial configuration. In addition, the wing span of the aircraft increases to 51.7 m and the folding portion from each side of the wing becomes 7.85 m. Such a large folding portion may affect the operational convenience at the airport and will make the aircraft taller when the wings are folded. That may create additional difficulties related to the aircraft storage.

If DOC and emission levels are compared against the reference aircraft, the increase in DOC demonstrates a substantial increase compared to the reference ATR-72. The most cost-effective aircraft version has 41% increase in DOC which is a substantial cost growth from the market standpoint. The DOC for the battery-optimal configuration increases by 46%. On the other hand, if emission levels are compared, the most DOC-efficient version has a reduction in equivalent CO_2 emission of 83% compared to the ATR-72, and the battery-optimal configuration has 86% emission reduction. From the comparison, the emission level of the all-electric aircraft reduces substantially, but such reduction of the emission comes at a significant cost increase. Moreover, DOC shows more sensitivity with respect to the configuration compared to the emission level. To minimize costs as much as possible, the DOC-optimal configuration was selected for future analyses.

Observing the wingspan deviations from the Part C airport requirements of 36 m, aircraft configurations minimized for DOC did not show major increases in wingspans. Consequently, it is possible to design an aircraft that will have no folding mechanism and will not have a significant DOC penalty so that the wing design complexity may be reduced substantially. An additional MDO study with a fixed wingspan constraint was performed to investigate the sensitivity of DOC to the configuration with a fixed span of 36 m. Table 7 demonstrates a comparison between the initial design, the optimal design without the span constraint, the optimal aircraft with a constrained span, and a reference ATR-72 to compare optimal models to their reference.

Table 7. Comparison between optimized concepts with and without the wing span constraint.

Parameter	Initial Design	DOC-Optimal Design	DOC-Optimal Design (Fixed Span)	ATR-72	Units
W_0	35,369	34,441	35,745	23,000	kg
W_e	27,869	26,941	28,244	13,311	kg
W_b	12,783	12,262	13,861	-	kg
$W_{fuel,mission}$	-	-	-	1913	kg
AR	11.0	10.86	10.0	12.0	-
b	38.7	39.6	36.0	27.05	m
λ	0.5	0.31	0.29	0.55	-
C_r	4.68	5.83	5.57	2.74	m
S_{wing}	136.0	145.4	129.3	61.0	m^2
$t/c|_{root}$	0.18	0.18	0.18	0.18	-
$t/c|_{tip}$	0.13	0.13	0.12	0.13	-
P/W	0.143	0.125	0.14	0.16	kW/kg
DOC	9603	9479	9573	6740	EUR/flight
m_{CO_2}	2045	1961	2217	11,838	kg
TOFL	1338	1381	1392	1367	m
LFL	1025	972	1027	1207	m

The aircraft with a fixed span has a higher weight due to a restricted planform and, as a consequence, more battery is required for the mission. The battery weight increased by 1600 kg compared to the optimal design without the span constraint. The power-to-weight

ratio also increased to satisfy the take-off requirement. However, the wing area is reduced, so it is less expensive to increase the motor power than increase the wing area. The DOC increased by 94 EUR/flight, which is not a large increase. At the same time, the wing has no folding mechanism and is easier to design and maintain. However, the emission level increases by a relatively small margin compared to the initial DOC-optimal configuration. At this moment, the configuration without folding is selected as the final decision.

The geometric summary of the selected aircraft is shown in Table 8. Single-slotted Fowler flaps were used for this aircraft. The empennage was initially sized within SUAVE using a constant tail volume fraction similar to existing aircraft in the class using data from Raymer [40] and then refined using AVL to ensure sufficient stability and trim during critical flight cases for the complete CG envelope obtained separately. The vertical tail was sized based both on the one-engine inoperative (OEI) case and the lateral stability condition of $C_{N_\beta} > 0.01573$ [66]. The propeller was positioned vertically as far as possible to reduce the possibility of the wing wake impinging on the propeller blades. The angle between the wing trailing edge and the propeller's lowest blade tip is equal to 14 deg, which should be sufficient for the majority of operational cases. The propeller features six blades and has a diameter of 3.56 m.

Table 8. Geometric properties of the SE^{2}A SR aircraft.

Parameter	Wing	Horizontal Tail	Vertical Tail	Units
AR	10.0	5.07	1.25	-
b	36.0	10.0	3.5	m
λ	0.29	0.55	0.8	-
$\Lambda_{C/4}$	0.0	15.0	26.0	deg
Γ	4.0	0.0	0.0	deg
C_r	5.58	2.5	3.13	m
$S_{planform}$	129.3	17.8	9.80	m^2
$t/c\|_{root}$	0.18	0.10	0.10	-
$t/c\|_{tip}$	0.12	0.10	0.10	-
Flap span ratio	0.6	-	-	-
Flap chord ratio	0.2	-	-	-
Aileron span ratio	0.25	-	-	-
Aileron chord ratio	0.20	-	-	-
Elevator span ratio	-	1.0	-	-
Elevator chord ratio	-	0.25	-	-
Rudder span ratio	-	1.0	0.8	-
Rudder chord ratio	-	0.25	0.25	-
V_{HT}	-	0.59	-	-
V_{VT}	-	-	0.024	-

The CG envelope was created using available information about the stick-fixed and stick-free neutral points, payload clouds, and multiple baggage arrangement cases. The CG-range is equal to 21.5% mean aerodynamic chord (MAC) starting at 12% and ending at 33.5% MAC.

Figure 14 shows the SE^{2}A SR payload-range diagram compared to the reference ATR-72 [67]. In addition, the obtained payload-range diagram was validated using a Breguet range equation for an all-electric aircraft defined by

$$R = \frac{1}{g}\eta_{total}C_{bat}\frac{L}{D}\frac{m_{bat}}{m_0} \tag{18}$$

where m_0 is the maximum take-off mass, g is the gravitational acceleration, and L/D is the cruise lift-to-drag ratio.
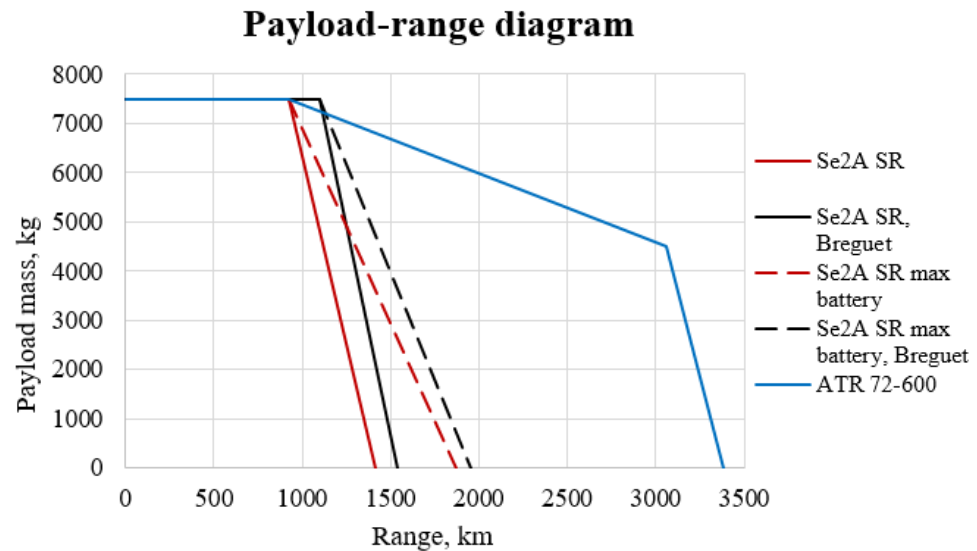
Figure 14. Payload-range diagrams for the SE^{2}A SR and ATR-72.

For the range analysis, multiple options were considered. The first option is the case when the battery mass remains constant, independent of changes in payload weight. This way, the battery volume is fixed and equal to the one used for the maximum passenger case. The second option is to have sufficient battery volume to replace missing passengers with an extra battery. Such an option is more problematic to achieve due to the increased battery size and additional growth of the already large belly fairing but is useful to analyze for the range sensitivity analysis. The comparison shows that although the SE^{2}A SR satisfies the harmonic range requirement, which matches the ATR-72, the ferry range is significantly limited due to the battery energy density and weight limitations. The absence of the payload extends the aircraft range to 1415 km, which is substantially smaller than the ATR-72 with its ferry range of 3380 km. Introduction of more battery which replaces the payload increases the ferry range until 1870 km, which is 455 km longer than the fixed battery weight case. However, this ferry range still does not introduce major range improvements compared to the ATR-72. Comparison between the SUAVE payload-range and Breguet payload-range diagrams show a difference of both harmonic and ferry ranges of 100 km. Such tendency happens due to the higher fidelity of SUAVE which includes all mission segments and calculates incremental energy consumption and aerodynamic characteristics, unlike the Breguet equation which considers a constant lift-to-drag ratio. On the other hand, minor deviations are expected and are satisfactory for the selected analysis.

To summarize current design outcomes, an all-electric SE^{2}A SR aircraft is capable of achieving the harmonic range similar to the reference ATR-72 and satisfies all prescribed TLRs. Moreover, its emission level is reduced by 81% compared to the reference aircraft. On the other hand, the ferry range of the all-electric aircraft is limited to no more than 1870 km compared to 3380 km for the ATR-72 and has a 42% increase in DOC with respect to the reference which will create substantial market application problems for this type of airplane.

Figure 15 shows a rendered image of the optimized SE^{2}A SR aircraft.

Figure 15. SE^{2}A SR aircraft geometry.

7. Sensitivity Analysis of the Aircraft Characteristics to Technology Advancements

After performing a conceptual design of a regional all-electric aircraft and analyzing obtained results, several questions still remain: What is the influence of novel technologies on the aircraft configuration? How much do the deviations of novel technology assumptions affect the airplane configuration? What technologies affect the aircraft geometry the most?

A sensitivity analysis of the SE^{2}A SR aircraft to the battery energy density with the absence of all novel airframe technologies was performed to determine what potential energy density could make all-electric regional aviation possible and how the aircraft characteristics are affected. The aircraft without novel airframe technologies assumed 5% laminar flow on the wing and empennage, 5% laminar flow for the fuselage, a limit load factor of 2.5, and no weight reduction due to composite materials. Technologies related to the propulsion system such as HTS motors remained since their absence immediately leads to the aircraft's infeasibility due to the Megawatt-level power required per motor. Furthermore, the performance characteristics of the aircraft without novel technologies were compared against the case if all technologies met the desired requirements. The sizing procedure for all configurations was performed for a similar mission profile and used similar methods to those described in Section 3 to ensure the satisfaction of all TLRs. Similar constraints based on TLRs were also implemented. As for the initial sizing, wing loading and aspect ratio sensitivity analyses were performed to determine a sweep of all possible aircraft that satisfy TLRs. For all possible configurations, the ones with minimum DOC were selected for each selected battery energy density. Finally, all characteristics were compared against the reference ATR-72 aircraft. Figure 16 shows the effect of battery energy density on the aircraft gross weight.

Results demonstrate that the absence of novel technologies significantly limits the feasibility of all-electric regional aviation unless substantially higher battery cell energy densities are reached. For instance, if the aircraft with all available airframe technologies can reach the MTOM of 40,000 kg at the pack energy density of 600 Wh/kg, the aircraft without airframe technologies can reach similar weights at 900 Wh/kg. In addition, weights approach an asymptotic value at high energy densities, so the effect of airframe technologies becomes more significant for high energy densities. For instance, if the pack energy density reaches 1000 Wh/kg, then the aircraft MTOW with all technologies becomes slightly less than 30,000 kg while similar weight is achieved by the aircraft without airframe technologies only at 1500 Wh/kg.
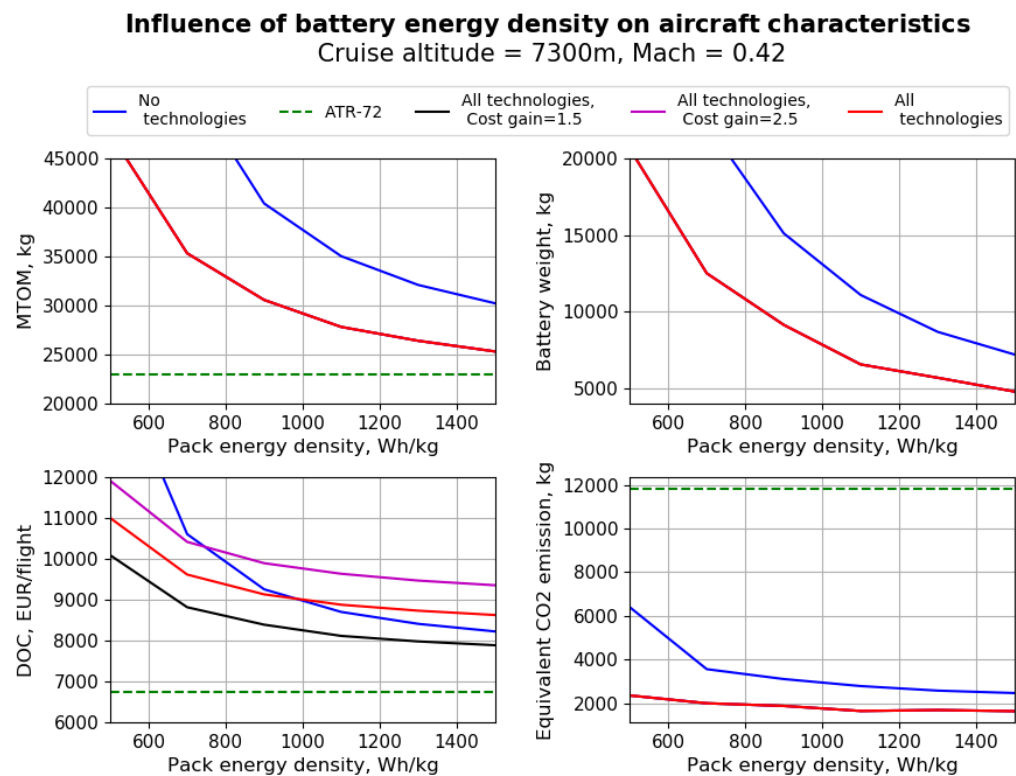
Influence of battery energy density on aircraft characteristics
Cruise altitude = 7300m, Mach = 0.42

Figure 16. Sensitivity to the battery energy density based on minimum DOC concepts.

To compare the DOC values, the aircraft without technologies did not include an additional maintenance cost penalty introduced for the aircraft with all airframe technologies. Moreover, a sensitivity analysis of the maintenance cost gain factor was performed to investigate its effect on the overall DOC and predict potential future DOC behavior. If DOC is compared, two trends can be observed. First, both aircraft have substantially higher DOC compared to the reference ATR-72, and the difference remains large even for high energy densities. On the other hand, the application of technologies affects the DOC. Comparing aircraft with and without technologies, there exists a point after which the DOC increases due to the airframe technologies and their maintenance complications and is equal to 980 Wh/kg. After this energy density, an aircraft without airframe technologies becomes cheaper to operate. Such a trend is a consequence of the maintenance cost gain and redistribution of dominant cost drivers, as shown in Table 9. For low battery energy densities, the most dominant DOC component is the capital cost which depends on the airframe and propulsion system weights. Due to significantly larger weights, these costs contribute to total DOC such that benefits of maintenance costs disappear. Moreover, more battery energy is required for the aircraft without technologies and slightly higher fees also contribute to a larger total DOC. On the other hand, with the increase in energy density, aircraft weights reduce substantially, so capital costs reduce as well. The overall distribution of costs becomes more evenly distributed for the aircraft without technologies, so lower maintenance cost effects become more significant. On the other hand, maintenance costs for the aircraft with technologies start dominating. That relationship leads to higher overall DOC for the aircraft with technologies at high battery energy densities. The present aircraft was designed having 700 Wh/kg of pack energy density which is still more beneficial than the aircraft without technologies. However, the maintenance penalty factor of 2 may be too optimistic. If the maintenance costs increase more, then the equilibrium point between the two DOCs will shift towards lower energy densities, as shown in Figure 16. The only possibility of approaching the reference aircraft DOC exists if maintenance cost gain is equal to 1. The maintenance cost of novel airframe technologies shall be considered later to ensure the financial applicability of novel technologies further.

Table 9. Comparison of DOC components depending on the battery energy density for the SE^{2}A SR aircraft in EUR/flight.

DOC Component	700 Wh/kg with Technologies	700 Wh/kg without Technologies	1300 Wh/kg with Technologies	1300 Wh/kg without Technologies
Energy	808	1438	700	1037
Crew	1369	1369	1369	1369
Maintenance	3199	1891	2937	1596
Capital	2233	3554	1928	2514
Fees	1994	2350	1799	1928
Total	9603	10,604	8734	8446

The effect of technology deviations on the aircraft weights and, as a consequence, applicability of all-electric aircraft is shown in Figures 17–19. In addition, points for extreme technology cases are summarized in Tables 10–13. A similar sizing approach, as discussed in Section 3, was used for the sizing with technology deviations. The wing loading, however, was fixed to the one that occurred after the MDO of the aircraft. In addition, to simplify the sensitivity and account for significant complexities to design an appropriate suction system for the fuselage, the fuselage was assumed fully turbulent for all technology sensitivities.
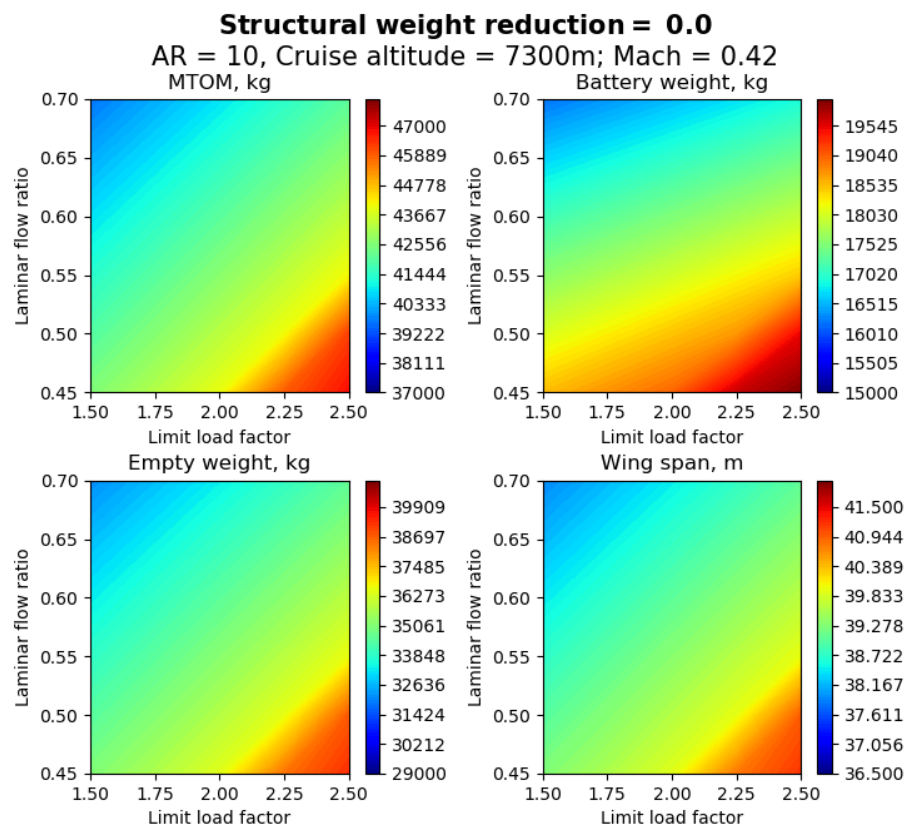

Figure 17. Sensitivity of aircraft characteristics to changes in technology levels at Structural weight reduction of 0.0.
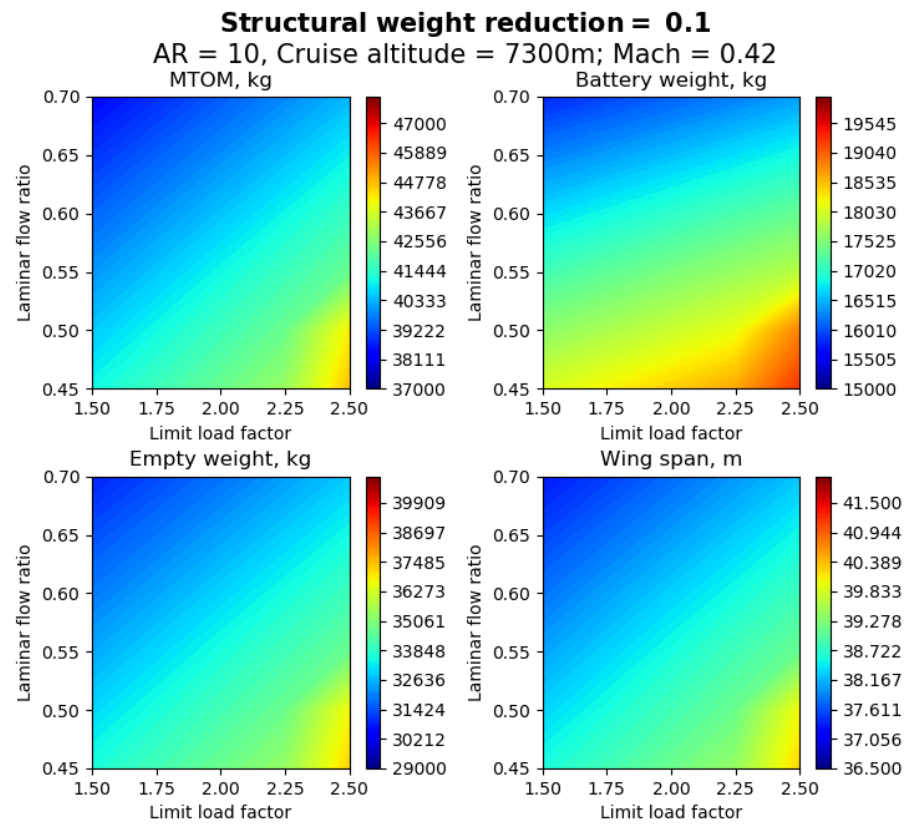
Figure 18. Sensitivity of aircraft characteristics to changes in technology levels at Structural weight reduction of 0.1.
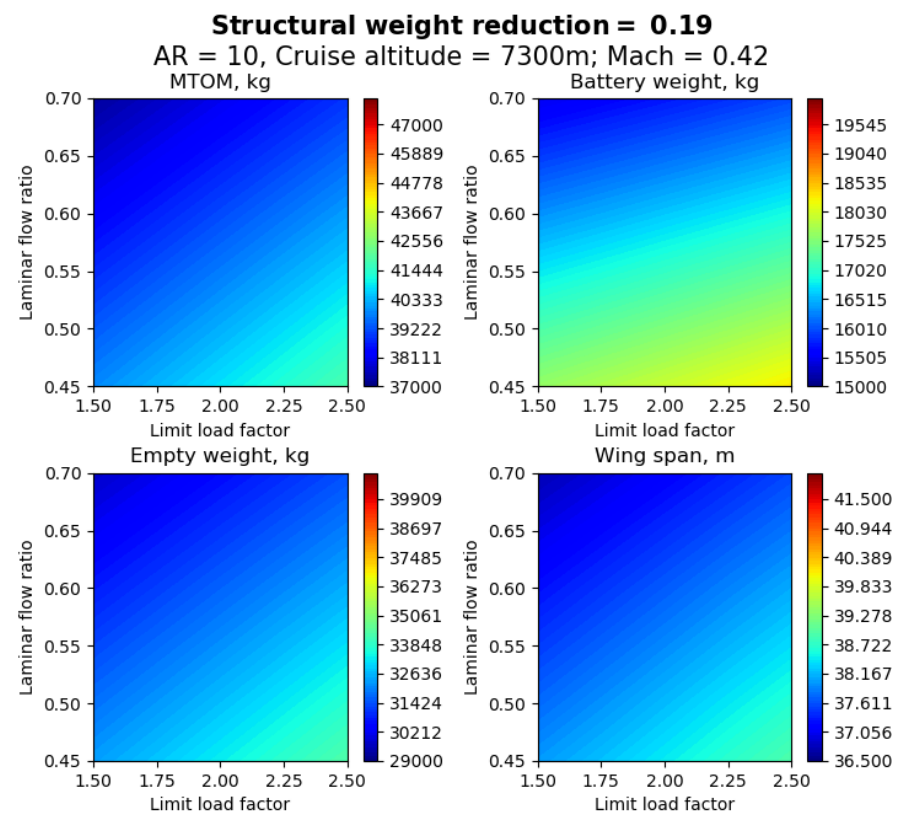

Figure 19. Sensitivity of aircraft characteristics to changes in technology levels at Structural weight reduction of 0.19.

Table 10. MTOM values for the airframe weight reduction of 0%.

	70% Laminar Flow	**45% Laminar Flow**	**Units**
limit load 1.5	39,665	42,500	kg
limit load 2.5	42,100	46,800	kg

Table 11. MTOM values for the airframe weight reduction of 19%.

	70% Laminar Flow	**45% Laminar Flow**	**Units**
limit load 1.5	37,300	39,800	kg
limit load 2.5	38,900	41,800	kg

Table 12. MTOM values for the limit load factor of 1.5.

	0% Airframe Weight Reduction	**19% Airframe Weight Reduction**	**Units**
70% laminar flow	39,665	37,300	kg
45% laminar flow	42,500	39,800	kg

Table 13. MTOM values for the limit load factor of 2.5.

	0% Airframe Weight Reduction	**19% Airframe Weight Reduction**	**Units**
70% laminar flow	42,100	42,500	kg
45% laminar flow	46,800	41,800	kg

Based on obtained results, if the weight sensitivity on the technology is compared for two other technologies where one technology has a constant value and the other technology is fixed at either their minimum or maximum, the laminar flow control shows the largest influence on the MTOM. Structural weight reduction plays the second most important role, and the load alleviation affects the aircraft MTOM the least compared to the other two technologies. For instance, for the airframe reduction of 0%, if the maximum possible boundary layer transition is possible, then the change in MTOW due to the load alleviation is equal to 2435 kg. However, if for the same airframe reduction factor, the load alleviation has its minimum value, then the change in MTOM is equal to 2835 kg due to the HLFC technology. If technologies are combined, then the effect of the MTOM is magnified.

8. Conclusions

The present manuscript investigated the influence of novel technologies on the feasibility of all-electric short-range aircraft with passenger capacity and performance characteristics similar to ATR-72. Three novel airframe technologies were considered: hybrid laminar flow control, active load alleviation, and advanced materials and structure concepts. In addition, superconducting electric motors and high energy density batteries were considered for the aircraft energy system.

Multiple tools were used and improved to assess the feasibility question. SUAVE was used to perform the initial sizing and sensitivity analyses and was also coupled with MATLAB to perform MDO studies. EMWET and FLOPS weight estimation methods and a weight penalty function for folding wings were integrated into SUAVE. The cubic spline method for a propeller was used to enable the aircraft sizing. AVL was used to assess the aircraft stability and control.

Two aircraft configurations were considered for the design: the conventional configuration with a high wing and wing-mounted propellers and the low wing with propellers mounted at the aft of the fuselage. The low-wing configuration was selected because it had lower DOC, lower weights, and is possible to have certifiable stability and control characteristics.

To refine the selected concept and determine the aircraft characteristics' sensitivity to the folding penalty and the objective function, a set of MDO studies were performed. The configuration without folding wings was selected due to a relatively small increase in DOC due to the fixed wingspan and reduced complexity of the wing design and maintenance due to the absence of the wing folding mechanism.

The importance of airframe technologies was assessed by comparing aircraft configurations with and without them. The presence of airframe technologies may reduce the required battery pack energy density by 300 Wh/kg compared to their absence. The difference in required energy density also increases with the increase of the battery energy density. However, the application of technologies becomes more expensive than their absence if the battery pack energy density exceeds 980 Wh/kg for a given maintenance cost gain factor of 2.

Comparison of the all-electric aircraft to the reference ATR-72 showed substantial reduction of CO_2 emission by 81% of the all-electric aircraft. On the other hand, DOC increase of 42% presents a significant limit to market success of such aircraft. Moreover, neither increase in battery energy density, nor reduction of maintenance costs change aircraft DOC significantly. The only possibility to have a comparable DOC level may appear if maintenance cost gain is absent and battery pack energy density exceeds 1000 Wh/kg. Moreover, the all-electric aircraft consumes a lot of energy to complete the mission which creates major uncertainties related to its energy-efficiency from the operational standpoint.

Finally, a sensitivity analysis of technology availability on the aircraft characteristics was performed. Simulations were performed for each technology combination from the most optimistic to its absence. Results demonstrated high sensitivity of aircraft weights to technology levels where the HLFC has the most influence, followed by the aircraft weight reduction and finishing with the load alleviation. The combined effect of technologies magnifies the differences in weight even further.

Future research steps will include a detailed conceptual design of the SE^{2}A SR aircraft. First of all, the design with available models for the laminar flow required power and additional weight penalties due to the implementation of all technologies and additional hardware will be performed. A more sophisticated assessment of the aircraft stability and control must be performed to ensure adequate flying qualities. Finally, higher fidelity analysis for the energy network and modeling of the motors and propellers will be considered.

Author Contributions: Conceptualization, S.K.; methodology, S.K.; software, S.K.; validation, S.K.; investigation, S.K.; writing—original draft preparation, S.K.; writing—review and editing, A.E.; visualization, S.K.; supervision, A.E.; project administration, A.E.; funding acquisition, A.E. All authors have read and agreed to the published version of the manuscript.

References

1. *Flightpath 2050-Europe's Vision for Aviation: Advisory Council for Aeronautics Research in Europe*; Publications Office of European Union: Brussels, Belgium, 2011. [CrossRef]
2. Friedrich, C.; Robertson, A. Hybrid-electric propulsion for aircraft. *J. Aircr.* **2015**, *52*. [CrossRef]
3. Hamilton, T.; German, B. Optimal airspeeds for scheduled electric aircraft operations. *J. Aircr.* **2019**, *56*. [CrossRef]
4. Kim, D.; Perry, A.; Ansell, J. A Review of Distributed Electric Propulsion Concepts for Air Vehicle Technology. In Proceedings of the 2018 AIAA/IEEE Electric Aircraft Technologies Symposium, Cincinnati, OH, USA, 12–14 July 2018. [CrossRef]
5. Finger, D.; Cees, B.; Braun, C. Initial Sizing Methodology for Hybrid-Electric General Aviation Aircraft. *J. Aircr.* **2020**, *57*, 1–11. [CrossRef]
6. Finger, D.; Cees, B.; Braun, C. Impact of Battery Performance on the Initial Sizing of Hybrid-Electric General Aviation Aircraft. *J. Aerosp. Eng.* **2020**, *33*, 1–18. [CrossRef]

7.   Finger, D.; Cees, B.; Braun, C. Comparative Assessment of Parallel-Hybrid-Electric Propulsion Systems for Four Different Aircraft. *J. Aircr.* **2020**. [CrossRef]

8.   De Vries, R.; Hoogreef, F.; Vos, R. Range Equation for Hybrid-Electric Aircraft with Constant Power Split. *J. Aircr.* **2020**, *67*. [CrossRef]

9.   De Vries, R.; Brown, M.; Vos, R. Preliminary Sizing Method for Hybrid-Electric Distributed-Propulsion Aircraft. *J. Aircr.* **2019**, *56*. [CrossRef]

10. Pornet, C.; Gologan, C.; Vratny, P.; Seitz, A.; Schmitz, O.; Isikveren, A.; Hornung, M. Methodology for Sizing and Performance Assessment of Hybrid Energy Aircraft. *J. Aircr.* **2015**, *52*. [CrossRef]

11. Sgueglia, A.; Schmollgruber, P.; Bartoli, N.; Benard, E.; Morlier, J.; Jasa, J.; Martins, J.; Hwang, T.; Gray, S. Multidisciplinary Design Optimization Framework with Coupled Derivative Computation for Hybrid Aircraft. *J. Aircr.* **2020**, *57*. [CrossRef]

12. Hepperle, M. Electric Flight-Potential and Limitations. October 2012, AVT-209 Workshop on Energy-efficient Technologies and Concepts Operation. Available online: https://elib.dlr.de/78726/ (accessed on 21 May 2021).

13. Pipestrel; Alpha Electro. 2021. Available online: https://perma.cc/7G4P-TBD3 (accessed on 3 June 2021).

14. Bye Aerospace; eFlyer. 2021. Available online: https://perma.cc/SW5M-MMH2 (accessed on 3 June 2021).

15. Siemens; Extra 330 LE Aircraft. 2017. Available online: https://perma.cc/5RC3-SWD8 (accessed on 3 June 2021).

16. Equation Aircraft; Equator P2 Xcursion. 2021. Available online: https://perma.cc/AR56-GTVR?type=image (accessed on 3 June 2021).

17. Jackson, P. *Jane's All the World's Aircraft*; IHS Markit: London, UK, 2015.

18. MagniX; MagniX Engines. 2021. Available online: https://perma.cc/ZA7W-Z75R (accessed on 3 June 2021).

19. Liu, Y.; Elham, A.; Horst, P.; Hepperle, M. Exploring Vehicle Level Benefits of Revolutionary Technology Progress via Aircraft Design and Optimization. *Energies* **2018**, *11*, 166. [CrossRef]

20. Beck, N.; Landa, T.; Seitz, A.; Boermans, L.; Liu, Y.; Radespiel, R. Drag Reduction by Laminar Flow Control. *Energies* **2018**, *11*, 252. [CrossRef]

21. Risse, K.; Stumpf, E. Conceptual Aircraft Design including Hybrid Laminar Flow Control. *CEAS Aeronaut. J.* **2014**, *5*, 333–343. [CrossRef]

22. Horst, P.; Elham, A.; Radespiel, R. Reduction of Aircraft Drag, Loads and Mass for Energy Transition in Aeronautics. In Proceedings of the DLRK 2020 Conference, Darmstadt, Germany, 1–3 September 2020. [CrossRef]

23. Gröhlich, M.; Böswald, M.; Winter, R. An iterative eigenvalue solver for systems with frequency dependent material properties. In Proceedings of the DAGA 2020, Hanover, Germany, 12–14 July 2020; pp. 900–903. Available online: https://elib.dlr.de/134937 (accessed on 3 June 2021).

24. Dähne, S.; Hühne, C. Gradient Based Structural Optimization of a Stringer Stiffened Composite Wing Box with Variable Stringer Orientation. In Proceedings of the World Congress of Structural and Multidisciplinary Optimisation, Braunschweig, Germany, 5–9 June 2020; pp. 814–826. [CrossRef]

25. Wunderlich, F.T.; Dähne, S.; Reimer, L.; Schuster, A.; Brodersen, O. Global Aero-Structural Design Optimization of More Flexible Wings for Commercial Aircraft. In Proceedings of the AIAA Aviation 2020 Forum, Virtual Event, 15–19 June 2020; Volume 33, pp. 1–18. [CrossRef]

26. Rossow, C.; Geyr, H.; Hepperle, M. The 1g-Wing, Visionary Concept or Naive Solution? DLR-IB-AS-BS-2016-121, Braunschweig, 2016. Available online: https://elib.dlr.de/105029/ (accessed on 3 June 2021).

27. Liu, X.; Sun, Q. Gust Load Alleviation with Robust Control for a Flexible Wing. *Shock Vib.* **2016**, *2016*. [CrossRef]

28. Ying, B.; Changchum, X. Gust load alleviation wind tunnel tests of a large-aspect-ratio flexible wing with piezoelectric control. *J. Aeronaut.* **2017**, *30*, 292–309. [CrossRef]

29. Beyer, Y.; Kuzolap, A.; Steen, M.; Diekmann, H.; Fezans, N. Adaptive Nonlinear Flight Control of STOL-Aircraft Based on Incremental Nonlinear Dynamic Inversion. In Proceedings of the 2018 AIAA Aviation Forum, Atlanta, GA, USA, 25–29 June 2018. [CrossRef]

30. Khalil, A.; Fezans, N. A Multi-Channel H Preview Control Approach to Load Alleviation Function Design. In Proceedings of the 2019 CEAS Conference on Guidance, Navigation and Control, Milano, Italy, 3–5 April 2019. Available online: https://elib.dlr.de/128625/ (accessed on 3 June 2021).

31. Fezans, N.; Joos, D.; Deiler, C. Gust Load Alleviation for a Long-Range Aircraft with and without Anticipation. *CEAS Aeronaut. J.* **2019**, *10*, 1033–1057. [CrossRef]

32. Ehlers, J.; Fezans, N. Airborne Doppler LiDAR Sensor Parameter Analysis for Wake Vortex Impact Alleviation Purposes. In Proceedings of the 2015 CEAS Conference on Guidance, Navigation and Control, Toulouse, France, 13–15 April 2015. [CrossRef]

33. Khalil, K.; Asaro, S.; Bauknecht, A. Active Flow Control Devices for Wing Load Alleviation. In Proceedings of the AIAA Aviation 2020 Forum, Virtual Event, 15–19 January 2020; pp. 1–22. [CrossRef]

34. Bishara, M.; Horst, P.; Madhusoodanan, H.; Brod, M.; Daum, B.; Rolfes, R. A Structural Design Concept for a Multi-Shell Blended Wing Body with Laminar Flow Control. *Energies* **2018**, *11*, 383. [CrossRef]

35. Stückl, S. Methods for the Design and Evaluation of Future Aircraft Concepts Utilizing Electric Propulsion Systems. Ph.D. Thesis, Technical University Munchen, Munchen, Germany, 2015. Available online: http://nbn-resolving.de/urn:nbn:de:bvb:91-diss-20160701-1255732-1-0 (accessed on 3 June 2021).

36. Thielmann, A.; Sauer, A.; Isenmann, R.; Wietschel, M. Technology roadmap energy storage for electric mobility 2030. *Fraunhofer* **2012**. Available online: https://perma.cc/6EKP-Z45X (accessed on 21 May 2021).
37. National Academies of Sciences, Engineering, and Medicine. *Commercial Aircraft Propulsion and Energy Systems Research: Reducing Global Carbon Emissions*; National Academies Press: Washington, DC, USA, 2016. [CrossRef]
38. Mconald, R. Advanced modeling in OpenVSP 48th. In Proceedings of the AIAA Aerospace Sciences Meeting Including the New Horizons Forum and Aerospace Exposition, Washington, DC, USA, 13–17 June 2016. [CrossRef]
39. Lukaczyk, T.; Wendroff, A.; Colonno, M.; Economon, T.; Alonso, J.; Orra, T.; Ilario, C. SUAVE: An Open-Source Environment for Multi-Fidelity Conceptual Vehicle Design. In Proceedings of the 16th AIAA ISSMO Multidisciplinary Analysis and Optimization Conference, Dallas, TX, USA, 22–26 June 2015. [CrossRef]
40. Raymer, D. *Aircraft Design: A Conceptual Approach*, 6th ed.; American Institute of Aeronautics and Astronautics: Washington, DC, USA, 2018. [CrossRef]
41. Gudmundsson, S. *General Aviation Aircraft Design: Applied Methods and Procedures*, 1st ed.; Butterworth-Heinemann: Oxford, UK, 2013. [CrossRef]
42. Torenbeek, E. *Synthesis of Subsonic Airplane Design*; Springer: Delft, The Netherlands, 1982. [CrossRef]
43. Roskam, J. *Airplane Design*, 2nd ed.; Darcorporation: Lawrence, KS, USA, 2003; Volume 1–8.
44. Ibrahim, K. Selecting Principal Parameters of Baseline Design Configuration for Twin Turboprop Transport Aircraft. In Proceedings of the 22nd Applied Aerodynamics Conference and Exhibition, Providence, RI, USA, 16–19 August 2004. [CrossRef]
45. Brake, H.; Wiegerinck, G. Low-power Cryocooler Survey. *Cryogenics* **2002**, *42*. [CrossRef]
46. Welstead, J.; Feldder, J. Conceptual Design of a Single-aisle Turboelectric Commercial Transport with Fuselage Boundary Layer Ingestion. In Proceedings of the 54th AIAA Aerospace Sciences Meeting, San DIego, CA, USA, 4–8 January 2016. [CrossRef]
47. Wells, D.; Horvath, B.; McCullers, L. *The Flight Optimization System Weights Estimation Method*; NASA TM 20170005851; NASA: Hampton, VA, USA, 2017. Available online: https://core.ac.uk/display/84913944 (accessed on 3 June 2021).
48. Elham, A.; La Rocca, G.; van Tooren, M. Development and Implementation of an Advanced, Design-sensitive Method for Wing Weight Estimation. *Aerosp. Sci. Technol.* **2013**, *29*, 100–113. [CrossRef]
49. Drela, M.; Youngren, H. Athena Vortex-lattice Method. Available online: https://perma.cc/D3J8-U8U5 (accessed on 3 June 2021).
50. Yarygina, V.; Popov, M. Development of the Weight Formula for a Folding Wing. *Russ. Aeronaut. (Iz.VUZ)* **2012**, *55*, 120–126. [CrossRef]
51. Senty, R.; Wickenheiser, T. *Propeller Performance and Weight Predictions Appended to the NAVY/NASA Engine Program*; NASA TM 83458; NASA: Cleveland, OH, USA, 1983. Available online: https://core.ac.uk/display/42851585 (accessed on 3 June 2021).
52. Brown, G.; Kascak, A.; Ebihara, B.; Johnson, D.; Choi, B.; Siebert, M.; Buccieri, C. *NASA Glenn Research Center Program in High Power Density Motors for Aeropropulsion*; NASA TM-2005-213800; NASA: Cleveland, OH, USA, 2005. Available online: https://core.ac.uk/display/10516384 (accessed on 3 June 2021).
53. Fujino, M.; Yoshizaki, Y.; Kawamura, Y. Natural-Laminar-Flow Airfoil Development for the Honda Jet. In Proceedings of the 20th AIAA Applied Aerodynamics Conference, St. Louis, MO, USA 24–26 June 2002. [CrossRef]
54. Certification Specifications and Acceptable Means of Compliance for Large Aeroplanes CS-25. June 2020. Available online: https://bit.ly/3uJCREt (accessed on 3 June 2021).
55. Hoelzen, J.; Liu, Y.; Bensmann, B.; Winnefeld, C.; Elham, A.; Friedrichs, J.; Hanke-Rauschenbach, R. Conceptual Design of Operation Strategies for Hybrid-Electric Aircraft. *Energies* **2018**, *11*, 217. [CrossRef]
56. U.S. Energy Information Administration. Annual Energy Outlook 2021. Available online: https://bit.ly/3wNOKKM (accessed on 3 June 2021).
57. Coe, P.; Applin, Z. *Low-Speed Stability and Control Characteristics of a Transport Model with Aft-Fuselage-Mounted Advanced Turboprops*; NASA TM-2535; NASA: Hampton, VA, USA, 1986. Available online: https://core.ac.uk/display/42841676 (accessed on 3 June 2021).
58. Riley, D.; Brandon, J.; Glaab, L. *Piloted Simulation Study of an ILS Approach of a Twin-pusher Business/Commuter Turboprop Aircraft Configuration*; NASA TM-451; NASA: Hampton, VA, USA, 1994. Available online: https://core.ac.uk/display/42787573 (accessed on 3 June 2021).
59. Scholz, D. Limits to Principles of Electric Flight. In Proceedings of the Deutscher Luft- und Raumfahrtkongress 2019, Darmstadt, Germany, 30 September–2 December 2019. [CrossRef]
60. Dallara, E. Aircraft Design for Reduced Climate Impact. Dissertation, Stanford University, 2011. Available online: https://perma.cc/3TDH-TB2S (accessed on 3 June 2021).
61. Baughcum, S.; Tritz, T.; Henderson, S.; Pickett, D. *Scheduled Civil Aircraft Emission Inventories for 1992: Database Development and Analysis*; NASA Contractor Report 4700; NASA: Hampton, VA, USA, 1996. Available online: https://core.ac.uk/display/42776850 (accessed on 3 June 2021).
62. Aircraft Engine Emissions Databank.ICAODoc 9646-AN/943, Excel Data-Base, 2019. Available online: https://bit.ly/34xCPEP (accessed on 3 June 2021).
63. Capuano, L. International Energy Outlook 2020 (IEO2020). Center for Strategic and International Studies 14 October 2020. Available online: https://perma.cc/9L4A-KAHA (accessed on 3 June 2021).
64. Greitzer, E.; Bonnefoy, P.; de la Rosa Blanco, E.; Dorbian, C.; Drela, M.; Hall, D.; Hansman, R.; Hileman, J.; Liebeck, R.; Lovegren, J.; et al. *N+3 Aircraft Concept Designs and Trade Studies*; NASA/CR—2010-216794/VOL1; NASA: Cleveland, OH, USA, 2010. Available online: https://core.ac.uk/display/10557296 (accessed on 3 June 2021).

65. Andersson, J.; P. Krus., P. A Multi-Objective Optimization Approach to Aircraft Preliminary Design. In Proceedings of the SAE World Aviation Congress, Montreal, QC, Canada, 8–11 September 2003. [CrossRef]
66. Donlan, C. An Interim Report on the Stability and Control of Tailless Airplanes. NACA Technical Report 796. August 1944. Available online: https://core.ac.uk/display/10516173 (accessed on 3 June 2021).
67. ATR-72 Series 600 Brochure. 2014. Available online: https://perma.cc/95KA-S7XS (accessed on 3 June 2021).

Article

Design and Optimization of a Large Turboprop Aircraft

Fabrizio Nicolosi [ID], Salvatore Corcione *[ID], Vittorio Trifari [ID] and Agostino De Marco [ID]

Department of Industrial Engineering, University of Naples Federico II, Via Claudio 21, 80125 Naples, Italy; fabrnico@unina.it (F.N.); vittorio.trifari@unina.it (V.T.); agostino.demarco@unina.it (A.D.M.)
* Correspondence: salvatore.corcione@unina.it

Abstract: This paper proposes a feasibility study concerning a large turboprop aircraft to be used as a lower environmental impact solution to current regional jets operated on short/medium hauls. An overview of this market scenario highlights that this segment is evenly shared between regional turboprop and jet aircraft. Although regional jets ensure a large operative flexibility, they are usually not optimized for short missions with a negative effect on block fuel and environmental impact. Conversely, turboprops represent a greener solution but with reduced passenger capacity and speed. Those aspects highlight a slot for a new turboprop platform coupling higher seat capacity, cruise speed and design range with a reduced fuel consumption. This platform should operate on those ranges where neither jet aircraft nor existing turboprops are optimized. This work compares three different solutions: a high-wing layout with under-wing engines installation and both two- and three-lifting-surface configurations with low-wing and tail tips-mounted engines. For each concept, a multi-disciplinary optimization was performed targeting the minimum block fuel on a 1600 NM mission. Optimum solutions were compared with both a regional jet such as the Airbus A220-300 operated on 1600 NM and with a jet aircraft specifically designed for this range.

Keywords: aerospace; aviation; aeronautics; aircraft; design; open access; special issue; MDPI; turboprop; regional market; MDAO; innovative; green aviation

1. Introduction

From a preliminary overview, nowadays, the regional aircraft market segment is mainly influenced by a combination of three factors. A first key parameter to be considered is the environmental impact reduction, as can be seen by ever-more ambitious targets envisaged by international associations such as the Air Transport Action Group (ATAG) and the International Air Transport Association (IATA) or the Clean Sky 2 consortium. In 2008, the ATAG board developed a set of environmental goals for the short, medium, and long term which were supported and reiterated by the IATA Board and the association's Annual General Meeting [1]. Those goals can be summarized in the followings: an average improvement in fuel efficiency of 1.5% per year from 2009 to 2020; a cap on net aviation CO_2 emissions from 2020 (carbon-neutral growth); and a reduction in net aviation CO_2 emissions of 50% by 2050, relative to 2005 levels. However, as pointed out in [2], most of the targets forecasted by IATA and ATAG for 2020 have not been achieved, and the expected carbon-neutral growth appears to be quite far. This highlights the need to stress even more the reduction of the civil aviation environmental impact as the main driving parameter in the design of new and greener aircraft models.

In terms of innovation aiming at reducing civil aviation environmental impact, the Clean Sky 2 Program of Horizon 2020 has accelerated by now the development and introduction of new technologies designed for entry into service in the 2025–2035 timeframe. According to the Clean Sky 2 development plan, by 2050, 75% of the world's fleet now in service (or on order) will be replaced by aircraft that can deploy Clean Sky 2 technologies [3]. High level objectives defined by Clean Sky 2 expects a reduction in CO_2, NO_X, and environmental noise from -20% to -30% in the 2014–2024 timeframe. Furthermore,

reductions of −75% in CO_2, −90% in NO_X, and −60% in environmental noise have been forecast by 2050.

In addition to the environmental impact topic, a second main factor currently influencing almost all market segments is represented by the recent COVID-19 outbreak, which has caused severe damage to the worldwide aviation industry.

Market forecasts made by the most important aircraft manufacturers at the beginning of 2020 have been completely changed by this unexpected event resulting in an overall reduction of air passengers (both international and domestic) of 50% in 2020 compared to 2019 [4]. In addition, the latest estimates made by the International Civil Aviation Organization (ICAO) [4] have highlighted a passenger demand drop from the 2020 originally planned forecasts by 2690 million (−60%), which has been related to a 370 billion US$ loss of gross passenger operating revenues. A partial recovery has been forecast by ICAO [4] for the first half of 2021 reducing the passenger revenue loss faced in 2020, equal to −369,768 million US$, to a value between −178,373 and −148,719 million US$.

However, when a full recovery from COVID-19 damages will be reached, most major airlines will still have to face the third main factor influencing the regional market scenario, which is represented by the need to replace several hundred heritage aircraft, especially in the segment from 20 to 150 seats, which are now close to the end of their useful commercial life.

The combination of all these factors will deeply influence the current aviation industry shaping the new generation of aircraft. On the one side, ever more mutable and demanding requirements will be asked by the market, resulting in a very challenging design process to come up with new aircraft solutions. On the other side, in the near future, new ways and possibilities will be accessible to the aerospace research sector with innovative technologies and disruptive new aircraft concepts probably making their appearance on the upcoming market scenario.

To have an idea of which could be possible future market needs in the post-pandemic scenario, especially in the regional market segment, some interesting information can be obtained from recent market analyses made by the major aircraft manufacturers concerning the small single-aisle aircraft segment up to 150 seats.

Dealing with possible future aircraft requirements, Airbus Global Market Forecast (Airbus S.A.S., Blagnac, France) [5] provides a useful statistical trend which highlights a continuous increment in average seats capacity and mission ranges for the single-aisle jet fleet. Figure 1 shows that up to 2017 aircraft seats average has increased from 140 to 169, while average mission ranges have experienced an increment from 422 NM to 586 NM. Figure 1 also highlights that there is a significant variation around the mean which can be attributed to different aircraft sizes. In addition to showing the wide spectrum of operations for which the airlines use these aircraft, Figure 1 demonstrates why the range capability of aircraft products is an important consideration for airlines and manufacturers, a capability which also equates to flexibility.
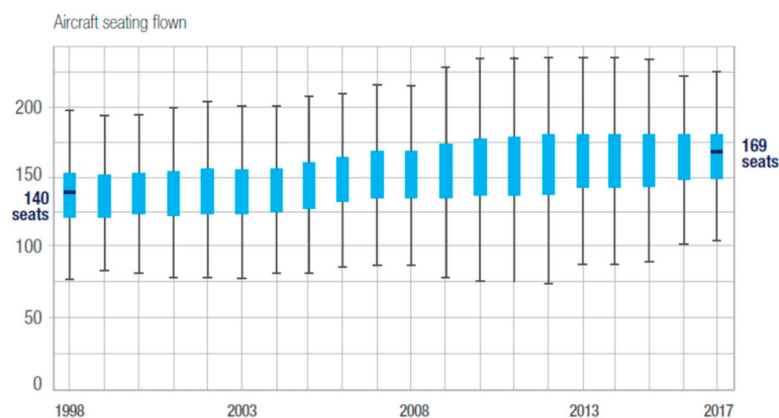

Figure 1. *Cont.*

Distance flown (nm)
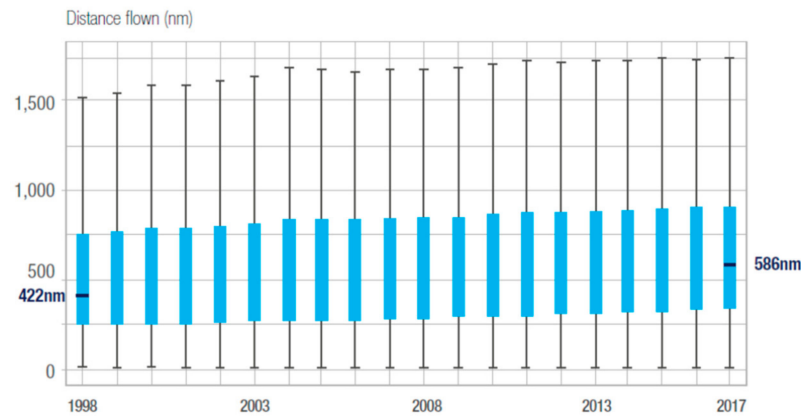
Figure 1. Distribution of single-aisle aircraft seats and ranges over the years. Reprinted from ref. [5].

As shown in Figure 2, up to 2016, both turboprop and regional jet aircraft were sharing the regional market evenly with a slightly increasing advantage of regional jets due to a higher seat capacity and longer mission distances than conventional regional turboprops. However, despite the regional jets success, turboprop engines are 10–30% more efficient than jet engines in terms of Specific Fuel Consumption (SFC), leading to a potential reduction of the amount of fuel used per mission as well as pollutant emissions. In fact, according to ATR forecasts [6], assuming all short haul flights operated by regional jets today are replaced by modern turboprops, 11% of overall regional aviation CO_2 emissions could be saved.

To design an advanced turboprop aircraft that could be competitive with respect to regional jets on short and medium haul, several key aspects must be assessed if compared to conventional turboprop designs. There is the need to increase the seats capacity, the aircraft must be designed for longer missions, and cabin noise and passenger comfort must be improved, as well as both the aerodynamic efficiency and the maximum cruise speed.

The authors have already faced the design of an advanced turboprop coupling higher seat capacity, improved cruise speed, and longer design range with a reduced fuel consumption within the framework of the European funded project named Innovative turbopROp configuratioN (IRON) [7–12]. The project deals with the design of an innovative large turboprop aircraft with rear engine installation.
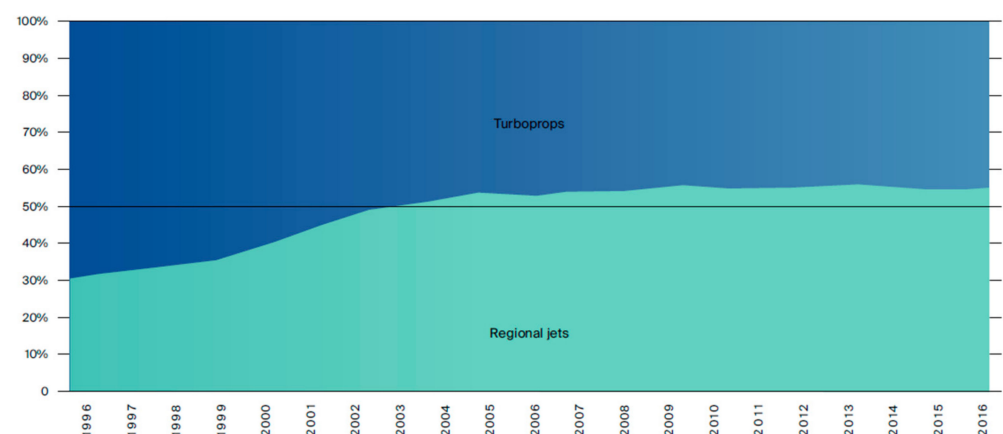
Figure 2. In-service fleet share of turboprops and regional jets. Reprinted from ref. [13].

Such a configuration shows several design issues dealing with the rear engine installation. The most comprehensive reference dealing with all key design aspects for a high-capacity propeller driven aircraft, including the rear engines installation, is the study performed by Goldsmith in [14], where a feasibility studies related to a possible conversion

of the McDonnell Douglas (Saint Louis, MO, USA) DC-9 from turbofan to turbo/prop-fan power plant is discussed.

Goldsmith's work shows useful evaluations dealing with the aircraft configuration feasibility, aerodynamics, weights, balance, and performance identifying three promising configurations with respect to the reference aircraft platform assumed as the DC-9 Super 80. The configurations proposed by Goldsmith exploited the results of the research programs carried out by NASA to develop technologies needed to implement potential fuel savings by adopting advanced turboprop engine architectures. These works highlighted 15–30% savings in aircraft block fuel compared to the state-of-the-art turbofan at the time by adopting advanced turboprop engines characterized by multi-bladed and high efficiently propellers that could be used at higher Mach numbers [15,16].

The selection of the most suitable configurations was made after a first qualitative comparison between many different possible layouts, followed by a multi-disciplinary quantitative analysis of three possible solutions. The first layout was an upper-wing-mounted propfan, indicated as Configuration 1 in Figure 3; the second one was a T-tail configuration with aft fuselage-mounted propfan, named Configuration 2 in Figure 3; and the last aircraft concept provided for a horizontal tail-mounted propfan, indicated as Configuration 3 in Figure 3. All modifications to the baseline platform were made by keeping constant both wing area and Maximum Take-Off Weight (MTOW) of the aircraft.

Configuration 1

Configuration 2
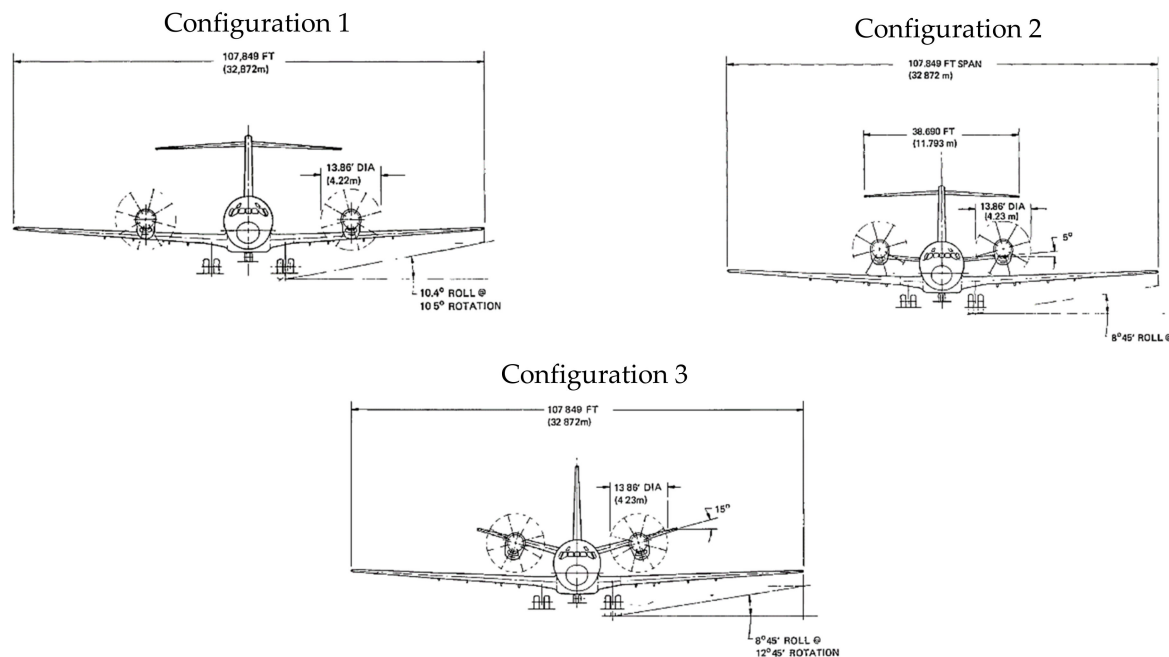
Configuration 3

Figure 3. Configuration selected by the NASA feasibility study. Reprinted from ref. [14].

As shown in [14], the first and third layouts were identified as promising solutions providing for a block fuel reduction of about 14% and a mean Direct Operating Cost (DOC) reduction ranging from 6% to 8% with respect to the reference aircraft. The rear-mounted engines installation provided a much larger center of gravity excursion, a higher horizontal tail weight, and higher values of the equivalent parasite area. However, while the T-tail configuration led to lower performance and DOC improvements than the wing-mounted engines installation, the horizontal tail-mounted engines layout mitigated the above-mentioned negative effects, allowing to reach similar, or even better, performance and DOC improvements, if compared with the conventional wing-mounted engine configuration. Moreover, in the case of turboprop or open rotors, rear engine installation reduces the cabin noise providing for a better passenger's comfort.

The high propulsive efficiency of propellers nowadays still makes them quite an attractive solution for regional aircraft flying up to high subsonic speeds. Different concepts for a

large turboprop aircraft can be found in the literature. A novel concept for highly efficient and ecological propeller driven aircraft is proposed in [17]. This aircraft, characterized by a high wing, T-tail, and four turboprop engines with large propeller diameters, has shown a potential Direct Operating Cost (DOC) reduction of about 11% while reducing trip fuel mass and therefore CO_2 emissions by about 14.9% compared to the reference aircraft Airbus A320 (Airbus S.A.S., Blagnac, France). A modified architecture of the concept proposed in [17] is shown in [18]. This solution, featured by a strut-braced wing with natural laminar flow, could potentially reduce fuel consumption and CO_2 emissions by about 36% with respect to a reference jet aircraft (A320). In addition, DOC could be potentially reduced by about 17% on a mission range of 755 NM. The improvements mainly come from the lower fuel consumption of turboprop engines compared to turbofan engines. Drawbacks are the 21% increase in block time due to the lower cruise speed compared to a jet aircraft and the additional mass due to the higher landing gear lengths caused by high propeller diameters.

Recent studies concerning innovative turboprop aircraft designs are shown in [19], where two configurations featuring tail-mounted propeller and fuselage-mounted ducted propellers have been assessed in terms of their key performance indicators assuming they are designed for a harmonic mission of 1530 km and 68 passengers and compared with a conventional aircraft with wing-mounted propellers similar to ATR-72-600 in terms of geometry and weight.

Although previous research works have already dealt with the comparison between existing turbofan aircraft and future turboprop models to highlight possible improvements in environmental impact and DOC, none of them starts from the design of a modern turboprop aircraft based on a set of Top-Level Aircraft Requirements (TLARs) related to a short/medium haul (e.g., 1600 NM) coupled with a seat capacity in line with market analysis trends (e.g., 130–150 seats). Conversely, they start from an existing turbofan platform trying to make a conversion to a different propulsive system. In addition, most of the studies are focused or on aircraft designed for longer missions with a slightly higher passenger number, or they focus the attention on smaller aircraft with similar design ranges but with a lower passenger capacity.

This work aims to investigate the combination of the selected mission range and seats capacity to design and optimize a possible modern turboprop platform suitable for an entry into service expected by 2035 and targeting the minimum environmental impact. Since there are no existing regional turbofans specifically designed for such a design range and seats capacity, this work does not limit its application in comparing the provided turboprop solutions with the current state of the art regional jet but also faces the design and optimization of a completely brand-new jet platform to perform fair comparison between a turboprop and jet driven aircraft both optimized for the same set of TLARs.

Such a comparison could represent useful information for aircraft designers who want to develop new aircraft suitable for regional applications by providing a good starting point in the decision process related to the preliminary design phase.

2. Aircraft Requirements and Critical Issues

The feasibility study starts from the definition of a specific set of TLARs, suitable for modern regional transport applications and in line with the main aircraft manufacturer market forecast, which is better illustrated in the Introduction. The TLARs driving the design of a large capacity turboprop are summarized in Table 1. As can be appreciated by looking at Table 1, to design a turboprop that could be competitive with respect to regional jets, there is the need to increase the seats capacity, as well as reduce the specific fuel consumption and the associated emissions. The cabin comfort must be improved by reducing the perceived noise and maximum aerodynamic cruise efficiency, the cruise speed value must be higher than the currently flying turboprop, and maximum lift coefficients at take-off and landing must be increased to be attractive with respect to regional jets in terms of ground performance.

Table 1. Topic Level Aircraft Requirements (TLARs).

Performance Requirements	
Passenger Capacity	130 pax at 32"
Range	1600 NM at Max payload (108 kg per pax), usual reserve (alternate + holding + reserves)
Cruise Speed	At FL300 ISA at 97% MTOW Mach (0.64–0.68)
Time to Climb	At MTOW-ISA-from 1500 ft to FL250 $\leq$ 16 min
Take off Field Length (TOFL)	ISA-SL at MTOW, TOFL $\leq$ 4600 ft (1400 m)
Landing Field Length (LFL)	ISA-SL at MLW, LFL $\leq$ 4600 ft (1400 m)

Starting from the work shown by Goldsmith [14] and exploiting the lesson learned within the frame of the European project IRON [7–12], the authors made several considerations about different aircraft configurations that can be drafted in facing the design of a large turboprop aircraft.

The increase of the number of passengers from 70 to 130–150 leads to heavier aircraft, which means having a larger wing area and increased wingspan, affecting both the size and weight of the landing gears, as well as their positions to keep similar ground performance. According to the ICAO/Federal Aviation Administration (FAA) [20] span category, for aircraft in this class, the wingspan is limited to 36.0 m. Moreover, to ensure ground stability requirements due to a heavier aircraft with a larger wingspan, a larger wheel track is required as well.

A conventional high-wing configuration can accommodate large propellers and could be a possible solution for a high-capacity turboprop. However, for the high-wing configuration, two landing gear installations are suitable, as shown in Figure 4: nacelle-mounted or fuselage-mounted within fuselage pods. These two solutions may lead to several issues if used for high-capacity turboprops. The nacelle-mounted landing gears would require very long and heavy legs, which may be difficult to retract inside the nacelles, while fuselage-mounted landing gear might require quite large and heavy pods to ensure an adequate wheel track. Moreover, for both these layouts, the length of the landing gear legs must be increased to achieve a sufficient value of the upsweep angle due to a longer fuselage.

Figure 4. Landing gear installation solution for a large propeller driven aircraft.

A low-wing configuration could solve this issue. However, as shown by the example in Figure 5, a high-capacity turboprop will need a large propeller diameter to comply with an increased thrust requirement due to a higher weight (about 12–14 ft according to the estimations made within the EU CS2 IRON project). Thus, it would be impossible to ensure the required engine clearance from the ground.

For these reasons, a new turboprop aircraft configuration should be characterized by a rear-mounted engine installation. This can lead to a more efficient wing, thanks to the possibility to extend the laminar flow region and reduce the cabin noise by installing engines far from the cabin. Conversely, such an engine installation would lead to a wing weight increment (no mass relief on the wing loading due to the weight of the engines). Furthermore, this configuration can provide for a very large center of gravity (CG) excursion, which can also affect aircraft performance. A wide range of the CG excursion could imply a very large horizontal tail to trim the aircraft in the most rearward

CG positions, resulting in a reduction of maximum lift capabilities, while, at the most forward CG position, the longitudinal Static Stability Margin (S.S.M.) could be very high, requiring for a large download on the horizontal tail to trim the aircraft. This would reduce the aerodynamic cruise efficiency, affecting the fuel consumption and the aircraft DOC. One possible solution to mitigate this aspect consists in a reasonable cut of the overall CG excursion (by limiting the aircraft operability with low passenger number), complying with typical aircraft missions.

Figure 5. Large propeller installation issues for a low wing aircraft configuration.

Given all the above considerations, by looking at the feasibility study performed by NASA [14], and thanks to the experience matured within the IRON project, the authors identified in the rear-engine installation the most promising layout.

Following the work of NASA, the authors also investigated a conventional configuration with engines installed on the wing, with the difference that, in this research, the configuration with the upper wing engine installation was discarded because of both propeller and nacelle sizes. This layout was replaced by a conventional high-wing configuration with engines installed under the wing, assuming that the main landing gear could be installed in fuselage pods. Another difference with the feasibility study performed by NASA is that the T-tail configuration with the rear engine installation was replaced by a three-lifting-surface layout.

The T-tail layout could ensure an adequate longitudinal static stability, as well as cruise aerodynamic efficiency, while probably providing for poor high-lift capabilities and balance issues due to a very afterward mass concentration. Moreover, the installation of a large propeller (12–14 ft of diameter) would require a pylon with a non-negligible span, making the latter comparable to a tailplane.

This configuration was discarded from the first stage of design and replaced by a three-lifting-surface layout which could ensure the required longitudinal stability potentially increasing as well as both aerodynamic efficiency and high-lift capabilities.

The introduction of a third lifting surface could help reduce the tail download required to trim the aircraft. Thus, the trimmed maximum lift coefficient (C_{Lmax}) could be increased while the trim drag contribution could be reduced, resulting in a higher value of the cruise aerodynamic efficiency. The potential increment of the C_{Lmax} could also lead to a reduced wing area providing for additional benefits on cruise aerodynamic efficiency as well as a reduction in aircraft weight (unless the third lifting surface would be heavier than the wing weight reduction).

Furthermore, the third lifting surface could allow to shift forward the aircraft neutral point position, as well as giving the possibility to optimize both the center of gravity excursion and the neutral point position, at fixed static stability margin, by changing wing, horizontal tail, and canard sizes together and their relative positioning. In short, the three lifting surfaces would extend the design space, allowing to cope with both aerodynamic cruise efficiency and maximum lift capabilities of the aircraft. In designing a three-lifting-surface aircraft, particular attention must be paid to evaluating the negative effects in terms of downwash introduced by the canard that acts on both the main wing and the horizontal tail, as shown in [9,11,12].

3. Investigation Workflow and Methods

Starting from the TLARs described in Table 1, for each of the considered aircraft configurations, a sensitivity analysis was carried out by changing the following design parameters:

- Wing planform (span, aspect ratio, sweep angle, and longitudinal wing position)
- Horizontal tail plane planform (span, aspect ratio, and sweep angle)
- Canard planform if present (span, aspect ratio, and longitudinal position)

The complete picture of the design space is shown in Table 2, where, for each of the previous design variables, the considered range of variation is indicated. A specific combination of the design parameters shown in Table 2 generates an aircraft that underwent to a Multi-Disciplinary Analysis process (MDA). The MDA involves all major disciplines of the preliminary aircraft design (i.e., weight, balance, aerodynamics, performance, and DOC). The single MDA cycle shown in Figure 6 and the full factorial Design of Experiments (DOE) represented in Table 2 were performed by means of JPAD (Java tool chain of Programs for Aircraft Design), software developed at the Industrial Engineering Department of the University of Naples Federico II [21–23].

JPAD includes several interconnectable analysis modules which can be used both in standalone mode and in a complete MDA cycle. One of the most important analysis modules is the one dedicated to the evaluation of the most important aircraft performance, which implements a smart simulation-based approach to analyze the complete mission profile including on-ground phases such as take-off and landing [24].

The analysis starts with a first estimation of the amount of fuel needed for the specified mission. Then, a balance analysis is carried out to determine the center of gravity excursion. For each center of gravity, the aerodynamic and stability module estimates the trimmed aircraft lift curve and the trimmed drag polar curve according to the following flight conditions: take off, climb, cruise, and landing. Finally, the performance module uses these data to make a detailed simulation of the initial mission profile estimating a new amount of fuel required to fulfill the mission. Thus, an iterative process is carried out until the first estimated fuel mass is equal to the one calculated by the mission profile analysis. Within the fuel mass iterative loop shown in Figure 6, a second nested iteration is carried out to make the take-off field length and cruise Mach number comply with the assigned TLARs. This is obtained by scaling the reference static thrust of all engines with a step of $\pm 2.5\%$. Together with this thrust scaling, engine weight is updated as well so that an intermediate weight convergence loop must be carried out as well. Both fuel mass and performance iterative loops have a maximum number of iterations fixed to 50. All configurations that do not converge within this limitation are supposed to be unfeasible so that a penalty will be added to those response surface points during the optimization process.

At the end of the convergence loop, other checks are performed on the analyzed configuration. These concern the operative maximum aft center of gravity position, which must be at least 5% of the wing Mean Aerodynamic Chord (MAC) more forward than the main landing gear position due to rotation issues, and the maximum fuel tank capacity, which must be greater than the estimated total mission fuel mass plus reserves.

The multidisciplinary optimization was carried out by imposing the following constraints:

- The minimum static stability margin (with the max aft. center of gravity position) must be greater than zero.
- Take-off and landing field lengths must be at most 1400 m.
- The time to climb from 1500 to 25,000 ft must be at most 16 min.
- The maximum cruise Mach number should be higher than 0.64 and should not exceed 0.68 to consider for propeller operative limitation in terms of compressibility issues.
- The distance between the main landing gear position (X_{LG}) and the maximum aft center of gravity position ($X_{CG,max,aft}$) must be greater than 5% of the mean aerodynamic chord to avoid ground stability issues.
- The estimated total mission fuel mass must be lower than wing fuel tank maximum capacity.

Table 2. Variables design space for each aircraft configuration.

Parameters	Wing Mounted Engines Configuration	Rear Mounted Engines Configuration	Three Lifting Surfaces
	Wing Design Parameters		
Span b_w (m)	32.0–35.5	32.0–35.5	32.0–35.5
Longitudinal position $X_{LE,W}$ (m)	13.0–16.0	18.0–22.0	19.0–22.0
Aspect Ratio AR_w	9.8–13.3	10.2–13.8	10.2–13.6
Sweep at leading edge $\Lambda_{LE,W}$ (°)	2.5–10.0	2.5–10.0	2.5–10.0
	Horizontal Tailplane Design Parameters		
Span b_H (m)	9.14–11.17	11.7–14.3	11.7–14.3
Longitudinal position $X_{LE,H}$ (m)	37.15 fixed value	30.0–32.0	30.0–32.0
Aspect Ratio AR_H	4.96 fixed value	4.40 fixed value	4.40 fixed value
Sweep at leading edge $\Lambda_{LE,H}$ (°)	$\Lambda_{LE,W} + 5.0$	$\Lambda_{LE,W} + 5.0$	$\Lambda_{LE,W} +5.0$
	Canard Design Parameters		
Span b_C (m)	n.a	n.a	7.2–8.8
Longitudinal position $X_{LE,C}$ (m)	n.a	n.a	5.0–8.0
Aspect Ratio AR_C	n.a	n.a	5.57 fixed value
Sweep at leading edge $\Lambda_{LE,C}$ (°)	n.a	n.a	10.0 fixed value
Total number of analyzed aircraft	972	6075	34,020
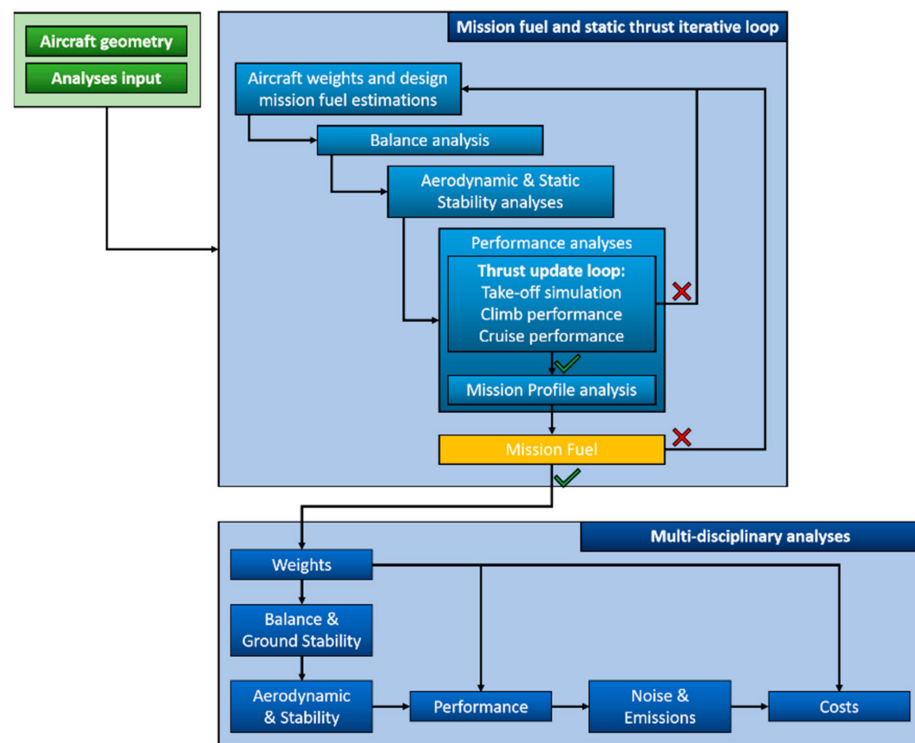
Figure 6. JPAD MDA workflow including thrust update inner loop.

All analyses were performed under several assumptions concerning masses and positions of main components, on-board systems, the center of gravity position to be used for each mission phase, fuel tank systems, laminar flow, and downwash effects (especially in the case of three-lifting-surface configuration). Fuselage length and maximum diameter were kept constant for all analyzed aircraft. Horizontal tailplane sweep angles at leading edge were assumed to be 5° greater than the related wing sweep angle at leading edge. Components and on-board systems masses were calculated using equations provided by Torenbeek [25], which indicate several corrections to be made according to the specific aircraft configuration. Center of gravity positions of the main aircraft

components were assumed according to Torenbeek [25] as well. Some assumptions were made concerning major on-board systems longitudinal position, as shown in Table 3. An example of aircraft components and on-board systems center of gravity position is shown in Figure 7 considering the case of a three-lifting-surface configuration.

Table 3. On-board systems assumptions for the MDA cycle of each aircraft configuration.

Assumption Concerning Systems and Equipment Positions	
Auxiliary Power Unit (APU)	87% fuselage length
Air Conditioning and Anti-Icing System	30% MAC ahead the wing root leading edge
Electrical System	42% fuselage length (half cabin)
Furnishings and Equipment	37% fuselage length
Control Surface Actuators	Using lifting surfaces positions weighted average with components masses
Instruments and Navigation System	8% fuselage length (cockpit)
Operating Items	21% fuselage length (close to the front galley)
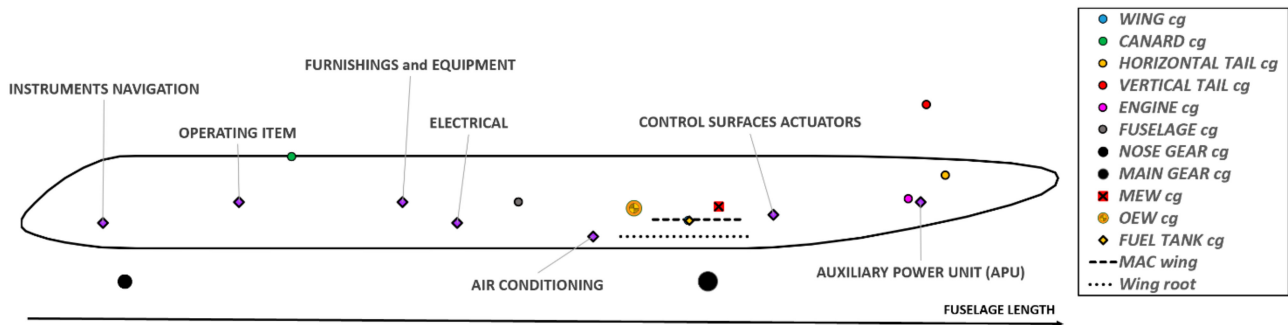
Figure 7. Example of aircraft main components and systems center of gravity positions for a three-lifting-surface configuration.

To take into account the aircraft weight reduction due to fuel consumption during the design mission, a variable center of gravity position must be considered for each phase, affecting in this way the aircraft stability and providing for a variable trim drag value. This effect was simulated by considering different center of gravity positions from the boarding diagram. For take-off and climb conditions, the maximum take-off weight center of gravity was considered. The cruise phase was evaluated assuming a center of gravity position related to an average fuel weight condition (starting from the maximum take-off weight). The landing condition was investigated assuming a center of gravity position related to the maximum landing weight (about 90% of the maximum take-off weight). Finally, the longitudinal static stability margin was estimated considering the most aft center of gravity position.

For each of the selected aircraft configurations, some assumptions and some technologies were envisaged, as shown in Figure 8 where their effects related to both aerodynamics (in terms of drag, maximum lift capabilities, and downwash on the horizontal tail plane) and weight estimation are summarized.

Technology	Wing-Mounted Engines			Rear-Mounted Engines			Three-Lifting Surfaces		
	Weight	Drag	Lift and Long. Stability	Weight	Drag	Lift and Long. Stability	Weight	Drag	Lift and Long. Stability
Wing NLF	-	-10dcs	-	-	-20dcs	-	-	-20dcs	-
Fuselage LG and pods	+7%Fuselage	+15dcs (pods)	-	-	-	-	-	-	-
Under-wing engine	-5%Wing	+ 10dcs	-0.2 C_{Lmax} Downwash at Htail 0.25 (at M=0.2)	-	-	-	-	-	-
Rear-mounted engine at Htail tip	-	-	-	+5%Wing +4%Fuselage +65%Htail	-	+0.2 C_{Lmax} +10% C_{LaH} Downwash at Htail 0.32 (at M=0.2)	+5% Wing +4% Fuselage +65% Htail	-	+0.2 C_{Lmax} +10% C_{LaH} Wing-Tail downwash
Canard Installation	-	-	-	-	-	-	+5% Fuselage	-	+0.15C_{Lmax} Downwash at Htail 0.53 (at M=0.2)

Figure 8. Technological assumptions for each considered aircraft configuration.

Wing-mounted engines configuration. This is the state-of-the-art of conventional turboprop configuration with a high-wing and T-tail layout. Thus, the horizontal tail-plane position was fixed according to vertical tail tip chord position with a fixed incidence angle equal to 0.0°. Furthermore, the horizontal tailplane aspect ratio was fixed to about 5.0 with the possibility to scale the span and the planform area. Engines positions were linked to the starting section of the wing outer panel, assuming laminar flow effects to be active only on the outer wing panel. Landing gears were assumed to be mounted in fuselage pods. Their positions were linked to the wing position assuming that wing and landing gears attachments are applied to the same fuselage frame. Furthermore, landing gear pods provide for a higher parasite drag, which was modeled considering an increment of about 15 drag counts. According to Torenbeek [25], wing mass were reduced by 5% due to wing-mounted engines. To account for landing gear fuselage pod installation, a further reduction of 5% of the wing mass was considered. Spoilers' installation effect on wing weight was modeled assuming an increment of the component mass of 2% while, for the fuselage, Torenbeek [25] suggested increasing the estimated mass by 8% due to pressurization effects and by 7% due to landing gears pods.

Rear-mounted engines configuration. This innovative configuration provides for a low-wing configuration with engines installed at the horizontal tailplane tips. This solution would avoid a large engine pylon needed to install a large turboprop engine with a propeller diameter of about 12 ft on the fuselage.

A similar solution is also investigated in [26], where the main configuration criticalities dealing with aircraft weight and balance are highlighted.

From preliminary calculations made by the authors, this configuration will require for a large engine pylon affecting the aircraft aerodynamics and interfering with the horizontal tail plane. A solution could be the adoption of a T-tail configuration. However, a large

pylon would provide an additional lift contribution at high aircraft attitudes leading to a larger longitudinal static stability margin with a detrimental effect on maximum trimmed lift coefficients. Moreover, a T-tail configuration would provide for a heavier vertical tail plane (due to the horizontal tail installation), heavy pylons to hold engines, and a heavier fuselage due to additional structural frames required to hold all the rear aircraft components. Thus, the authors selected a simplified configuration merging the horizontal tail with the pylon. This solution, already investigated within the frame of the European funded project named IRON, could yield to a reduced overall mass increment as well as to provide for a reasonable value of the aircraft longitudinal stability. The horizontal tail is fuselage mounted, and it was assumed to have a variable pitch angle (i_H). The horizontal tailplane Aspect Ratio (AR_H) was fixed at 4.40 for structural considerations regarding the engine installation. Being the considered layout a low-wing configuration, landing gears were assumed to be wing-mounted. This will help to limit the required fuselage pods size to accommodate landing gear legs since only wheels and a small legs portion should be retracted inside them. Thus, the detrimental impact that large fuselage pods could have on fuselage weight and aerodynamic drag will be reduced. According to the selected main landing gear installation, its position was linked to the wing at 60% of the MAC. According to Torenbeek [25], wing mass was increased by 2% to consider for wing spoilers. Concerning the fuselage, Torenbeek [25] suggested increasing the estimated mass by 8% due to pressurization effects and by 4% due to rear engine installation. Moreover, the horizontal tailplane mass was increased by 65% on the base of preliminary evaluations of combined aerodynamic loading and engine inertial contributions. Unlike the wing, the horizontal tailplane usually works with negative aerodynamic loads, thus the engine mass does not provide for load relief effects. Thanks to the rear engine installation, the whole wing was supposed to work in laminar flow conditions, reducing the wing parasite drag of about 20 drag counts.

Three-lifting-surface configuration. This configuration, as well as the rear-mounted engine aircraft, provides for a rear engine installation at the horizontal tailplane tips. As for the previous layout, the horizontal tail was supposed to have a variable pitch angle according to the specific flight phase (same values assumed for the rear-mounted configuration) and the tail aspect ratio was kept constant at 4.40 due to structural reasons linked to the engine installation. The same horizontal tailplane mass increment of 65% was assumed due to the same structural considerations made for the rear-mounted engines solution. The same assumptions also applied for the main landing gear position, horizontal tail mass increment, and laminar flow effects on the wing. The amount of storable fuel is linked to the estimated tank capacity calculated assuming standard spar positions and using the volume equation proposed by Torenbeek [25].

4. Results

Once the MDA analysis cycle for each aircraft model investigated with the DOE was completed, results dealing with some of the most important design objectives were gathered. Figure 9a illustrates the complete cloud of points analyzed by the MDA process for the three-lifting-surface configuration in terms of block fuel versus maximum take-off weight and maximum aerodynamic cruise efficiency. In addition, Figure 9b,c show how the constraint on the static stability margin (S.S.M. $\geq$ 0.0) reduces the number of possible candidate solutions in two different planes: block fuel versus maximum take-off weight and block fuel versus maximum aerodynamic cruise efficiency. Blue circles represent all solutions that are compliant with the imposed constraint on the S.S.M. The same applies for each additional constraint included in the optimization problem.
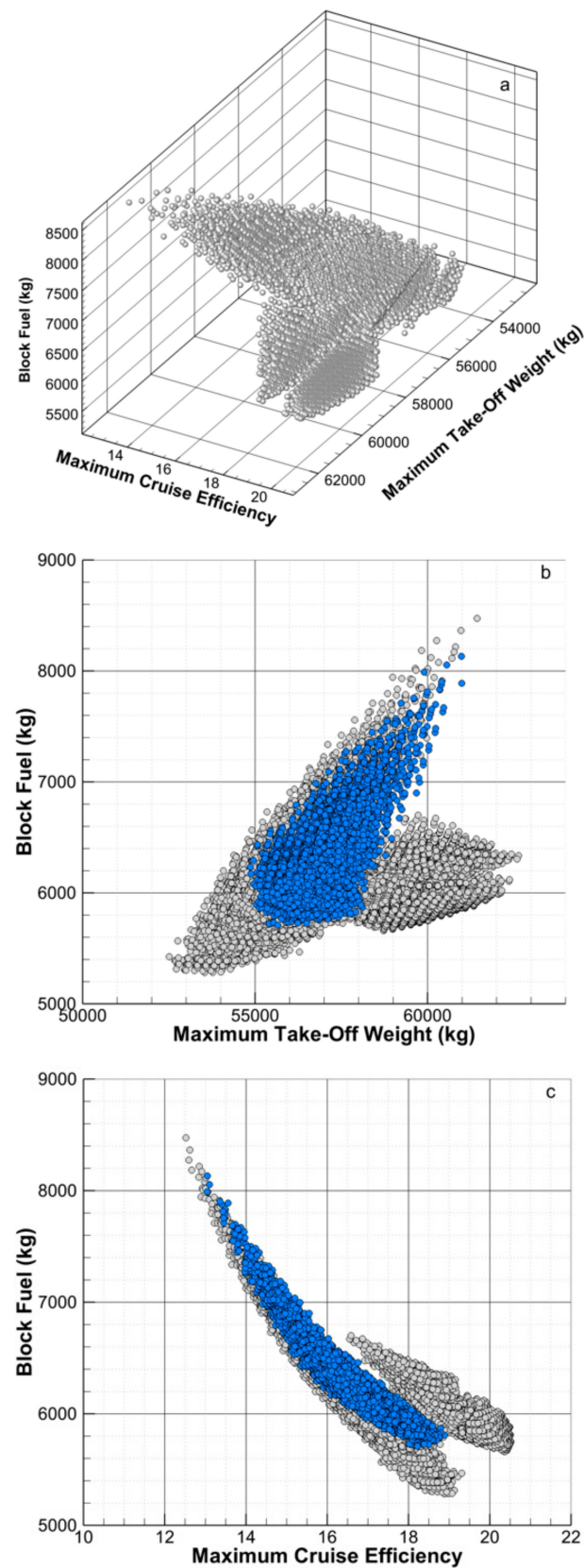
Figure 9. Results of design of experiments for the three-lifting-surface: (**a**) complete cloud of points; (**b**) effect of the S.S.M constraint on possible candidate solutions in the plane block fuel versus MTOW; and (**c**) effect of the S.S.M constraint on possible candidate solutions in the plane block fuel versus cruise maximum efficiency.

The optimization problem defined in Equation (1) was mainly focused on the minimization of the environmental impact provided by each configuration. Thus, the block fuel was considered as the only objective function.

$$
\left\{
\begin{array}{l}
\text{Minimize the Block fuel on a mission range of 1600 NM} \\
\text{with respect to lifting surfaces planform design variables and relative positioning} \\
\text{subject to :} \\
\text{S.S.M} \geq 0.0 \\
\text{Take} - \text{off field lenght \& Landing field length} \leq 1400 \text{ m} \\
\text{Climb time from 1500 ft to 25,000 ft} \leq 16 \text{ min} \\
\text{Cruise Mach number } 0.64 \leq \text{M}_{cr} \leq 0.68 \\
\left\| X_{\text{LG}} - X_{\text{CG,max},aft} \right\| \geq 5\% \text{MAC} \\
\text{Estimated mission fuel} \leq \text{Max storable fuel mass}
\end{array}
\right.
\tag{1}
$$

Although aircraft are typically designed aiming at minimizing the DOC, this quantity was not considered inside the objectives set. Main contributions to DOC are due to aircraft weight, cruise Mach number, and mission block fuel. However, concerning the aircraft weight for a fixed configuration, its variation inside the obtained response surface is mainly due to the mission block fuel. Thus, the effect of the aircraft maximum take-off weight on the DOC is strictly based on the block fuel variation. In addition, following the lessons learned from the EU project IRON, the response surface cruise Mach number variation was limited to a narrow range from 0.64 to 0.68. Those limits were driven by market requirements for the lower bound and by propeller tip compressibility issues for the upper bound. In this range, the effect of the cruise Mach number on the aircraft DOC resulted to be of second order with respect to the mission block fuel. For all these reasons and considering the additional limitations brought by the imposed set of constraints to the DOC value, the latter was not considered as an objective function. However, its value, in terms of both total and cash DOC, was monitored to make a comparison between the optimized configurations.

To demonstrate the above, Figures 10–12 show the variation of the estimated total DOC with respect to the block fuel for each analyzed configuration, highlighting all feasible solutions compliant with the imposed set of constraints. It must be noted that the minimum feasible block fuel almost corresponds to the minimum DOC solution. In addition, the range of variation of the total DOC value for each aircraft configuration resulted to be very limited.
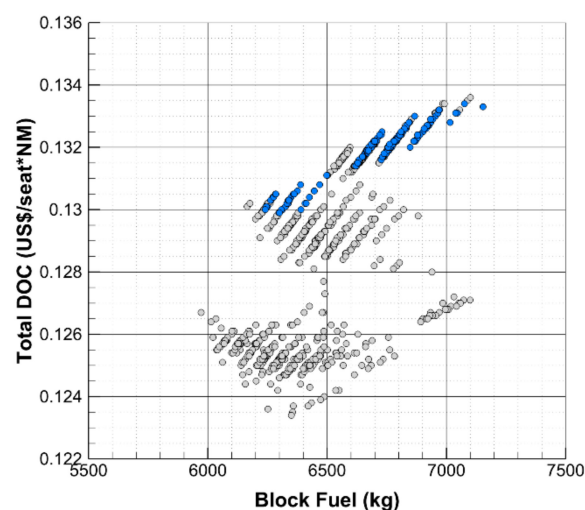

Figure 10. Total DOC versus block fuel for the wing-mounted engines configuration. Blue circles represent the solutions compliant with the imposed set of constraints.
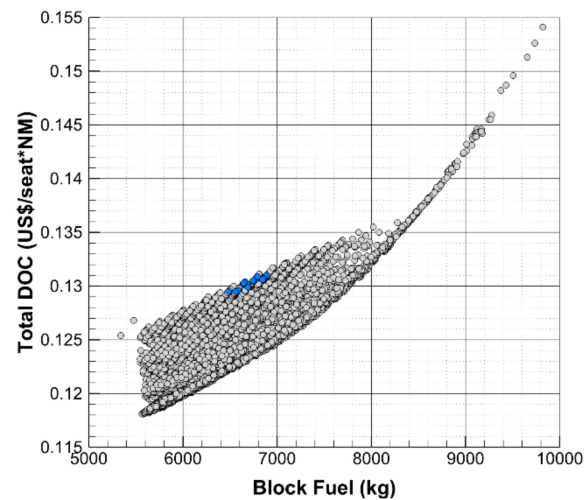
Figure 11. Total DOC versus block fuel for the rear-mounted engines configuration. Blue circles represent the solutions compliant with the imposed set of constraints.
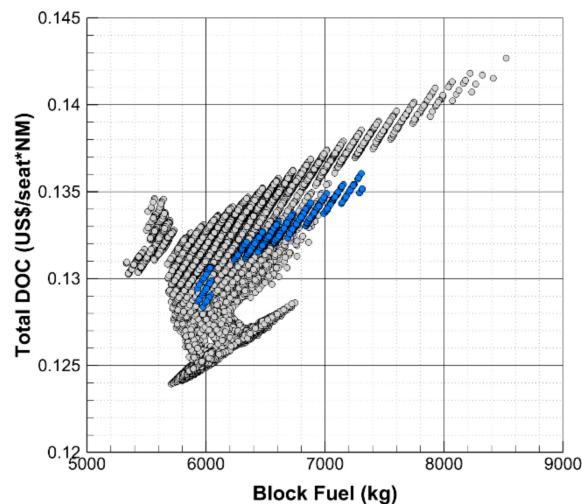
Figure 12. Total DOC versus block fuel for the three-lifting-surface rear-mounted engines configuration. Blue circles represent the solutions compliant with the imposed set of constraints.

Selected optima aircraft models are compared in Figure 13 including a visual representation of their center of gravity excursion, while their main characteristics are summarized in Table 4.

Both the wing- and rear-mounted engine aircraft are characterized by a wing area of about 105 m^2 and wing aspect ratio of about 12, while the three-lifting-surface aircraft has a reduced wing area (about 100 m^2) thanks to the additional lift contribution provided by the canard.

The two configurations with rear-mounted engines present a very large horizontal tail area (about 44% of the wing area) due to the need to balance a very large center of gravity excursion, as illustrated in the boarding diagrams from Figure 13.

Nevertheless, the three-lifting-surface configuration presents a higher aerodynamic cruise efficiency thanks to the positive effect of the forward lifting surface (the canard) on the global trim drag contribution. It is worth noticing that the total aircraft wetted area (which is linked to the parasite drag) is slightly higher for the three-lifting-surface compared with the rear-mounted engine configuration.

All three optimal configurations are stable with respect to the most aft center of gravity position with a reduced Static Stability Margin (S.S.M.), as shown in Table 4. In the authors'

opinion, the obtained S.S.M. value is acceptable and compliant with an improved flight control system, which is forecasted for entry into service 2035.

Using the main performance and DOC as rules of comparison of the three optimal large capacity turboprop configurations, the three-lifting-surface configurations was proven to be the best solution among the considered layouts. In fact, although with very similar values of ground performance, the three-lifting-surface aircraft provides for the lowest value of the block fuel, thanks to the improved cruise aerodynamic efficiency, as well as for the lowest maximum take-off weight.

Despite the additional component, the main reason behind the three-lifting-surface configuration reduced max take-off weight is related to the different engine weight coupled with a lower amount of block fuel. Focusing on the engine mass, this value was linked to the value of the static thrust inside the workflow in Figure 6, where, to match both the required take-off field length and cruise Mach number, the static thrust was adjusted iteratively.
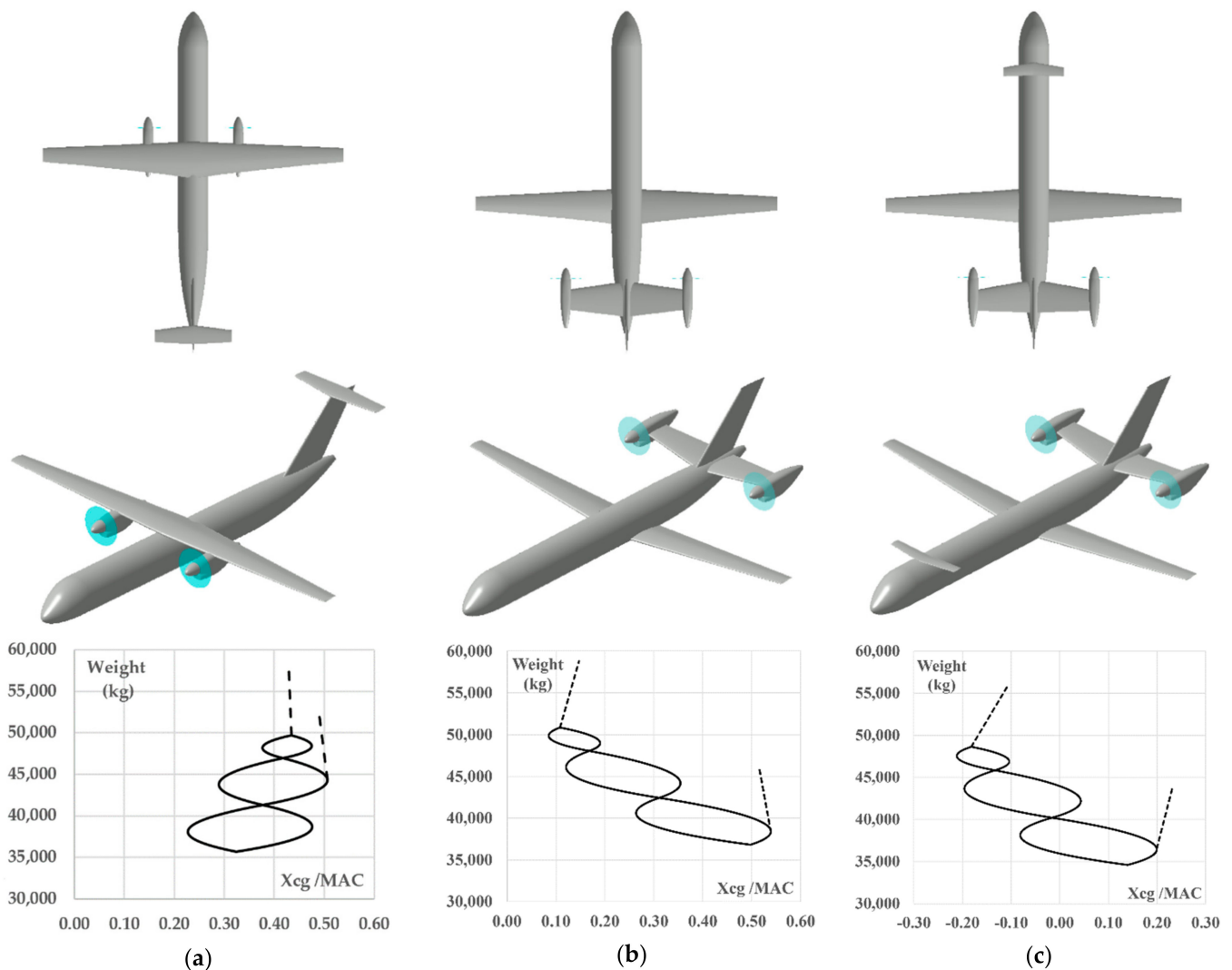

Figure 13. Selected optima solutions for each aircraft configuration: (**a**) optimized high wing with under wing-mounted engines configuration and its boarding diagram; (**b**) optimized low wing with rear-mounted engines configuration and its boarding diagram; and (**c**) optimized three-lifting-surface with rear-mounted engines configuration and its boarding diagram.

Table 4. Comparison between optima large capacity turboprop configurations.

Parameters	Wing Mounted Engines	Rear Mounted Engines	Three-Lifting-Surface
Wing area, S_w (m^2)	104.4	104.6	101.2
Horizontal tail area, S_H (m^2)	16.83	46.5	44.82
Vertical tail area, S_V (m^2)	25.0	25.0	25.0
Canard area, S_C (m^2)	-	-	9.37
Wing aspect ratio, AR_w	12.07	12.04	12.02
Horizontal tail aspect ratio, AR_H	5.00	4.40	4.40
Vertical tail aspect ratio, AR_V	1.37	1.37	1.37
Canard aspect ratio, AR_C	-	-	5.57
Fuselage length, l_f (m)	38.04	38.04	38.04
Fuselage diameter, d_f (m)	3.535	3.535	3.535
Single engine static thrust, T_0 (lbf)	23,603	26,054	23,027
Single Engine Mass (kg)	3367	4122	3297
Max Take-Off Weight (kg)	57,419	58,794	56,640
Operating Empty Weight (kg)	35,665	36,820	34,593
Design Payload (kg)	14,040	14,040	14,040
Max forward CG (% MAC)	22.7%	8.5%	1.2%
Max afterward CG (% MAC)	50.6%	53.9%	23.3%
Aerodynamic cruise efficiency (at 97% MTOW)	16.7	16.6	17.6
Maximum aerodynamic cruise efficiency	18.4	17.8	18.8
Static Stability Margin (%)	3.64	1.16	1.95
C_{Lmax}	1.63	1.57	1.79
$C_{Lmax, TO}$	2.39	2.30	2.52
$C_{Lmax, LND}$	2.97	2.86	3.10
Take-Off Field Length (m)	1396	1380	1380
Landing Field Length (m)	1339	1384	1336
Climb Time (1500 ft–25,000 ft at 190 kt) (min)	15.0	13.0	15.7
Max Cruise Mach Number	0.64	0.67	0.66
Block time—1600 NM (min)	239	234	237
Block fuel—1600 NM (kg)	6259	6479	5958
Total DOC—1600 NM (¢/seat NM)	13.02	12.95	12.83
Cash DOC—1600 NM (¢/seat NM)	7.68	7.70	7.54

By comparing the three-lifting-surface configuration with the rear-mounted engines configuration, the single engine mass is reduced by about 1000 kg (2000 kg for both engines), which justifies the difference in the maximum take-off weight and the lower value of the three-lifting-surface configuration block fuel. On the other hand, the comparison between the three-lifting-surface model and the high wing with wing-mounted engines configuration highlights similar static thrust and engine weight values. However, the reduced aerodynamic efficiency of the wing-mounted engines configuration, due to the set of assumptions shown in Figure 8, coupled with a heavier fuselage led to higher values of both maximum take-off weight and block fuel with respect to the three-lifting-surface model.

A reduced block fuel mass is also linked to a lower amount of pollutant emissions (at fixed engine database); thus, the three-lifting-surface configuration resulted to be the greenest among the investigated configurations. Moreover, thanks to a lighter structure (lowest Operating Empty Weight (OEW)) and the reduced amount of fuel needed for the design mission of 1600 NM, this aircraft also provided the lowest total DOC and cash DOC. Those are mainly influenced by the block fuel mass, the block time, and the aircraft utilization, expressed in terms of block hours per year and calculated as proposed in the book by Kundu [27].

The reference regional jet aircraft was modeled using the JPAD software considering a set of TLARs related to the Airbus A220-300. The main information concerning this aircraft was retrieved from several public sources, including the aircraft manual, the European

Aviation Safety Agency (EASA) type-certificate data sheets, public aircraft data archives, and the Base of Aircraft Data (BADA) database considering aircraft models similar to the A220-300 [28–32]. A data summary of the most important aircraft characteristics is provided in Table 5.

Table 5. Main data concerning the A220-300.

| TLAR	
Accommodation (Typical-Full Economy)	135
Design range (typical)	3100 NM
Take-Off Field Length (Max Take-Off Weight, ISA conditions, Sea Level)	1890 m
Landing Field Length (Max Take-Off Weight, ISA conditions, Sea Level)	1509 m
Cruise Mach number (typical)	0.78
Cruise altitude (typical)	37,000 ft
Max cruise Mach number at 37,000 ft	0.82
Max operating altitude	41,000 ft
Alternate cruise range (assumed by authors)	200 NM
Alternate cruise altitude (assumed by authors)	20,000 ft
Holding duration (assumed by authors)	30 min
Holding altitude (assumed by authors)	1500 ft/min
Residual fuel reserve (assumed by authors)	5%
Geometrical and Operational Data	
Wing area	112.3 m^2
Wingspan	35.1 m
Wing aspect ratio	10.97
Fuselage length	38.71 m
Fuselage diameter	3.7 m
Single engine static thrust	24,400 lbf
Engine by-pass ratio	12:1
Max Take-Off Weight	67,585 kg
Max Landing Weight	58,740 kg
Max Zero-Fuel Weight	55,792 kg
Operating Empty Weight	37,081 kg
Max Payload	18,711 kg
Max Fuel Mass	17,726 kg
BADA averaged climb speed (CAS)	271 kt
BADA averaged rate of climb	1642 ft/min
BADA maximum rate of climb	2862 ft/min
BADA averaged descent speed (CAS)	218 kt
BADA averaged rate of descent	2186 ft/min
BADA maximum rate of descent	3700 ft/min

A complete case study concerning this aircraft model and its implementation inside the JPAD software was carried out by authors and reported in [33]. Here, starting from publicly available data concerning the aircraft geometry and using the aircraft 3-views for the geometry digitization process, a parametric model was generated. The latter was used to perform a complete multi-disciplinary analysis cycle, as described in Figure 6, neglecting the static thrust update loop but including the mission fuel feedback loop.

It must be noted that, in terms of DOC, the fuel price value needed to perform the analysis was assumed according to IATA fuel price monitor [34], while aircraft price was assumed considering reference data reported in [35]. Engine unit costs were deducted from [36] as well.

The main output of the JPAD multi-disciplinary analysis was compared with aircraft data reported in Table 5 to validate the calculation case. A summary of this comparison is reported in Table 6, while a comparison in terms of payload–range diagram is provided in Figure 14, where the main differences between the two charts can be addressed to the gap between the values of the Max Zero-Fuel Weight (MZFW), the OEW, and the max fuel mass of the A220-300 with respect to the values calculated by JPAD.

Table 6. Comparison between JPAD output and A220-330 data in Table 5.

Parameters	JPAD	A220-300 (Table 5)	Difference (%)
Max Take-Off weight (kg)	66,911	67,585	−1.00%
Max Landing weight (kg)	56,875	58,740	−3.18%
Max fuel mass (kg)	17,233	17,726	−2.78%
Max Zero-Fuel Weight (kg)	55,017	55,792	−1.39%
Operating Empty Weight (kg)	36,306	37,081	−2.09%
Take-Off Field Length (m)	1814	1890	−4.02%
Landing Field Length (m)	1575	1509	+4.37%
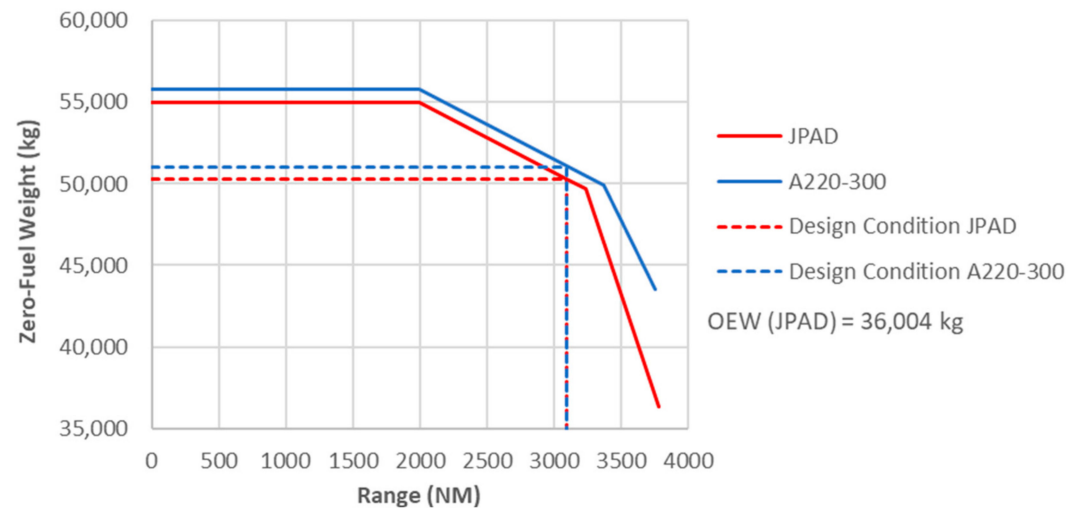
Figure 14. Payload–range chart calculated with JPAD compared with the A220-300 Payload-Range chart. Adapted from ref. [28].

Once the A220-300 JPAD model was validated, it was used to perform an additional simulation considering the design range from the set of TLARs in Table 1. In addition, to compare this reference regional jet with all three optimal turboprop aircraft layouts, its payload mass was modified to comply with the design payload of 14,040 kg used for each high-capacity turboprop configuration.

Finally, a comparison between the three optimal configurations and a reference regional jet platform, assumed as the Airbus A220-300, is presented in Table 7 considering a mission of 1600 NM.

As shown in Table 7, all high-capacity turboprop configurations provide a beneficial effect on the amount of block fuel related to the design mission of 1600 NM. However, it must be noted that the considered reference regional jet is designed for a mission range of 3300 NM, thus the aerodynamic efficiency and the take-off weight are not optimized for a 1600 NM mission range. Although this seems to be an unfair comparison, it must be highlighted that this study aims to compare the benefit in terms of fuel consumption that a new large capacity turboprop, specifically designed for short/medium haul, would have with respect to the existing state-of-the-art RJ also currently operated on this kind of missions.

In addition to this comparison, the authors also designed a possible new regional jet aircraft using the same set of TLARs of the turboprop aircraft. Only the cruise Mach number was shifted from 0.64 to 0.78 since this is a jet-driven aircraft. This comparison, shown in Table 7, was added to demonstrate that, even if a regional jet specifically designed on such a mission range existed, the proposed large turboprop aircraft would still provide benefits in terms of environmental impact. The major drawback of the turboprop solution is represented by a higher total DOC value mainly due to the reduced block speed.

Table 7. Comparison with the reference regional jet in terms of block time, block fuel, and DOC (percent differences, in brackets, with respect to the regional jet).

Design Mission: 1600 NM	Wing Mounted Engines	Rear Mounted Engines	Three-Lifting-Surface	RJ Designed at 1600 NM	Ref. RJ
Take-off weight (kg)	57,419 (−3.11%)	58,794 (−0.79%)	56,640 (−4.42%)	54,378 (−8.24%)	59,260
Cruise Mach number	0.64 (−17.95%)	0.67 (−14.10%)	0.66 (−15.38%)	0.78 (+0.0%)	0.78
Aerodynamic Cruise efficiency	16.7 (0.0%)	16.6 (−0.60%)	17.6 (+5.38%)	17.2 (+2.99%)	16.7
Relative cruise SFC (w.r.t. RJ)	−19.22%	−17.02%	−18.56%	-	-
Utilization (h/year)	3353 (+0.60%)	3346 (+0.39%)	3350 (+0.51%)	3329 (−0.12%)	3333
Block Time (min)	239 (+6.22%)	234 (+4.00%)	237 (+5.33%)	222 (−1.33%)	225
Block Fuel (kg)	6259 (−10.40%)	6479 (−7.24%)	5958 (−17.24%)	6569 (−5.96%)	6985
Total DOC (¢/seat*NM)	13.02 (−13.37%)	12.95 (−13.84%)	12.83 (−14.63%)	12.03 (−19.96%)	15.03
Cash DOC (¢/seat*NM)	7.68 (−7.69%)	7.70 (−7.45%)	7.54 (−9.37%)	8.32 (+0.00%)	8.32

The design of this new regional jet was accomplished using the same multi-disciplinary analysis and optimization workflow adopted for all proposed turboprop configurations. Starting from the TLARs shown in Table 1 and considering as baseline the JPAD parametric model of the A220-300, the set and ranges of design parameters reported in Table 8 were considered.

Table 8. Variables design space for the regional jet model designed on a 1600 NM mission profile.

Parameters	Wing Design Parameters
Span b_w (m)	32.0–35.1
Longitudinal position $X_{LE,W}$ (m)	10.0–13.0
Aspect Ratio AR_w	9.10–12.19
Sweep at leading edge $\Lambda_{LE,W}$ (°)	25.0–35.0
	Horizontal Tailplane Design Parameters
Span b_H (m)	10.75–13.14
Longitudinal position $X_{LE,H}$ (m)	31.6 fixed value
Aspect Ratio AR_H	5.12 fixed value
Sweep at leading edge $\Lambda_{LE,H}$ (°)	$\Lambda_{LE,W}$ + 5.0

The optimization problem carried out for this aircraft is represented in Equation (2) where the block fuel was assumed as the only objective function. It must be noted that the optimization problem is the same as the one considered for all turboprop aircraft, except for the time to climb condition and the cruise Mach number, which was considered to change in the range from 0.78 to 0.82 corresponding to the typical and maximum Mach numbers of the A220-300, respectively. The previous climb time condition was not included in the set of constraints since this aircraft is supposed to operate at a higher cruise altitude (37,000 ft instead of 30,000 ft).

$$
\begin{cases}
\text{Minimize the Block fuel on a mission range of 1600 NM} \\
\text{with respect to lifting surfaces planform design variables and relative positioning} \\
\text{subject to :} \\
\text{S.S.M} \geq 0.0 \\
\text{Take} - \text{off field lenght \& Landing field length} \leq 1400 \text{ m} \\
\text{Cruise Mach number } 0.78 \leq M_{cr} \leq 0.82 \\
\left\| X_{LG} - X_{CG,max,aft} \right\| \geq 5\% MAC \\
\text{Estimated mission fuel} \leq \text{Max storable fuel mass}
\end{cases}
\tag{2}
$$

The MDA workflow adopted for the analysis of each regional jet models included in the design space was the same as the one shown in Figure 6, where the engine static thrusts were modified iteratively to match the requirements in terms of cruise Mach number and take-off field length. However, the rubberized engine database used for the performance

simulation was the same used to analyze the A220-300 parametric model, thus the same SFC was considered at fixed altitude and cruise Mach number.

To make a fair comparison with the optima turboprop solutions, the selection of the optimum regional jet aircraft was driven by the minimization of the block fuel targeting the lowest environmental impact. The DOC was estimated only for comparison purposes.

A geometrical comparison between the baseline regional jet model and the selected optimum jet aircraft is shown in Figure 15.
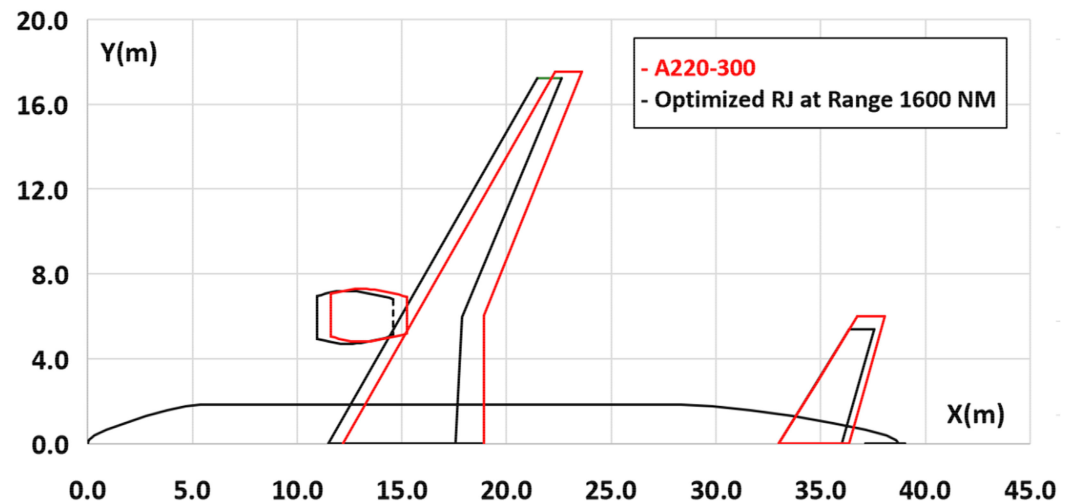

Figure 15. Comparison between top views of the baseline regional jet model (red) and the selected optimum regional jet aircraft (black).

Starting from the results shown in Table 7, a first comparison that can be made is between the proposed turboprop solutions and the existing state of the art regional jet (the last column of Table 7) typically operated on short/medium haul with a seats capacity similar to the required value of 130.

Focusing on each turboprop platform, the high-wing configuration with wing-mounted engines has the greatest advantage in terms of mean cruise SFC with a reduction of -19.22% and provides for the second best reduction in take-off weight (-3.11%). However, the cruise aerodynamic efficiency shows no improvements, with respect to the reference regional jet, and the cruise Mach number is the lowest among all analyzed turboprop aircraft models. Thus, this configuration is the worst in terms of block time providing for an additional little negative effect on the block fuel.

From the combination of all these effects, this aircraft may be a good candidate to challenge a regional jet on this kind of missions with an overall block fuel reduction of 0.40% and only 15 min of additional block time. In term of DOC, good results were reached as well, with a reduction of -13.37% in total DOC and -7.68% in cash DOC. However, despite the beneficial effect provided by the smaller block fuel mass, this aircraft is the worst in terms of both utilization and block time, leading to the lowest reduction in total DOC. On the other hand, being the effect of the block fuel much more effective on the cash DOC rather than on the total DOC, this configuration provides for a slightly lower cash DOC value with respect to the one with low-wing and rear-engine installation.

The second high-capacity turboprop configuration showed the lowest reduction in term of block fuel (-7.24%), with respect to the reference regional jet, since the beneficial effect provided by the smaller value of the mean cruise SFC (-17.02%) is mitigated by a very little reduction in MTOW (-0.79%) and a lower value of the cruise aerodynamic efficiency (-0.60%). On the other hand, the cruise Mach number was the greatest among all analyzed turboprop configurations, leading to the lowest increment in block time with respect to the reference regional jet. However, being this effect very limited, the related effect on the block fuel is also very limited. In terms of DOC, comparing this configuration with all other turboprop platforms, the lower block time provides for a better value of the

utilization parameter which positively affects all costs contributions. Major drawbacks are provided by the increased amount of block fuel (and so of the fuel price) and by the take-off weight (the highest among all turboprop configurations) which influences maintenance costs. However, those effects are smaller than the one provided by the utilization, making this aircraft the second best solution in terms of total DOC reduction with respect to the reference regional jet. As for the previous case, the effect of the block fuel on the cash DOC is much more effective than on the total DOC, providing for the worst reduction of this value.

As stated above, the three-lifting-surface configuration resulted to be the best turboprop configuration. This was further confirmed by the comparison with the reference regional jet, from which this innovative high-capacity turboprop aircraft has highlighted the greatest reduction both in term of block fuel and DOC. In particular, this aircraft provided a mean cruise SFC reduction similar to the first configuration (-18.56% instead of -19.22%) together with the lowest value of the take-off weight and the highest value of the cruise aerodynamic efficiency (-4.42% and $+5.38\%$, respectively, if compared to the reference regional jet). A cruise Mach number slightly lower than the second configuration led to intermediate values of both block time and utilization between the first two analyzed aircraft models.

A second comparison that can be made is between the proposed turboprop solutions with the regional turboprop designed according to the same set of TLARs.

Considering that this aircraft was optimized on the same set of TLARs adopted for each turboprop aircraft, the amount of block fuel needed to operate the 1600 NM design mission is obviously reduced with respect to the one related to the A220-300 parametric model. Although with block fuel values in line with some of the analyzed optima turboprop models, the three-lifting-surface configuration still provide for a beneficial effect in terms of environmental impact with respect to this possible regional jet model achieving a fuel saving of about 611 kg (-9.30%).

Conversely, the new regional jet represents the best solution in terms of total DOC having both an improved block time with respect to the optima turboprop aircraft and the lowest take-off weight. In particular, by comparing the three-lifting-surface configuration with this newly designed regional jet, there is a total DOC increment of about $+6.65\%$. However, dealing with the cash DOC, which is not influenced by the beneficial effect provided by a reduced take-off weight, the three-lifting-surface configuration allows achieving the same cost saving shown with respect to the A220-300 model of about -9.37%. Thus, the proposed three-lifting-surface configuration represents the best solution in terms of both environmental impact and cash DOC.

5. Conclusions

This paper considers the possible design of a modern high-capacity turboprop aircraft that could potentially reduce the environmental impact of regional aircraft with respect to the current state-of-the-art regional jet widely adopted on short/medium hauls. The study investigated three possible architectural solutions for a large capacity turboprop aircraft. A multi-disciplinary analysis and optimization process was carried out to assess the best solution complying with the imposed design space boundaries and operative constraints.

By comparing the results obtained for each optimum turboprop aircraft with respect to a reference regional jet model, represented by the Airbus A220-300 operated on a range of 1600 NM, this study highlighted a maximum potential fuel saving of about -17.24% considering a three-lifting-surface configuration.

In addition, to make a fair comparison between the analyzed turboprop aircraft platforms and a regional jet, a brand-new turbofan aircraft was designed using the same set of TLARs used for the turboprop configurations. It must be noted that such a regional jet aircraft, coupling a design range of 1600 NM with a seat capacity of 130 passengers, does not exist in the current regional market scenario. By comparing the best analyzed turboprop configuration with this regional jet model, the initial block fuel saving of 7.24% reaches a

lower value of −5.96%, still proving that a modern optimized turboprop platform could provide for a beneficial effect in terms of environmental impact.

For the sake of completeness, a comparison between all optimal turboprop configurations and both the analyzed regional jet models was carried out also in terms of DOC. Starting with the existing reference regional jet model, being the latter not optimized on a 1600 NM mission range, all turboprop models provide for a cost reduction in terms of both total and cash DOC (max reduction of about −14.63%). However, considering a regional jet specifically designed for such a mission range, it can be highlighted that the jet aircraft represents the best solution in terms of total DOC (−6.65% with respect to the best analyzed turboprop configuration) but not in terms of cash DOC due to the higher block fuel (+9.37% with respect to the best analyzed turboprop configuration).

Since this work is not focused on the investigation of the best possible turboprop aircraft architecture, implementing future technologies or layouts, the performed investigation only considered three possible configurations of a large capacity turboprop assumed to be compliant with an entry into service by the year 2035. A wider study, extended to a larger portfolio of innovative, or even disruptive, configurations should be performed to find a better solution with respect to the one proposed in this paper.

Author Contributions: Conceptualization, S.C.; funding acquisition, F.N.; investigation, S.C. and V.T.; methodology, S.C. and V.T.; software, S.C., V.T. and A.D.M.; supervision, F.N.; writing—original draft, S.C. and V.T.; writing—review & editing, F.N. and A.D.M. All authors have read and agreed to the published version of the manuscript.

Institutional Review Board Statement: Not applicable.

Informed Consent Statement: Not applicable.

Data Availability Statement: The data presented in this study are available on request from the corresponding author. Since this work has its roots in findings of a European research project involving several industrial partners data are not publicly available.

Conflicts of Interest: The authors declare no conflict of interest.

Abbreviations

The following abbreviations are used in this manuscript.

APU	Auxiliary Power Unit
ATAG	Air Transport Action Group (www.atag.org)
ATR	Avions de Transport Régional (www.atr-aircraft.com)
BADA	Base of Aircraft Data (www.eurocontrol.int/model/bada)
CAS	Calibrated Air Speed
CG	Center of Gravity
CS2	Clean Sky 2 (www.cleansky.eu)
DOC	Direct Operating Cost
DOE	Design of Experiments
EASA	European Aviation Safety Agency (www.easa.europa.eu)
EU	European Union
FAA	United States Federal Aviation Administration (www.faa.gov)
FL	Flight Level

IATA	International Air Transport Association (www.iata.org)
ICAO	International Civil Aviation Organization (www.icao.int/Pages/default.aspx9)
IRON	Innovative turbopROp configuration
ISA	International Standard Atmosphere
JPAD	Java tool chain of Programs for Aircraft Design
LFL	Landing Field Length
LG	Landing Gear
MAC	Mean Aerodynamic Chord
MDA	Multi-Disciplinary Analysis
MDAO	Multi-Disciplinary Analysis and Optimization
MLW	Maximum Landing Weight
MTOW	Maximum Take-Off Weight
MZFW	Max Zero-Fuel Weight
NASA	United States National Aeronautics and Space Administration (www.nasa.gov)
NLF	Natural Laminar Flow
OEW	Operating Empty Weight
RJ	Regional Jet
S.S.M.	Static Stability Margin
SFC	Specific Fuel Consumption
TLARs	Top-Level Aircraft Requirements
TOFL	Take-Off Field Length

Symbols

The following symbols are used in this manuscript.

¢	United States dollar cent
AR_C	canard aspect ratio
AR_H	horizontal tailplane aspect ratio
AR_V	vertical tail aspect ratio
AR_W	wing aspect ratio
b_C	canard span
b_H	horizontal tailplane span
b_W	wingspan
$C_{L\alpha,H}$	horizontal tail lift curve slope
C_{Lmax}	maximum lift coefficient
$C_{Lmax,LND}$	maximum lift coefficient at landing
$C_{Lmax,TO}$	maximum lift coefficient at take-off
C_{O2}	carbon dioxide
dcs	drag counts
d_f	fuselage diameter
i_H	horizontal tailplane root incidence angle
l_f	fuselage length
M	Mach number
M_{cr}	cruise Mach number
NM	nautical mile
NO_X	nitrogen dioxide
S_C	canard area
S_H	horizontal tailplane area
S_V	vertical tailplane area
S_W	wing area
T_0	single engine static thrust
US$	United States dollar
$\Lambda_{LE,C}$	canard sweep angle at the leading edge
$\Lambda_{LE,H}$	horizontal tailplane sweep angle at the leading edge
$\Lambda_{LE,W}$	wing sweep angle at the leading edge
X_{cg}	center of gravity longitudinal position
$X_{CG,max,aft}$	max aft center of gravity longitudinal position
$X_{LE,C}$	canard root leading edge longitudinal position
$X_{LE,H}$	horizontal tail root leading edge longitudinal position
$X_{LE,W}$	wing root leading edge longitudinal position
X_{LG}	main landing gear longitudinal position

References

1. Climate Change. Available online: https://perma.cc/X2GW-2J8N (accessed on 25 January 2021).
2. Scholz, D. Review of CO_2 Reduction Promises and Visions for 2020 in Aviation. In Proceedings of the Deutscher Luft- und Raumfahrtkongress 2020 (DLRK 2020), Online, 1–3 September 2020. [CrossRef]
3. European Union. Clean Sky 2 Joint Undertaking Development Plan. Available online: https://perma.cc/JL26-EGYQ (accessed on 30 April 2021).
4. ICAO, Air Transport Bureau. Effects of Novel Coronavirus (Covid-19) on Civil Aviation: Economic Impact Analysis. Available online: https://perma.cc/AU9L-48B7 (accessed on 30 April 2021).
5. Airbus. Global Market Forecast 2018–2037. Available online: https://perma.cc/5WT8-GSDB (accessed on 30 April 2021).
6. ATR. Turboprop Market Forecast 2018–2037. Available online: https://perma.cc/X4VZ-JKW8 (accessed on 30 April 2021).
7. Nicolosi, F.; Corcione, S.; Della Vecchia, P.; Trifari, V.; Ruocco, M. Aerodynamic design and analysis of an innovative regional turboprop configuration. In Proceedings of the 31st ICAS Conference (International Council of the Aeronautical Sciences), Belo Horizonte, Brazil, 9–14 September 2018; Available online: https://hdl.handle.net/11588/736423 (accessed on 30 April 2021).
8. Nicolosi, F.; Corcione, S.; Della Vecchia, P.; Trifari, V.; Ruocco, M.; De Marco, A. Design and aerodynamic analysis of a regional turboprop innovative configuration. In Proceedings of the Aerospace Europe 6th CEAS Conference, Bucharest, Romania, 16–20 October 2017; Council of European Aerospace Societies: Brussels, Belgium, 2017. Available online: https://hdl.handle.net/11588/696609 (accessed on 30 April 2021).
9. Corcione, S.; Nicolosi, F.; Della Vecchia, P.; Ciliberti, D.; Cusati, V. High lift aerodynamic characteristics of a three lifting surfaces turboprop aircraft. In Proceedings of the AIAA Aviation 2019 Forum, Dallas, TX, USA, 17–21 June 2019; American Institute of Aeronautics and Astronautics: Reston, VA, USA, 14 June 2019. AIAA 2019–2884. [CrossRef]
10. Nicolosi, F.; Corcione, S.; Trifari, V.; Cusati, V.; Ruocco, M.; Della Vecchia, P. Performance evaluation and DOC estimation of an innovative turboprop configuration. In Proceedings of the 2018 Aviation Technology, Integration, and Operations Conference, Atlanta, Georgia, 25–29 June 2018; American Institute of Aeronautics and Astronautics: Reston, VA, USA, 24 June 2018. AIAA 2018–3662. [CrossRef]
11. Nicolosi, F.; Corcione, S.; Ciliberti, D.; Cusati, V. Aerodynamic characteristics of an innovative large turboprop through wind tunnel tests including propulsive effects. In Proceedings of the AIAA AVIATION 2020 FORUM, Virtual Event, 15–19 June 2020; American Institute of Aeronautics and Astronautics: Reston, VA, USA, 8 June 2020. AIAA 2020–2623. [CrossRef]
12. Cusati, V.; Nicolosi, F.; Corcione, S.; Ciliberti, D.; Della Vecchia, P. Longitudinal stability issues including propulsive effects on an innovative commercial propeller-driven aircraft. In Proceedings of the AIAA Aviation 2019 Forum, Dallas, TX, USA, 17–21 June 2019; American Institute of Aeronautics and Astronautics: Reston, VA, USA, 14 June 2019. AIAA 2019–2882. [CrossRef]
13. Bombardier Commercial Aircraft. Market Forecast 2017–2036. Available online: https://perma.cc/9Q7A-753T (accessed on 30 April 2021).
14. Goldsmith, M. *A Study to Define the Research and Technology Requirements for Advanced Turbo/Propfan Transport Aircraft*; NASA: Washington, DC, USA, 1981. Available online: https://core.ac.uk/display/42857722 (accessed on 30 April 2021).
15. Whitlow, J.B., Jr.; Siviers, G.K. *Fuel Savings Potential of the NASA Advanced Turboprop Program*; NASA: Washington, DC, USA, 1984. Available online: https://core.ac.uk/display/42848326 (accessed on 30 April 2021).
16. Sullivan, W.E.; Turnberg, J.E.; Violette, J.A. *Large-Scale Advanced Prop-Fan (Lap) Blade Design*; NASA: Washington, DC, USA, 1984. Available online: https://core.ac.uk/display/42834130 (accessed on 30 April 2021).
17. Johanning, A.; Scholz, D. Novel Low-Flying Propeller-Driven Aircraft Concept for Reduced Direct Operating Costs and Emissions. In Proceedings of the 28th Congress of the International Council of the Aeronautical Sciences, ICAS 2012, Brisbane, Australia, 23–28 September 2012; Optimage Ltd.: Edinburgh, UK, 2012. ISBN 978-0-9565333-1-9. Available online: http://Airport2030.ProfScholz.de (accessed on 30 April 2021).
18. Johanning, A.; Scholz, D. Investigation of a Novel Turboprop-Driven Aircraft Concept Including Future Technologies. In *Innovative Design and Development Practices in Aerospace and Automotive Engineering*; Bajpai, R., Chandrasekhar, U., Eds.; Springer: Singapore, 2016; Lecture Notes in Mechanical Engineering; Available online: http://india.ProfScholz.de (accessed on 28 April 2021). [CrossRef]
19. Vos, R.; Hoogreef, M.F.M. A System-Level Assessment of Tail-Mounted Propellers for Regional Aircraft. In Proceedings of the 31st ICAS Conference (International Council of the Aeronautical Sciences), Belo Horizonte, Brazil, 9–14 September 2018; Available online: http://resolver.tudelft.nl/uuid:a1674c88-2df1-4365-8c3a-efde47de7f8c (accessed on 30 April 2021).
20. ICAO Aerodrome Reference Code. Available online: https://perma.cc/UD6U-EUJ9 (accessed on 30 April 2021).
21. Nicolosi, F.; De Marco, A.; Attanasio, L.; Della Vecchia, P. Development of a java-based framework for aircraft preliminary design and optimization. *J. Aerosp. Inf. Syst.* **2016**, *13*, 234–242. [CrossRef]
22. De Marco, A.; Cusati, V.; Trifari, V.; Ruocco, M.; Nicolosi, F.; Della Vecchia, P. A Java Toolchain of Programs for Aircraft Design. In Proceedings of the Aerospace Europe 6th CEAS Conference, Bucharest, Romania, 16–20 October 2017; Council of European Aerospace Societies: Brussels, Belgium, 2017. Available online: http://hdl.handle.net/11588/696606 (accessed on 30 April 2021).
23. Trifari, V.; Ruocco, M.; Cusati, V.; Nicolosi, F.; De Marco, A. Multi-Disciplinary Analysis and Optimization Java Tool for Aircraft Design. In Proceedings of the 31st ICAS Conference (International Council of the Aeronautical Sciences), Belo Horizonte, Brazil, 9–14 September 2018. Available online: http://hdl.handle.net/11588/748237 (accessed on 30 April 2021).

24. De Marco, A.; Trifari, V.; Nicolosi, F.; Ruocco, M. A Simulation-Based Performance Analysis Tool for Aircraft Design Workflows. *Aerospace* **2020**, *7*, 155. [CrossRef]

25. Torenbeek, E. *Synthesis of Subsonic Airplane Design*; Delft University Press: Delft, The Netherlands, 1976; ISBN 978-94-017-3202-4. Available online: http://resolver.tudelft.nl/uuid:229f2817-9be9-49b6-959a-d653b5bac054 (accessed on 30 April 2021).

26. Schouten, T.J.E. Assessment of Conceptual High-Capacity Regional Turbopropeller Aircraft. Master's Thesis, Aerospace Engineering at Delft University of Technology, Delft, The Netherlands, 30 April 2018. Available online: http://resolver.tudelft.nl/uuid: 236ad212-eb0b-443d-a40d-602ec6fe64f9 (accessed on 30 April 2021).

27. Kundu, A.K. *Aircraft Design*; Cambridge University Press: Cambridge, UK, 2010; ISBN 9780511844652. [CrossRef]

28. Airport Planning Publication. Tech. Rep. BD500-3AB48-32000-00 Issue 13. Available online: https://perma.cc/PKT3-K4QP (accessed on 30 April 2021).

29. Type-Certificate Data Sheet for BD-500 (A220 Series). In *Tech. Rep. EASA.IM.A.570*; European Aviation Safety Agency (EASA): Cologne, Germany, 2019. Available online: https://perma.cc/2TUL-KALL (accessed on 30 April 2021).

30. Type-Certificate Data Sheet for PW1500G Series Engines. In *Tech. Rep. EASA.IM.A.090*; European Aviation Safety Agency (EASA): Cologne, Germany, 2018. Available online: https://perma.cc/L243-JHZU (accessed on 30 April 2021).

31. BOMBARDIER BD-500 CSeries CS300. Available online: https://perma.cc/J26A-U69U (accessed on 30 April 2021).

32. Nuic, A.; Poles, D.; Mouillet, V. BADA: An advanced aircraft performance model for present and future ATM systems. *Int. J. Adapt. Control Signal Process.* **2010**, *24*, 850–866. [CrossRef]

33. Trifari, V. Development of a Multi-Disciplinary Analysis and Optimization Framework and Applications for Innovative Efficient Regional Aircraft. Ph.D. Thesis, University of Naples Federico II, Naples, Italy, 17 April 2020.

34. Jet Fuel Price Monitor. Available online: https://perma.cc/S3KC-WNV4 (accessed on 30 April 2021).

35. Airbus 2018 Price List Press Release. Available online: https://perma.cc/42VR-39YS (accessed on 30 April 2021).

36. JetBlue Picks Pratt over CFM for Engines Valued at $1.03 Billion. Available online: https://perma.cc/AL3M-Z8EJ (accessed on 30 April 2021).

Article

Sources of Onboard Fumes and Smoke Reported by U.S. Airlines

Judith Anderson (ORCID)

Department of Air Safety, Health, & Security, Association of Flight Attendants-CWA AFL-CIO, 501 3rd St. N.W., Washington, DC 20001, USA; judith@afanet.org

Abstract: This paper describes the relative frequency of reports of oil and hydraulic fluid fumes in the ventilation supply air ("fume events") compared to other types of fumes and smoke reported by U.S. airlines over 10 years. The author reviewed and categorized 12,417 fume/smoke reports submitted to the aviation regulator to comply with the primary maintenance reporting regulation (14 CFR § 121.703) from 2002–2011. The most commonly documented category of onboard fumes/smoke was electrical (37%). Combining the categories of "bleed-sourced", "oil", and "hydraulic fluid" created the second most prevalent category (26%). The remaining sources of onboard fumes/smoke are also reported. To put the data in context, the fume event reporting regulations are described, along with examples of ways in which certain events are underreported. These data were reported by U.S. airlines, but aviation regulations are harmonized globally, so the data likely also reflect onboard sources of fumes and smoke reported in other countries with equivalent aviation systems. The data provide insight into the relative frequency of the types of reported fumes and smoke on aircraft, which should drive design, operational, and maintenance actions to mitigate onboard exposure. The data also provide insight into how to improve current fume event reporting rules.

Keywords: aircraft; fume event; reporting; engine oil; hydraulic fluid; electrical

1. Introduction

The majority of commercial and military aircraft are designed to extract (or "bleed") the cabin and flight deck ventilation air from an engine compressor located upstream of the cabin and flight deck, whether the compressor is in the main aircraft engines or an auxiliary engine in the tail of the aircraft called the auxiliary power unit (APU). The problem with this "bleed air" design is that the oil that lubricates the engine compressors can contaminate the ventilation supply air. This can be caused by an actual mechanical failure or by the effects of engine parts subjected to physical and thermal stress during engine power setting changes, improper oil drainage/reingestion, or overfilling of an oil reservoir during servicing [1–4]. Additionally, small amounts of oil seep past the engine/APU bearing chamber seals into the compressor air flow, which is considered normal and acceptable if the volume of oil loss over time is within defined limits [1–4]. When oil contaminates the bleed air stream, the fumes are delivered to the cabin and flight deck located downstream of the compressor. The APU (and, less often, the main engines) can also ingest hydraulic fluid that has spilled or leaked from a burst line, a worn part, or overfilling during servicing. The ingested hydraulic fluid is also heated in a compressor and, likewise, contaminates the ventilation air supplied to the flight deck and cabin. Engine oil and hydraulic fluid fumes contain a complex mixture of compounds, including base stocks, additives, and decomposition products generated upon exposure to heat and moisture [1,5]. Because current systems are not equipped with bleed air filters, these contaminants are mixed with the ventilation air and delivered to the occupied zones through the cabin and flight deck air supply vents.

Of the compounds that can contaminate the aircraft air supply system, oil and hydraulic fluid have received the most attention because of decades of reports of compromised flight safety and security when crewmembers are either impaired or incapacitated by acute

symptoms inflight [6–9]. Additionally, these "fume events" are associated with operational impacts, such as diversions, cancellations, and repeat events [10,11], as well as reports of chronic neurological and respiratory illness [12,13].

However, there are other sources of supply air contamination onboard aircraft, including engine exhaust, deicing fluid, birds, engine wash, and ambient pollution. Additionally, there are sources of airborne chemical contaminants inside the cabin and flight deck, including electrical systems (e.g., lights, heaters, doors, and entertainment systems), fans (e.g., ventilation recirculation, cooling blowers, etc.), ducting (blown or clogged), and defective batteries.

Globally, within the aviation industry, there is discussion and debate over the relative frequency and nature of the different types of onboard fumes/smoke reported by crewmembers to airlines and by airlines to regulatory agencies. The answers to these questions of "how often" and "what type" of onboard fumes are important because they directly influence the debate regarding what design, operational, and maintenance regulations are needed (if any) to mitigate exposure to fumes. Some reports recommend engineering control measures and worker training programs to prevent onboard exposure to engine oil and hydraulic fluid fumes to mitigate the associated flight safety and crew health hazards [14–16]. Other reports downplay the frequency and seriousness of engine oil and hydraulic fluid fume events, acknowledging that they occur, but referring to them as "smell events" and claiming that they are either "rare" or "extremely rare" [17–20], rendering additional engineering and maintenance control measures unnecessary.

The aviation regulator in the United States (Federal Aviation Administration, FAA) has acknowledged that airlines underreport fume events [21] and that some of the fume event data that airlines submit is not reported properly [22]. However, even the number of events that airlines document with the FAA significantly underrepresents the actual number of events because airlines are not required to report either events that occur during ground operations or events for which fumes or smoke were present, but a mechanical fault was not subsequently identified. Further, the FAA has significantly undercounted the number of oil and hydraulic fume event reports it received from U.S. airlines [23].

To identify the most effective means to mitigate exposure to onboard fumes and smoke, it is helpful to start by assessing the relative frequency of the sources of onboard fumes and smoke that are documented.

2. Materials and Methods

On 14 March 2014, the author filed a Freedom of Information Act (FOIA) request with the FAA, formally asking for a copy of reports of fumes and smoke in the cabin/flight deck that the FAA received from U.S. airlines occurring from 1 January 2002 through 31 December 2011 and including one or more of the following search terms: fume, odor, smell, smoke, bleed air. On 19 May 2015, the FAA sent the author two spreadsheets, one of which contained 15,885 reports that met the author's criteria and had been reported by airlines to comply with the agency's Service Difficulty Reporting (SDR) regulation (14 CFR § 121.703). The other spreadsheet contained 366 reports that also met the author's criteria and had been reported by airlines to comply with the agency's Accident and Incident Data System (AIDS) rule (Order 8020.11D, 2018). Other than a cursory review of the narrative fields, the AIDS data are not summarized in this study.

For each SDR fume/smoke report, the author reviewed the narrative field ("remarks") and other relevant details to determine the source of the fumes or smoke. The author excluded reports that did not involve actual fumes or smoke in the cabin or flight deck, and then categorized the remaining reports according to the specified/implied source of fumes (Table 1), based on a combination of the text in the narrative field and professional judgement. The categories were applied consistently throughout the data set according to objective criteria, wherever possible. For some reports, selecting the category involved a degree of personal judgement, for example, fumes from a failed or defective fan were generally classified as "fan", even though some of the failures were electrical rather than

mechanical. For narratives that described an unfamiliar mechanical condition or fault, the author relied on the professional judgement of two senior airline mechanics and two commercial airline pilots, respectively.

Table 1. Types/sources of onboard fumes/smoke.

Types/Sources of Onboard Fumes/Smoke (N = 15)
Air conditioning packs ("packs")
Battery (smoking, defective)
Bird strike (into engine)
Bleed source (specifics undefined)
Deicing fluid
Duct (blown, disconnected, clogged) and duct insulation
Electrical item/system
Engine oil
Engine wash
Fan
Fuel/exhaust
Hydraulic fluid
Oven (in the galley)
Other, not otherwise classified
Source not identified/report too vague to classify

When airline staff submit a fume/smoke report to the FAA's SDR system, they cite the "maintenance manual" chapter assigned to the report internally. These chapters were created by the Air Transport Association (ATA) and define both how airline pilots classify abnormal conditions in their logbooks, and how maintenance workers classify aircraft system troubleshooting and repairs in the maintenance records, all of which are traceable to the aircraft tail number. As another source of insight into sources of documented fumes and smoke inflight, the author summarized the airline-defined ATA chapters for the whole data set and for the three leading sources of fumes.

3. Results

Of the 15,885 reports, the author excluded 3468 reports that did not involve an actual smoke or fume in the cabin or flight deck. Examples include "lens of smoke goggle was cracked" or "test of smoke detector failed". Those narratives included the word "smoke", but it is clear that no smoke was present.

3.1. Types of Onboard Fumes/Smoke Reported by U.S. Airlines

A total of 12,417 reports remained, including 12,382 reports that were assigned to one source category based on the narrative description, and 35 reports that were assigned to two categories, creating a total of 12,452 source types (Figure 1). Electrical fumes were the most documented type of report (37%). The combination of "bleed-sourced", "engine oil", and "hydraulic fluid" represented the second most documented type of report (26%). The third most documented mechanical failure that generated smoke or fumes was fans (8.5%), followed by air conditioning packs (6.4%), and fuel/exhaust (5.2%). A total of 1.8% of the reports were "other, not otherwise classified", which included sources that did not fit the other categories, such as engine failures, blown tires, and lightning strikes. Notably, for 9.1% of the reports, either the mechanical fault that created the fumes/smoke was either not identified or the airline supplied insufficient information for the author to reliably classify the source (e.g., "fumes reported during climb in the aft cabin").
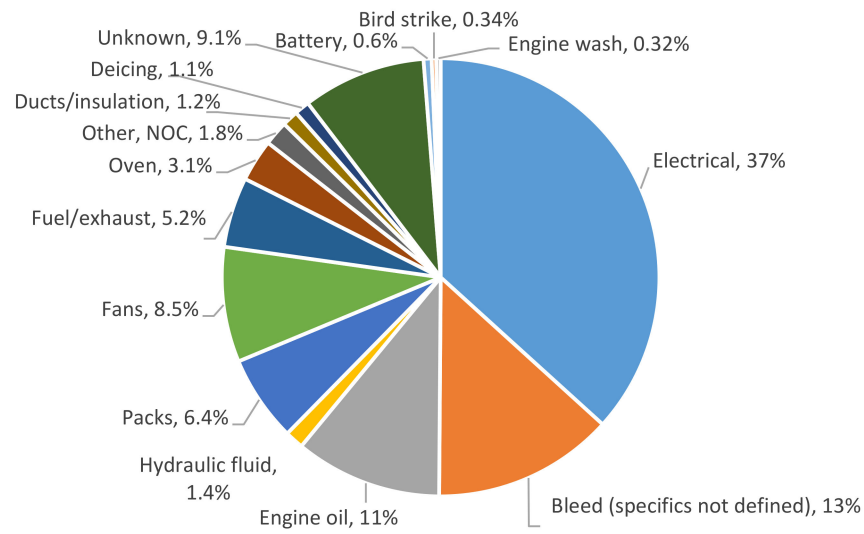
Figure 1. Sources of onboard fumes/smoke reported by U.S. airlines, 2002–2011 (*n* = 12,452).

3.2. ATA Chapters, Whole Dataset

Airlines classified 89% of the 12,417 reports into the nine ATA chapters listed in Figure 2, led by air conditioning (45%), and followed by lights (9.1%), equipment/furnishings (8.5%), airborne APU (8.1%), and engine (6.1%). The "other" category (Figure 2) represents reports that airlines classified into 29 additional ATA chapters, ranging from one to 211 reports per chapter.
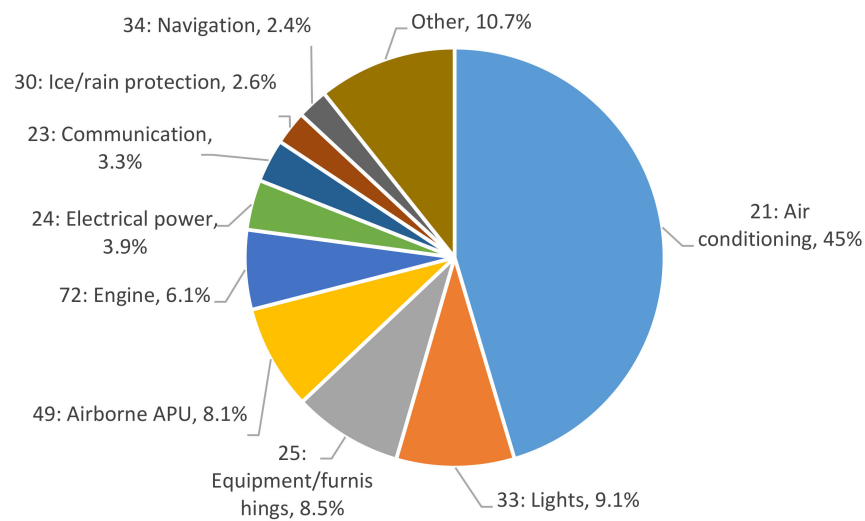

Figure 2. ATA chapters assigned by airlines to fumes/smoke reports, 2002–2011 (*n* = 12,417).

3.3. ATA Chapters, Onboard Electrical Fumes/Smoke

Of the 4573 reports that the author classified as electrical, the most commonly cited ATA chapters were lights (24%), air conditioning (15%), and equipment/furnishings (13%). The nine ATA chapters for 89.2% of these electrical reports are listed in Figure 3. Airlines classified the remaining 10.8% of the electrical reports into one of 24 additional ATA chapters (listed as "other" in Figure 3), reflecting the number and diversity of electrical systems onboard.
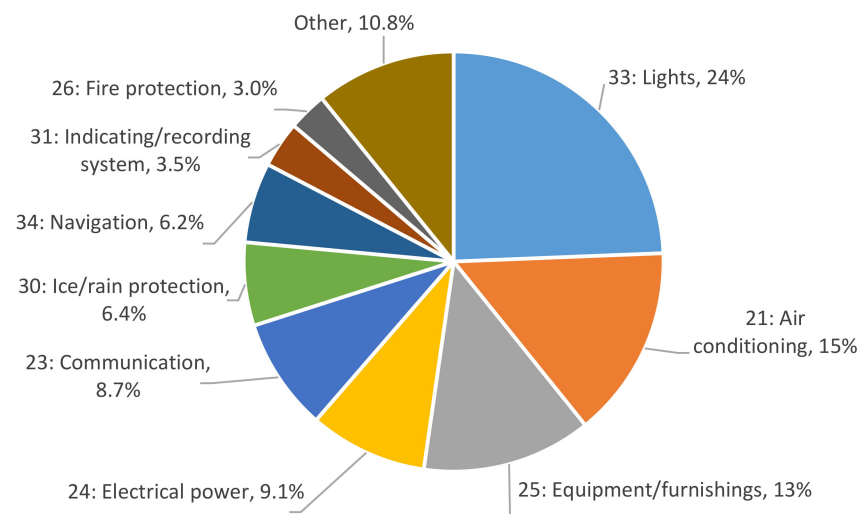
Figure 3. ATA chapters assigned by airlines to 4573 reports of electrical fumes/smoke.

3.4. ATA Chapters, Onboard Fume Events (Engine Oil, Hydraulic Fluid)

Of the 3360 reports that the author classified as either engine oil, bleed-sourced, or hydraulic fluid, the most commonly cited ATA chapters were air conditioning (51%), engine (20%), APU (18%), hydraulic power (3.7%), pneumatic (1.6%), and bleed air (1.1%) (Figure 4). Airlines classified the remaining 3.9% of these reports in one of 20 additional ATA chapters (listed as "other" in Figure 4). Note that four of the 3360 fume reports were classified as both oil and hydraulic fluid because maintenance found both contaminants in the bleed system during troubleshooting, but each of those four reports only had one assigned ATA chapter.
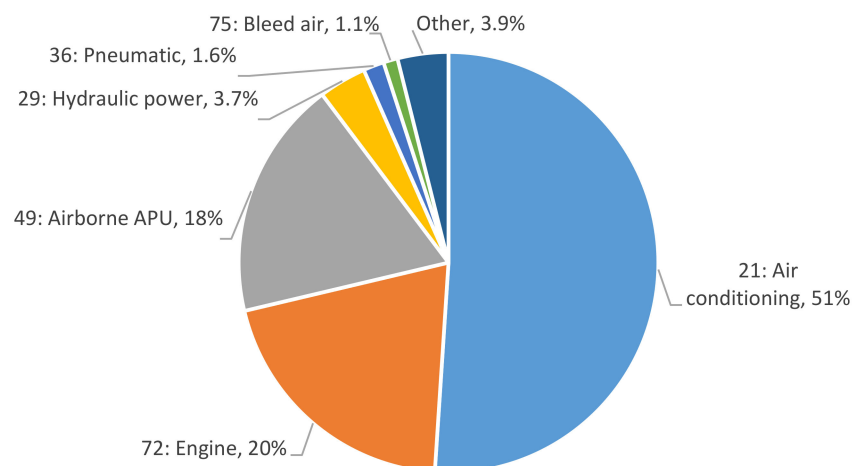
Figure 4. ATA chapters assigned by airlines to 3360 fume events (oil, hydraulic, bleed).

3.5. ATA Chapters, Onboard Fan-Sourced Fumes, and Smoke

Failures or malfunctions in a total of 23 types of fans were referenced in the fume and smoke reports (Table 2), eight of which appear to be related to the air conditioning system and are indicated with bold text in Table 2. Of the 1058 reports that the author classified as "fans", airlines classified the vast majority (96%) as air conditioning (ATA chapter 21). Airlines classified the remaining 4% of fan failures into one of 11 ATA maintenance manual chapters.

Table 2. Types of fans referenced in fume/smoke reports.

Types of Fans (N = 23) Identified as Sources of Fumes or Smoke in Airline Reports
Air Conditioning Condenser Cooling Fan
Advisory fan
Aft rack cooling fan
APU oil cooling fan
Attitude heading reference unit fan
Avionics cooling blower fan
Avionics vent blower
Cargo compartment fan
Cargo SD fans 1 and 2
Cargo smoke blower
Chiller fan (forward and aft)
Equipment cooling fan
Exhaust fan
Extract fan
Flight deck recirculation air fan
Galley oven fan
Ground cooling fan
Heat exchanger cooling fan
Instrument cooling fan
Inverter fan
Lavatory fan
Radio rack cooling fan
Recirculated air fan

3.6. Other Sources of Onboard Fumes/Smoke

In all, 6.4% of the 12,452 source types for the 12,417 reports (*n* = 793) were classified as "air conditioning packs" (indicated as "packs" in Figure 1) and 13% (*n* = 1667) were classified as "bleed, specifics not defined". There is more judgement involved with these categories than the others because, generally, the pack itself is not as much a *source* of contamination as it is a *sink* for sources of upstream contaminants. Those contaminants can be internal (e.g., leaking oil seal in the engine) or external (e.g., ingested exhaust fumes) and the soiling may build up gradually or be associated with a specific upstream failure. Additionally, the pack contains electrical components, which can fail. For these types of air supply system-sourced fumes, the author and, often, one of the selected experts (two pilots and two senior mechanics) had to make a judgement call as to whether the fumes were more likely sourced to the pack, bleed air upstream of the pack, or another external source. Generally, the "packs" category was chosen if a mechanical fault was later found in the pack. Such mechanical faults were typically not specified but were suggested because all or part of the pack was replaced. Conversely, the "bleed, specifics not defined" category was chosen if the fumes were reported during an engine power setting change (usually take-off/climb or descent), no mechanical fault was subsequently found (or inferred) in the pack, and an external source (such as exhaust fumes) was not referenced. A small subset of pack failures were classified as "engine oil" if the description of fumes was consistent with oil and the air cycle machine bearings in the pack would have been oil-lubricated.

In all, 1.8% of the 12,452 source types (*n* = 224) were classified as "other, not otherwise classified". The sources in this category included engine failures (unless oil fumes were specified), supply air from a ground cart, lightning strikes, blown tires, lavatory fluid, and maintenance products, such as grease or solvents.

Only 10 of the 12,417 fume/smoke reports cited odors that were sourced to either lavatory fluid or waste (e.g., servicing issue, blocked drain, leaking lav seals), so these were not assigned an independent category. Additionally, despite anecdotal reports that nail polish is a significant source of onboard fumes, there were only six reports that mentioned the smell of either nail polish or acetone, and the maintenance response indicated that none

of those reports were sourced to either product. Presumably, lavatory odors and nail polish are easily identifiable and, generally, do not require maintenance intervention.

4. Discussion

4.1. Airline Reporting Rules for Onboard Fumes/Smoke

In the U.S., commercial airlines are required to report each "failure, malfunction, or defect" that causes "smoke, vapor, toxic or noxious fumes" to accumulate or circulate in the flight deck or cabin during flight (defined as "wheels up") (14 CFR § 121.703(a)(5)). Airlines are also required to report ground-based events if the airline is of the "opinion" that flight safety could have been "endangered" had the aircraft continued (14 CFR § 121.703(c)). There are comparable SDR rules for charter flights, too (14 CFR § 135.415). These "Service Difficulty Reporting" (SDR) rules will not capture fume events for which the causal defect is not apparent during a ground-based inspection. For example, oil fumes that contaminate the bleed air through a worn engine part subjected to thermal or physical stress during an engine power setting change inflight need not be reported if that same part does not leak under ground-based conditions during a maintenance inspection. As well, when maintenance workers overfill the oil or hydraulic fluid reservoir, the subsequent spillage into the bleed air is a recognized source of fumes [24–26], but spillage is not a mechanical defect, so does not need to be reported.

In this dataset, 9.1% (*n* = 1135) of the SDR reports from airlines to the FAA do not offer insight into the relevant mechanical defect or failure. It is not clear if the fault is not described or not known when the report is submitted. Technically, though, it is the *defect* that is reportable, not the presence of fumes. Even though, there may not be an actual defect and, even when there is, maintenance troubleshooting can be "trial and error" [27], which can delay defect identification.

In addition to the SDR regulation for reporting onboard fumes and smoke, U.S. airlines must also report each "interruption to a scheduled flight" caused by a known *or suspected* (emphasis added) mechanical difficulty or malfunction, which is not required to be reported under the SDR rule (14 CFR § 121.705). However, it is difficult to assess the degree to which airlines comply with this rule because there is no central, searchable FAA database; rather, these "mechanical interruption reports" are maintained by individual FAA Certificate Management Offices, and only for one year.

Finally, U.S. airlines must also report "occurrences which affect or could affect safety of operations", including onboard fumes/smoke, to the FAA's "Accident and Incident Data System" (AIDS) per Order 8020.11D (2018). The author's 2014 FOIA request included AIDS reports with one or more of the same search terms requested for the SDR data, but U.S. airlines only submitted 2.3% as many fume/smoke reports to meet Order 8020.11D as compared to the SDR regulation (*n* = 366 compared to 15,885) during the same time period. It would be reasonable to assume that AIDS reports are the more serious events during which safety of operations was (or could have been) compromised. To test this hypothesis, the author compared the contents in the narrative fields of the AIDS and SDR datasets (which were selected based on the same set of search terms during the same time frame) and concluded that the nature and seriousness of the reports is comparable. It appears that the AIDS regulation is either ignored or misunderstood, and that compliance is not enforced.

In summary, then, if airline staff do not identify a mechanical source of reported fumes, or if the fumes occur before take-off, then the event is not reportable. If airline staff do identify a mechanical source of fumes, then the airline must report to the SDR database. If a mechanical source was suspected and the flight plan was affected, then the airline must report to the "mechanical interruption" database. In both of those scenarios, if safety either was or could have been compromised, then the airline must also report to the AIDS system. However, ground-based fume events can still compromise safety, fumes can occur without obvious mechanical defects, and an airline is unlikely to report the same event to two reporting systems. As a result, these reports of fumes and smoke are only a subset of the

actual events, and the data that do exist get scattered, all making an accurate assessment of the relative and absolute frequencies of different sources of onboard fumes and smoke even more difficult.

In addition to the complying with FAA reporting rules, U.S. airlines must report fume and smoke events to the U.S. National Transportation Safety Board (NTSB), if the event meets the NTSB definition of either an "accident" or "serious incident" (49 CFR § 830.5, 49 CFR § 830.2). Some fume events meet the NTSB reporting criteria, such as when a crewmember is hospitalized for more than 48 h during the seven days post-flight, sustains internal organ damage, or is unable to perform normal flight duties.

Another source of fume event data for the U.S. fleet is the "Aviation Safety Reporting System" (ASRS) database, hosted by the National Aeronautics and Space Administration (NASA). ASRS catalogues aircraft incident reports for a broad range of unsafe conditions from pilots, cabin crew, maintenance workers, air traffic controllers, and dispatchers. Reporting is voluntary and confidential, with the goal of circulating information about safety issues within the industry to prevent reoccurrences. Of 341 ASRS "smoke/fire/fumes/odor" events that crewmembers reported in 2016–2017, 35% were sourced to the air supply system and 20% were sourced to electrical faults [28].

4.2. Underreporting Engine Oil and Hydraulic Fume Events

Unfortunately, even within the narrowed scope of the reporting rules for fume and smoke events, there is evidence of airline underreporting. Some of the underreporting is cited for fume events in general. For example, in 2006, the FAA issued a bulletin for its maintenance inspectors, acknowledging poor airline compliance with the fume event reporting regulations. Specifically, the agency noted that "there have been concerns raised about numerous reports of [fume] events on commercial air carrier/operator aircraft. During the FAA's analysis of this [sic] data, it appears as though there are numerous [airlines] who may not have reported these events as required by regulation" [21].

There is evidence, however, that some underreporting is specific to oil and hydraulic fume events, reducing both the number of reports and the relative frequency of those events. For example, a review of fume events consistent with oil and hydraulic fluid sources at one U.S. airline over 18 months in 2009–2010 found that the airline had only reported 38% of 87 fume events documented by crewmembers to the FAA SDR system [11]. Part of this discrepancy is explained by the airline not consistently complying with the reporting rules, but part of it is explained by regulatory language that does not require airlines to report a significant fraction of documented events, as described above.

An example of underreporting specific to engine oil fumes is a 2013 report that the FAA sent to two Congressional committees regarding a law requiring the FAA to conduct research and development into sensor and filtration technology, specific to preventing exposure to oil fumes in the bleed air on commercial aircraft [29]. The FAA reported to Congress that officials had "mined" their fume event databases from 2002–2011, inclusive, for reports that included one or more of the search terms "fume, odor, smell, smoke, and bleed air", and that U.S. airlines had only reported 69 oil fume events and no hydraulic fluid events during those 10 years [23]. The FAA told Congress that, since the occurrence of these events was "extremely low", it could not justify spending its resources to research and develop bleed air sensors and filters. However, this analysis of those same cited reports from just one of the FAA databases using the same search terms identified oil as a source of fumes in 1353 reports, hydraulic fluid as a source in 173 reports, and bleed air contaminants consistent with oil/hydraulic fluid in 1667 reports. This type of underreporting reduces the relative frequency of these reports and downplays the need for relevant regulatory control measures.

Finally, underreporting oil and hydraulic fluid fume events is not limited to U.S. airlines. In 2011, the European Aviation Safety Agency (EASA) published comments it had received in response to the question of whether a rulemaking to address oil fumes in the cabin and flight would be justified. EASA noted multiple claims by advocates for pilots,

cabin crew, and passengers that European airlines underreport (a word used 53 times in the report) fume events and that the safety impacts are downplayed [30]. Likewise, a report by the Australian Transport Safety Bureau (ATSB) noted evidence that Australian airlines underreport fume events, both to the ATSB and to the aviation regulator [31]. An Australian Senate Enquiry into fume events on one particularly problematic aircraft type noted "strong evidence of a tendency of pilots to under-report [fume events]", citing a combination of pressure from airline management and lack of training [32]. The International Civil Aviation Organization (ICAO) has formally recommended that airlines "encourage flight and cabin crew members to report fume events", referring to crew reports as "essential to assist airline maintenance technicians in identifying the root cause of an event and taking corrective action to prevent reoccurrence" [14]. Currently, though, fume event reporting to aviation regulators is largely limited to maintenance defect reporting.

4.3. Estimates of the Frequency of Engine Oil and Hydraulic Events

The answer to the question of how often oil and hydraulic fluid fume events happen during commercial airline flights is a subject of considerable debate within the industry. It is important to get an accurate answer because, as the FAA's 2013 report to Congress illustrates [23], the answer will influence the regulatory agenda. The FAA itself acknowledges this reality in a 2016 bulletin in which the agency notified airlines "that some data required by [the SDR rule] is not being entered properly" and that "[b]ecause of poor data integrity, the FAA, manufacturers, and air carriers are unable to accurately detect trends necessary to proactively mitigate risk" [22].

One of the first estimates of how often oil and hydraulic fluid fume events occur was published in a 2002 U.S. National Research Council (NRC) committee report about aspects of aircraft air quality associated with potentially negative impacts on crew and passenger health. The report referenced fume event data collected at three airlines "over several years", which ranged from 0.9 events per 10,000 flights on Boeing 737 aircraft up to 39 events per 10,000 flights for the British Aerospace 146 [33]. The NRC committee issued a series of recommendations to the FAA, including that the agency "rigorously demonstrate" the "adequacy" of its cabin air regulations. In response, the FAA acknowledged that its "rulemaking has not kept pace with public expectation and concern about air quality and … [n]o present airplane design … incorporates an air contaminant monitoring system to ensure that the air provided to the occupants is free of hazardous contaminants … " [34]. As of this writing, the FAA has still not initiated a rulemaking on this subject.

In 2010, the FAA published an informational bulletin for airlines, stating that the agency " … continues to receive over 900 reports a year on [all sources of] smoke or fumes in the cabin and or cockpit" [35]. Based on the number of flights in 2010 [36], this translates into 0.9 events per 10,000 flights. The FAA noted that, "in fact, it is not unusual to receive more than one report during a 24-h period. For instance, on one day in April of 2010, five reports of smoke in the cockpit came in from one [airline]. All these incidents prompted the flightcrew to declare emergencies and divert to the nearest airport" [35].

In 2013, the International Air Transport Association (IATA) reported on its analysis of operational safety reports from more than 150 airlines covering almost 31 million flights during the period 2008–2012 [37]. Of these, 3444 reports were categorized as "smoke, fumes, and odor", which is equivalent to about one reported event per 10,000 flight cycles. Engine-related fumes were the most commonly reported source (23%), followed by electrical-related fumes (15%). Maintenance action was the most common operational effect (25%).

In 2015, FAA-funded researchers published their review of engine oil and hydraulic fluid fume events identified in FAA, NTSB, and NASA databases from 2007–2012 and sorted them by aircraft type. They concluded that U.S. airlines reported fume events on almost every aircraft type at an average frequency of two events per 10,000 flights [38], which translates into an average of 5.3 events per day based on the number of flights operated

during that time [36]. The authors reported "substantial variation" in the frequency of reports by aircraft type, with the maximum being eight reported events per 10,000 flights.

4.4. Recommendations to Improve Data Collection for Onboard Fumes/Smoke

Beyond the need for better compliance and enforcement of existing regulations, this review of SDR data from 2002–2011 provides insight into how fume reporting regulations could be improved.

First, SDR data would be more representative if airlines were required to report the presence of onboard fumes/smoke during ground operations, not just inflight. Industry sources confirm that the APU (which is the typical bleed air source during ground operations, whether at or away from the gate) is a source of oil and hydraulic fluid fumes [25]. Reports confirm that APU oil fumes, which contaminate the cabin or flight deck air during ground operations, can generate reports of crew ill health [11]. Additionally, if fumes that manifest on the ground are not resolved, they can continue inflight [25], which can affect both the safety of operations [26] and the health of the crew and passengers [11]. For these reasons, ground-based fume events should be documented and prevented.

Second, reported onboard fumes/smoke for which there is no obvious mechanical fault should still be reportable. For example, overfilling an oil or hydraulic fluid reservoir is a recognized source of fumes [26,39]. Additionally, some faults (such as oil leakage through a worn but not defective engine seal) that introduce fumes to the cabin air may only happen during the stress of a high-engine power setting, for example, and may not be recreated during routine ground-based troubleshooting [40]. Maintenance staff may not identify the relevant mechanical failure even for serious events, such as those involving pilot impairment and incapacitation [6]. SDR data would be more representative and useful if the presence of fumes/smoke caused by even a suspected defect or failure (defined to include spills and leaks) was reportable.

Third, it would be easier for SDR database users to answer the "how often" and "what type" questions regarding onboard fumes/smoke if the FAA's report categories were more tailored to the actual sources of fumes (see Figure 1), or if airlines could choose more than one category. For example, a pull-down menu for airlines to select standardized responses to the question of "source" would assist with subsequent analyses. The narrative field for each report can provide useful details but is too technical to be interpreted by software. Currently, when an airline submits a report, they must choose the most relevant category ("nature condition"), as defined by the FAA. One of the FAA categories is "smoke/fumes/odors/sparks", but only 76% of the 3360 events the author classified as "oil", "hydraulic", or "bleed-sourced" were categorized as such. U.S. airlines categorized another 16% of those bleed air reports as "fluid loss" and assigned the remaining 8% to one of 13 additional categories. For the full dataset (*n* = 12,417, all sources), airlines classified 84% of the reports as "smoke/fumes/odor/sparks" and 5.4% as fluid loss. In both cases, selecting only the "smoke/fumes/odor/sparks" category to search for fume and smoke reports seems reasonable but would underestimate the number of relevant reports.

Lastly, a crewmember reporting system for fume events to supplement the existing maintenance reporting systems is needed and must be accompanied by suitable training programs to ensure that crewmembers know how to recognize and respond to different types of onboard fumes and smoke [14]. This point has been raised since at least 2002, starting with an NRC committee, which recommended that the FAA establish a crewmember reporting system to collect air quality event data and associated symptom reports [33]. The following year, Congress passed a law requiring the FAA "to establish an air quality incident reporting system" [41]. Nine years later, Congress again required the FAA to "establish a systematic reporting standard for smoke and fume events in aircraft cabins" [42]. In 2017, the Cabin Air Safety Act of 2017 was introduced to the floor of the U.S. Senate, and the Know Before You Fly Act was introduced to the floor of the U.S. House. Again, these bills called on the FAA to establish a system for crewmembers and mechanics to report fume events on commercial aircraft, but neither bill was passed. In early 2018, the

FAA recommended that airlines "assess current policy and procedures" regarding their procedures to differentiate and mitigate smoke and fumes, but the FAA did not mandate event reporting [43]. Most recently, in October 2018, Congress mandated that the FAA "issue guidance for airline crews and maintenance technicians to report incidents of smoke or fumes on board an aircraft operated by a commercial air carrier" [44]. In March 2021, the FAA launched a cabin air quality website that includes a link to a voluntary, deidentified reporting system operated by NASA and a link to the FAA's maintenance defect reporting system [45]. However, the FAA has still not implemented crewmember reporting systems for fume events on commercial aircraft.

5. Conclusions

Of the onboard fumes/smoke that U.S. airlines reported to the regulatory agency over a 10-year period, electrical-sourced fumes and smoke were the most prevalent (37%), reflecting the number and diversity of onboard electrical systems and associated faults (Figures 1 and 3).

Bleed air issues (i.e., either confirmed or suspected engine oil and hydraulic fluid fumes) were the second most prevalent type of reported fumes/smoke (26%), and airlines internally classified 89% of those reports as either air conditioning, engine, or APU (Figures 1 and 4). Oil fumes were reported almost eight times more frequently than hydraulic fluid fumes (Figure 1).

Fans were the third most prevalent source of reported fumes/smoke (8.5%), most of them related to the air conditioning systems (Figure 1, Table 2). It would be worth investigating how to either improve the design of these fans or to implement an inspection program (e.g., measure vibration or electrical current draw) as preventive maintenance.

It is important to note that, although these data were reported by U.S. airlines, the harmonized nature of regulations that govern aircraft design, maintenance, and operating practices means that the data likely also reflect the onboard sources of fumes and smoke reported in other countries with equivalent aviation systems.

To more accurately count the number and types of fumes/smoke on U.S.-registered aircraft, it would be helpful if the FAA improved its current maintenance reporting regulations by requiring airlines to report both ground-based events and those for which a mechanical fault is not readily identified. In addition, there is a need for the FAA—and its equivalent regulatory bodies around the world—to implement a reporting system for crewmembers to gather data on the health and safety implications of exposure to air supply system-sourced fumes onboard, as per the recommendation of the ICAO [14].

Finally, the proportion of reported fume events that involve engine oil/hydraulic fluid described here, in conjunction with a more expansive review of the frequency of reported fume events on US airlines [38] and reports that flight safety can be compromised (cited above) support the installation and operation of equipment to filter and monitor bleed air contaminants in real time when aircraft are in operation. In the U.S., research into suitable technologies was most recently called for in legislation passed in 2012 [29] and 2018 [44]. Progress is slow, but there is progress, nonetheless; in late 2020, an FAA-funded research consortium held its first meeting on technologies intended to monitor bleed air contaminants and detect events in real time.

Acknowledgments: The author particularly thanks the two commercial pilots and two airline mechanics for their insights into the sources of fumes and smoke in so many of the reports described in this paper, and also for their patience and good humor.

Conflicts of Interest: The author declares no conflict of interest.

Abbreviations

The following abbreviations are used in this manuscript.

APU	Auxiliary Power Unit
ASRS	Aviation Safety Reporting System
ATA	Air Transport Association
ATSB	Australian Transport Safety Bureau
FAA	United States Federal Aviation Administration
NASA	United States National Aeronautics and Space Administration
NRC	United States National Research Council
NTSB	United States National Transportation Safety Board
SDR	Service Difficulty Report

References

1. Johnson, D.W. Turbine engine lubricant and additive degradation mechanisms. In *Aerospace Engineering*; Intech Open: London, UK, 2018; p. 19. Available online: https://doi.org/10.5772/intechopen.82398 (accessed on 12 April 2021).
2. USPTO. *Seal Assembly and Method for Reducing Aircraft Engine Oil Leakage*; U.S. Patent No. 10927845; assigned to The Boeing Company; Lin, C.-H., Horstman, R., Bates, G., Eds.; US Patent & Trademark Office: Washington, DC, USA, 2021. Available online: https://perma.cc/8D7V-Q863 (accessed on 9 April 2021).
3. Michaelis, S. Aircraft clean air requirements using bleed air systems. *Engineering* **2018**, *10*, 142–172. Available online: https://doi.org/10.4236/eng.2018.104011 (accessed on 14 April 2021). [CrossRef]
4. Chupp, R.E.; Hendricks, R.C.; Lattime, S.B.; Steinetz, B.M. *Sealing in Turbomachinery, NASA/TM—2006-214341*; National Aeronautics and Space Administration, Glenn Research Center: Cleveland, OH, USA, 2006. Available online: https://perma.cc/PY5C-4LHU (accessed on 12 April 2021).
5. Van Netten, C.; Leung, V. Hydraulic fluids and jet engine oil: Pyrolysis and aircraft air quality. *Arch. Environ. Health* **2001**, *56*, 181–186. Available online: https://doi.org/10.1080/00039890109604071 (accessed on 12 April 2021). [CrossRef] [PubMed]
6. AAIB. *Bulletin No. 9/2020, G-EUYB (AAIB-26125), Air Accidents Investigation Branch*; UK Department for Transport: Aldershot, UK, 2020. Available online: https://perma.cc/GWD2-RWVW (accessed on 12 April 2021).
7. AAIB. *Bulletin No. 3/2013, G-FCLA (EW/G2012/10/09). Air Accidents Investigation Branch*; UK Department for Transport: Aldershot, UK, 2013. Available online: https://perma.cc/QE5D-SLDX (accessed on 9 April 2021).
8. Montgomery, M.R.; Wier, G.T.; Zieve, F.J.; Anders, M.W. Human intoxication following inhalation exposure to synthetic jet lubricating oil. *Clin. Toxicol.* **1977**, *114*, 423–426. Available online: https://doi.org/10.3109/15563657708988205 (accessed on 12 April 2021). [CrossRef] [PubMed]
9. Armstrong, H.G. Noxious fluids and gases in aviation. In *Chapter XI in Principles and Practice of Aviation Medicine*; The Williams & Wilkins Company: Baltimore, MD, USA, 1939; pp. 178–180.
10. AAIB. *Bulletin No. 12/2019, G-YMMU (EW/G2019/07/01). Air Accidents Investigation Branch*; UK Department for Transport: Aldershot, UK, 2019. Available online: https://perma.cc/JDZ5-CL54 (accessed on 9 April 2021).
11. Murawski, J.T.L. Case study: Analysis of reported contaminated air events at one major U.S. airline in 2009–2010. In Proceedings of the 41st International Conference on Environmental Systems, Portland, Oregon, 17–21 July 2011; American Institute of Aeronautics & Astronautics: Reston, VA, USA, 2011. Paper ID: AIAA2011-5089. Available online: https://doi.org/10.2514/6.2011-5089 (accessed on 12 April 2021). [CrossRef]
12. Michaelis, S.; Burdon, J.; Howard, C.V. Aerotoxic syndrome: A new occupational disease? *Public Health Panor.* **2017**, *3*, 198–211. Available online: https://apps.who.int/iris/handle/10665/325308 (accessed on 12 April 2021).
13. Bobb, A.J.; Still, K.R. *Known Harmful Effects of Constituents of Jet Oil Smoke*; Report No TOXDET-03-04; Naval Health Research Center Detachment (Toxicology), Wright Patterson Air Force Base: Dayton, OH, USA, 2003. Available online: https://perma.cc/DNY6-AGZS (accessed on 12 April 2021).
14. ICAO. *Circular No. 344-AN/202: Guidelines on Education, Training and Reporting Practices Related to Fume Events*; Approved by and published under the authority of the Secretary General; International Civil Aviation Organization: Montreal, QC, Canada, 2015; ISBN 978-92-9249-856-6. Available online: https://perma.cc/R4UZ-DNQH (accessed on 12 April 2021).
15. AAIB. *Bulletin No. 4/2007, G-JECE (EW/C2005/08/10). Air Accidents Investigation Branch*; UK Department for Transport: Aldershot, UK, 2007. Available online: https://perma.cc/7JX9-8JBC (accessed on 12 April 2021).

16. Reddall, H.A. Elimination of Engine Bleed Air Contamination. In Proceedings of the SAE Golden Anniversary Aeronautic Meeting, Hotel Statler, Los Angeles, CA, USA, 11–15 October 1955; SAE Technical Paper 550185. SAE Aerospace: Warrendale, PA, USA, 1955. Available online: https://doi.org/10.4271/550185 (accessed on 14 April 2021).

17. Schuchardt, S.; Koch, W.; Rosenberger, W. Cabin air quality—Quantitative comparison of volatile air contaminants at different flight phases during 177 commercial flights. *J. Build. Environ.* **2019**, *48*, 498–507. Available online: https://doi.org/10.1016/j.buildenv.2018.11.028 (accessed on 14 April 2021). [CrossRef]

18. EASA. *Research Project: CAQ Preliminary Cabin Air Quality Measurement Campaign*; Report No. EASA_REP_RESEA_2014_4; Schuchardt, S., Bitsch, A., Koch, W., Rosenberger, W., Eds.; European Aviation Safety Agency: Cologne, Germany, 2017; Available online: https://perma.cc/EN8D-6YY7 (accessed on 9 April 2021).

19. FAA. *Bleed Air Contaminants: A review, DOT/FAA/AM-15/20*; Day, G.A., Ed.; Civil Aerospace Medical Institute, Federal Aviation Administration: Oklahoma City, OK, USA, 2015. Available online: https://perma.cc/4SGU-GN9T (accessed on 9 April 2021).

20. Boeing. Memorandum by the Boeing Company, Seattle, Washington. Submitted to: Air Travel and Health: An Update. UK House of Lords Science and Technology Committee, 1st Report of Session 2007–2008, Published by the Authority of the UK House of Lords. The Stationery Office Limited: London, UK, 2007; pp. 113–115. Available online: https://perma.cc/54L7-E5HR (accessed on 9 April 2021).

21. FAA. Flight Standards Information Bulletin for Airworthiness (FSAW) 06-05A: Guidance for Smoke/Fumes in the Cockpit/Cabin. U.S. Federal Aviation Administration: Washington, DC, USA, 2006. Available online: https://perma.cc/N89W-AL8R (accessed on 12 April 2021).

22. FAA. *Information for operators (InFO) 16009: Title 14 of the Code of Federal Regulations (14 CFR) Part 121, § 121.703 Service Difficulty Reports (SDR)*; Federal Aviation Administration, Flight Standards Service: Washington, DC, USA, 2016. Available online: https://perma.cc/G4T4-PV86 (accessed on 9 April 2021).

23. FAA. Report to Congress on Public Law 112-95, FAA Modernization and Reform Act of 2012, Section 917: Research and Development of Equipment to Clean and Monitor the Engine and Auxiliary Power Unit Bleed Air Supplied on Pressurized Aircraft. Prepared for FAA's Quality, Integration and Executive Services in Response to FAA's Aviation Safety legislative Implementation Plan by FAA's Office of Accident Investigation & Prevention. U.S. Federal Aviation Administration: Washington, DC, USA, 2013. Available online: https://perma.cc/F6SU-KVLG (accessed on 9 April 2021).

24. BFU. Study of Reported Occurrences in Conjunction with Cabin Air Quality in Transport Aircraft. Report No. BFU 803.1-14; Bundesstelle Für Flugunfalluntersuchung, German Federal Bureau of Aircraft Accident Investigation: Braunschweig, Germany, 2014. Available online: https://perma.cc/XPR9-GE6E (accessed on 9 April 2021).

25. Airbus. A Clean APU Means Clean Cabin Air, Flight Airworthiness Support Technology (FAST). *Airbus SAS* **2013**, *52*, 4–9. Available online: https://perma.cc/8PJ2-NVP8 (accessed on 9 April 2021).

26. AAIB. *Report on the Serious Incident to Boeing 757-236, G-CPER on 7 September 2003*; Air Accidents Investigation Branch, UK Department for Transport: Aldershot, UK, 2005. Available online: https://perma.cc/VJ66-3FLR (accessed on 12 April 2021).

27. Overfelt, R.A.; Jones, B.W.; Loo, S.M.; Haney, R.L.; Neer, A.J.; Andress, J.R.; Yang, X.; Zitova, A.; Prorok, B.C.; Fergus, J.W.; et al. *Sensors and Prognostics to Mitigate Bleed Air Contamination Events*; Report No. RITE-ACER-CoE-2012-05, Report Prepared for the Federal Aviation Administration; National Air Transportation Center of Excellence for Research in the Intermodal Transport Environment (RITE) Airliner Cabin Environment Research Program (ACER): Washington, DC, USA, 2012. Available online: https://perma.cc/HCZ8-J687 (accessed on 12 April 2021).

28. O'Connor, M.; Stolzer, A. Hazard Identification: Voluntary Safety Reports of Potential Contaminated Bleed Air Events. NIOSH Western States Division and Embry-Riddle Aeronautical University. In Proceedings of the Aerospace Medical Association Annual Scientific Meeting, Las Vegas, NV, USA, 5–9 May 2019; Available online: https://perma.cc/6RAL-BPUP (accessed on 14 April 2021).

29. U.S. Public Law 112-381, §917. Research and Development of Equipment to Clean and Monitor the Engine and APU Bleed Air Supplied on Pressurized Aircraft. 14 February 2012. Available online: https://perma.cc/26SZ-557F (accessed on 12 April 2021).

30. EASA. *Comment Response Document on Notice of Proposed Amendment 2009–10: Cabin Air Quality Onboard Large Aeroplanes*; European Aviation Safety Agency: Cologne, Germany, 2011; Available online: https://perma.cc/ZLS5-W2FM (accessed on 13 April 2021).

31. ATSB. *An Analysis of Fumes and Smoke Events in Australian Aviation, 2008–2012*; Aviation Research Report AR-2013-213; Australian Transport Safety Bureau: Canberra, Australia, 20 May 2014. Available online: https://perma.cc/Y2XQ-KSFL (accessed on 13 April 2021).

32. PCA. Chapter 6: Conclusions and recommendations. See Section 6.1.8; In *Air Safety and Cabin Air Quality in the BAE 146 Aircraft*; Senate Rural and Regional Affairs and Transport References Committee of the Parliament of the Commonwealth of Australia: Canberra, Australia, 2000; ISBN 0-642-71093-7. Available online: https://perma.cc/TQ2E-VPG2 (accessed on 13 April 2021).

33. NRC. *The Airliner Cabin Environment and the Health of Passengers and Crew*; U.S. National Research Council; National Academy Press: Washington, DC, USA, 2002; 326p, ISBN 0-309-08289-7. Available online: https://perma.cc/5L4Y-DJT7 (accessed on 14 April 2021).

34. FAA. Response to recommendation 1—Air quality and ventilation. In *Report to the Administrator on the National Research Council Report, The Airliner Cabin Environment and the Health of Passengers and Crew*; U.S. Federal Aviation Administration: Washington, DC, USA, 2002. Available online: https://perma.cc/9QTP-CS82 (accessed on 14 April 2021).

35. FAA. *Information for Operators (InFO 10019): Smoke/Fumes in the Cabin/Cockpit of Transport Category Aircraft*; U.S. Federal Aviation Administration Flight Standards Service: Washington, DC, USA, 2010. Available online: https://perma.cc/E6TB-Q8RE (accessed on 12 April 2021).

36. BTS. T-100 Data, All U.S. Carriers, All Airports (2002–2020). Bureau of Transportation Statistics, U.S. Department of Transportation, 2002–2011. Available online: https://perma.cc/3RVC-SSGQ (accessed on 13 April 2021).

37. IATA. Global Safety Information Center STEADES Analysis: Smoke and Fumes (Smells in the Cabin and on the Flight Deck). Safety Trend Evaluation, Analysis, and Data Exchange System. Global Safety Information Center, International Air Transport Association: Montreal, Canada, 2013. Available online: https://perma.cc/GAK9-66HW (accessed on 14 April 2021).

38. Shehadi, M.; Jones, B.; Hosni, M. Characterization of the Frequency and Nature of Bleed Air Contamination Events in Commercial Aircraft. *Indoor Air* **2016**, *26*, 478–488. Available online: https://doi.org/10.1111/ina.12211 (accessed on 12 April 2021). [CrossRef] [PubMed]

39. ASHRAE. Section 8.6 (Hydraulic Fluid) and Section 8.7 (Engine Oil). In *Air Quality within Commercial Aircraft*; ANSI/ASHRAE Standard 161-2018; American Society of Heating Refrigerating, and Air Conditioning Engineers: Atlanta, GA, USA, 2018; ISSN 1041-2336. Available online: https://perma.cc/QDN6-EMJG (accessed on 13 April 2021).

40. AAIB. Bulletin No. 6/2009, G-BYAO (EW/C2006/10/08). In *Air Accidents Investigation Branch*; UK Department for Transport: Aldershot, UK, 2009. Available online: https://perma.cc/Y5YQ-Q7MF (accessed on 13 April 2021).

41. U.S. Public Law 108-176, § 815(b)(5). Air Quality in Aircraft Cabins. 12 December 2003. Available online: https://perma.cc/DY4P-UHB8 (accessed on 13 April 2021).

42. U.S. Public Law 112-381, §320(a)(4). Study of Air Quality in Aircraft Cabins. 14 February 2012. Available online: https://perma.cc/26SZ-557F (accessed on 13 April 2021).

43. FAA. *Safety Alert for Operators (SAFO) 18003: Procedures for Addressing Odors, Smoke and/or Fumes in Flight*; Federal Aviation Administration, Flight Standards Office: Washington, DC, USA, 2018. Available online: https://perma.cc/GA2E-WWAJ (accessed on 13 April 2021).

44. U.S. Public Law 115-254, §326. Aircraft Air Quality. 5 October 2018. Available online: https://perma.cc/H4UK-UPQ8 (accessed on 13 April 2021).

45. FAA. *Information for Operators (InFO) 21002: Cabin Air Quality Educational Materials*; Federal Aviation Administration, Flight Standards Office: Washington, DC, USA, 2021. Available online: https://perma.cc/CS46-CW4E (accessed on 13 April 2021).